Influence of oxygen fugacity on the viscosity of CO_2-, H_2O-, and halogen-bearing basaltic melts

Dissertation

zur Erlangung des mathematisch-naturwissenschaftlichen Doktorgrades

„Doctor rerum naturalium“

der Georg-August-Universität Göttingen

im Promotionsprogramm Geowissenschaften/Geographie

der Georg-August University School of Science (GAUSS)

vorgelegt von

Wiebke Pischel

aus Hildesheim

Göttingen, 2018

Betreuungsausschuss

Prof. Dr. Sharon L. Webb
Abteilung experimentelle und angewandte Mineralogie
Geowissenschaftliches Zentrum der Georg-August-Universität Göttingen

Dr. Burkhard C. Schmidt
Abteilung experimentelle und angewandte Mineralogie
Geowissenschaftliches Zentrum der Georg-August-Universität Göttingen

Mitglieder der Prüfungskommission

Referent 1
Prof. Dr. Sharon L. Webb
Abteilung experimentelle und angewandte Mineralogie
Geowissenschaftliches Zentrum der Georg-August-Universität Göttingen

Referent 2
Prof. Dr. Harald Behrens
Institut für Mineralogie
Leibniz Universität Hannover

Weitere Mitglieder der Prüfungskommission:

Prof. Dr. Gerhard Wörner
Abteilung Geochemie
Geowissenschaftliches Zentrum der Georg-August-Universität Göttingen

Dr. Burkhard C. Schmidt
Abteilung experimentelle und angewandte Mineralogie
Geowissenschaftliches Zentrum der Georg-August-Universität Göttingen

Dr. Sara Fanara
Abteilung experimentelle und angewandte Mineralogie
Geowissenschaftliches Zentrum der Georg-August-Universität Göttingen

Dr. Kirsten Techmer
Abteilung Kristallographie
Geowissenschaftliches Zentrum der Georg-August-Universität Göttingen

Tag der mündlichen Prüfung: 10.12.2018

Abstract

The aim of this study is to demonstrate the effect of chlorine (Cl^-), fluorine (F^-), water (H_2O) and carbon dioxide (CO_2) on the viscosity of basaltic melts and a comparison to literature models. The basaltic composition is similar to a melt of flat-topped volcano from Mid-Atlantic Ridge (MAR). The iron content was decreased, to avoid crystallisation of the glass. The study is divided into three series with different oxygen fugacity adjusted by diverse synthesis conditions.

Series (I), (II) and (III) represents basaltic melts doped with Cl^-, F^- and (Cl^- + F^-), which were synthesised in a 1 atm furnace at 1473 K for 4 to 9 h in air. Afterwards, all series (II) glasses are redox equilibrated in a vertical gas mixing furnace at 1473 K for up to 20 h under a carbon dioxide and hydrogen gas atmosphere. Therefore, different oxygen fugacity can be generated and results in diverse Fe^{2+}/Fe_{total}. The hydrous glasses with 0.5, 1.5 and 3.5 wt% H_2O and CO_2-bearing glasses with 1000 to 3500 ppm CO_2 of Series (III) were synthesised in the internally heated pressure vessel (IHPV). The experiments were performed at 1550 K and 300 MPa for 24 h with a rapid quench device. In addition to H_2O and CO_2-bearing glasses, dry and CO_2-free glasses are synthesised in the IHPV.

The high viscosity is measured by the micropenetration technique in the range of $10^{8.5}$ to $10^{13.5}$ Pa s. The Raman spectroscopy and colorimetric micro-determination of Fe^{2+} content can be used for structural analysis. The volatiles (F^-, H_2O and CO_2) decrease the viscosity of basaltic melts, whereas the addition of F^- shows the smallest effect on the viscosity and CO_2 results in the strongest decrease in viscosity. The addition of 12.56 mol% H_2O in halogen-free basalt results in a decrease in viscosity by 5.2 log units, whereas the presence of 0.34 mol% CO_2 to a basaltic melt results in a strong decrease in viscosity by 0.7 log units. The addition of 7.73 mol% F^- to basaltic glass results in a decrease in viscosity by 2.5 log units. Amounts with up to 2.53 mol% Cl^- in basaltic melts result in an increase in viscosity, whereas further addition of chlorine results in a decrease in viscosity. The comparison of the experimental viscosity data of basaltic melts reflects that the current viscosity models do not consider all volatiles (Cl^-, F^- and CO_2) and the models are calibrated for diverse amounts of volatiles (Giordano et al. 2008; Duan 2014; Sehlke and Whittington 2016). Especially, the variable effect of chlorine on the viscosity of peralkaline and peraluminous silicate melts should be noted in future models.

Furthermore, the addition of volatiles to basaltic melts changes the Fe^{2+}/Fe_{total}. In peralkaline melts, the addition of fluorine results in a oxidation of Fe^{2+} to Fe^{3+}, which reflects an increase in polymerisation due to the increase in network formers. The addition of water results in a depolymerisation of the structure due to increasing Fe^{2+}/Fe_{total}. The addition of OH groups in halogen-free and –bearing basaltic glasses shows a linear decrease in Fe^{2+}/Fe_{total}, whereas

the total water content shows an exponential trend. The OH groups describe the water species, which is incorporated into the melt structure. A linear relation between the addition of chlorine and iron speciation cannot be confirmed. Also, no dependence between CO_2 content and Fe^{2+}/Fe_{total} is observed. Kress and Carmichael (1991) developed a model for the determination of Fe^{2+}/Fe_{total} by means of melting temperature, oxygen fugacity and melt composition. The model considers the amounts of Al_2O_3, FeO_{total}, CaO, Na_2O and K_2O. The results of the iron determination show that the volatiles (F^- and H_2O) have a strong effect on the Fe^{2+}/Fe_{total}. Thus, the volatiles have to be included by future models.

The falling sphere technique was used to extend the measurable viscosity range of CO_2-bearing basaltic melts to low viscosity ranges. This experiment was performed at 1223 K and 200 MPa for 5 h in a water cooled RQ-CSPV (rapid quench - cold seal pressure vessels). In this temperature range, the CO_2-bearing basaltic glass crystallises and the actual experiments cannot be realised with the present basaltic composition.

Zusammenfassung

In dieser Studie wurden Volatile zu einer basaltischen Schmelze hinzugefügt und deren strukturellen Änderungen angedeutet. Das Ziel dieser Arbeit ist es, den Einfluss von Chlor (Cl^-), Fluor (F^-), Wasser (H_2O) und Kohlendioxid (CO_2) auf die Viskosität einer basaltischen Schmelze zu demonstrieren und in Kontext mit aktueller Literatur zu setzen. Die basaltische Zusammensetzung entspricht einer Schmelze vom „flat-topped volcano“ aus dem Mittelatlantischen Rücken (MAR). Da es während der ersten Experimente zu Kristallisation kam, wurde der Eisengehalt verringert. Die Studie unterteilt sich in drei Serien mit unterschiedlicher Sauerstofffugazität durch verschiedene Synthesebedingungen.

Die Serie (I), (II) und (III) beschreibt basaltische Gläser angereichert mit Cl^-, F^- und (Cl^- + F^-), welche in einem 1 atm Ofen bei 1473 K für 4 bis 9 h synthetisiert wurden. Anschließend erfuhr die Serie (II) eine Redox-Äquilibrierung in einem vertikalen Gasmischungsofen bei 1473 K für bis zu 20 h unter einer CO_2 und H_2 Atmosphäre. Dadurch konnten verschiedene Sauerstofffugazitäten eingestellt und somit unterschiedliche Fe^{2+}/Fe_{total} hervorgerufen werden. Wasserhaltige Gläser mit 0.5, 1.5 und 3.5 Gew% H_2O und CO_2-haltige Gläser mit 1000 bis 3500 ppm CO_2 wurden in einer intern beheizten Gasdruckanlage (IHPV) synthetisiert (Serie (III)). Die Experimente wurden bei 1550 K und 300 MPa für 24 h durchgeführt und mit 150 K min^{-1} gequencht.

Die hohen Viskositäten wurden mit Hilfe der Mikropenetrationstechnik im Bereich von $10^{8.5}$ bis $10^{13.5}$ Pa s bestimmt, wohingegen die strukturelle Änderung mittels Ramanspektroskopie und die Bestimmung der Eisenverhältnisse durch die nasschemische kolorimetrische Mikro-Bestimmung des Fe^{2+} Gehaltes ermittelt wurde. Die Volatile F^-, H_2O und CO_2 verringern die Viskosität von basaltischen Schmelzen, wobei F^- die geringste und CO_2 die stärkste Viskositätsabnahme zeigt. Der Einbau von 12.56 Mol% H_2O in Halogen-freien Basalten führt zu einer Viskositätsabnahme von 5.2 log Einheiten, wohingegen der Einbau von 0.34 Mol% CO_2 eine Viskositätsabnahme von 0.7 log Einheiten zeigt. Der Einbau von 7.73 Mol% F^- führt zu einem Sinken der Viskosität um 2.5 log Einheiten. Geringe Mengen von 2.53 Mol% Cl^- in basaltischen Schmelzen führen zu einem Viskositätsanstieg, wohingegen der weitere Einbau von Chlor zu einer Abnahme der Viskosität führt. Der Vergleich der experimentellen Viskositätsdaten der basaltischen Schmelzen zeigt, dass die aktuellen Modelle für Viskositäten nicht alle Volatile (Cl^-, F^- und CO_2) berücksichtigen und lediglich für geringe Gehalte kalibriert wurden (Giordano et al. 2008; Duan 2014; Sehlke and Whittington 2016). Insbesondere der unterschiedliche Einfluss von Chlor auf die Viskosität von peralkalischen und peraluminösen Schmelzen sollte beachtet werden. Des Weiteren wird der Einfluss von CO_2 auf die Viskosität von silikatischen Schmelzen in keinem aktuellen Modell thematisiert. Diese Ergebnisse sollten in zukünftige Viskositätsmodelle mit einbezogen werden.

Darüber hinaus führt der Einbau von Volatilen in basaltische Gläser zu einer strukturellen Veränderung des Fe^{2+}/Fe_{total}. In peralkalinen Schmelzen resultiert der Einbau von Fluor zu einer Oxidation von Fe^{2+} zu Fe^{3+}, dies führt zu einem Anstieg der Polymerisation durch den steigenden Netzwerkbildneranteil. Der Einbau von Wasser führt hingegen zu einer Depolymerisierung der Struktur infolge des sinkenden Fe^{2+}/Fe_{total}. Die OH Gruppen in Halogen-freien Basalten zeigen eine nahezu lineare Abnahme von Fe^{2+}/Fe_{total}, wohingegen die Auftragung gegen den totalen Wassergehalt zu einer exponentiellen Abnahme führt. Die OH Gruppen beschreiben die Wasserspezifikation, welche in die Schmelzstruktur eingebaut wird. Ein linearer Zusammenhang zwischen dem Einbau von Chlor und einer Veränderung der Eisenspezifikation konnte nicht bestätigt werden. Auch das Vorhandensein von CO_2 lässt keine lineare Beziehung zum Fe^{2+}/Fe_{total} erkennen. Kress and Carmichael (1991) haben ein Modell zur Berechnung des Fe^{2+}/Fe_{total} mit Hilfe der Schmelztemperatur, der Sauerstofffugazität und der Schmelzzusammensetzung aufgestellt. Dieses Modell berücksichtigt lediglich die Gehalte von Al_2O_3, FeO_{total}, CaO, Na_2O und K_2O. Die Ergebnisse der Eisenbestimmung zeigen, dass die Volatile (F^- und H_2O) einen großen Einfluss auf das Fe^{2+}/Fe_{total} haben und demnach mit in die Kalkulation einbezogen werden müssten.

Um den hohen Viskositätsbereich zu erweitern, sollten die niedrigen Viskositäten von CO_2-haltigen basaltischen Gläsern mit Hilfe der „falling sphere“ Methode ermittelt werden. Diese Experimente wurden bei 1223 K und 200 MPa für 5 h in einer wassergekühlten RQ-CSPV („rapid quench - cold seal pressure vessels“) durchgeführt. In diesem Temperaturbereich zeigte sich, dass die CO_2-haltigen Gläser kristallisieren und das eigentliche Experiment nicht mit dieser basaltischen Zusammensetzung realisierbar ist.

Danksagung

Ein besonderer Dank geht an Frau Prof. Dr. Sharon Webb und Herrn Dr. Burkhard Schmidt, die mir diese Doktorarbeit ermöglicht haben und mich in den letzten Jahren stets hervorragend betreut haben. Für ihr stets offenes Ohr und ihre Diskussionsbereitschaft bin ich sehr dankbar.

Im Weiteren möchte ich mich auch bei meinen Gutachtern und der Prüfungskommission Prof. Dr. Sharon Webb, Prof. Dr. Harald Behrens, Prof. Dr. Gerhard Wörner, Dr. Burkhard C. Schmidt, Dr. Sara Fanara und Dr. Kirsten Techmer für ihre Tätigkeit bedanken.

Ein besonderer Dank gilt meiner Freundin und Arbeitskollegin Tamara Busche für ihre hilfreichen Diskussionen und Unterstützung während meiner Promotion. Außerdem möchte ich mich bei meinen Kollegen und Freunden für die nette Arbeitsatmosphäre bedanken, vor allem bei Max Schanofski, Dr. Sara Fanara, Bettina Schlieper-Ludewig, Marina Horstmann, Alexander Masurowski und Petra Wolfrath.

Des Weiteren möchte ich mich herzlich bei Herrn Dr. Kronz für seine Hilfe an der Mikrosonde und Herr Dr. Klein für die Betreuung an der Computertomographie bedanken. Ein weiterer Dank gilt Prof. Dr. McCammon von der Fakultät für Biologie, Chemie und Geowissenschaften am Bayerischen Geoinstitut für die Durchführung der Mössbauer Spektroskopie Messungen.

Ganz herzlich bedanke ich mich bei Herrn Florian Kiesel für sein Korrekturlesen und der hilfreichen Kritik an meiner Dissertation.

Für die Ermutigung und Unterstützung während meiner Promotion bedanke ich besonders bei meinen Eltern. Der größte Dank gilt meinem Verlobten Sören Henning, der immer für mich da war und seiner stets konstruktiven Kritik während der Schreibphase sowie seinem Korrekturlesen.

Table of Contents

Preface

Basalt is an essential mafic igneous rock, which is formed in diverse tectonic environments such as mid-ocean ridges, island arcs, back-arc basins, intra-plate oceanic islands, large igneous provinces and intra-continental rifts. The terrestrial basalt represents the composition of the partial melting of the upper mantle. Furthermore, basalt is the most evolved magma due to fractional crystallisation in the Earth's crust (Gill 2010).

Temperature, oxygen fugacity, halogen and volatile content were found to be significant parameters affecting the Fe^{2+}/Fe_{total} (Kress and Carmichael 1991; Baasner et al. 2013b; Webb et al. 2014; Knipping et al. 2015). In this respect, Liebske et al. (2002) observed a decrease in viscosity by 1.7 log units for andesitic melts due to increasing Fe^{2+}/Fe_{total} from 0.42 to 0.79. Further authors discussed the effect of Fe^{2+}/Fe_{total} on the viscosity and heat capacity of silicate melts (Kress and Carmichael 1988; Kress and Carmichael 1991; Duan 2014; Webb et al. 2014; Duan 2014). This is of particular relevance for the preparation of a viscosity model, which is based only on the melt composition. Besides the Fe^{2+}/Fe_{total}, the volatiles affect the viscosity of silicate melts. Baasner et al. (2013a) suggested that F^- and H_2O decrease the viscosity of all silicate melts, whereas Cl^- shows an increase in viscosity of peralkaline melts. Furthermore, there is no data on the effect of CO_2 on the viscosity of basaltic melts. The different strong influence of volatiles has to be considered by the viscosity model, whereas the diverse effects of chlorine in peralkaline and peraluminous melts has to be noted.

The thesis is subdivided into four chapters. The first chapter describes the effect of halogens on the viscosity of basaltic melts. In the second chapter, the influence of varying oxygen fugacity on the viscosity is characterised. The third chapter focuses on the presence of H_2O and CO_2 in basaltic melts and their influence on the viscosity. The last chapter describes the falling sphere technique and the approach by CO_2-bearing basaltic melts. This thesis presents new viscosity data for volatile-bearing basaltic glasses with a varying oxygen fugacity, whereby the complex basaltic formation can be explained.

Introduction

Stebbins (2016) described glass as a “frozen and supercooled” liquid that is not in thermodynamic equilibrium. For this reason, the glass cannot reach a lower energy state and the molecules do not form a crystal. Glasses can be subdivided into natural or synthetic forms. Natural glasses form by rapid cooling processes out of melts as the melt freezes in a disordered structure with no long-range. The most important natural glass is obsidian. In the past, obsidian was used as weapons, tips for spears and arrows (Schaeffer et al. 2012). Today we use synthetic glasses as hollow-wares and flat glasses, fibre-optic cables and biomedical applications. Detailed knowledge on the physical and chemical properties of the glass forming melts is very important. Understanding of versatility and formation processes of natural glasses leads to further development of new applications.

Of the various different effects that different elements have on melt/glass structure and physical properties, iron is of great interest. The element iron exists in two stable oxidation states (Fe^{2+} and Fe^{3+}) in silicate melts. In general, the ferrous (Fe^{2+}) iron appears as a network modifier or charge compensator, whereas the ferric (Fe^{3+}) iron behaves as a network former (Mysen 1991; Virgo and Mysen 1985). Virgo and Mysen (1985) demonstrated that the ferric iron in oxidised silicate melts is in tetrahedral coordination, whereas the ferric iron in more reduced melts is coordinated as an octahedral structure unit similar to the ferrous iron. Consequently, a depolymerisation results by conversion of ferric iron from tetrahedral to octahedral coordination with changing fO_2 as well as the excepted change from Fe^{3+} to Fe^{2+}. Sack et al. (1980) describes the ferrous to ferric iron ratio as a function of composition, melt temperature, oxygen fugacity and volatile content. The structural position of ferrous and ferric iron in silicate melts shows an effect on the viscosity, heat capacity and density (Kress et Carmichael 1988). Thus, natural melts with defined Fe^{2+}/Fe_{total} indicate the redox conditions of the source regions during the evolution of the glasses. Furthermore, the iron speciation allows conclusions about melting and crystallisation histories (Christie et al., 1986). In all of these discussion, however, the effect of composition of Fe^{2+}/Fe_{total} needs to be remembered.

Natural basaltic magmas contain water and carbon dioxide as well as halogens such as chlorine and fluorine. The concentration of water varies from 0.10 to 1.00 wt% in basaltic magmas from mid-ocean ridges (Danyushevsky, 2001), whereas higher concentrations up to 6 wt% are found in Island Arc basalts (Wallace, 2005). Besides H_2O, carbon dioxide is the second most important volatile in magmatic systems (Morizet et al. 2001; Cartigny et al. 2008; Morizet et al. 2015). The study of Cartigny et al. (2008) indicates that MORB samples from mid-Atlantic ridges can contain up to 57 000 ppm CO_2 (Cartigny et al. 2008). The incorporation of volatiles in basaltic melts is limited to a maximum solubility depending on pressure. Wanless et al. (2011) measured chlorine concentrations up to 0.07 wt% in basaltic

melts and a higher concentration in basaltic andesite melts up to 0.31 wt% from mid-ocean ridge samples. Fluorine is found in glasses from Mid-Atlantic Ridges with an average concentration of 0.02 wt% (Byers et al. 1986) as well as 0.06 wt% in “MORB-like” basalts from Galapagos Archipelago plume (Byers et al. 1986; Koleszar et al. 2009). Both volatiles are found in melt inclusions from Siberia trap flood basalts with up to 0.94 wt% for chlorine (Bratsk dolerite) and 1.95 wt% for fluorine (Ust-Ilimsk dolerite) (Black et al. 2012). The presence of volatiles changes the structure and the physical behaviour of the melt and effects the eruption mechanism for different volcanoes; with high viscosity, low-volatile magmas tending toward explosive eruptions.

Structure of silicate glasses

The basis for the network structure of oxide glasses were identified in the publication “the atomic arrangement in glass” by W.H. Zachariasen (1932). The author suggests that the energy difference between glass and crystal with the same composition is very small. Zachariasen supposed some basic rules for the formation of oxide glasses:

(1) Coordination number of cations should be small,
(2) Oxygen ions should not bond to more than two cations,
(3) Oxygen polyhedrons should share corners and not edges or areas,
(4) Minimum three corners of oxygen polyhedrons should connect with other collective polyhedrons.

The basis for glasses are network forming cations that form the polyhedron structure (figure 1). SiO_2, B_2O_3, P_2O_5 and Fe_2O_3 are identified as network formers, because they freeze to the vitreous at low cooling rates (Schaeffer et al. 2012). In pure SiO_2-glasses all Si^{4+}-ions are linked by O^{2-}-ion bridges (bridging oxygen (BO)). The Si^{4+} form tetrahedra with 4 O^{2-} anions. Further structural units are formed by network-modifier cations such as alkaline (e.g. Li_2O, Na_2O and K_2O) and alkaline-earth metals (e.g. MgO, CaO and BaO). The addition of network modifiers into the structure leads to a break within the network structure. Due to that, some O^{2-}-ions are bonded to only one silicon polyhedron (non-bridging oxygen (NBO)) (Stebbins 2016). Further addition of network-modifiers results in a decrease of Si-O-Si bondings in the glass structure (Scholze 2012). Due to the increasing number of NBO’s and the accompanying decreasing number of BO’s, the melt viscosity decreases (Schaeffer et al. 2012). In addition to the network modifiers, the alkali or alkaline-earth metal cations act as charge balancers to compensate the charge differences that the incorporation of Fe^{3+} and Al^{3+} atoms in tetrahedral coordination (Stebbins 2016).

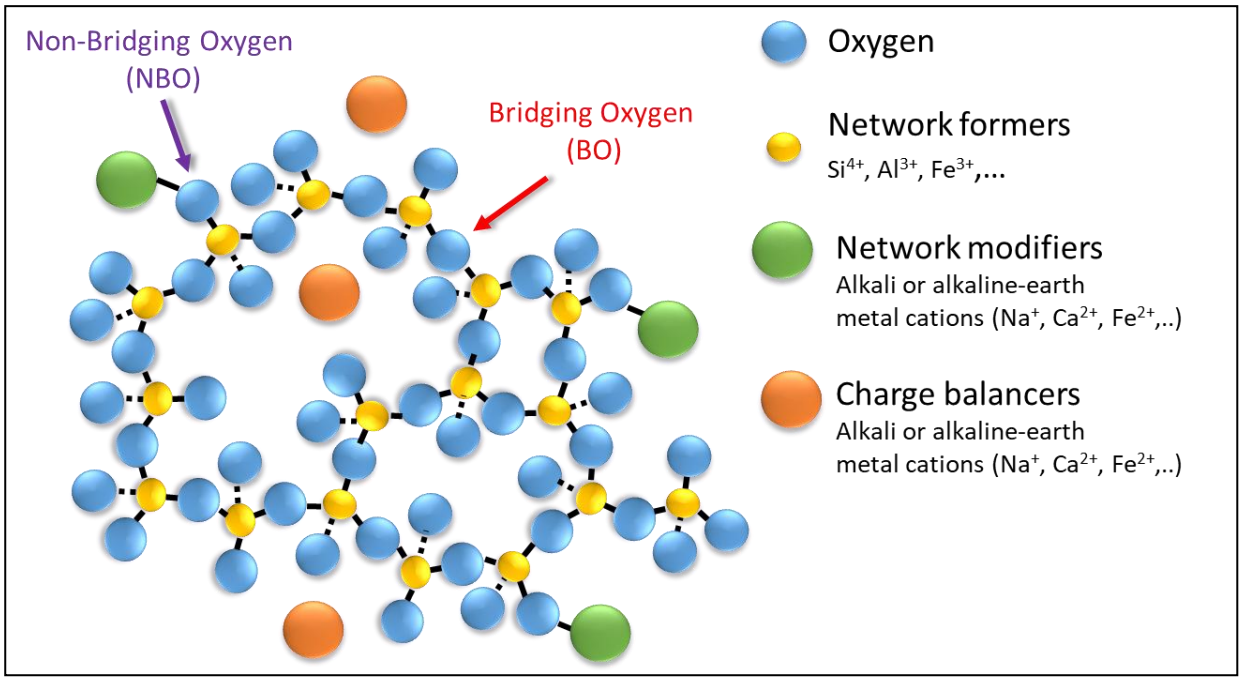

Figure 1: Network structure of oxide glasses, modified after Stebbins (2016).

Part A – The effect of Cl^- and F^- on the viscosity of the present MORB composition

1. Abstract

The rheology of halogen-free and –bearing basaltic glasses was investigated by micropenetration method in a range between $10^{8.5}$ and $10^{13.5}$ Pa s. Furthermore, the heat capacity was determined and compared to several models from the literature (Richet and Bottinga 1984; Stebbins et al. 1984; Richet 1987; Lange and Navrotsky 1992). In addition to temperature-related effects, the structural modification is useful to understand the incorporation mechanism of halogens in basaltic glasses. The present basaltic composition is similar to an average mid-ocean ridge basalt from the American Mid-Atlantic Ridge valley (Le Roex et al. 1996). This basaltic composition was doped with varying Cl^-, F^- and (Cl^- + F^-) concentrations and synthesised at 1423 and 1473 K in a 1 atm furnace.

The presence of fluorine in peralkaline melts results in a decrease in viscosity due to the bonding of F^- to network-former cations (Si-F) (Giordano et al. 2004). Thus, the addition of 7.73 mol% fluorine to basaltic glass results in a decrease in viscosity by 2.5 log units. The incorporation of F^- in basaltic melts results in a conversion of Fe^{2+} to Fe^{3+} resulting in an increase of network formers (Fe^{3+}). This study suggests that the decreasing effect of fluorine on viscosity appears despite the associated increasing Fe^{3+} content increases the viscosity.

The effect of chlorine on the viscosity of peralkaline melts depends on diverse incorporation mechanisms. The addition of a small amount of chlorine (<1.50 mol%) to a basaltic glass does not show a significant effect on viscosity. The addition up to 2.53 mol% Cl^- results in an increase in viscosity, whereas the further addition of Cl^- results in a strong decrease in viscosity. These two trends indicate that several parameters (e.g. melt composition) will influence the viscosity and associated structures in melt. An essential point is the incorporation mechanism of chlorine in peralkaline melts. The increasing viscosity can be explained by the formation of a complex of Cl^- and network modifier cations due to the alkali loss in the structure (Na^++Cl^- complex), which results in decreasing number of NBO and increasing number of BO. The decreasing viscosity is based on the breakage of network formers bonds, whereby the number of BO decreases due to bonding of chlorine to network-former cations (Si-Cl). There is no measureable effect of chlorine concentration on the iron speciation (Sandland et al. 2004; Evans et al. 2008; Baasner et al. 2013a). A combination of both halogens effects the viscosity of basaltic glass in a different way due to the diverse incorporation mechanisms. A high Cl^-/F^- ratio results in a slight decrease in viscosity by 0.3 log units, whereas a lower Cl^-/F^- leads to a stronger decrease in viscosity by 1.5 log units.

2. Introduction

Basalt is an essential mafic igneous rock that contains SiO_2 within the range of 45 to 52 wt% and a total alkali content ($Na_2O + K_2O$) of less than 5 wt% (Gill 2010). Basaltic melts have a lower viscosity and a lower volatile content than more evolved melts (e.g. rhyolite). In general, the basaltic melt erupts by a low explosive pyroclastic flow, whereas in water basaltic melt forms pillow lavas or sheet flows. The rapid quench enables the formation of basaltic glass in nature (Gill 2010).

The effect of halogens on the viscosity of silicate melts is widely discussed in the literature (Giordano et al. 2008; Baasner et al. 2013a, 2013b; Baasner et al. 2014; Webb et al. 2014). Several authors have shown that the presence of fluorine in silicate melt results in a decrease in viscosity. Zeng and Stebbins (2000) concluded that F^- prefers the bonding to small cations such as Al-F or Si-F bonding, whereas recent studies show that the presence of F^- in peralkaline glasses favour a bonding to network-modifier cations like Ca^{2+} and Na^+ (Baasner et al. 2014). Both assumptions explain the depolymerisation of the structure and the resulting decrease in viscosity.

Few studies have examined the role of chlorine on the viscosity of silicate melts. Baasner et al. (2013a) reported that the presence of chlorine in peralkaline melts has a different effect on the viscosity than in peraluminous melts due to the structural role of Cl^-. The authors suggest an increase in viscosity of peralkaline melts by the formation of a complex with network-modifier cations (Na^+, Ca^{2+}). In contrast to peralkaline melts, the Cl^- ions in peraluminous melt do not act as network modifiers, but instead as charge-balancers. It has also been observed that the addition of chlorine to basaltic melts results in a decrease in viscosity due to an increase in Fe^{2+}/Fe_{total} (Webb et al. 2014). In this study we focus on the thesis of a relation between the presence of Cl^- and the transition of Fe^{3+} to Fe^{2+}. On the basis of a relation between halogens and iron, we investigate the dependence of Fe^{2+}/Fe_{total} on F^-.

3. Experimental methods

3.1. Starting materials

The synthetic basaltic andesite composition is similar to that of an average mid-ocean ridge basalt from the American Mid-Atlantic Ridge valley (Le Roex et al. 1996). The iron total content was decreased, to avoid crystallisation of the glass. Four peralkaline series were prepared from a mixture of oxides (SiO_2, TiO_2, Al_2O_3, MgO, Fe_2O_3 and MnO_2) and carbonates (Na_2CO_3, K_2CO_3 and $CaCO_3$). The magnesium oxide was dried at 1273 K and the other chemicals at 773 K for 24 h. The theoretical composition of powders was weighed out and decarbonated in a $Pt_{90}Rh_{10}$ crucible in a 1 atm $MoSi_2$ furnace at 1273 K overnight. After the decarbonation the melts were heated up to 1523 K for 3 h and crushed and remelted twice to improve the chemical homogeneity. For the halogen-bearing melts the present glasses were doped with fluorine (NH_4F), chlorine (NH_4Cl) or both halogens and synthesised at temperatures between 1423 and 1473 K for 4-9 h. The added amount of NH_4Cl and NH_4F was based on an expected loss of ~60 % chlorine and ~2 % fluorine during the synthesis (Webb et al. 2014). The glass compositions are given in table 1.

Table 1: Composition of halogen-free and halogen-bearing glasses determined by electron microprobe. The analysis of each glass is based on the average of 10 measurements with the standard deviation (σ). Standards were: albite (Na), sanidine (K), wollastonite (Ca, Si), titanium dioxide (Ti), rhodonite (Mn), hematite (Fe), sodium chloride (Cl), olivine (Mg), anorthite (Al) and topaz (F).

Oxides/ ions mol%	BA-0	BA-Cl	BA-Cl-2	BA-Cl-3	BA-Cl-4	BA-Cl-F	BA-Cl-F-2	BA-Cl-F-3	BA-F	BA-F-2
SiO_2	54.97 ±0.16	54.01 ±0.15	54.34 ±0.16	53.89 ±0.15	54.18 ±0.15	53.40 ±0.14	51.41 ±0.12	51.95 ±0.15	53.72 ±0.16	50.73 ±0.12
Na_2O	4.68 ±0.08	3.85 ±0.08	3.59 ±0.05	4.08 ±0.06	4.26 ±0.05	3.78 ±0.05	3.62 ±0.02	4.02 ±0.04	4.50 ±0.05	4.25 ±0.04
K_2O	0.16 ±0.02	0.13 ±0.02	0.09 ±0.03	0.13 ±0.02	0.15 ±0.01	0.12 ±0.03	0.11 ±0.04	0.14 ±0.02	0.17 ±0.03	0.15 ±0.03
TiO_2	1.07 ±0.03	1.04 ±0.05	1.04 ±0.05	1.02 ±0.04	1.04 ±0.04	1.04 ±0.04	1.00 ±0.03	0.99 ±0.05	1.06 ±0.05	0.98 ±0.04
FeO_{total}	2.54 ±0.12	2.39 ±0.07	2.25 ±0.13	2.73 ±0.05	1.92 ±0.12	2.41 ±0.08	2.27 ±0.10	2.79 ±0.07	2.44 ±0.13	2.25 ±0.07
Al_2O_3	9.52 ±0.09	9.31 ±0.05	9.39 ±0.05	9.14 ±0.06	9.22 ±0.06	9.23 ±0.05	8.95 ±0.06	8.84 ±0.06	9.35 ±0.05	8.81 ±0.04
MgO	12.75 ±0.07	12.39 ±0.07	12.38 ±0.06	12.35 ±0.08	12.43 ±0.09	12.29 ±0.08	11.81 ±0.08	11.94 ±0.10	12.54 ±0.09	11.67 ±0.07
CaO	14.13 ±0.09	13.81 ±0.10	14.12 ±0.09	13.87 ±0.08	14.04 ±0.03	14.28 ±0.10	13.47 ±0.05	13.53 ±0.05	13.82 ±0.04	13.26 ±0.10
MnO	0.16 ±0.03	0.15 ±0.04	0.14 ±0.02	0.15 ±0.02	0.16 ±0.02	0.16 ±0.03	0.15 ±0.02	0.17 ±0.02	0.18 ±0.02	0.16 ±0.01
Cl^-	0.02 ±0.01	2.82 ±0.01	2.53 ±0.01	2.73 ±0.02	1.92 ±0.02	2.15 ±0.02	1.96 ±0.01	3.28 ±0.01	0.00 ±0.01	0.02 ±0.03
F^-	0.00 ±0.00	0.12 ±0.01	0.13 ±0.00	0.00 ±0.04	0.00 ±0.04	1.13 ±0.04	5.25 ±0.10	2.35 ±0.02	2.24 ±0.02	7.73 ±0.08
γ [1]	0.78	0.77	0.77	0.78	0.78	0.78	0.7	0.78	0.78	0.78
NBO/T [2]	0.45	0.42	0.41	0.43	0.44	0.43	0.42	0.45	0.44	0.43
NBO/T [3]	0.45	0.47	0.45	0.48	0.47	0.48	0.54	0.55	0.47	0.46

[1] γ is an indicator for the degree of polymerisation of the melt (Webb et al. 2014)

$\gamma = (Na_2O + K_2O + MnO + FeO + CaO + MgO) / (Na_2O + K_2O + MnO + FeO + CaO + MgO + Al_2O_3 + Fe_2O_3)$

[2] *NBO/T calculated without halogens (chlorine and fluorine)*

[3] *NBO/T calculated assuming* $2Cl^- = 1O^{2-}$ *or* $2F^- = 1O^{2-}$

4. Analytical methods

4.1. Element analysis

4.1.1. Microprobe

The chemical compositions of basaltic glasses were determined by a JEOL JXA 8900 electron microprobe equipped with a wavelength dispersive spectrometer (WDS – figure 2). The glass pieces were fixed in epoxy resin and polished to a 1 µm polishing level. The sample tablet was coated with a silver solution to minimise the electrostatic charge and was vapour-plated with a carbon film. The glasses were measured in WDS mode with an acceleration voltage of 15 kV and a beam current of 15 nA using a defocused beam size of 20 to 30 µm. Precise analysis were performed by the measurement of the following standards: albite (Na), sanidine (K), wollastonite (Ca, Si), titanium dioxide (Ti), rhodonite (Mn), hematite (Fe), sodium chloride (Cl), olivine (Mg), anorthite (Al) and topaz (F). Table 1 lists an average of 10 microprobe analysis of each sample.

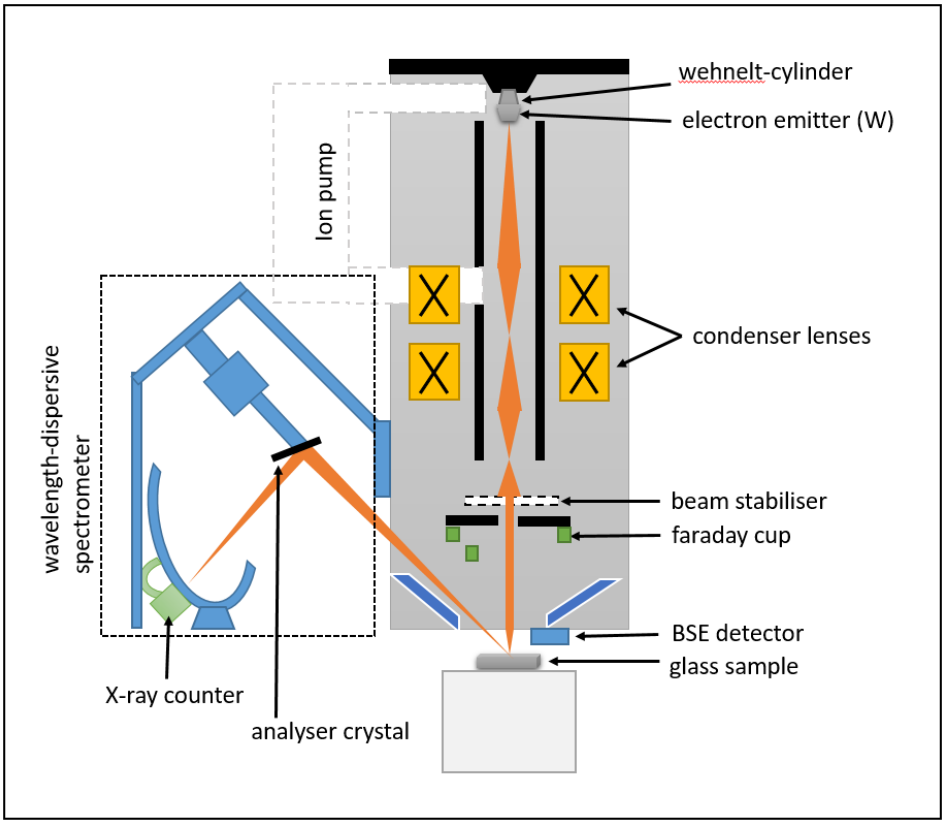

Figure 2: Schematic illustration of a microprobe, modified after Markl (2015).

4.1.2. Micro-XRF Fluorescence spectrometer

The Micro X-ray Fluorescence spectrometer M4 Tornado by Bruker was used to determine the chemical composition and the homogeneity of the present glasses. A schematic construction of the Micro X-ray Fluorescence spectrometer is presented in figure 3. The source material of the X-ray tube is rhodium and the spot on the sample is lower than 20 µm for Mo Kα with a polycarpellary lenses. The glasses were measured with an acceleration voltage of 50 kV and a beam current of 200 µA. This method requires a planar sample surface, whereby the method allows a quick element analysis. The calibration was performed with in-house standards, which allow a correction factor for each element.

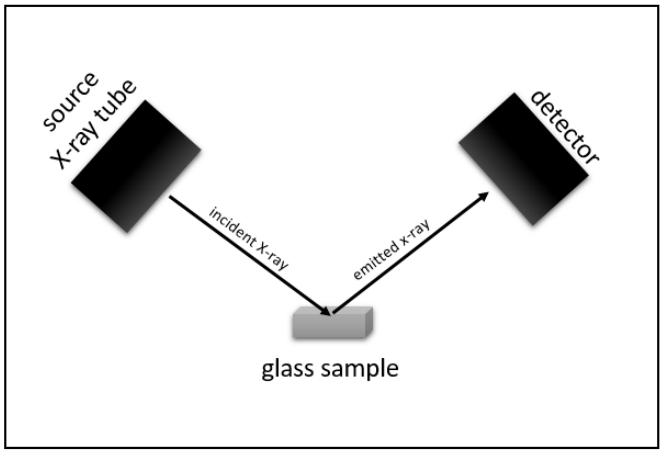

Figure 3: Simple schematic illustration of Micro X-ray Fluorescence spectrometer, modified after Flude et al. (2017).

4.2. Density

The density is described as the ratio between the mass and the volume of a solid body. The glass density was determined by means of the Mettler Toledo balance equipped by a density attachment. The measurement of the density is based on the Archimedean method. The calculation results from the weighing of a solid body in air (m_{air}) and in ethanol (m_{eth}) at room temperature (Bockris et al. 1956). Bockris et al. (1956) describes the formula:

$$\rho_{sample} = \frac{m_{air}}{m_{air} - m_{eth}} * \rho_{eth} \qquad \textit{Equation 1}$$

where ρ_{eth} describes the density of ethanol during the measurement. This density can be calculated by the following equation:

$$\rho_{eth} = -0.000848 * T\,(°C) + 0.806405 \qquad \textit{Equation 2}$$

which is published in CRC Handbook of chemistry and Physics (Weast 1989). The average of the density is determined by five measurements and the reproducibility is controlled by Al_2O_3 single crystal with a known density (ρ) of 3.987 g cm^{-3} (Sternheimer 1967).

4.3. Iron determination

4.3.1. Colorimetric micro-determination of ferrous iron in glasses

The Fe^{2+}/Fe_{total} was measured by colorimetric micro-determination of ferrous iron. This wet chemistry method is based on the principle of Wilson (1960), which is described by Schuessler et al. (2007). The measurement is performed with UV/VIS-spectrometer (figure 4). The accuracy of the method is verified by measurements on the international standard basalt W-1. The glass samples were dissolved in a mixture of hydrogen fluoride and ammonium vanadate for 24 h. The ferrous iron must stay chemically inactive during the analytical procedure and this can be assured by the addition of pentavalent vanadium (pH ~ 5) (Schuessler et al. 2007).

$$V^{5+} + Fe^{2+} \overset{pH\sim 5}{\Longleftrightarrow} V^{4+} + Fe^{3+} \qquad \textit{Equation 3}$$

After neutralisation with saturated boric acid, a 2:2-Bipyridyl solution was added to the sample solution, whereby the Fe^{2+} forms a red coloured complex. This complex can be measured with the UV/VIS-spectrometer (AvaSpec-UV/VIS/NIR – dual channel broad band spectrometer) and represents the Fe^{2+} concentration.

$$2NH_2OH * HCl + 4Fe^{3+} \leftrightarrow 4Fe^{2+} + N_2O + H_2 + 6H^+ + 2Cl^- \qquad \textit{Equation 4}$$

Afterwards, Fe^{3+} was completely reduced to Fe^{2+} by the addition of hydroxylamine hydrochloride as a reducing agent. The solution can also be measured with the spectrometer and this results in the total iron absorbance (forms Fe^{2+}). The Fe^{2+}/Fe_{total} is calculated directly by dividing the absorbance of Fe^{2+} by that of the iron total. The precision of the analysis was checked by a double measurement. The chapter 5.2.1. (Comparison of analysis of diverse geological standards) describes the calibration by means of geological standards for the colorimetric micro-determination of ferrous in glasses.

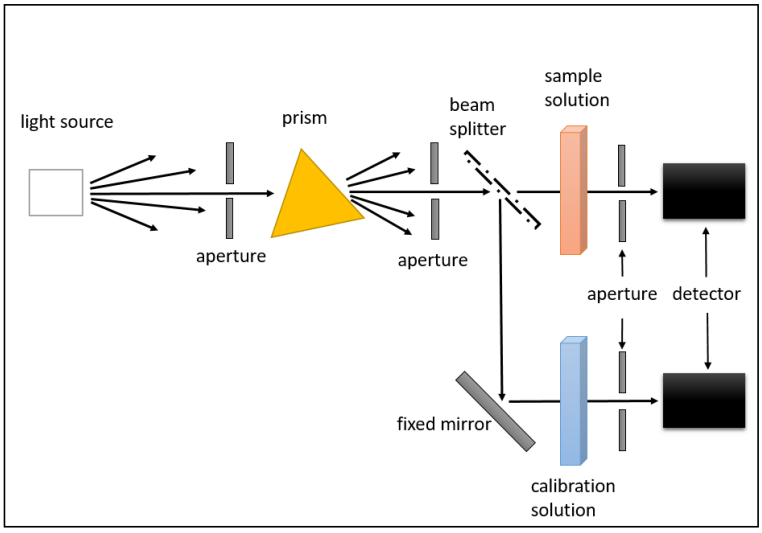

Figure 4: Schematic illustration of UV/VIS-spectrometer, modified after Perkampus (1986).

4.3.2. Moessbauer spectroscopy

Moessbauer spectroscopy is based on the moessbauer effect. This effect is the recoil-free emission and the atomic nuclei generate the resonant absorption of γ-radiation (Gütlich et al. 2010; Häggström et al. 1969). The method provides insight into the oxidation state of specific atoms like Fe^{2+} and Fe^{3+} as well as the magnetic properties (Jayasuriya et al., 2004). The experimental setting consists of an absorber (sample), a radioactive source (like 57 cobalt) and the detector (see figure 5). The basic principle is the motion of the source to the absorber with a controlled velocity. The change of the source nuclear transition energy effects the emission of γ-radiation as described by the Doppler-Effect. The double-side polished glass samples have a thickness of 1.45 to 1.60 mm and were fixed in the aperture in Pb-foil in front of the source. The measurements were conducted at room temperature. The results represent the relative areas of resonant absorption doublets of Fe^{2+} and Fe^{3+}, whereas the distinction between the oxidation states of the specific iron atoms is possible. The measurements were performed in cooperation with Dr. McCammon from Bavarian Research Institute of Experimental Geochemistry and Geophysics (BGI).

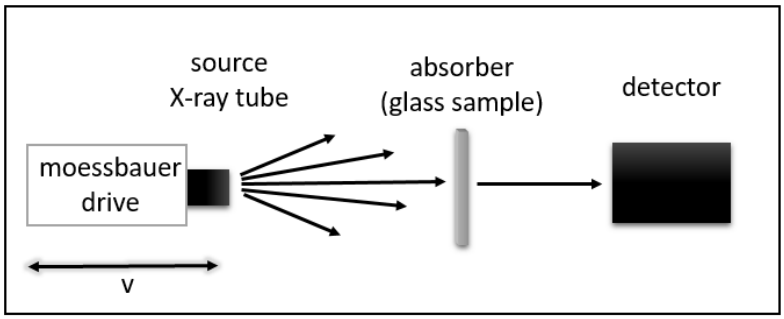

Figure 5: Schematic illustration of Moessbauer spectroscopy, modified after Gütlich et al. (2010).

4.3.3. Calculation of Fe^{2+}/Fe_{total} after Kress and Carmichael (1991)

The Fe^{2+}/Fe_{total} model by Kress and Carmichael (equation 5) was used to check the results of the wet chemistry and Moessbauer analysis:

$$ln\left(\frac{X_{Fe2O3}}{X_{FeO}}\right) = a * ln(f_{O2}) + \frac{b}{T} + c + \sum_i d_i * X_i + e * \left[1 - \frac{T_0}{T} - ln\left(\frac{T}{T_0}\right)\right] + f * \frac{P}{T} + g * \frac{(T-T_0)*P}{T} + h * \frac{P^2}{T} \qquad \textit{Equation 5}$$

where X_{Fe2O3} and X_{FeO} are the mol fraction of Fe_2O_3 and FeO, the parameters (*a* to *g*) describe some fixed values in natural melts (see Kress and Carmichael (1991)), fO_2 describes the experimental oxygen fugacity (log fO_2 -0.68 at 1 atm), P is the pressure (Pa), T defines the experimental temperature (K) and T_0 is a constant value of 1673 K.

4.4. Micropenetration viscometry

The viscosity can be analysed by heating glass samples to a temperature above T_g, where the melt structure is in thermodynamic equilibrium. The high melt viscosity was measured using the Netzsch TMA 420 dilatometer micropenetration method in the range of $10^{8.5}$ to $10^{13.5}$ Pa s. The method is based on the penetration of a 1 or 2 mm diameter Al_2O_3 sphere (r). The sphere was forced into the melt with a constant force (F) depending on the temperature. A schematic description of the micropenetration technique is shown in figure 6. The viscosity (η) is calculated by the depth of penetration (l) as a function of time (t) (Pocklington 1940):

$$\eta = \frac{0.1875 * F * t}{\sqrt{r} * \sqrt{l^3}} \qquad \textit{Equation 6}$$

The melting temperature of selected metals (Bi – 271.4°C, Zn – 419.6°C, Al – 660.3°C, NaCl - 801°C, Ag - 961.8°C) enables a temperature calibration as described in Webb et al. (2014). The calibration of the S type thermocouple results in a temperature error of ± 0.5°C. The accuracy of the method is verified by the standard glass DGG-1 and the results were compared with data from Meerlender (1974). The viscosity-temperature data was fitted and described with an Arrhenian equation:

$$log_{10}\eta = A_{Arr} + \frac{B_{Arr}}{T} \qquad \textit{Equation 7}$$

where A_{Arr} and B_{Arr} represent the fit parameter and T describes the experimental temperature in K. Further interpretation of the viscosity-temperature data can be done using the Vogel-Fulcher-Tamman fit (VFT after Fulcher (1925) and Tammann and Hesse (1926)).

$$log_{10}\eta = A_{VFT} + \frac{B_{VFT}}{T - C_{VFT}} \qquad \textit{Equation 8}$$

with two variable fitting parameters B_{VFT} and C_{VFT} as well as a constant value A_{VFT} with -4.55 (log_{10} of $10^{-4.55}$ Pa s). The VFT equation describes the data as a curve, whereby the micropenetration data can be combined with diverse viscosity methods like the falling sphere measurement. The range of micropenetration viscosity is too small to allow a statistically relevant use of VFT, unless A_{VFT} is held constant.

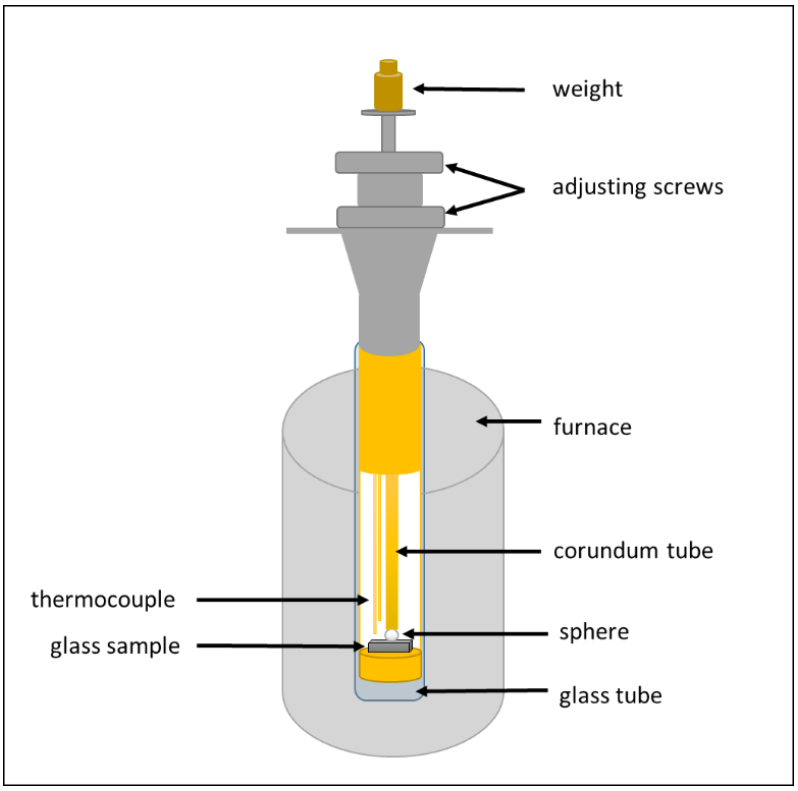

Figure 6: Schematic description of the micropenetration technique, modified after principle by Pocklington (1940).

4.5. Differential scanning calorimetry

The Netzsch DSC 464C scanning calorimeter was used to measure the heat capacity of the glasses (C_{pg}) and melts (C_{pl}) as a function of temperature. The glass samples were heated with a rate of 20 K min^{-1} through the glass transition temperature. The high temperature end of the glass transition range can be estimated to occur at the temperature for which the viscosity is 10^9 Pa s. The heat capacity was calculated by the difference of the sample measurement against an empty crucible (Webb 2008). A schematic description is shown in figure 7. The calorimeter was calibrated from the measurement of a single crystal of Al_2O_3 compared to the experimental data from Robie et al. (1978). The equation from Maier and Kelley (1932):

$$c_{pg} = a + bT + cT^{-2} \qquad \textit{Equation 9}$$

with three variable parameters (a, b, c) and the temperature in K, was fitted for the data of C_{pg} to the onset of the glass transition peak with an acceptable accuracy. After an extrapolation of the Maier-Kelly fit, the C_{pg} above T_g can be identified. Richet et al. (1986) described the configurational heat capacity (C_p^{conf}) as the necessary energy of the structural changes from glass to liquid state. The C_p^{conf} describes the difference of the heat capacity of the melts and the glasses.

Adam and Gibbs (1965), Richet (1984) and Mysen and Richet (2005) define the following equation to calculate the theoretical viscosity:

$$log_{10}\eta = A_e * \frac{B_e}{ln10*\left[S_{conf}(T_g^{12}) + \int_{T_g^{12}}^{T} \frac{c_p^{conf}}{T} dT\right]*T}$$ *Equation 10*

where A_e and B_e are parameters and $S_{conf}(T_g)$ describe the configurational entropy at the glass transition temperature (T_g^{12}). Toplis (1998) and Webb (2005) suggested that $B_e/S_{conf}(T_g)$ ratio describes the flow mechanism of the melt, which depends on the smallest rearranging structural unit and the average energy barrier to structural rearrangement. The derivation of this equation includes the incorrect assumption that S_{conf} and C_p^{conf} are constant for temperatures below that at which viscosity is 10^{12} Pa s. Despite this assumption the equation is used in an effort to understand the S_{conf} and C_p^{conf} and structure of silicate melts as can be determined by viscosity and thermodynamic measurements. An important parameter in understanding DSC data is the fictive temperature (T_f), which depends on the cooling rate through the glass transition range (Stebbins 2016; Dingwell and Webb 1990; Stebbins 2016). Moynihan et al. (1976) describe T_f as a function of the structural relaxation time near the equilibrium of the melts. Here the fictive temperature T_f is determined by the integration of heat capacity curves with a heating rate of 20 K min^{-1} on glasses which had been cooled from temperature above T_g at a rate of 20 K min^{-1} (Moynihan et al. 1976).

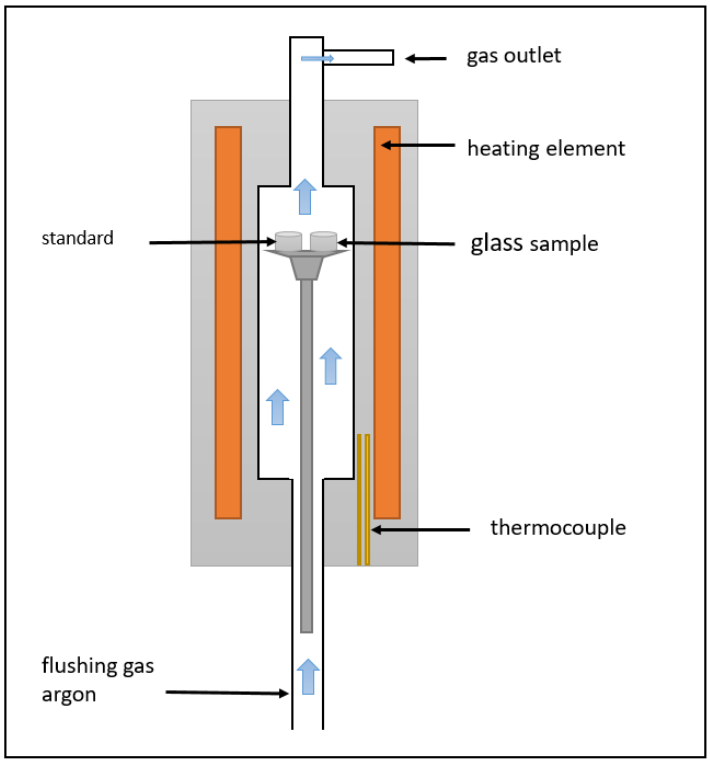

Figure 7: Schematic illustration of a differential scanning calorimeter, modified after description by Webb (2008).

4.6. Raman spectroscopy

The Raman spectroscopy was used to determine the Fe^{2+}/Fe_{total} in the present basaltic glasses. The method is based on the Raman effect, which is described as interaction between light and matter. The measurements were performed with a Horiba Jobin-Yvon Labram HR800UV equipped with an Olympus BX41 microscope. The diode laser (488 nm) with a laser power of 50 mW was used to measure the samples at room temperature. The schematic setup of the Raman spectroscopy is given in figure 8.

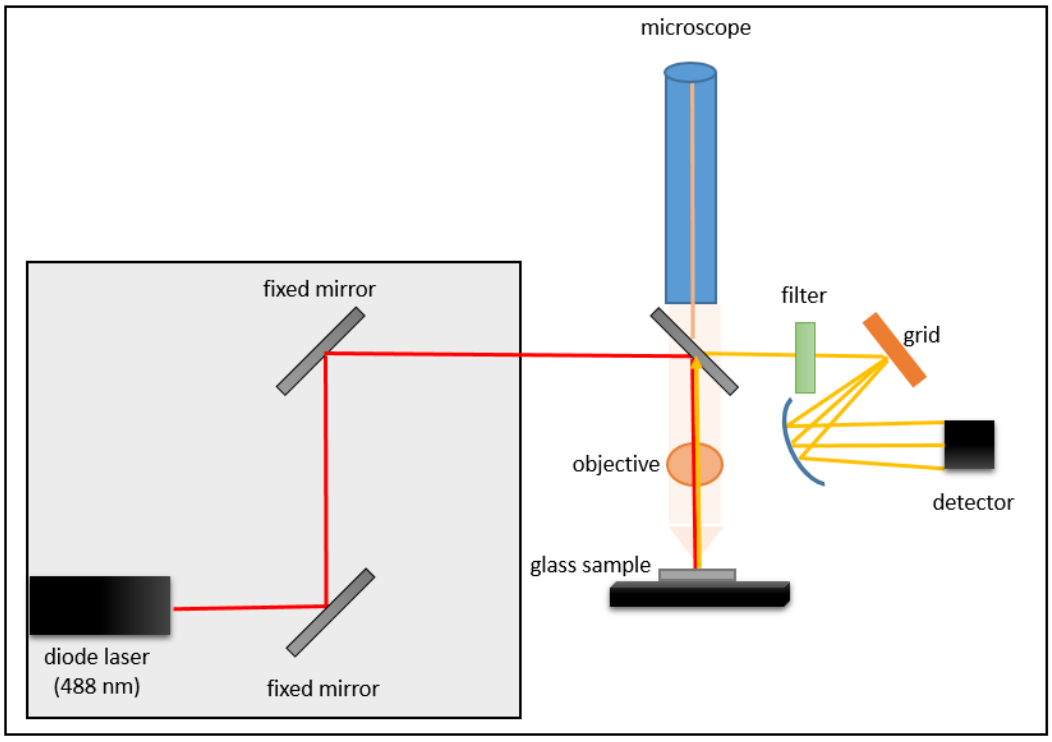

Figure 8: Schematical illustration of Raman spectroscopy, modified after Ferraro and Nakamoto (1994).

The precision of the measurements is checked by a silicon standard and the peak should be located around 520.4 nm with a high intensity (< 15000 arbitrary units). All spectra were recorded three times at the same measurement condition and at different areas to check the homogeneity of the glass pieces. The spectra were adjusted by temperature and frequency correction of the Raman intensity (R(v)) after Long (1977). The following equation is described by Di Muro et al. (2009).

$$R(v) = v_0^3 * \left(1 - \exp\left(\frac{-hcv_i}{kT}\right)\right) * \left(\frac{v_i}{v_{0-}v_i}\right)^4 \qquad \textit{Equation 11}$$

where v_0 describes the frequency of laser excitation line, h defines the Planck's constant, c is the velocity of light, v_i describes the frequency of Raman shift, k is the Boltzmann constant and T defines the sample temperature.

5. Results

5.1. Density determination

Table 2 illustrates the influence of halogens on the density of the synthesised peralkaline glasses of series I and starting composition of series II and III. The addition of 3.65 mol% chlorine to basaltic glasses results in a decrease in density from 2.69 to 2.67 g cm^{-3} (figure 9). In comparison, the addition of 7.73 mol% fluorine to basaltic glasses shows a slight increase in density from 2.69 to 2.70 g cm^{-3}. This reflects that fluorine has a different structural behaviour than chlorine. The addition of (Cl^- + F^-) results in a slight decrease in density from 2.69 to 2.68 g cm^{-3}. Figure 10 shows the calculated excess chlorine for the glasses with (Cl^- + F^-) and allows a direct correlation with the chlorine-bearing glasses. The calculated values (Cl^- - F^-) are consistent with the chlorine-bearing glasses and follow the blue linear regression line.

Table 2: Fe^{2+}/Fe_{total}, density ρ and molar volume of the series I and start composition of series II and III.

Sample	Fe^{2+}/Fe_{total} wet chemistry	$\Delta Fe^{2+}/Fe_{total}$ [a] wet chemistry	ρ (g cm^{-3})	σ (g cm^{-3})	molar volume (cm^3 mol^{-1})
BA-0	0.18	0.01	2.693	0.001	23.45
BA-Cl-II (1.50 Cl^-)	0.19	0.01	2.679	0.002	23.36
BA-Cl-4 (1.92 Cl^-)	0.18	0.01	2.672	0.004	23.44
BA-Cl-2 (2.53 Cl^-)	0.17	0.01	2.675	0.003	23.28
BA-Cl-3 (2.73 Cl^-)	0.21	0.02	2.674	0.003	23.38
BA-Cl (2.82 Cl^-)	0.18	0.01	2.673	0.001	23.29
BA-Cl-III (3.65 Cl^-)	0.16	0.01	2.668	0.002	23.17
BA-Cl-F (2.15/1.13 Cl^-/F^-)	0.18	0.02	2.678	0.004	23.15
BA-Cl-F-II (1.42/0.76 Cl^-/F^-)	0.29	0.01	2.680	0.002	22.93
BA-Cl-F-III (3.90/2.18 Cl^-/F^-)	0.19	0.02	2.673	0.003	22.73
BA-Cl-F-3 (3.28/2.35 Cl^-/F^-)	0.29	0.01	2.679	0.004	22.78
BA-Cl-F-2 (1.96/5.25 Cl^-/F^-)	0.16	0.01	2.677	0.003	22.53
BA-F (2.24 F^-)	0.13	0.01	2.693	0.003	23.14
BA-F-II (4.33 F^-)	0.12	0.01	2.701	0.003	22.71
BA-F-III (4.90 F^-)	0.11	0.01	2.698	0.001	22.61
BA-F-2 (7.73 F^-)	0.08	0.01	2.701	0.002	22.61

[a] $\Delta Fe^{2+}/Fe_{total}$ is derived from the error propagation.

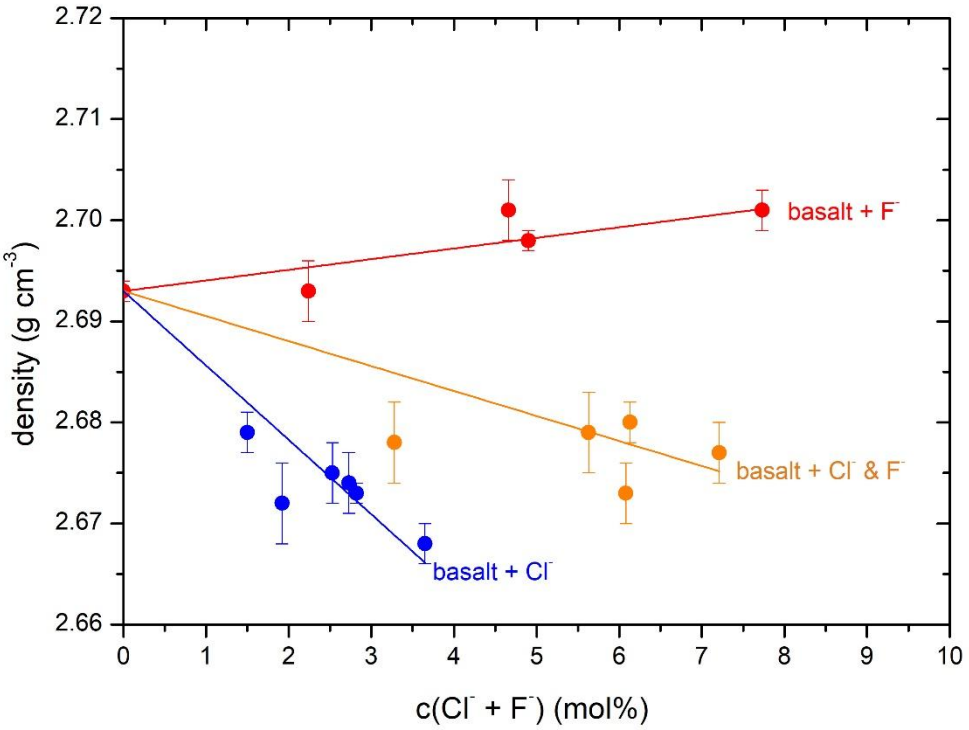

Figure 9: Density of basaltic glasses of series I as a function of halogen content.

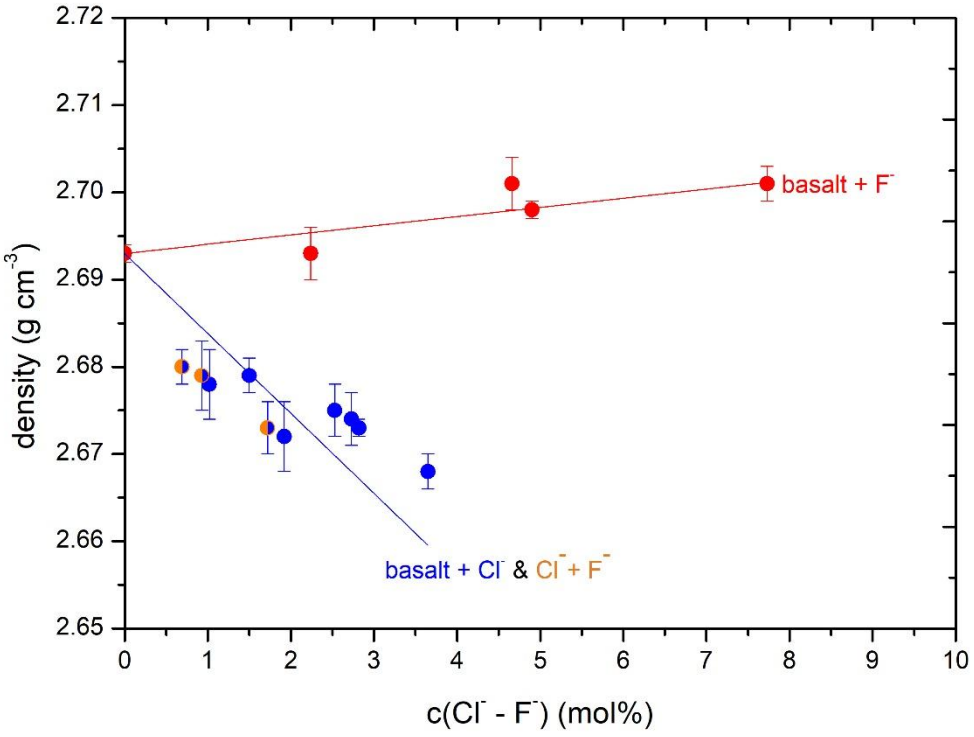

Figure 10: Density of basaltic glasses of series I as a function of the concentration of (Cl$^-$ - F$^-$).

Another possible effect on the density of peralkaline melts could be the iron ratio. Figure 11 illustrates the density as a function of Fe^{2+}/Fe_{total}. It is obvious that the iron speciation does not affect the density of the chlorine-bearing basaltic glasses. The addition of chlorine to a basaltic glass results in a decrease in density from 2.69 to 2.67 g cm^{-3}, but the Fe^{2+}/Fe_{total} does not consistently affect the density. The addition of fluorine to a peralkaline glass results in a slight decrease in density and is independent of the iron speciation. The density of the fluorine-bearing glass with a high iron ratio of 0.16 (2.24 mol% F^-) is similar to the density of the glass that is characterised by a low iron ratio of 0.08 (7.73 mol% F^-). The addition of (Cl^- + F^-) leads to a small decrease in density and figure 11 shows that the high iron speciation ratio (0.29) has no significant influence on the density. Thus, the density is mainly controlled by the halogen content and the iron speciation has no significant effect on the density).

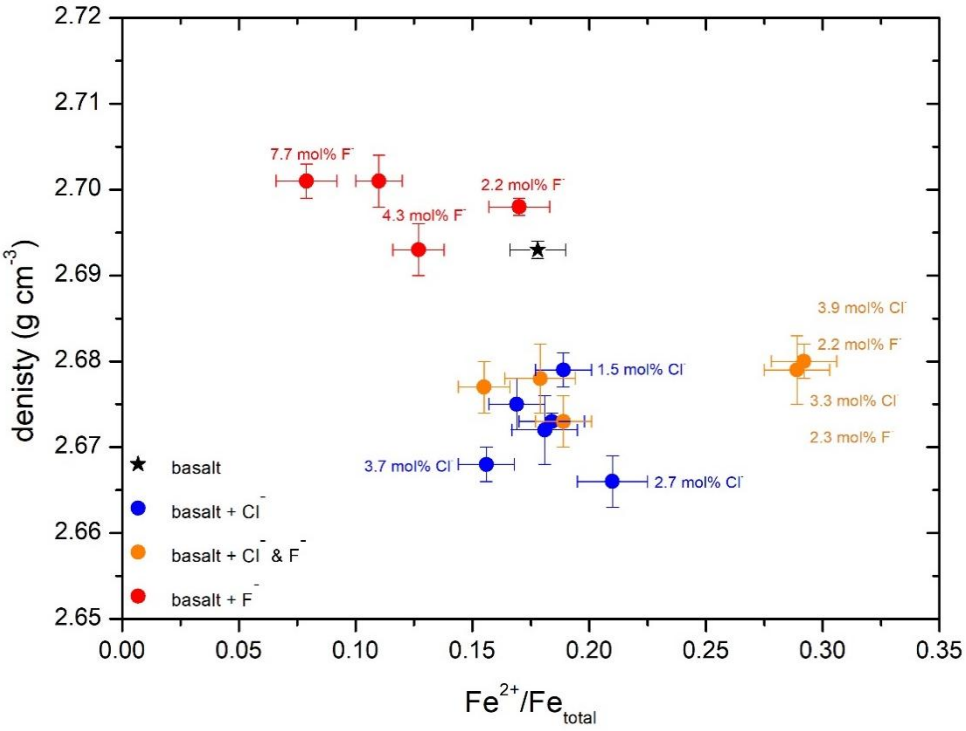

Figure 11: Density as a function of Fe^{2+}/Fe_{total} of halogen-bearing basaltic glasses.

Figure 12 illustrates the effect of halogens on the molar volume of halogen-bearing basaltic glass. The molar volume describes the volume, which 1 mol requires in the melt structure (Bockris et al. 1956). The addition of 3.65 mol% Cl^- to basaltic glasses results in a small decrease in molar volume from 23.45 to 23.17 cm^3 mol^{-1}. In comparison, the addition of 7.73 mol% F^- to basaltic glasses shows a strong decrease in molar volume from 23.45 to 22.61 cm^3 mol^{-1}. The addition of (Cl^- + F^-) to basaltic glass results in a strong decrease in molar volume from 23.45 to 22.53 cm^3 mol^{-1}. These results are consistent with data of fluorine-bearing basaltic glasses. This illustrates that chlorine and fluorine occupy different structural positions.

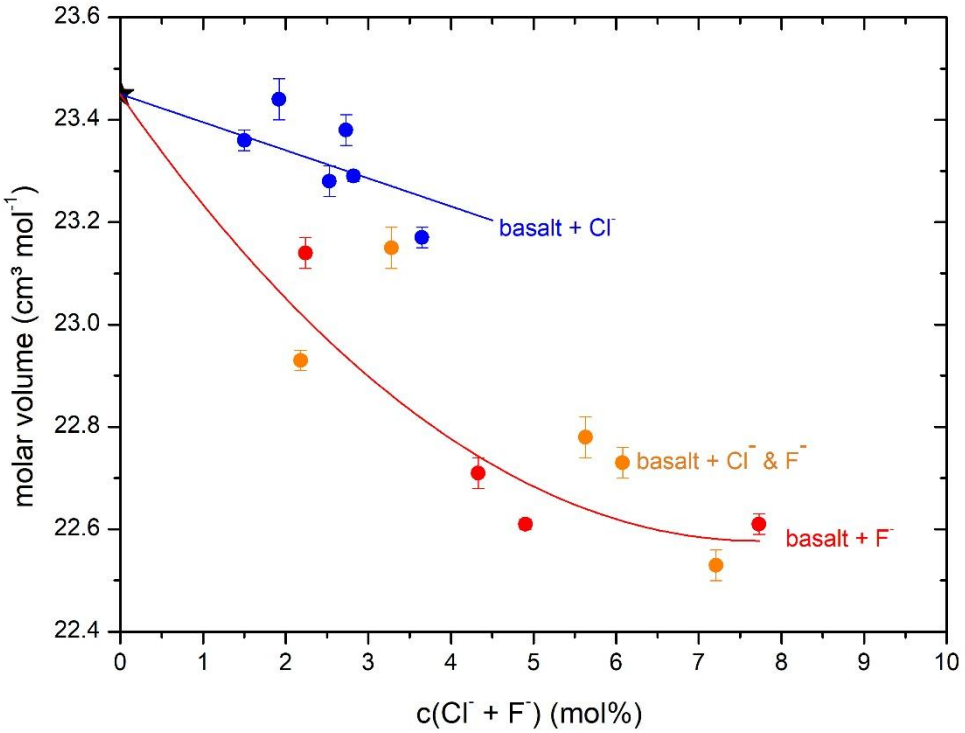

Figure 12: Partial molar volume of basaltic glasses of series I as a function of halogen content.

5.2. Effect of Iron

5.2.1. Comparison of analysis of diverse geological standards

The study from Schuessler et al. (2007) describes the procedure of Fe^{2+} determination with a comparison of diverse international reference materials and in-house standards. Figure 13 demonstrates the measured Fe^{2+}/Fe_{total} of this study (black circles) versus iron ratio of their study (grey circles) for the same standard samples. Schuessler and coworkers showed that the measured values correlate well with the recommended Fe^{2+}/Fe_{total} with the exception of the granites GS-N and GA. The granites have a higher Fe^{2+}/Fe_{total} than the recommend data. The different ratios are explained by the presence of undissolved refractory minerals containing significant amounts of Fe^{3+} in granite samples (Schuessler et al. 2007).

The method of colorimetric micro-determination of ferrous iron in silicate rocks and glasses (e.g. Wilson 1960; Schuessler et al. 2007) was used to determine Fe^{2+}/Fe_{total}. The analysis method was checked with some reference materials with a known composition (table 3) and compared to Schuessler et al. (2007). Additionally, hematite was analysed and the iron ratio fits into the model. Figure 13 shows that the present Fe^{2+}/Fe_{total} data confirm the results of Schuessler and co-workers. The Institute for Mineralogy of Leibniz Universität Hannover analysed two of our samples and obtained agreement with an accuracy of ± 0.03 (dashed lines).

Table 3: Results of wet chemistry on the international reference materials and in-house standards.

Sample	Fe^{2+}/Fe_{total} recommend [a]	Fe^{2+}/Fe_{total} this study	$\Delta Fe^{2+}/Fe_{total}$
Hematite	>0.01	0.02	0.01
PU-3 Andesite	0.39	0.41	0.01
GA - Granite	0.52	0.61	0.03
G-1 - Granite	0.50	0.67	0.04
GH - Granite	0.63	0.64	0.06
Biotite Mica-Fe	0.74	0.77	0.02
W-1 - Diabase	0.88	0.85	0.03

[a] References for recommended values: Fairbairn et al. (1950-51) and Schuessler et al. (2007).

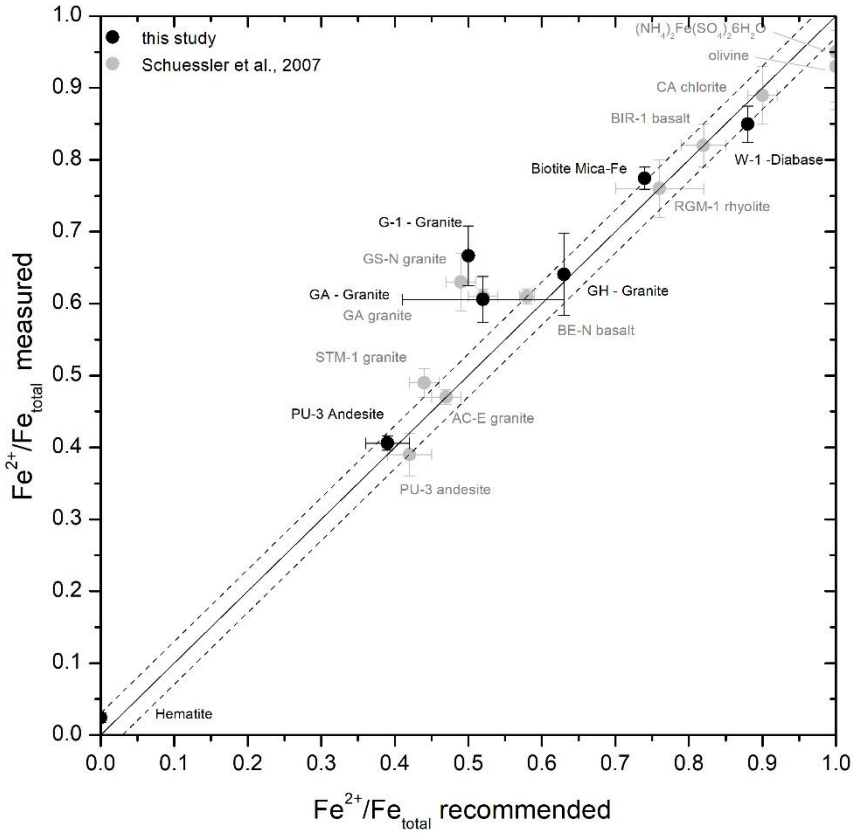

Figure 13: Measured Fe^{2+}/Fe_{total} ratios of international geological standards from this study (black circles) compared to Schuessler et al. (2007) (grey circles). The solid line shows a 1:1 correlation and the dashed lines represents an error interval of ± 0.03.

5.2.2. Comparison of diverse iron analysis

Table 4 gives an overview of the results of the diverse iron analysis that were used for synthesised glasses within this study. The FeO_{total} and Fe^{2+}/Fe_{total} were each analysed by wet chemistry (micro-colorimetry). The reproducibility of iron ratios is given by two reference materials (PU-3 Andesite and W-1 Diabase, table 3). The accuracy of the wet chemistry analysis of FeO_{total} was checked by external methods (electron microprobe and X-ray fluorescence) and the Fe^{2+}/Fe_{total} results of the wet chemistry analysis were compared with Moessbauer spectroscopy. Figure 14 presents the results of the FeO_{total} analysis of the three methods. The microprobe results show a good correlation with the wet chemistry data (red circles, see 1:1 correlation), whereas the total iron contents of X-ray fluorescence (black rectangles) differ from the microprobe data. The X-ray fluorescence overestimates the iron total content for all glasses.

Table 4: Results of FeO_{total} analysis of wet chemistry compared to microprobe and X-ray fluorescence as well as the results of Fe^{2+}/Fe_{total} of wet chemistry compared to Moessbauer spectroscopy.

Sample	**FeO_{total} (wt%)**			**Fe^{2+}/Fe_{total} (atoms)**	
	wet chemistry	microprobe	X-ray fluorescence	wet chemistry	Moessbauer spectroscopy
BA-0	5.26	5.26	5.68	0.18	0.16
BA-Cl-4 (1.92 Cl^-)	5.40	5.68	5.92	0.18	n.a.
BA-Cl-2 (2.53 Cl^-)	4.83	4.61	5.32	0.17	0.09
BA-Cl-3 (2.73 Cl^-)	5.40	5.49	5.62	0.21	n.a.
BA-Cl (2.82 Cl^-)	5.04	4.76	5.10	0.18	0.18
BA-Cl-F (2.15/1.13 Cl^-/F^-)	5.16	4.93	5.28	0.18	0.12
BA-Cl-F-3 (3.28/2.35 Cl^-/F^-)	5.43	5.49	5.78	0.29	n.a.
BA-Cl-F-2 (1.96/5.25 Cl^-/F^-)	5.12	4.94	5.37	0.16	0.12
BA-F (2.24 F^-)	5.42	5.24	5.68	0.13	0.07
BA-F-2 (7.73 F^-)	5.51	5.24	5.73	0.08	0.09

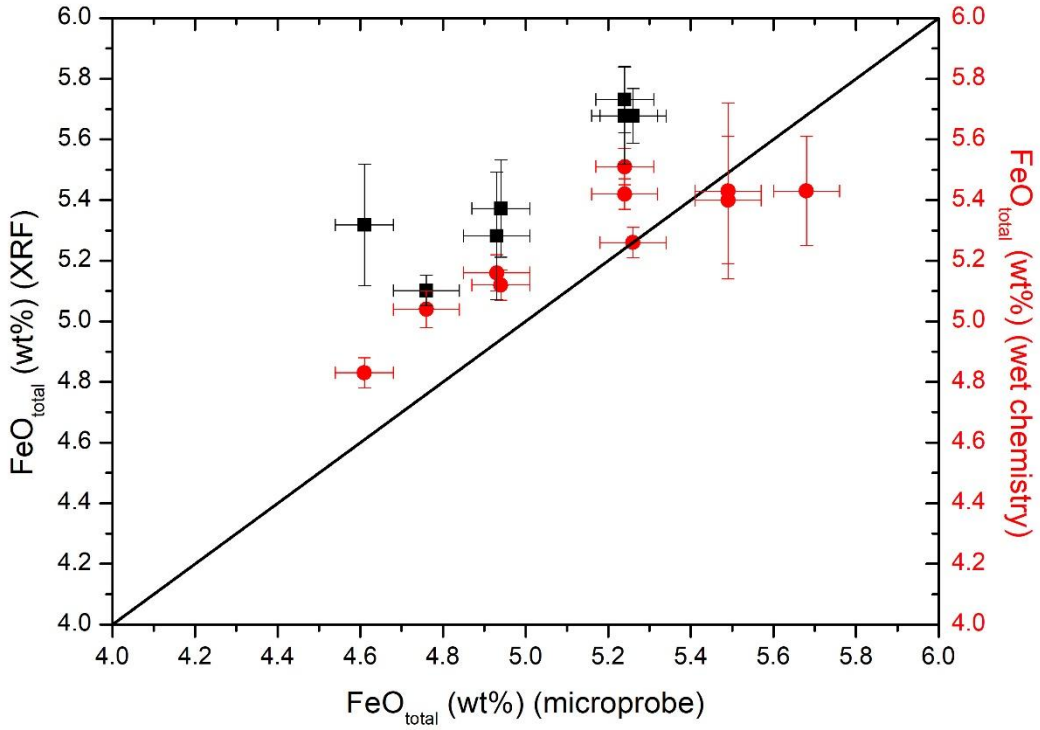

Figure 14: Comparison of the total iron FeO_{total} (in wt%) determined by microprobe versus X-ray fluorescence (black rectangles) and wet chemistry (red circles). The solid line shows a 1:1 correlation.

The Moessbauer spectroscopy was performed to calculate the Fe^{2+}/Fe_{total} as additional comparison method to wet chemistry. The data in table 5 shows the Moessbauer parameters that provide information about the structural coordination state of iron. The chemical (isomer) shift (CS) enables the differentiation in Fe^{2+} and Fe^{3+} by the relation of the charge density of atomic electrons at the nucleus and the chemical bonding (Häggström et al. 1969). Figure 15 shows the graphic chart of the isomer shift versus the quadrupole splitting (QS). The iron ratios shown in table 4 were calculated by the data of table 5. Figure 16 illustrates that the Moessbauer spectroscopy shows a lower Fe^{2+}/Fe_{total} ratio than the data of the wet chemistry method. The calculated ratio of the Moessbauer spectroscopy has a high error due to error propagation from the calculation and conversion shown in Jayasuriya et al. (2004), Häggström et al. (1969), Jayasuriya et al. (2004) and Gütlich et al. (2010). Therefore, the results of Moessbauer spectroscopy are comparable to the results of the wet chemistry within the error range.

Table 5: Moessbauer parameters of halogen-free and halogen-bearing basaltic glasses.

Sample	Fe^{2+}				Fe^{3+}			
	CS (mm s^{-1})	ΔCS (mm s^{-1})	QS (mm s^{-1})	ΔQS (mm s^{-1})	CS (mm s^{-1})	ΔCS (mm s^{-1})	QS (mm s^{-1})	ΔQS (mm s^{-1})
BA-0	1.001	0.064	1.967	0.110	0.263	0.010	1.263	0.022
BA-Cl	1.075	0.079	2.005	0.134	0.267	0.014	1.321	0.028
BA-Cl-2	0.873	0.116	2.007	0.237	0.271	0.021	1.307	0.036
BA-Cl-F	1.033	0.053	2.156	0.110	0.265	0.011	1.276	0.019
BA-Cl-F-2	1.070	0.061	2.138	0.127	0.254	0.013	1.292	0.023
BA-F	0.968	0.093	2.043	0.191	0.271	0.017	1.282	0.035
BA-F-2	1.005	0.058	1.974	0.118	0.271	0.012	1.284	0.020

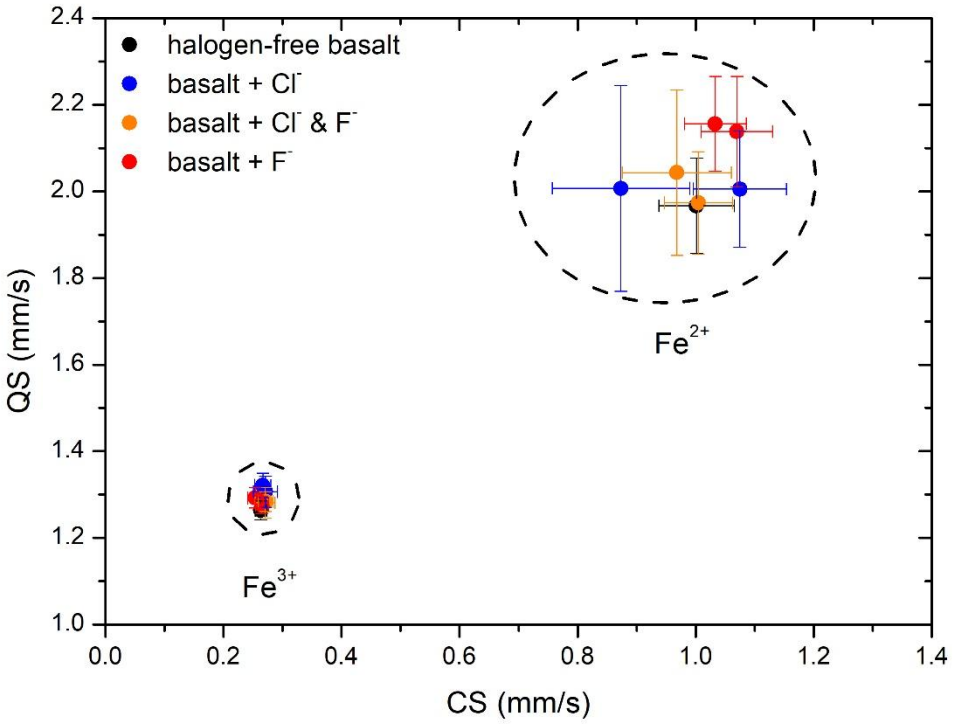

Figure 15: The isomer shift as a function of quadrupole splitting measured by Moessbauer spectroscopy.

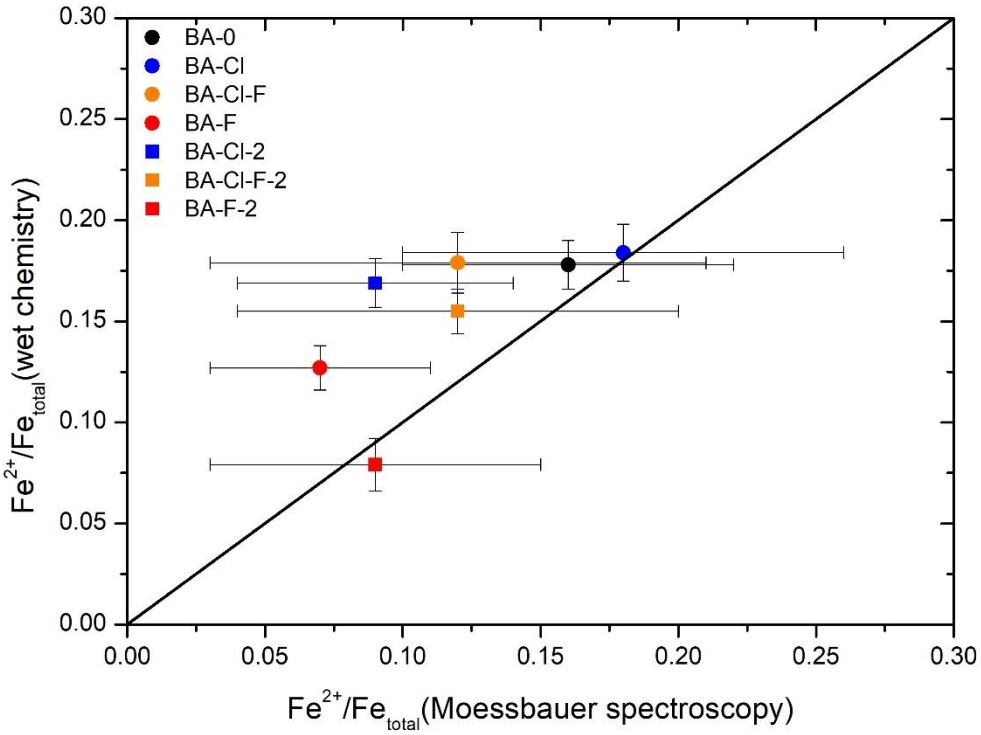

Figure 16: Comparison of Fe^{2+}/Fe_{total} of basaltic glasses determined by Moessbauer spectroscopy relative to the iron speciation of the wet chemistry method. The solid line shows a 1:1 line.

5.2.3. Fe^{2+}/Fe_{total} iron ratios depend on chlorine and fluorine

Figure 17 demonstrates the effect of halogens on the Fe^{2+}/Fe_{total}. The fluorine-bearing glasses show a strong decrease of Fe^{2+}/Fe_{total} from 0.18 to 0.08 due to the addition of 7.73 mol% fluorine (red circle). The presence of fluorine in basaltic glass results in a conversion of network-modifying Fe^{2+} to network-forming Fe^{3+}. This results in a polymerisation of the melt structure. For this reason, the Raman spectroscopy was performed in this study to indicate a structure modification by increasing halogen contents (5.2.4. Raman-spectra: Effect of Fe^{2+}/Fe_{total} iron ratio on the structure).

The study of Webb et al. (2014) indicated a dependence of the iron speciation on the presence of chlorine in basaltic melts. The Fe^{2+}/Fe_{total} was found to increase strongly by the addition of Cl^- in peralkaline melt. This observation was interpreted as the addition of Cl^- ions resulting in a conversion of network-forming Fe^{3+} to network-modifying Fe^{2+} iron cations for glasses synthesised in air at a constant oxygen fugacity (Webb et al. 2014). Furthermore, the authors suggested that the addition of 2.82 mol% Cl^- to the basaltic melts results in an increasing Fe^{2+}/Fe_{total} ratio from 0.13 to 0.43. In contrast to these earlier findings, the addition of 2.82 mol% Cl^- to the present basalt in this study does not have a significant influence on the Fe^{2+}/Fe_{total} (blue circle).

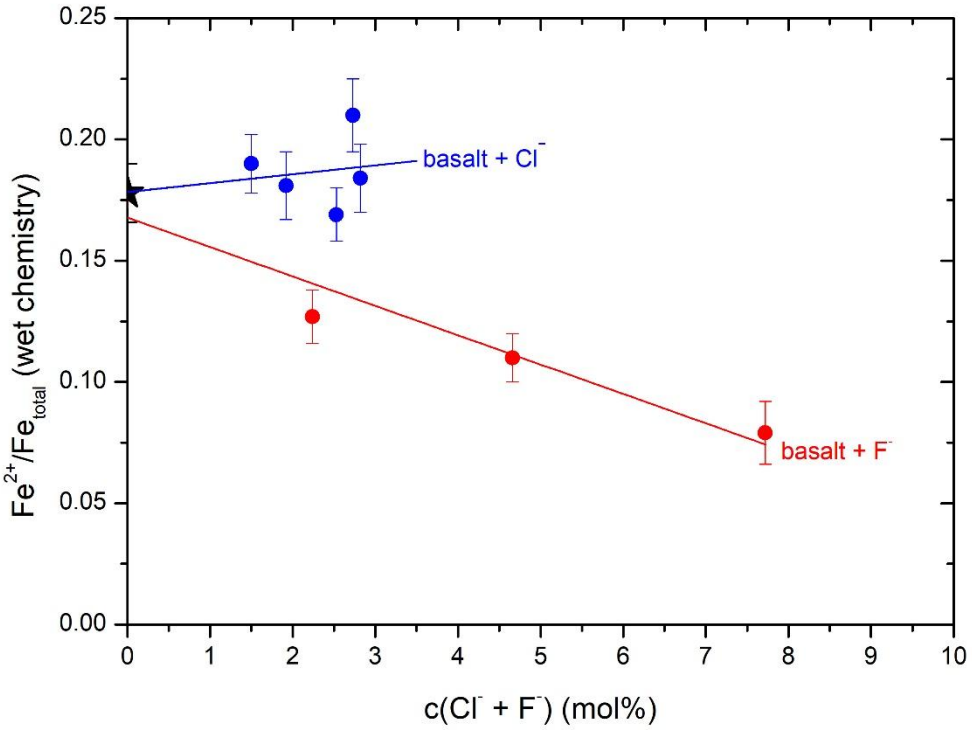

Figure 17: The Fe^{2+}/Fe_{total} iron ratio of the glasses as a function of halogen content.

5.2.4. Raman-spectra: Effect of Fe^{2+}/Fe_{total} iron ratio on the structure

Figure 18 shows the Raman spectra of the halogen-free and halogen-bearing basaltic glasses after a frequency and temperature correction of the Raman intensity after Long (1977). The spectra can be subdivided into a low frequency region (LF: 200 to 600 cm^{-1}), intermediate region (MF: 600 to 800 cm^{-1}) and high frequency region (HF: 800 to 1200 cm^{-1}) after the classification by Mysen and Richet (2005). Di Muro et al. (2009) describes the HF region as sensitive for the redox conditions as well as the best band to observe the effect of iron speciation on glass.

Figure 18 shows a comparison of Raman spectra of halogen-free and –bearing basaltic glass. These glasses show a slight asymmetric peak around 940 cm^{-1}. The presence of 7.73 mol% F^- results in a more distinct shoulder than the spectra of halogen-free basalts. The MF region does not change with the additon of halogens to the present peralkaline melts, whereas the low frequency regions show an increase of the peak around 530 cm^{-1} in intensity (see figure 19). All halogen-bearing spectra reflect a shoulder around 530 cm^{-1} as well as a slight asymmetric peak around 940 cm^{-1}. The addition of F^- decreases the Fe^{2+}/Fe_{total} iron ratio (figure 17) and thus the modificated HF peak of the spectra indicates the influence of fluorine on the glass structure.

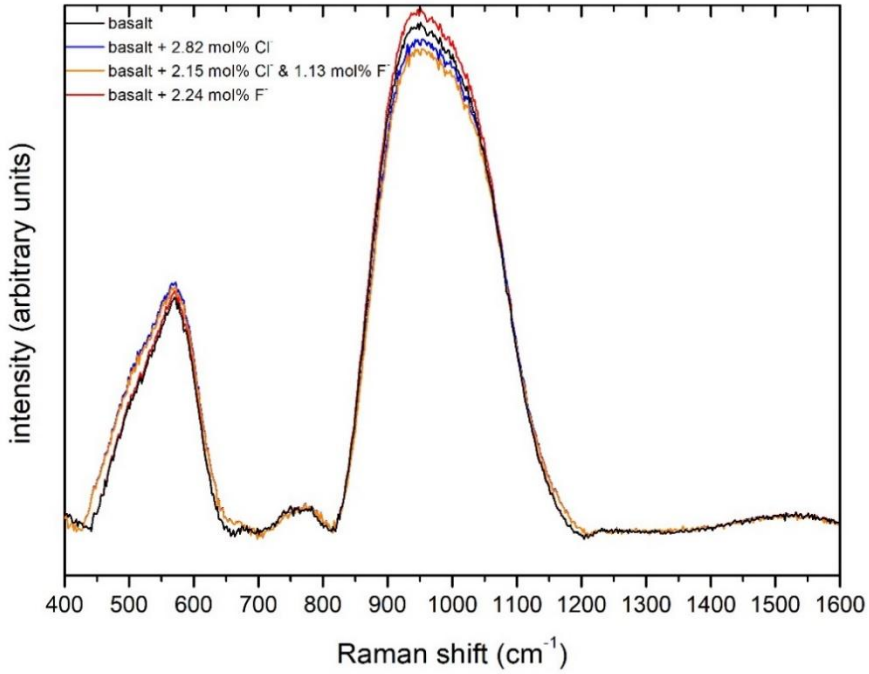

Figure 18: Raman spectra after Long correction: Direct comparison of Raman spectra of halogen-free and halogen-bearing basaltic glasses.

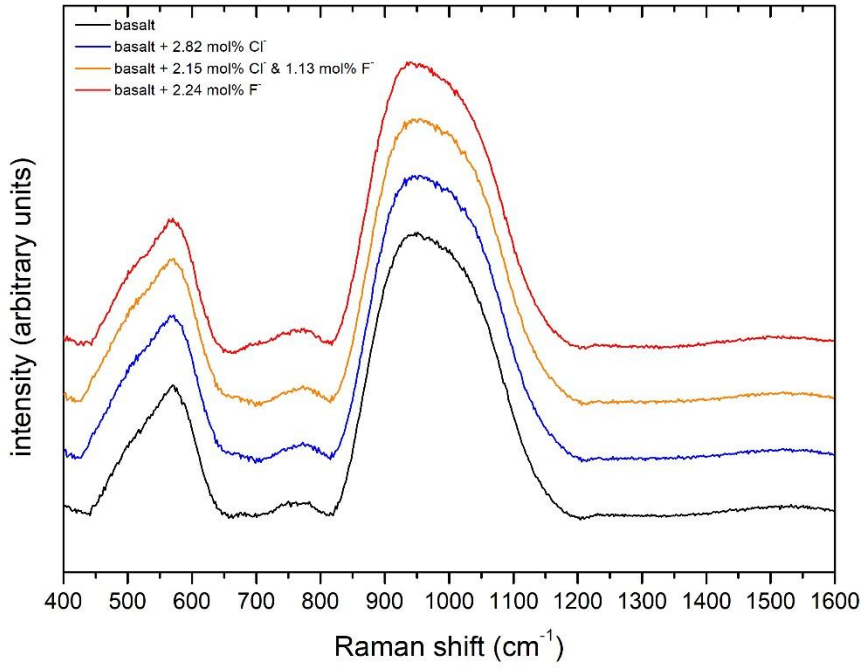

Figure 19: Raman spectra after Long correction: Overview on the Raman spectra of halogen-free and halogen-bearing basaltic glasses.

5.3. Viscosity

The micropenetration viscometry technique was used to determine viscosity of halogen-free and halogen-bearing basaltic melts in the range of $10^{8.5}$ to $10^{13.5}$ Pa s. Table 6 shows the viscosity data with the related experimental temperature. Table 7 lists the parameters for the Arrhenian fit of the viscosity data as well as the glass transition temperature (T_g^{12}). This temperature describes the viscosity at 10^{12} Pa s, whereas it is possible to compare the viscosity with literature data.

Table 6: Micropenetration viscosity data of halogen-free and -bearing basaltic glasses at diverse experimental temperatures. The error in viscosity is 0.06 log_{10} Pa s and the temperature has an error ± 0.5 K.

BA-0		BA-Cl		BA-Cl-2		BA-Cl-3		BA-Cl-4	
T (K)	$log_{10}\eta$ (Pa s)	T (K)	$log_{10}\eta$ (Pa s)	T (K)	$log_{10}\eta$ (Pa s)	T (K)	$log_{10}\eta$ (Pa s)	T (K)	$log_{10}\eta$ (Pa s)
935.4	12.60	935.6	12.65	935.3	13.18	934.5	12.83	942.5	12.59
945.4	12.22	940.4	12.47	945.4	12.62	942.1	12.69	952.4	12.00
955.5	11.76	945.3	12.03	955.4	12.20	952.5	12.18	962.2	11.55
965.6	11.30	950.3	11.81	965.4	11.86	962.0	11.75	972.1	11.05
975.6	10.92	955.5	11.70	975.5	11.20	972.4	11.24	982.0	10.66
980.5	10.69	965.4	11.30	985.7	10.92	984.7	10.74	987.4	10.53
985.6	10.46	975.5	10.85	995.7	10.56	997.4	10.28	992.5	10.21
996.1	10.10	985.6	10.58	1006.0	10.17	1009.4	9.82	1002.3	9.87
1006.0	9.75	995.7	10.10	1016.2	9.87			1012.5	9.24
1016.1	9.39	1005.7	9.84	1025.9	9.45				
1025.9	9.06	1015.8	9.46	1036.3	8.97				
1035.9	8.74	1025.8	9.09						
BA-Cl-F		BA-Cl-F-2		BA-Cl-F-3		BA-F		BA-F-2	
T (K)	$log_{10}\eta$ (Pa s)	T (K)	$log_{10}\eta$ (Pa s)	T (K)	$log_{10}\eta$ (Pa s)	T (K)	$log_{10}\eta$ (Pa s)	T (K)	$log_{10}\eta$ (Pa s)
905.1	12.83	905.1	12.47	912.3	13.25	915.2	12.86	8845.0	13.13
915.1	12.41	915.4	11.98	922.2	12.80	925.3	12.29	895.0	12.29
925.3	11.77	925.2	11.52	932.1	12.56	935.3	11.82	905.1	11.80
935.3	11.34	936.7	11.19	952.3	11.45	945.3	11.48	915.1	11.60
945.3	11.04	945.7	10.78	962.0	11.28	955.4	11.16	925.3	11.30
955.4	10.78	955.4	10.43	972.1	10.58	960.5	10.76	935.3	10.93
965.5	10.53	965.5	10.05	982.0	10.50	965.5	10.54	945.7	10.31
975.6	10.00	976.0	9.70	991.9	10.00	975.5	10.09	955.4	10.13
985.6	9.78	985.6	9.51			985.6	9.83	965.6	9.60
995.6	9.42	991.5	9.17			990.7	9.81	975.5	9.37
1005.4	9.06	995.8	8.85			995.7	9.61	985.8	8.91
						1005.9	9.04	995.6	8.64

Table 7: Parameters for the Arrhenian fit of micropenetration viscosity data.

Sample	A_{Arr} (log10 Pa s K)	ΔA_{Arr} (log10 Pa s K)	B_{Arr} (log10 Pa s K)	ΔB_{Arr} (log10 Pa s K)	T_g^{12} (K)	ΔT_g^{12} (K)	$\eta @ T_g^{12}$ (log10 Pa s)
BA-0	-27.66	0.39	3.76	0.04	949.1	0.2	12.00
BA-Cl-4 (1.92 Cl^-)	-33.61	1.24	4.35	0.12	953.4	0.6	12.20
BA-Cl-2 (2.53 Cl^-)	-28.69	0.76	3.91	0.07	960.5	0.3	12.49
BA-Cl-3 (2.73 Cl^-)	-29.26	0.93	3.94	0.09	955.6	0.4	12.33
BA-Cl (2.82 Cl^-)	-26.83	0.79	3.68	0.08	948.5	0.3	11.97
BA-Cl-F (2.15/1.13 Cl^-/F^-)	-23.74	1.02	3.30	0.10	922.6	0.4	11.01
BA-Cl-F-3 (3.28/2.35 Cl^-/F^-)	-27.12	1.67	3.68	0.16	941.9	0.7	11.70
BA-Cl-F-2 (1.96/5.25 Cl^-/F^-)	-25.15	0.78	3.40	0.07	915.3	0.3	10.67
BA-F (2.24 F^-)	-25.74	1.06	3.43	0.10	932.3	0.4	11.31
BA-F-2 (7.73 F^-)	-25.84	0.97	3.43	0.09	906.2	0.4	10.29

T_g^{12} – temperature at viscosity of 10^{12} Pa s calculated from Arrhenian fit
$\eta @ T_g^{12}$ – the viscosity measured in the halogen-bearing melt at the same temperature as the halogen-free melt has a viscosity of 10^{12} Pa s (Webb et al. 2014)

Figure 20 shows the $\log_{10}$ viscosity (Pa s) of the fluorine-bearing melts as a function of inverse temperature (K^{-1}). The lines represent the Arrhenian fits, which are fitted by equation 7. Fluorine decreases the viscosity for all basaltic melts. The addition of 2.24 mol% fluorine to the basaltic melt results in a decrease in viscosity by 0.7 log units and the further addition of 7.73 mol% fluorine shows a decrease in viscosity by 2.5 log units. These trends of 2.24 and 7.73 mol% fluorine-bearing melts agree with data from starting composition of series III (4.90 mol% F^-, see Part C (3.1. Starting materials) and table 30). This relative decrease of the melt viscosity by the addition of fluorine is greater at low than at high F^- contents.

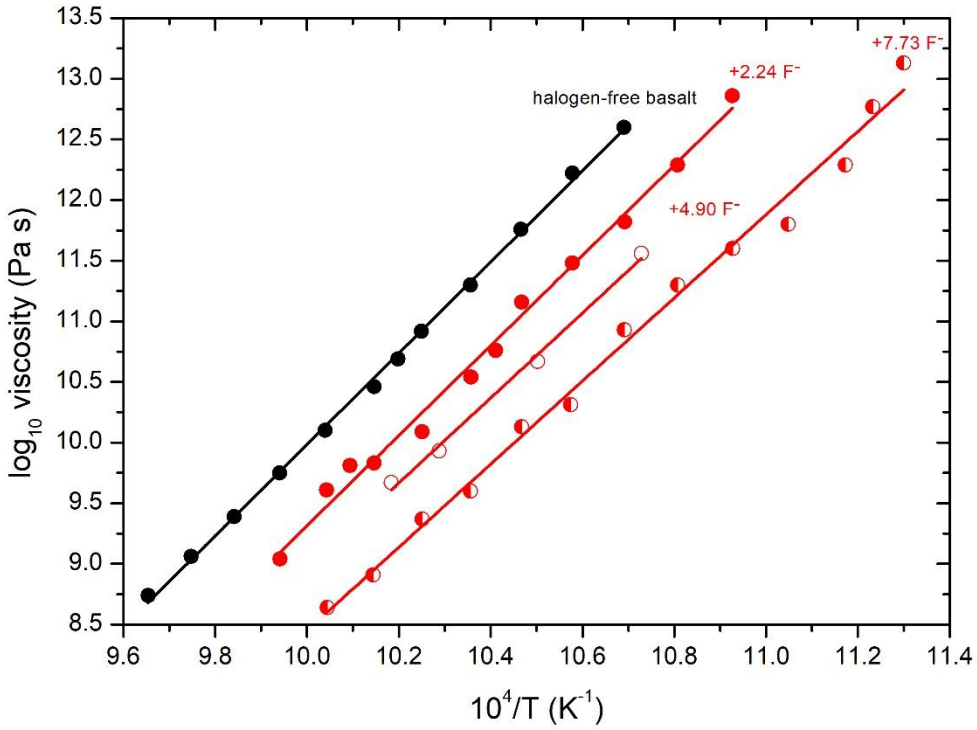

Figure 20: Effect of fluorine on viscosity of basaltic melts. The error bars are smaller than the circles.

Figure 21 demonstrates the influence of chlorine on the viscosity of basaltic melts. The addition of 2.53 mol% chlorine results in increase in viscosity by 0.6 log units and the addition of 2.73 mol% chlorine results in an increase in viscosity by 0.3 log units. The melt with 2.83 mol% Cl^- has a similar to viscosity and follows the same trend as the halogen-free basalt. The effect of chlorine on the viscosity was further tested with two chlorine-bearing melts of series II and III (see table 16 and 30). The addition of a small amount of chlorine (1.50 mol% Cl^-) does not show an effect on viscosity, whereas the further addition of 1.92 mol% chlorine results in a decrease in viscosity by 0.3 log unit. As a consequence, the addition of 1.50 and 1.92 mol% Cl^- compared to the halogen-free basaltic melts does not change the viscosity. Therefore, the effect of viscosity is not only a function of chlorine but also by further elements or effects.

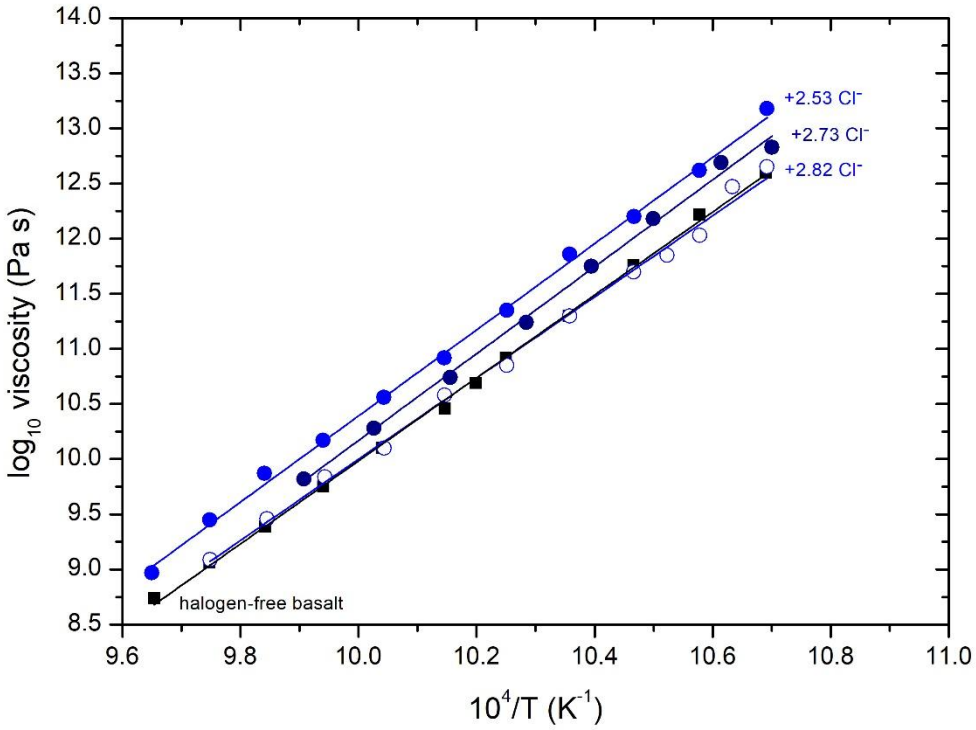

Figure 21: Effect of chlorine on viscosity of basaltic melts. The error bars are smaller than the circles.

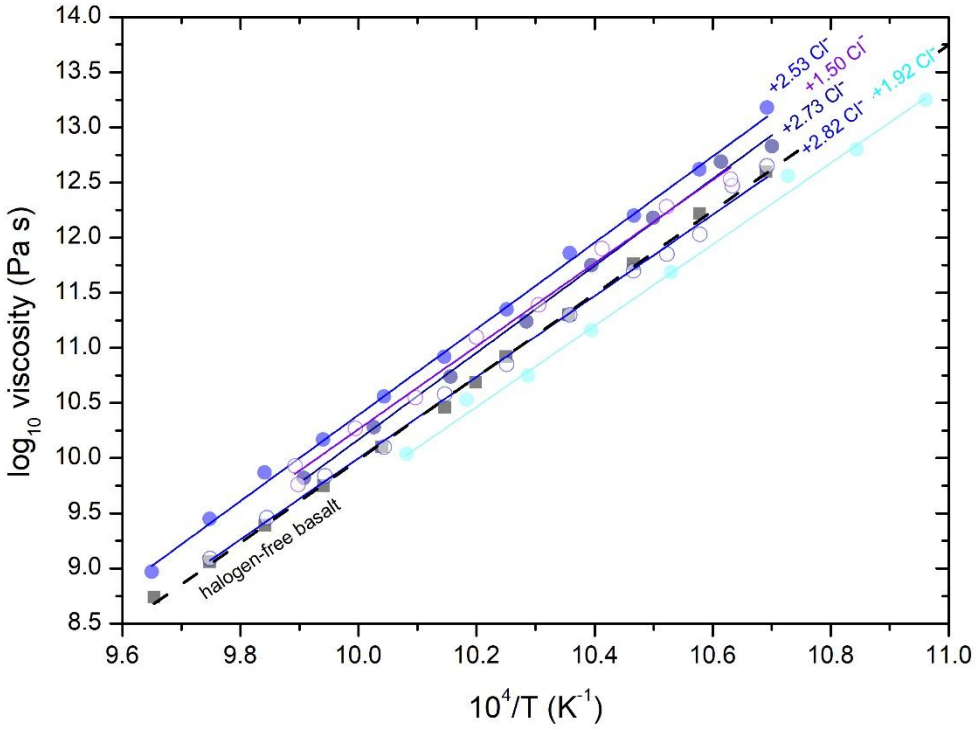

Figure 22: Effect of chlorine on viscosity of further basaltic melts. The error bars are smaller than the circles.

The influence of a combination of chlorine and fluorine on the viscosity of basaltic melts is demonstrated by figure 23. A high chlorine to fluorine ratio results in slight decrease in viscosity by 0.3 log units, whereas a lower Cl^-/F^- results in a stronger decrease in viscosity by 1.5 log units. This diagram shows that chlorine hinders the decreasing effect of fluorine on viscosity.

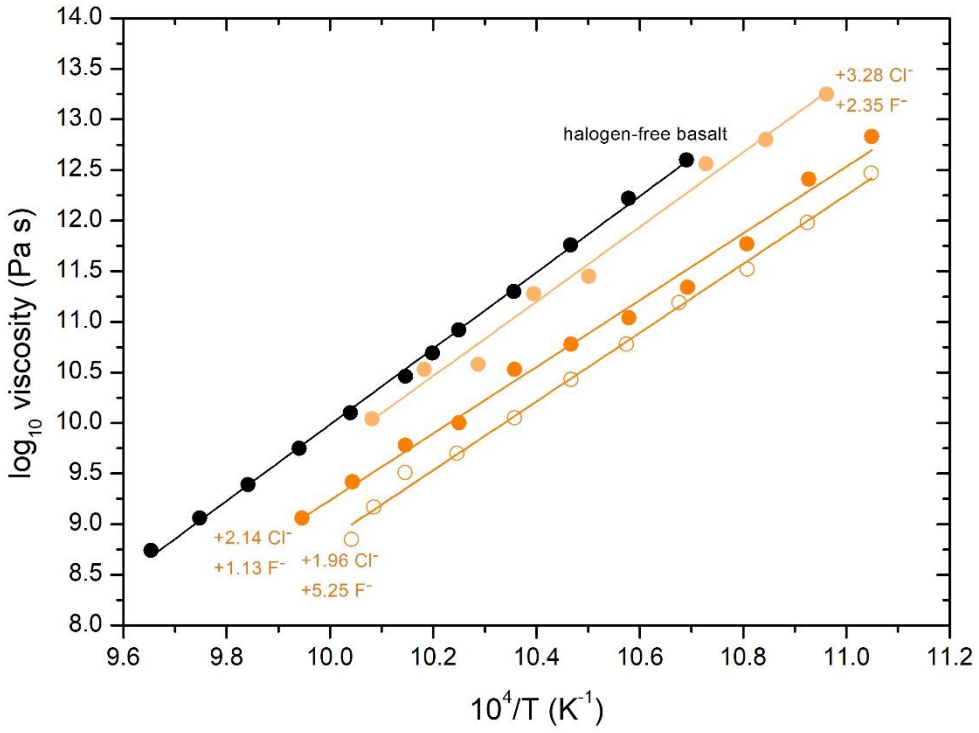

Figure 23: Effect of chlorine and fluorine on viscosity of basaltic melts. The error bars are smaller than the circles.

Figure 24 illustrates the glass transition temperature T_g^{12} from the Arrhenian fit as a function of halogen content. The addition of fluorine to the basaltic melts results in a decrease in T_g^{12} accompanied by the effect of iron speciation (see figure 17). In contrast to the fluorine-bearing melts, the addition of chlorine to a peralkaline melts shows two trends. Firstly, the addition of chlorine up to 2.53 mol% leads to an increase of T_g^{12} by 10 K. Secondly, further increase in the amount of chlorine results in a decrease of T_g^{12} by 15 K. The addition of both halogens to the basaltic melts does not provide useful results for the T_g^{12} trends due to the contrary effects of Cl^- and F^- on viscosity.

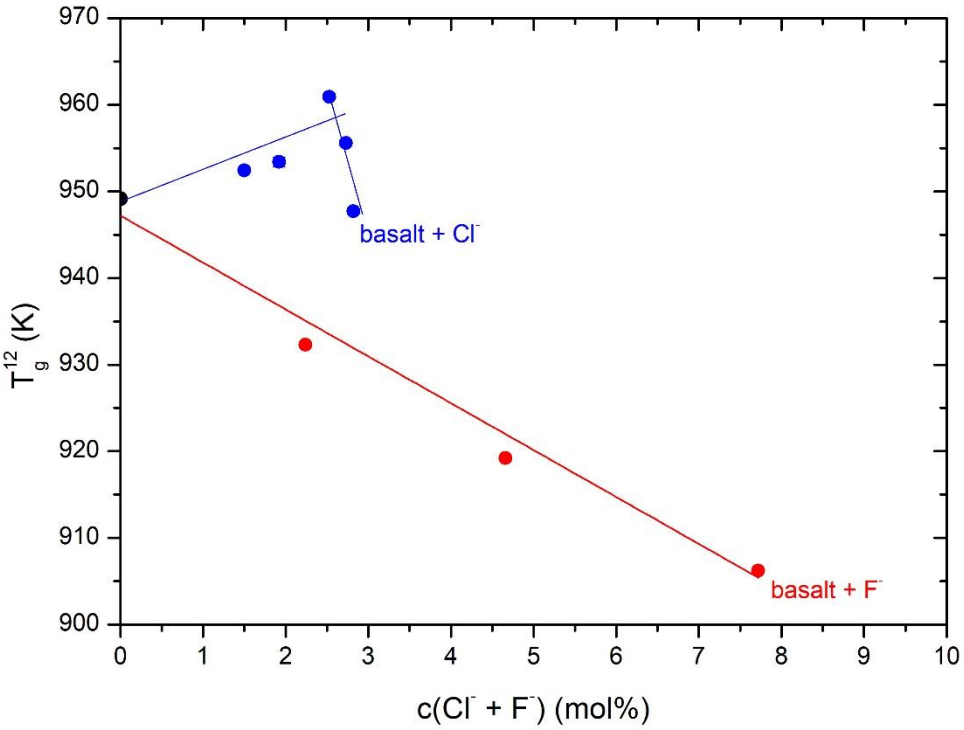

Figure 24: Glass transition temperature as a function of chlorine and fluorine content. The error bars are smaller than the circles.

The Vogel-Fulcher-Tamman (VFT) fit function describes the measured viscosity data as a curve compared to the linear function of an Arrhenian fit (see chapter: analytical methods). The data of Vogel-Fulcher-Tamman fit and the glass transition temperature (T_g^{12}) are shown in table 8. T_g^{12} enables a comparison of diverse viscosity data by a constant viscosity of 10^{12} Pa s. In addition to the Arrhenian fit, the VFT fit describes the data as a curve, whereby the micropenetration data can be combined with diverse viscosity methods like the falling sphere measurements. The fit does not work with three free parameters, therefore the value of A_{VFT} has to be fixed on a constant number. Some other authors have demonstrated that good results were obtained with a value between $10^{-3.5}$ to $10^{-5.5}$ Pa s (Toplis 1998; Baasner et al. 2013a). For the present composition a value of $10^{-4.55}$ Pa s gives the best results (Giordano et al. 2008).

Figure 25 illustrates the comparison of the Arrhenian fit (dashed line) and VFT fit (line) of the viscosity data of fluorine-bearing and halogen-free basaltic melts. Although the VFT fit describes the viscosity data as a curve in the high viscosity regions the deviation between the fits is small. The temperature-related decreasing viscosity effect does not follow a linear behaviour (Fulcher 1925; Tammann and Hesse 1926) and thus the VFT fit is the better choice for extrapolation than the Arrhenian equation.

Table 8: Parameters for the Vogel-Fulcher-Tamman (VFT) to the micropenetration viscosity data.

Sample	A_{VFT}[a] (log_{10} Pa s K)	B_{VFT} (log_{10} Pa s K)	ΔB_{VFT} (log_{10} Pa s K)	C_{VFT} (log_{10} Pa s K)	ΔC_{VFT} (log_{10} Pa s K)	T_g[12] (K)	ΔT_g[12] (K)
BA-0	-4.55	5904.89	52.98	597.70	3.42	949.5	0.1
BA-Cl-4 (1.92 Cl^-)	-4.55	5267.96	155.09	635.08	9.86	953.4	0.2
BA-Cl-2 (2.53 Cl^-)	-4.55	6022.53	104.39	595.76	6.46	959.7	0.2
BA-Cl-3 (2.73 Cl^-)	-4.55	6064.55	171.27	588.52	10.52	955.0	0.3
BA-Cl (2.82 Cl^-)	-4.55	6113.56	102.65	579.19	6.41	948.6	0.3
.BA-Cl-F (2.15/1.13 Cl^-/F^-)	-4.55	6515.72	166.91	528.92	10.64	922.6	0.3
BA-Cl-F-3 (3.28/2.35 Cl^-/F^-)	-4.55	6434.13	251.21	552.17	17.13	940.9	0.3
BA-Cl-F-2 (1.96/5.25 Cl^-/F^-)	-4.55	6122.08	149.24	528.91	10.64	898.8	0.5
BA-F (2.24 F^-)	-4.55	5931.34	133.72	574.01	8.61	932.4	0.3
BA-F-2 (7.73 F^-)	-4.55	6028.50	185.57	541.18	11.88	905.4	0.4

[a] *fixed values on -4.55 Pa s K*

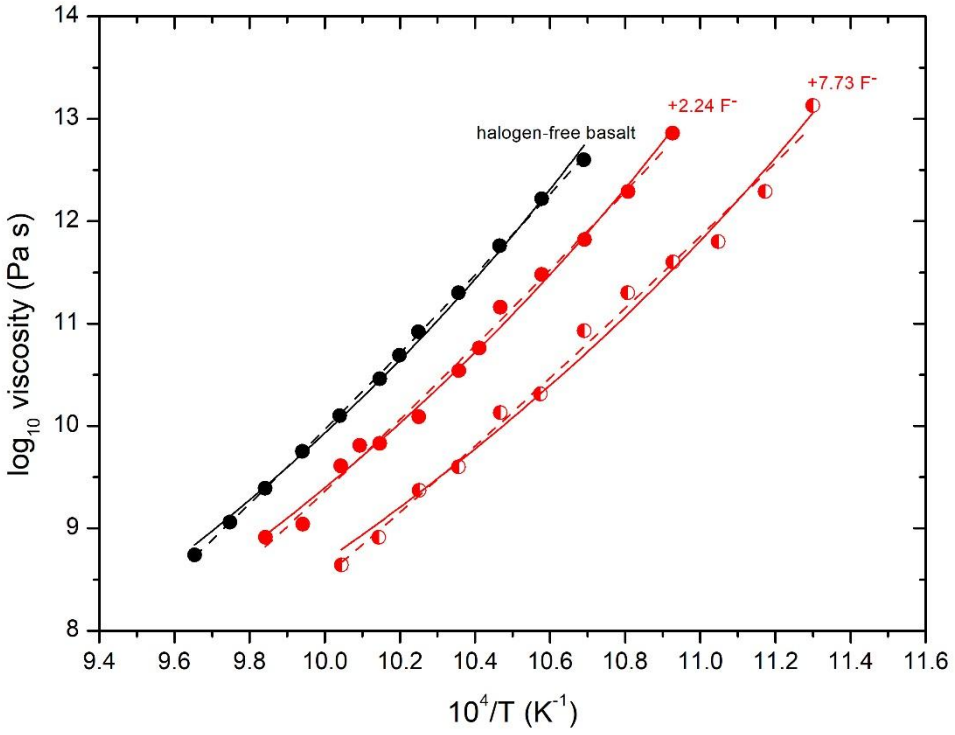

Figure 25: Comparison of the Arrhenian fit (dashed line) and VFT fit (line) of the viscosity data of fluorine-bearing basaltic melts. The error bars are smaller than the circles.

Table 9 gives a comparison of the calculated T_g^{12} for the Arrhenian and VFT fit. Both regressions correspond well for the micropenetration viscosity data.

Table 9: Comparison of the calculated T_g^{12} from the Arrhenian and Vogel-Fulcher-Tamman equation.

Sample	$T_g^{12}{}_{Arr}$ (K)	$\Delta T_g^{12}{}_{Arr}$ (K)	$T_g^{12}{}_{VFT}$ (K)	$\Delta T_g^{12}{}_{VFT}$ (K)
BA-0	949.1	0.2	949.5	0.1
BA-Cl-4 (1.92 Cl^-)	953.4	0.6	953.4	0.2
BA-Cl-2 (2.53 Cl^-)	960.5	0.3	959.7	0.2
BA-Cl-3 (2.73 Cl^-)	955.6	0.4	955.0	0.3
BA-Cl (2.82 Cl^-)	948.5	0.3	948.6	0.3
BA-Cl-F (2.15/1.13 Cl^-/F^-)	922.6	0.4	922.6	0.3
BA-Cl-F-3 (3.28/2.35 Cl^-/F^-)	941.9	0.7	940.9	0.3
BA-Cl-F-2 (1.96/5.25 Cl^-/F^-)	915.3	0.3	898.8	0.5
BA-F (2.24 F^-)	932.3	0.4	932.4	0.3
BA-F-2 (7.73 F^-)	906.2	0.4	905.4	0.4

5.4. Heat capacity

Figure 26 shows the results of heat capacity (c_p) measurements in J mol^{-1} K^{-1} for all halogen-free and halogen-bearing basaltic melts. The measurements were performed with a constant heating and cooling rate of 20 K min^{-1}. The addition of halogens to the present peralkaline melt shows a shift of the onset temperature of the glass transition peak to lower or higher temperatures as a function of composition.

A detailed overview of the glass transition peak of the halogen-bearing melts is given in figure 27 and 28. The addition of fluorine results in a shift of the glass transition peak to lower temperature compared to the halogen-free basaltic melt. In contrast to that, the addition of chlorine results in a shift of the glass transition peak towards a higher temperature compared to the halogen-free basaltic melts. The addition of 2.82 mol% chlorine shows the strongest influence on the onset temperature, whereas lower chlorine contents reflect a diffuse behaviour. The effect of both halogens on basaltic melts correlates well with the data of the individual halogens. Figure 28 shows that the glass transition peak of the basaltic melts with 1.96 mol% Cl^- and 5.25 mol% F^- shifts to lower temperature. This lower onset temperature is similar to that of the composition with only fluorine. The basaltic melt with 2.15 mol% Cl^- and 1.13 mol% F^- result in a minor changes from the halogen-free basalt due to the lower fluorine content. The addition of 3.28 mol% Cl^- and 2.35 mol% F^- to the basaltic melt results in an increase of the onset temperature due to the high Cl^-/F^- ratio.

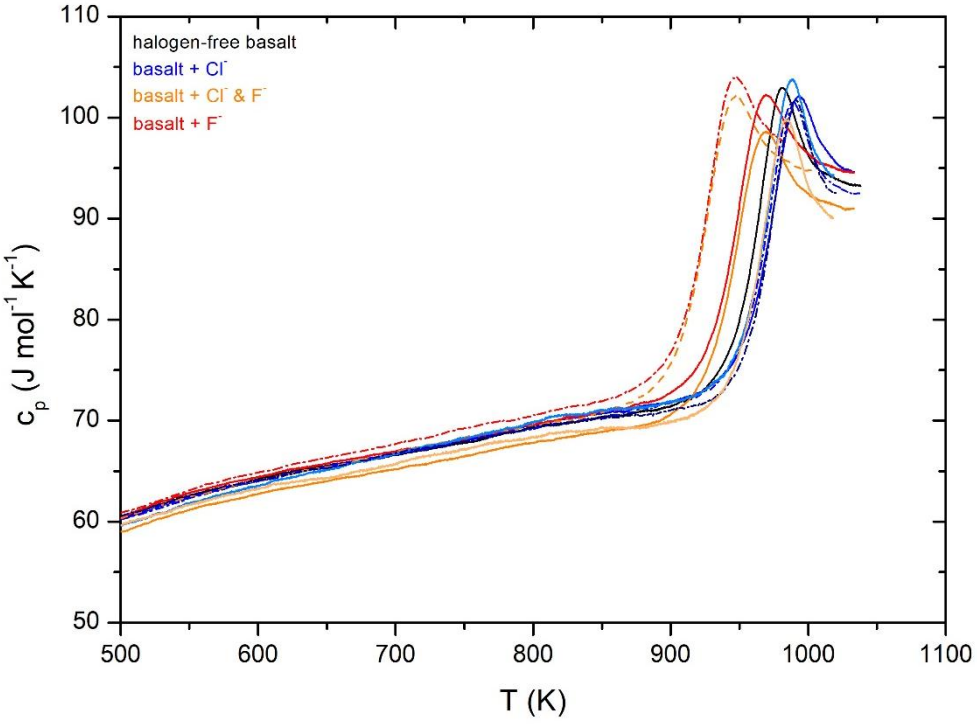

Figure 26: Summary of the heat capacity data for halogen-free basalt melts and melts with added chlorine and fluorine as function of temperature.

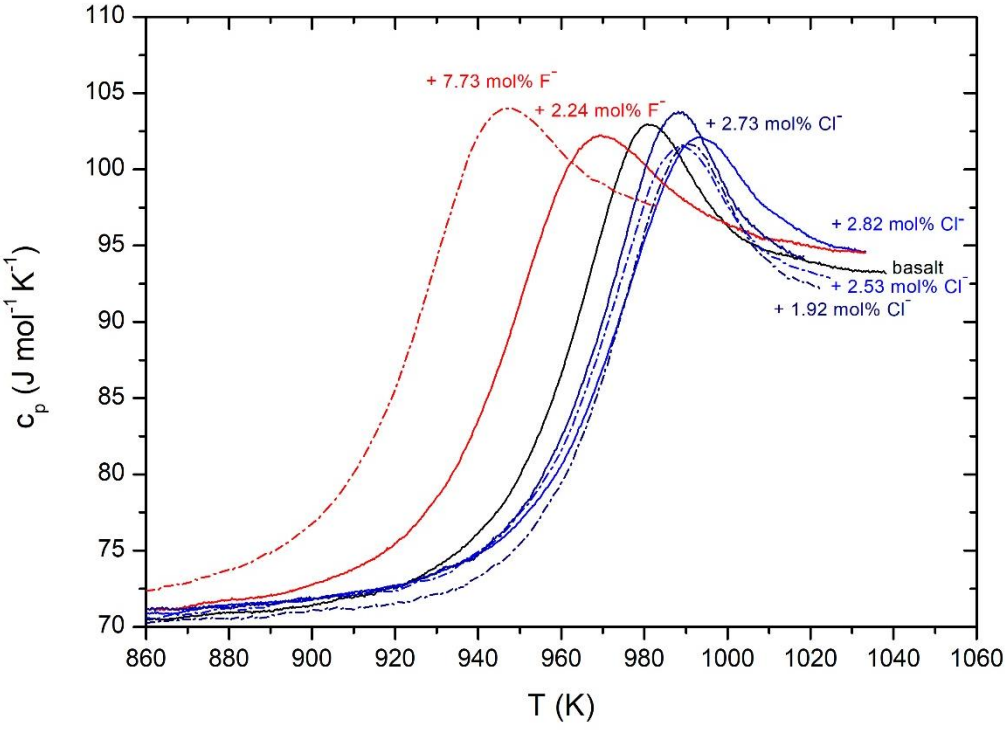

Figure 27: Detailed view of the heat capacity data of figure 26 with the description of the halogen content. The data represents the halogen-free basalt (black), the chlorine-bearing melts (blue) and the fluorine-bearing melts (red).

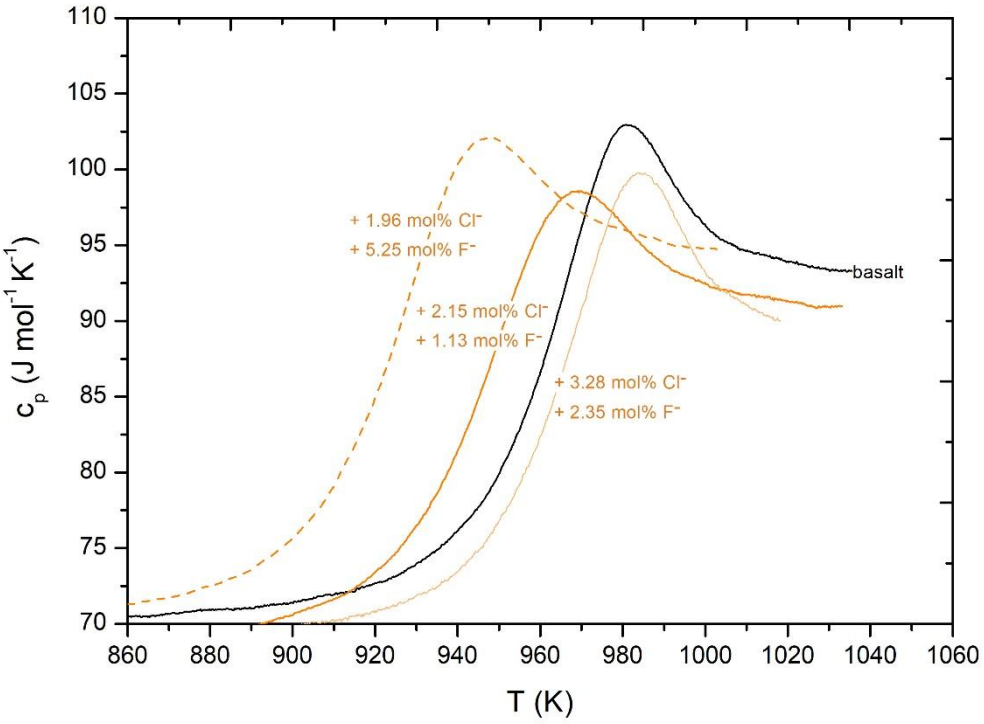

Figure 28: Detailed view of the heat capacity data of figure 26 with the description of the halogen content. The data demonstrates the halogen-free basalt (black) and the basaltic melts with both halogens (orange) with different halogen contents.

The interpretation of the heat capacity data is based on the description from Maier and Kelley (1932) and Moynihan et al. (1976) (see section 4.5. Differential scanning calorimetry). The Maier-Kelley-fit (MK) was extrapolated to the maximum temperature of the heat capacity data (figure 29). The heat capacity of the glass (C_{pg}) can be directly read from the Maier-Kelley-fit. It is important to note that C_{pg} shows the same temperature as C_{pl}. Furthermore, the C_p^{conf} can be determined by the difference of C_{pl} and C_{pg}. Table 10 lists the relevant fit parameters of the Maier-Kelley-regression as well as C_{pl} and C_{pg} for each melt. The interpretation of MK-fit varies by the individual setting of the Maier-Kelley-regression (red line) close to the data and as a result the fit has an error of about 3 %.

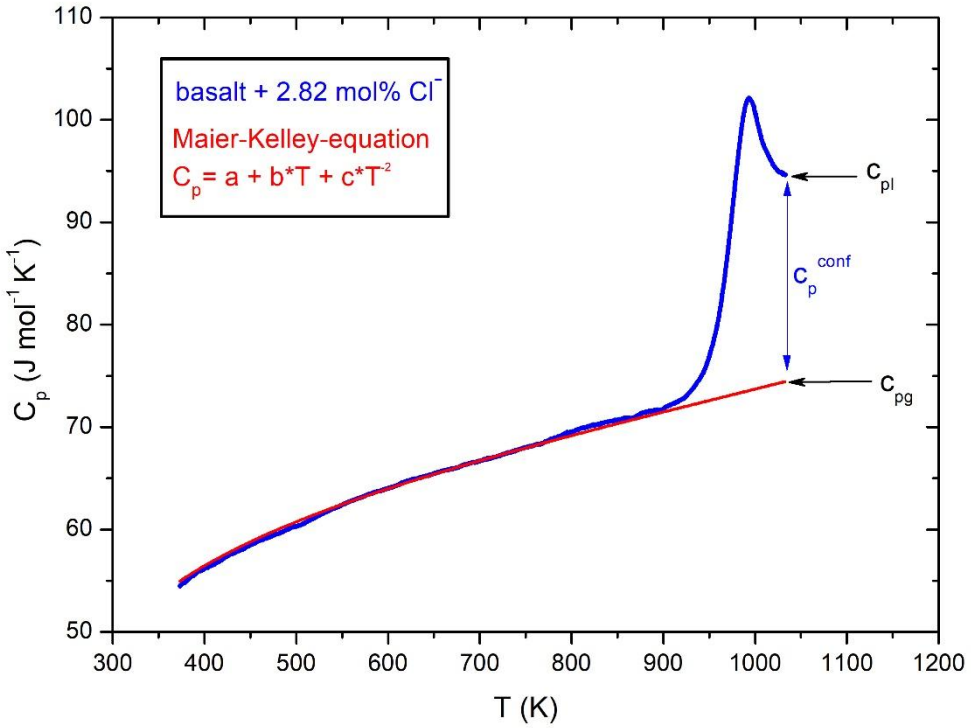

Figure 29: Heat capacity as a function of temperature for chlorine-bearing basaltic melt with the heat capacity of the glass (C_{pg}) and the melt (C_{pl}) as well as the configurational heat capacity (C_p^{conf}). Interpolated after Maier-Kelley-fit (red fit).

Table 10: Parameters for the Maier-Kelley-fit and the heat capacity of the glasses and the melts.

Sample	Maier-Kelley parameters							
	a ($J\,g^{-1}K^{-1}$)	Δa ($J\,g^{-1}K^{-1}$)	b ($10^{-4}J\,g^{-1}K^{-1}$)	Δb ($10^{-4}J\,g^{-1}K^{-1}$)	c ($10^{-4}J\,g^{-1}K^{-1}$)	Δc ($10^{-4}J\,g^{-1}K^{-1}$)	C_{pl} ($J\,mol^{-1}K^{-1}$)	C_{pg} ($J\,mol^{-1}K^{-1}$)
BA-0	0.891	0.001	3.177	0.001	-1.675	0.011	93.34	74.47
BA-Cl-4 (1.92 Cl^-)	0.908	0.001	2.823	0.002	-1.968	0.002	92.18	73.89
BA-Cl-2 (2.53 Cl^-)	0.872	0.001	3.436	0.001	-1.653	0.012	92.55	74.97
BA-Cl-3 (2.73 Cl^-)	0.900	0.001	3.519	0.001	-2.132	0.002	96.23	77.22
BA-Cl (2.82 Cl^-)	0.857	0.001	3.423	0.001	-1.612	0.008	93.10	73.92
BA-Cl-F (2.15/1.13 Cl^-/F^-)	0.900	0.001	4.042	0.002	-1.045	0.015	89.60	72.32
BA-Cl-F-3 (3.28/2.35 Cl^-/F^-)	0.951	0.002	2.551	0.002	-2.479	0.019	90.03	72.45
BA-Cl-F-2 (1.96/5.25 Cl^-/F^-)	0.870	0.001	3.506	0.015	-1.725	0.014	94.74	74.62
BA-F (2.24 F^-)	0.854	0.001	3.568	0.001	-1.346	0.014	94.07	75.16
BA-F-2 (7.73 F^-)	0.862	0.001	3.822	0.015	-1.683	0.014	97.57	75.58

Table 11 shows the parameters of the heat capacity measurement, which are described in chapter A (4.5. Differential scanning calorimetry). The addition of 7.73 mol% fluorine to the basaltic melt results in an increase of the configurational heat capacity from 18.86 to 21.99 J mol^{-1} K^{-1}, whereas the chlorine-bearing melts do not show a linear dependence of C_p^{conf}. Firstly, the addition of 2.53 mol% chlorine to the basaltic melt results in a decrease in C_p^{conf} from 18.86 to 17.58 J mol^{-1} K^{-1}. Subsequently, the chlorine-bearing melt with 2.82 mol% Cl^- shows an increase in C_p^{conf} to 19.18 J mol^{-1} K^{-1}. The melts with both halogens show a decrease in C_p^{conf} from 18.86 to 17.27 J mol^{-1} K^{-1} due to the increasing Cl^-/F^-. Whereas the melt with 1.96 mol% Cl^- and 5.25 mol% F^- shows an increase in C_p^{conf} from 18.86 to 20.13 J mol^{-1} K^{-1} due to the decreasing Cl^-/F^-. These results correlate well with the chlorine as well as fluorine contents.

Table 11: Parameters of the configurational heat capacity and entropy for the viscosity at the glass transition temperature (measured with heating rate of 20 K min^{-1}).

Sample	T_f^{20} (K)	C_p^{conf} (J $mol^{-1}K^{-1}$)	$S_{conf}(T_g^{12})$ (J $mol^{-1}K^{-1}$)	$\Delta S_{conf}(T_g^{12})$ (J $mol^{-1}K^{-1}$)	B_e (kJ mol^{-1})	ΔB_e (kJ mol^{-1})
BA-0	949	18.86	11.55	0.15	418.29	5.02
BA-Cl-4 (1.92 Cl^-)	953	18.29	9.36	0.43	340.17	14.99
BA-Cl-2 (2.53 Cl^-)	960	17.58	9.94	0.36	400.52	12.67
BA-Cl-3 (2.73 Cl^-)	954	19.01	11.19	0.96	402.19	33.92
BA-Cl (2.82 Cl^-)	948	19.18	12.65	0.42	457.38	14.51
BA-Cl-F (2.15/1.13 Cl^-/F^-)	923	17.27	13.25	0.65	466.02	22.03
BA-Cl-F-3 (3.28/2.35 Cl^-/F^-)	942	17.58	12.49	0.95	447.34	33.53
BA-Cl-F-2 (1.96/5.25 Cl^-/F^-)	916	20.13	15.09	0.61	492.81	20.23
BA-F (2.24 F^-)	932	18.91	12.16	0.49	432.22	16.58
BA-F-2 (7.73 F^-)	905	21.99	15.50	0.83	526.89	27.54

A_e are fixed on -4.55 Pa s K

T_f^{20} (calculated fictive temperature) have a standard deviation of ± 2 K

In figure 30, the configurational heat capacity C_p^{conf} of the halogen-free and -bearing basaltic melts is plotted as a function of halogen content. The addition of 7.73 mol% F^- to the basaltic melt results in the highest C_p^{conf} of 21.9 J mol^{-1} K^{-1}, whereas the addition of 2.15 mol% Cl^- & 1.13 mol% F^- to the basaltic melt shows the lowest configurational heat capacity with a decrease in C_p^{conf} from 18.86 to 17.27 J mol^{-1} K^{-1}. The chlorine-bearing melts show two trends. The addition of 2.53 mol% chlorine to the present basaltic melt results in a decrease the C_p^{conf} from 18.86 to 17.58 J mol^{-1} K^{-1} and the further addition of chlorine (> 2.53 mol%) results in an increase in C_p^{conf} from 17.58 to 19.18 J mol^{-1} K^{-1}. This trend effects the C_p^{conf} of basaltic melts with both halogens, whereby a high Cl^-/F^- results in a decrease in C_p^{conf} and a smaller Cl^-/F^- results in an increase in C_p^{conf}.

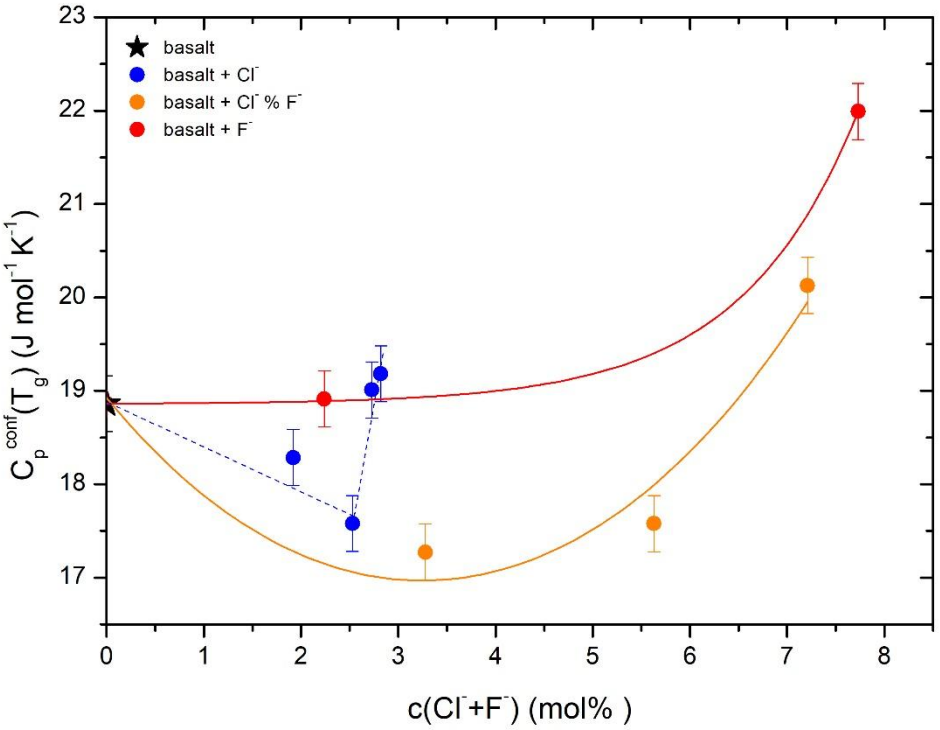

Figure 30: Configurational heat capacity C_p^{cont} as a function of halogens of basaltic melts.

Furthermore, the configurational entropy (S_{conf}) gives information about the rearrangement of the structure. The addition of fluorine to the basaltic melt results in an increase in configurational entropy S_{conf} (figure 31). The addition of 7.73 mol% fluorine to the basaltic melt results in a strong increase in the configurational entropy from 11.55 to 15.50 J mol^{-1} K^{-1}. Compared to the fluorine-bearing melts, the addition of 1.92 mol% chlorine to the halogen-free basaltic melt results in a decrease in S_{conf} from 11.55 to 9.36 J mol^{-1} K^{-1}. The further addition of chlorine induces in an increase in S_{conf} to 12.65 J mol^{-1} K^{-1} (blue points). The addition of (Cl^- + F^-) to the present basaltic melts results in an increase in S_{conf} from 11.55 to 15.09 J mol^{-1} K^{-1}. Consequently, the addition of fluorine has the stronger effect on the structure of peralkaline melts.

As mentioned in section 5.2.3. (Fe^{2+}/Fe_{total} iron ratios depend on chlorine and fluorine), the addition of halogens to the present basaltic melts has an effect on the iron speciation. Therefore, S_{conf} is considered as a function of iron speciation in figure 32. The addition of fluorine results in an increase in S_{conf} by a simultaneous decrease in Fe^{2+}/Fe_{total}. The (Cl^- + F^-)-bearing melts show a similar increase in S_{conf} as a function of iron speciation depending on the Cl^-/F^- ratio. Furthermore, the chlorine-bearing glasses show an increase in S_{conf} from 9.36 to 12.65 J mol^{-1} K^{-1} by a constant Fe^{2+}/Fe_{total}. For this reason, S_{conf} is not only a function of iron speciation but also halogen contents (figure 31).

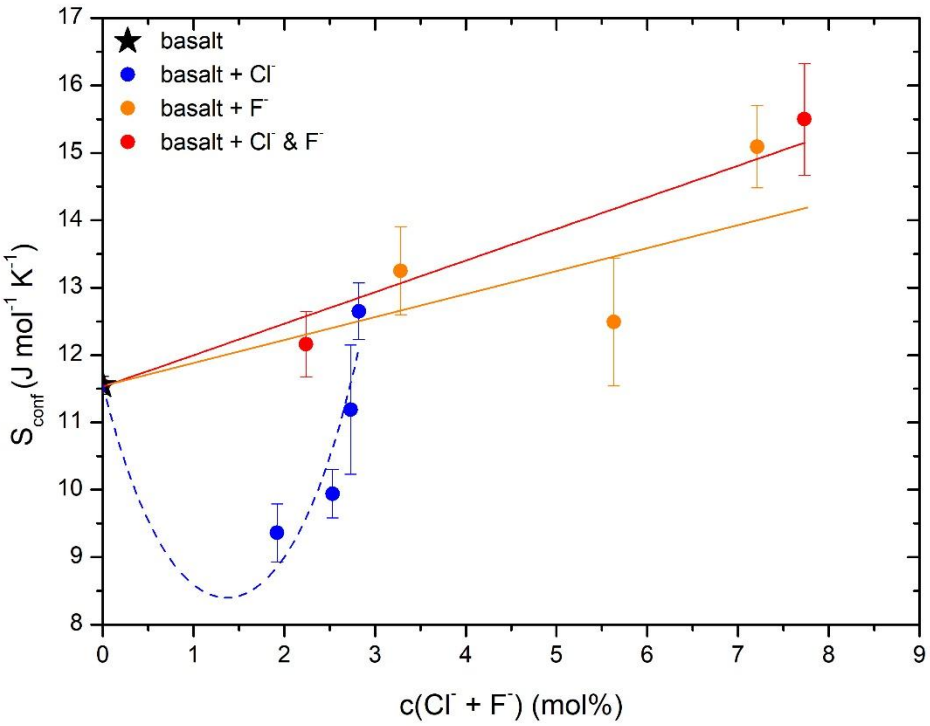

Figure 31: Configurational entropy S_{conf} as a function of halogens of basaltic melts.

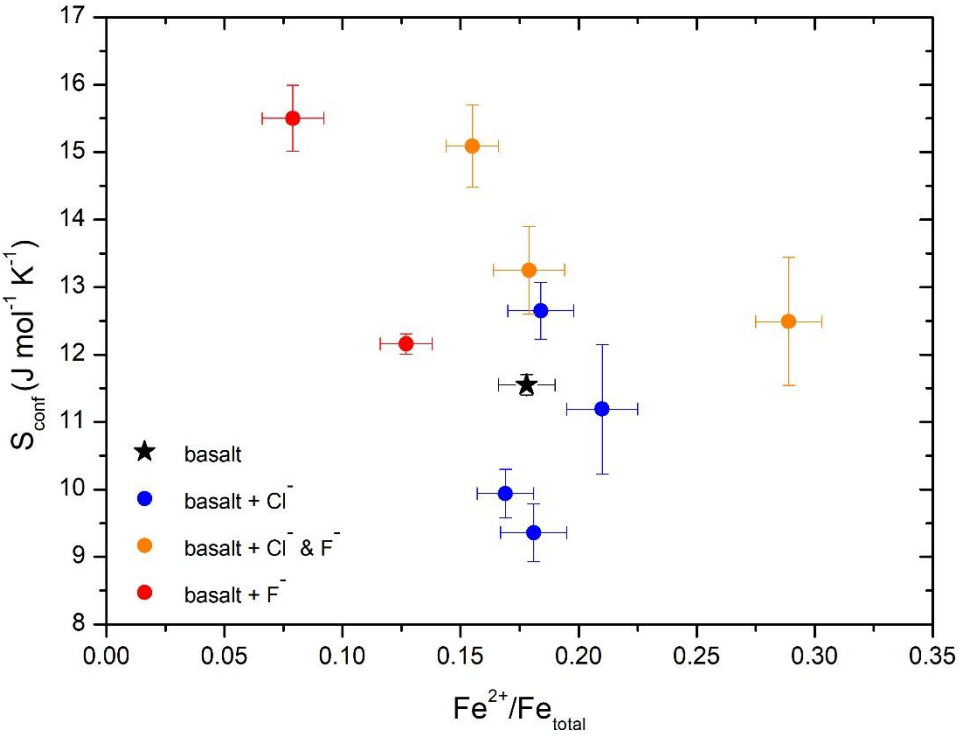

Figure 32: Configurational entropy S_{conf} as a function of iron speciation of basaltic melts.

The B_e values as a function of the sum of chlorine and fluorine for halogen-free and –bearing basaltic melts are represented in figure 33. Richet (1984) describes the constant B_e as the potential energy effect on viscous flow (see section 4.5. Differential scanning calorimetry). The addition of F^- and (Cl^- + F^-) to the basaltic melts results in an increase in B_e from 418.29 to 526.89 kJ mol^{-1} (492.81 kJ mol^{-1} for BA-Cl-F-2), which reflects a decrease in polymerisation of glass structure. Furthermore, the presence of 2.53 mol% chlorine in the basaltic melt shows a decrease in B_e, but the further addition of chlorine results in an increase in B_e from 340.17 to 457.38 kJ mol^{-1}. The decrease in B_e indicates a depolymerisation, whereas the increase in B_e value shows an increasing polymerisation (Richet 1984). The presented trends show a similar behaviour like the dependence of the configurational entropy (S_{conf}) on halogen contents (see figure 31).

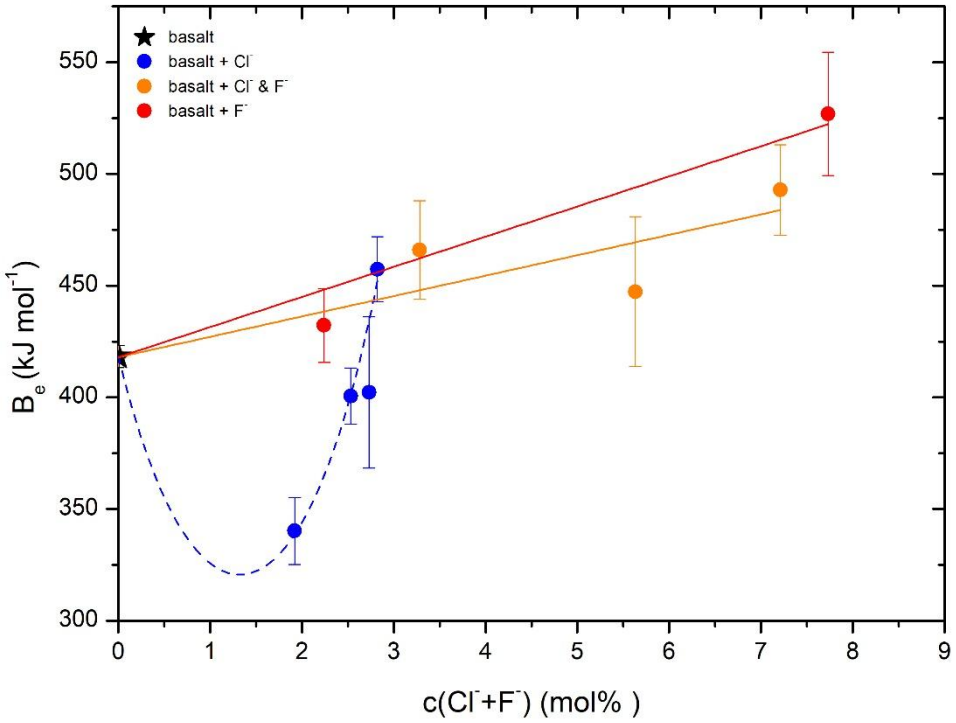

Figure 33: B_e as a function of the sum of chlorine and fluorine for basaltic melts.

Figure 34 illustrates the dependence of configurational entropy (S_{conf}) on B_e of the halogen-free and –bearing basaltic melts. The diagram clearly shows the linear relation between S^{conf} and B_e for all halogen-bearing melts. $B_e/S_{conf}(T_g)$ enables indications on the flow mechanism (Webb 2005). In figure 35, the dependence of B_e/S_{conf} on the halogen content of basaltic melts is represented. The increasing fluorine content (up to 7.73 mol%) in basaltic melts results in a decrease in B_e/S_{conf} from 36.22 to 33.99. The addition of 2.53 mol% Cl^- to the basaltic melts shows an increase in B_e/S_{conf} from 36.22 to 40.29, whereas the presence of

more Cl^- results in a strong decrease of B_e/S_{conf} from 40.29 to 35.94. The presence of both halogens in basaltic melts results in a balanced B_e/S_{conf} between 36.22 to 35.17, the highest F^-/Cl^- shows a decrease in B_e/S_{conf} from 35.17 to 32.66. It becomes obvious that the effect of fluorine is stronger than the chlorine effect.

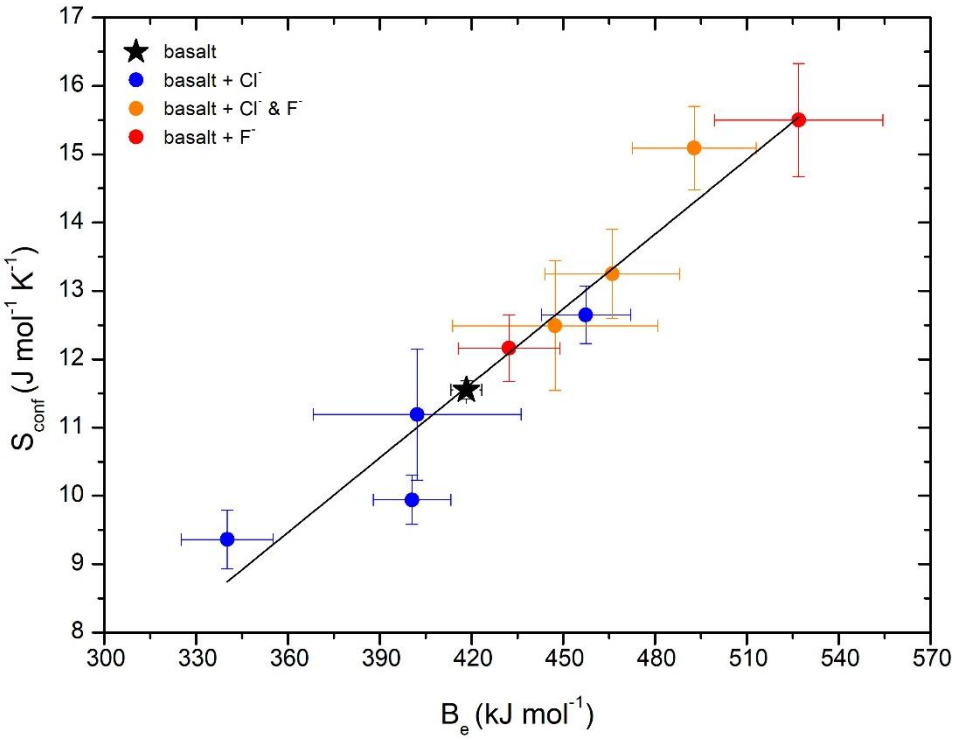

Figure 34: Configurational entropy S_{conf} as a function of B_e of basaltic melts.

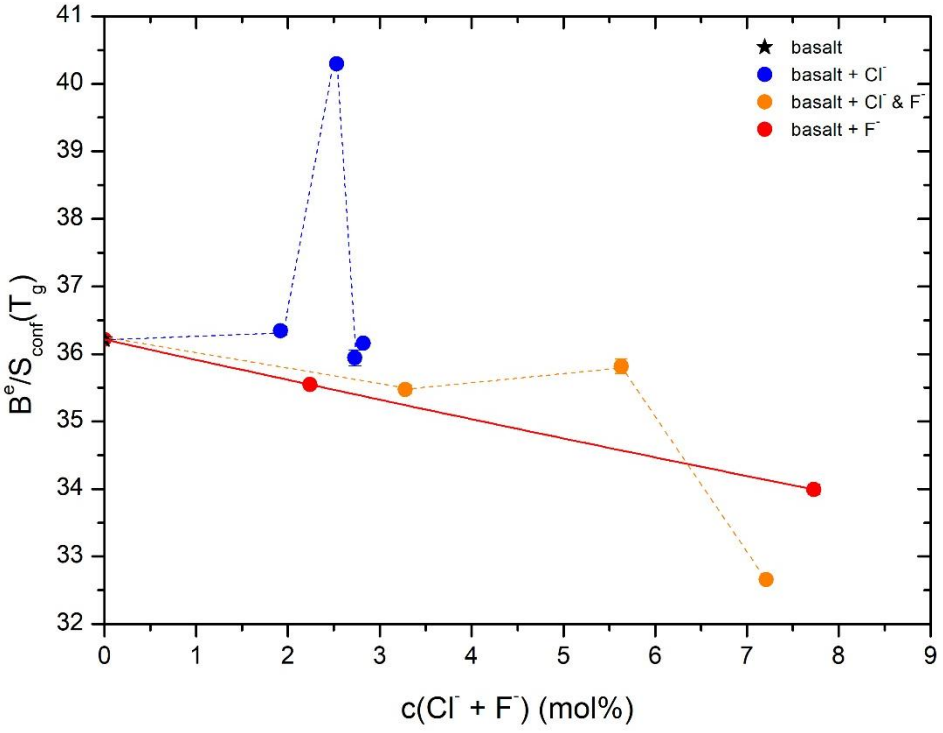

Figure 35: B_e/S_{conf} terms as a function of halogen content for halogen-free and –bearing basaltic melts.

Richet and Bottinga (1984) discussed that the heat capacity of glass is generally close to 24.90 J g^{-1} $atom^{-1}$ K^{-1}. This value is the 3R/g atom (R = gas constant), which describes the highest possible heat capacity of solids with harmonic vibrations (Dulong and Petit limit) and represents another method to estimate c_{pg}. Figure 36, 37 and 38 represents 3R fits of halogen-bearing glasses compared to halogen-free glass for F^-, Cl^- and (Cl^- + F^-), which apply well to the heat capacity of glasses of 24.9 J g^{-1} $atom^{-1}$ K^{-1} within an error 5 %. The 3R-fits correlate well for the halogen-free basaltic melt (black line), whereas the model underestimates the halogen-bearing melts. Further values of C_{pg} and C_p^{conf} can be determined (table 12) on the basis of the 3R-fit (figure 36, 37 and 38) by means of Richet and Bottinga (1984).

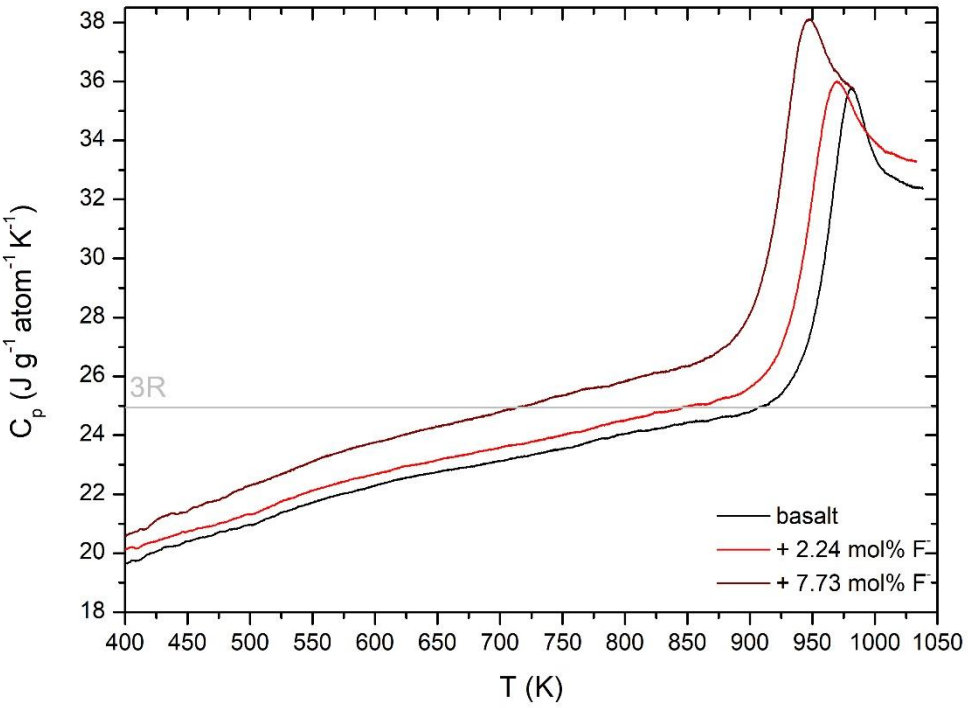

Figure 36: Plots of 3R - Dulong and Petit limit - for heat capacity calculated in mole per atoms for the fluorine-bearing melts.

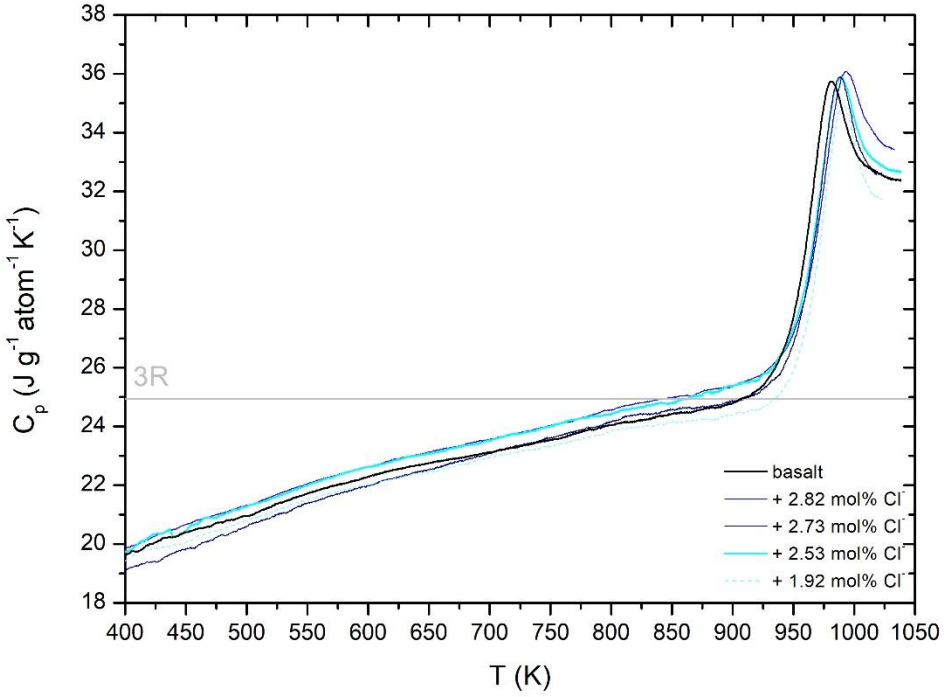

Figure 37: Plots of 3R - Dulong and Petit limit - for heat capacity calculated in mole per atoms for the chlorine-bearing melts.

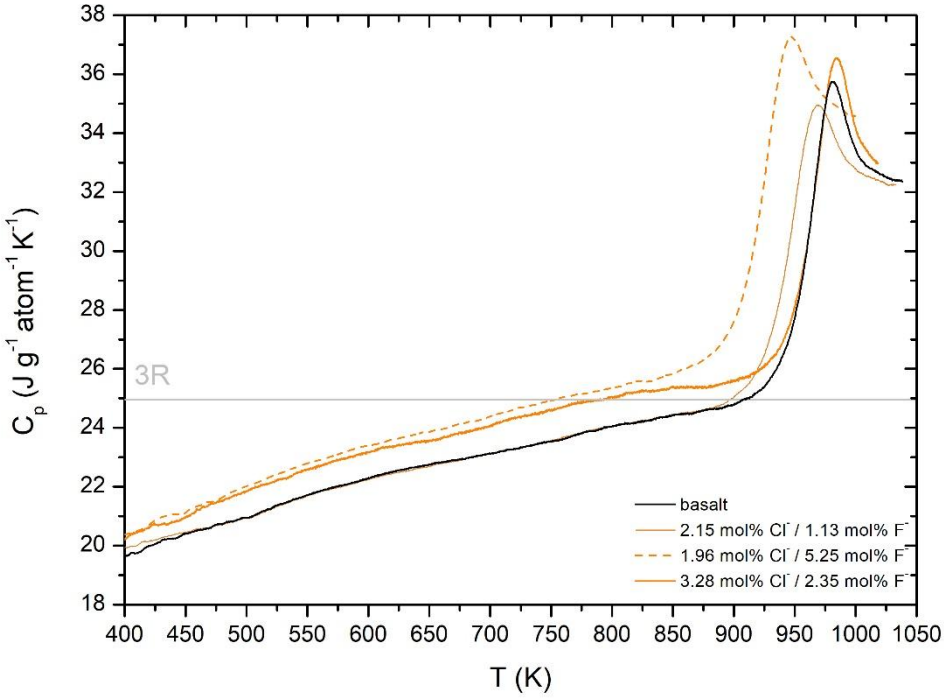

Figure 38: Plots of 3R - Dulong and Petit limit - for heat capacity calculated in mole per atoms for the (Cl^- + F^-)-bearing melts.

Table 12 shows a comparison of C_{pg} and C_p^{conf} of the Maier-Kelley-fit (MK) and the 3R-fit. The MK shows a significant higher C_{pg}, whereby the C_p^{conf} gives lower values compared to the 3R-fit. Figure 39 represents the C_p^{conf} of the MK- and 3R-fit as a function of halogen content. It is seen clearly that the $C_p^{conf\ 3R}$ are larger than $C_p^{conf\ MK}$. This variation reflects the underestimation of C_{pg}^{3R} in figure 36, 37 and 38, whereas the $C_p^{conf\ MK}$ are overestimated. In general the 3R-fits correlate well with the halogen-free basaltic melts, whereas the halogen-bearing basaltic melts differ from the 3R-fit and the MK-fit would lead to better results.

Table 12: Comparisons of the heat capacity of the glasses, the melts and the configurational heat capacity are determined by the MK and 3R-fit.

Sample	C_{pg}^{MK} ($J\ mol^{-1}\ K^{-1}$)	C_{pg}^{3R} ($J\ mol^{-1}\ K^{-1}$)	$C_p^{conf\ MK}$ ($J\ mol^{-1}\ K^{-1}$)	$C_p^{conf\ 3R}$ ($J\ mol^{-1}\ K^{-1}$)
BA-0	74.47	71.94	18.86	21.39
BA-Cl-4 (1.92 Cl-)	73.89	72.43	18.29	19.75
BA-Cl-2 (2.53 Cl-)	74.97	70.61	17.58	21.94
BA-Cl-3 (2.73 Cl-)	77.22	72.12	19.01	24.11
BA-Cl (2.82 Cl-)	73.92	70.55	19.18	22.55
BA-Cl-F (2.15/1.13 Cl-/F-)	72.32	70.36	17.27	19.24
BA-Cl-F-3 (3.28/2.35 Cl-/F-)	72.45	70.52	17.58	19.51
BA-Cl-F-2 (1.96/5.25 Cl-/F-)	74.62	68.45	20.13	26.30
BA-F (2.24 F-)	75.16	70.74	18.91	23.33
BA-F-2 (7.73 F-)	75.58	68.14	21.99	29.43

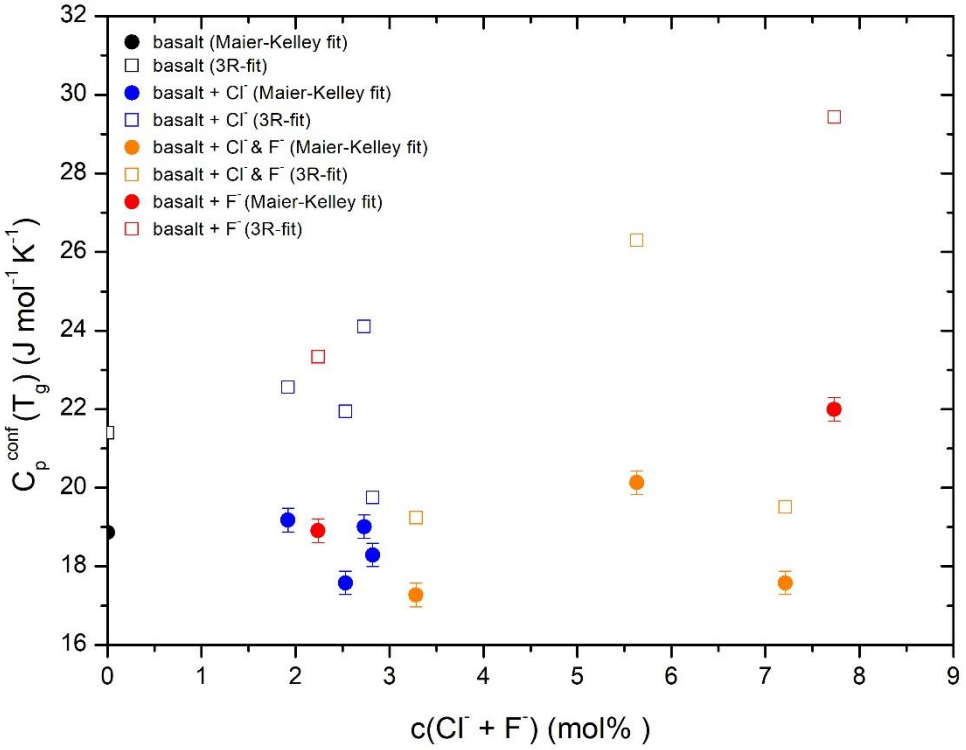

Figure 39: Comparison of C_p^{conf} of Maier-Kelley-fit (filled circles) and 3R-fit (open rectangles) of halogen-bearing basaltic melts.

6. Discussion

Our experiments have shown that the addition of halogens effects the melt viscosity. The halogens were incorporated in complex and different bondings as well as in other structure environments. In a modified model after Di Muro et al. (2009), the Raman intensity ratio of low to high frequency regions (LF/HF) enables the observation of the effect of halogens on the structure. The calibration lines from Di Muro et al. (2009) allowed a precise determination of iron redox state based on the LF/HF intensity ratios and iron ratios. Figure 40 shows that the normalised intensity ratios (LF/HF) increase with increasing halogen content. This indicates a relationship between the presences of halogens and the glass polymerisation degree.

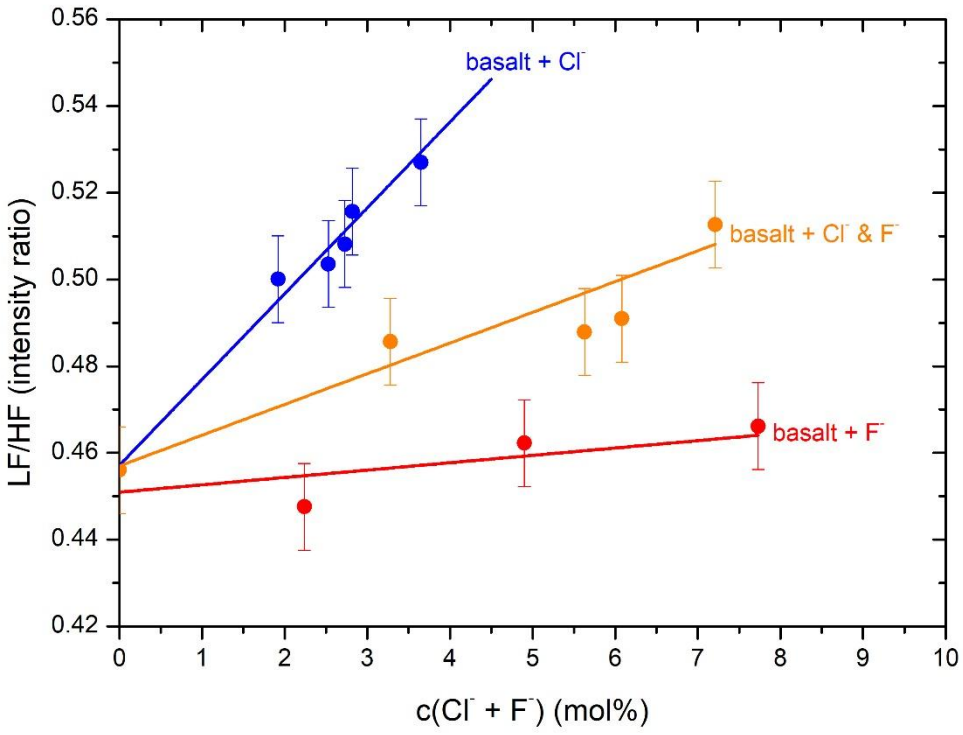

Figure 40: Effect of halogens on the LF/HF Raman intensity ratio of halogen-bearing basaltic glasses.

6.1. Fluorine-bearing basaltic glasses

6.1.1. Influence of fluorine on the viscosity of basaltic melts

The addition of 2.24 mol% fluorine to the basaltic melt results in a decrease in viscosity by 0.7 log units, whereas the presence of 7.73 mol% F^- results in a decrease in viscosity by 1.6 log unit. The first incorporation of fluorine (2.24 mol%) results in the most significant decrease in viscosity, whereas the increasing fluorine content results in a slighter decrease in viscosity. Webb et al. (2014) and Robert et al. (2015) have shown the decreasing effect of fluorine on the viscosity of basaltic melts. This effect is represented in figure 41. The addition of <4 mol% F^- to the fu06 basaltic composition shows the strongest effect on the viscosity, whereby the decreasing viscosity effect is lower with > 4 mol% F^- (Robert et al. 2015). Webb et al. (2014) demonstrates that the addition of 4.64 mol% F^- to their basaltic composition results in a decrease in viscosity by 1.5 log units, which shows the smallest effect. The different trends appear due to the decreasing SiO_2 contents (Dingwell and Mysen 1985). The addition of 4.90 mol% F^- to the present basaltic composition results in a decrease of SiO_2 from 54.97 to 52.49 mol% (table 1). Furthermore, the presence of 4.64 mol% F^- in X24 shows a decrease of SiO_2 from 54.79 to 53.84 mol% (Webb et al. 2014). The starting composition of Robert et al. (2015) has an already lower SiO_2 content (52.70 ± 0.50 mol%) than the present and X24 basaltic composition. By the addition of 1.98 to 6.43 % F^- the SiO_2 content is expected to be much lower, which effects the low viscosity. Dingwell and Mysen (1985) suggested that the addition of fluorine to silicate melts disrupts the three-dimensional network structure. The lower the SiO_2 content in the melt structure, the more effect has the addition of fluorine on the decreased amount of Si-O bondings. Webb et al. (2014) suggested that the addition of fluorine results in an increase in Fe^{2+}/Fe_{total}, but this effect cannot be proven by the present data (figure 42). Figure 42 shows that the addition of fluorine to the present basaltic melt results in a decrease in Fe^{2+}/Fe_{total} by 0.10. This oxidation of ferrous to ferric iron would result in a polymerisation of structure, but this oxidation has no significant effect on the viscosity. In summary, the decreasing F^- content results in a decrease in viscosity for all samples. The different decreasing viscosity trends can be explained by diverse melt compositions (varied FeO_{total} content) and Fe^{2+}/Fe_{total} (different melting temperature - Kress and Carmichael (1991)).

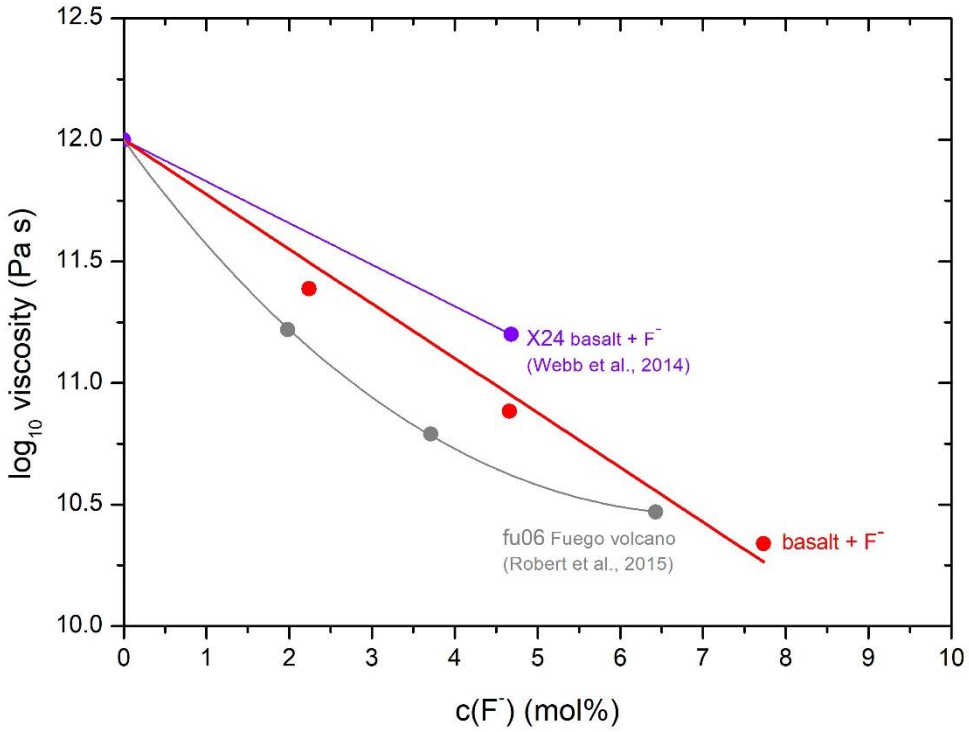

Figure 41: The change in viscosity due to the addition of chlorine at the same temperature as the original melt has a viscosity of 10^{12} Pa s. Literature data: Webb et al. (2014) - violet circles ; Robert et al. (2015) – grey circles. The error bars are smaller than the circles.

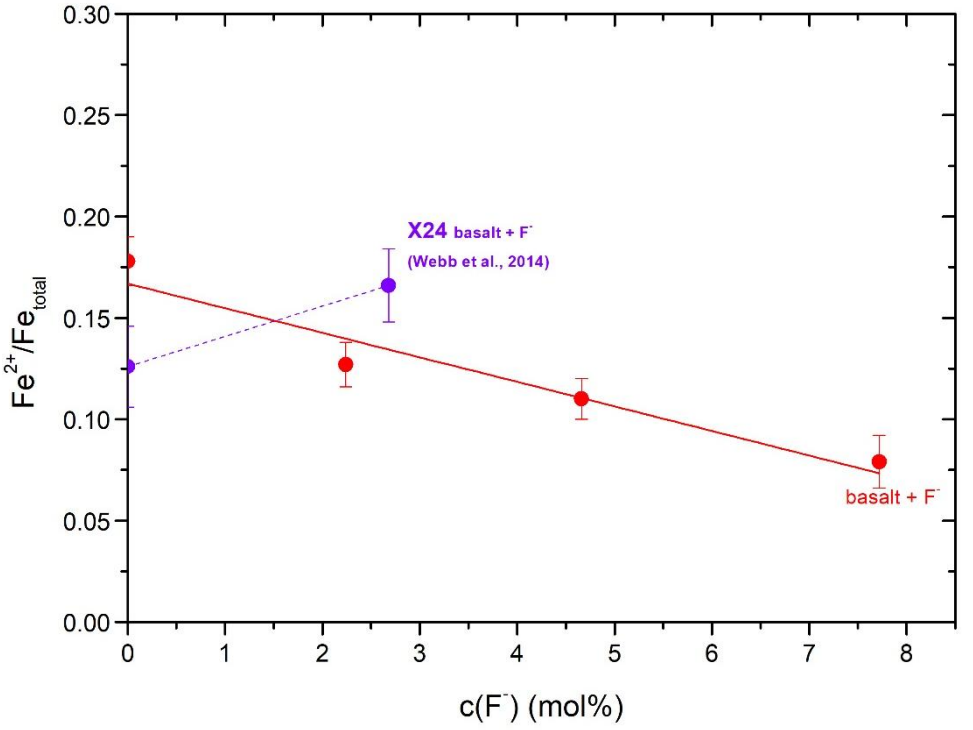

Figure 42: Fe^{2+}/Fe_{total} iron ratio as a function of fluorine for the present basaltic glass compared to X24 basaltic glass (Webb et al. 2014).

6.1.2. Influence of fluorine on the heat capacity of basaltic melts

In figure 43, a comparison of configurational heat capacity c_p^{conf} as function of fluorine content of diverse silicate melts is shown. The addition of 7.73 mol% fluorine results in an exponential increase in c_p^{conf} from 18.86 to 21.99 J mol^{-1} K^{-1}. The data by Webb et al. (2014) shows that the addition of 4.64 mol% F^- to basaltic composition results in a slight increase in c_p^{conf} from 20.66 to 21.40 J mol^{-1} K^{-1} (violet circles). The higher c_p^{conf} values can be explained by the higher FeO_{total} content (~ 10 wt% FeO_{total}) compared to the present basalt with (~ 5 wt% FeO_{total}). Baasner et al. (2013a) showed that the addition of ~ 2 mol% F^- to the NCS and NACS composition results in the smallest decreasing effect of c_p^{conf} (by 0.45 J mol^{-1} K^{-1}). Therefore, the melt composition and especially the FeO_{total} are the main parameters for the deviation of the c_p^{conf} values.

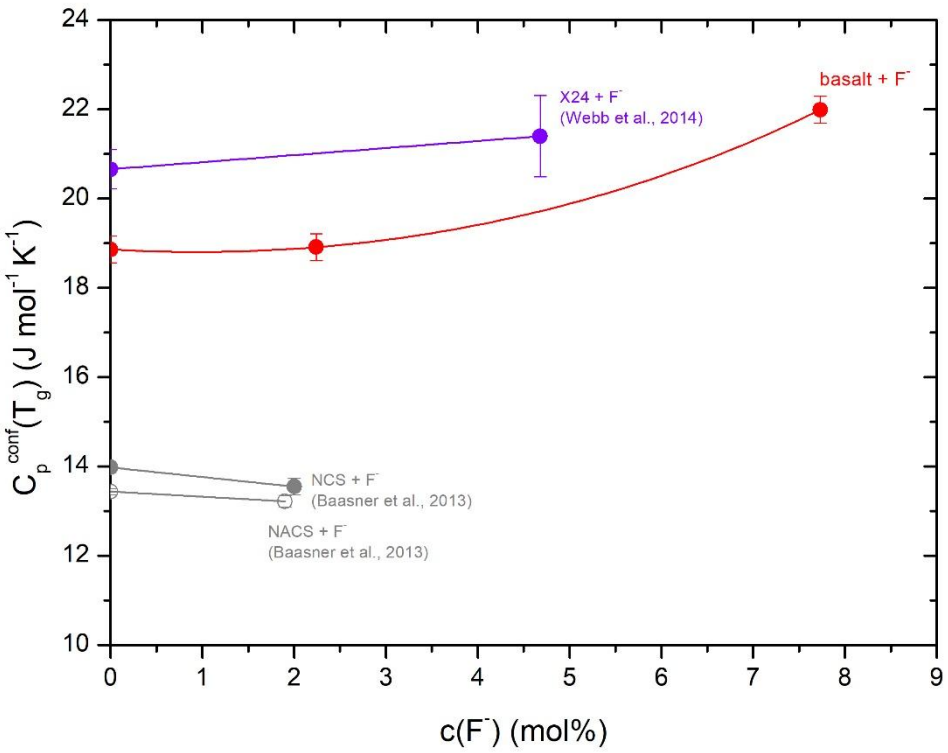

Figure 43: Comparison of configurational heat capacity c_p^{conf} as function of fluorine content of silicate melts. Literature data: Webb et al. (2014) - violet circles ; Baasner et al. (2013a)- Na_2O-CaO-Al_2O_3-SiO_2 melts (NACS – grey open circles) and Na_2O-CaO-SiO_2 melts (NCS – grey close circles).

6.1.3. Effect of fluorine on structure of peralkaline melt

The presence of fluorine in peralkaline melts modifies the network structure. The results of Raman spectroscopy show an asymmetric peak near 935 cm^{-1} as well as a shoulder around 530 cm^{-1}, which shows an increase in intensity due to the addition of fluorine. Our results are consistent with the data from Mysen and Virgo (1985b). The authors observed a band near

935 cm^{-1}, which describes the Si-F stretch band in fluorinated silicate complexes. Mysen and Virgo (1985a) suggested that the addition of fluorine to a silica glass results in a breakage of a bridging oxygen (BO) bond, which is replaced by two non-bridging fluoride ions. Compared to the silica melts, the addition of fluorine to an alumina-silica glass results in different incorporation mechanisms. The formation of Si-F bonds occurs by the replacement of Si-O-(Si, Al) bridging bonds. A further incorporation process results from the movement of Al and Na from their charge-balancing roles and the creation of complexes with these two cations. The excess cations are connected by NBOs, whereby the structure experiences a depolymerisation. These results correlate well with the NMR study from Stebbins and Zeng (2000). This study shows that fluorine prefers the bonding to small cations with a higher charge such as Al-F and few Si-F bonding. Recent studies have shown that this assumption applies for peraluminous glasses, whereas the addition of F in peralkaline glasses would favour the bonding to network-modifying cations like Ca as well as Na (Baasner et al. 2014). Therefore, the presence of fluorine in the present glasses results in a connection by non-bridging bonds, whereby the viscosity decreases due to depolymerisation of the structure. Furthermore, Mysen and Virgo (1985b) indicated a weak band near 560 cm^{-1} for glasses with the highest fluorine content. This band correlates with the shoulder around 530 cm^{-1} due the addition of halogens. The density measurements show a slight increase from 2.69 to 2.70 g cm^{-3} (7.73 mol% fluorine), but it does not indicate a depolymerisation of the structure.

6.2. Chlorine-bearing basaltic glasses

6.2.1. Influence of chlorine on the viscosity of basaltic melts

The addition of 2.53 mol% chlorine to the present basaltic melt increases the viscosity due to a polymerisation of the structure. But the further addition of chlorine (>2.53 mol%) results in a decrease in viscosity by 0.5 log units (2.82 mol% chlorine) due to a depolymerisation of the network structure (figure 44). Webb et al. (2014) shows that the addition of 0.57 mol% Cl_2O_{-1} (1.14 mol% Cl^-) and 1.41 mol% Cl_2O_{-1} (2.82 mol% Cl^-) to a basaltic composition results in a decrease in viscosity by 0.5 log units (pink line). The first addition of 1.14 mol% Cl^- to X24 deviates from the present chlorine-bearing basaltic trend (blue line), whereas the further addition of 2.82 mol% Cl^- to X24 correlates with the present melt. The iron-free basaltic melt (HX24 - Webb et al. (2014)) follows the similar trend of the present basaltic melt (blue line) which indicates an effect of FeO_{total} content on the viscosity. The present basaltic melt has a lower FeO_{total} content (~ 5 wt%), compared to the X24 (~ 10 wt%). Dingwell and Mysen (1985) investigated albite melts with a FeO_{total} content ~ 5 wt% and showed a small decrease in viscosity by the addition of chlorine (turquoise line). Therefore, the FeO_{total} content is not the only effect on the viscosity. Furthermore, Baasner et al. (2013a) suggested that the addition of Al_2O_3 to silicate melts strongly increases the viscosity, but the Al_2O_3 content of the

present basaltic melt similar to X24 (~9 mol%). Therefore, some other elements like Na_2O and CaO also have an effect on the viscosity. Webb et al. (2014) suggested the hypothesis that the presence of chlorine in basaltic melt increases the Fe^{2+}/Fe_{total}, whereby the number of network-modifiers (Fe^{2+}) increases (figure 45). This results in a decrease in viscosity due to a depolymerisation effect. Figure 45 shows that the addition of chlorine to the present basaltic melts does not result in an increase in Fe^{2+}/Fe_{total} compared to X24 basalt. Therefore, the suggestion from Webb et al. (2014) cannot be proven by the present data in figure 45. The different viscosity trends resulted of the diverse incorporation mechanisms of chlorine in the basaltic melts. For the exact determination, the chlorine environment has to be measure with NMR spectroscopy.

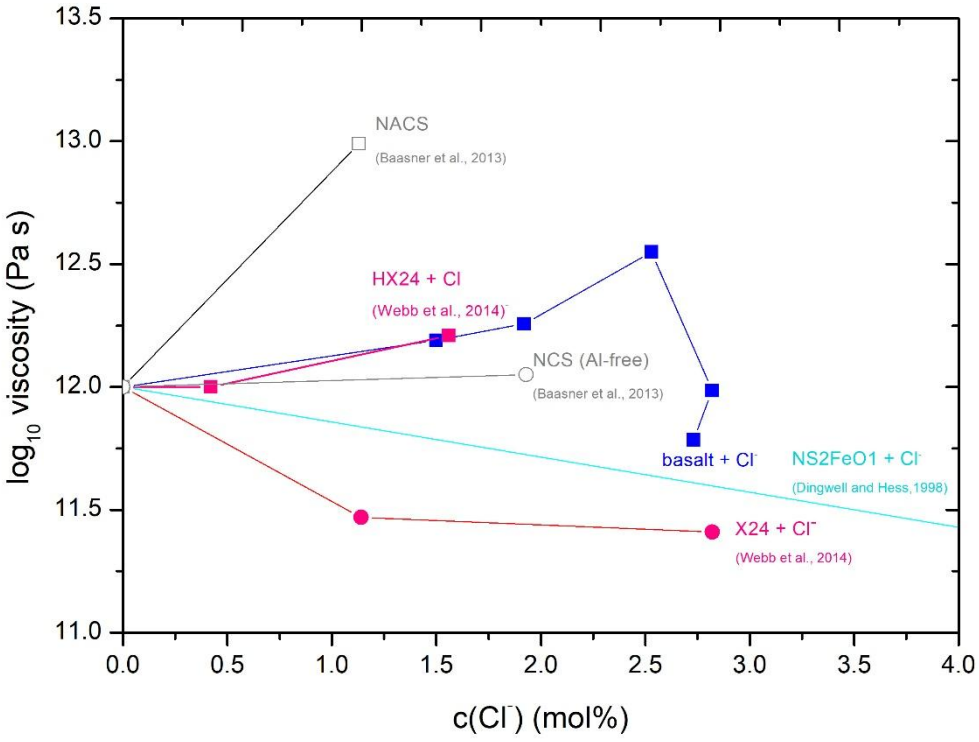

Figure 44: The change in viscosity due to addition of chlorine at the same temperature as the original melt has a viscosity of 10^{12} Pa s. Present chlorine-bearing basaltic melt (blue circles) - Literature data: Baasner et al. (2013a)- Na_2O-CaO-Al_2O_3-SiO_2 melts (NACS – grey open rectangles) and Na_2O-CaO-SiO_2 melts (NCS – grey close rectangles); Dingwell and Hess (1998)- albite melt (turquoise line); Webb et al. (2014) – basaltic melt (pink circles) and haplo-basaltic melt (pink rectangles). The error bars are smaller than the circles.

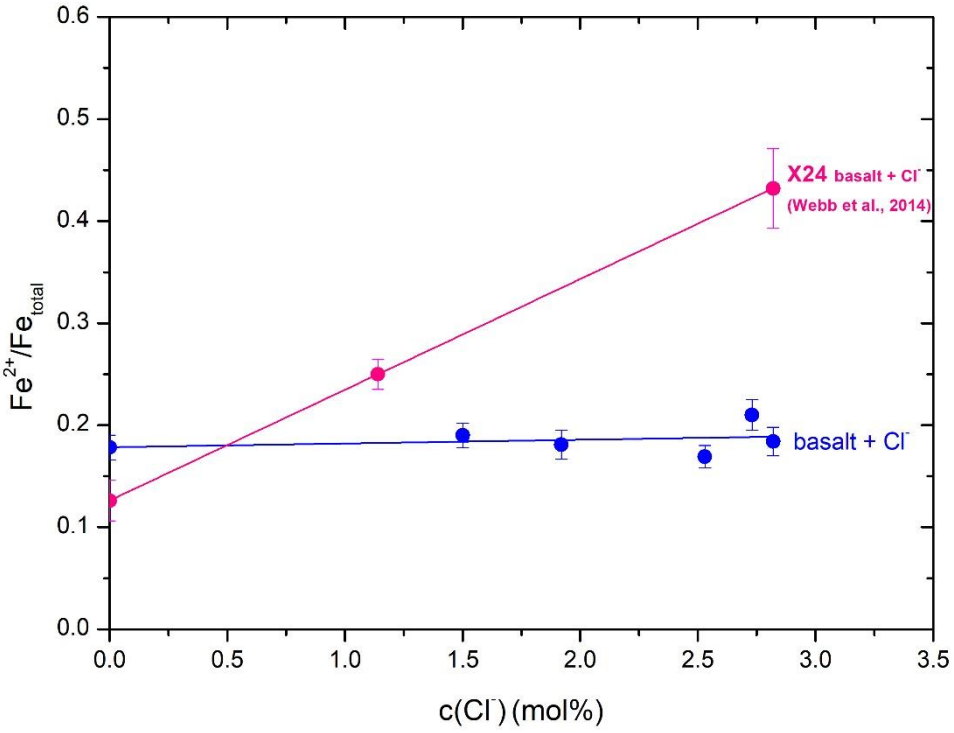

Figure 45: Fe^{2+}/Fe_{total} iron ratio as a function of chlorine for the present basaltic glass compared to X24 basaltic glass (Webb et al. 2014).

6.2.2. Influence of fluorine on the heat capacity of basaltic melts

Comparison of configurational heat capacity (C_p^{conf}) as function of chlorine content of diverse silicate melts is demonstrated in figure 46. The presence of 2.53 mol% Cl^- in the present basaltic melt results in a decrease in c_p^{conf} from 18.86 to 17.58 J mol^{-1} K^{-1}, whereas the further addition of chlorine (> 2.53 mol%) results in an increase in C_p^{conf} from 17.58 to 19.18 J mol^{-1} K^{-1}. Webb et al. (2014) shows that the addition of 1.41 mol% Cl_2O_{-1} (2.82 mol% Cl^-) to a basaltic composition results in a decrease in C_p^{conf} from 20.66 to 18.35 J mol^{-1} K^{-1} (pink line). In comparison to the present basaltic melt, Webb et al. (2014) showed a similar trend of the iron-free basaltic melt (HX24 – open pink rectangles). Therefore, the higher C_p^{conf} values (X24) result by higher FeO_{total} contents around ~ 10 wt%. Generally, the melt composition shows a larger effect on the C_p^{conf} than the FeO_{total} contents, which is shown by the data from Baasner et al. (2013a). The authors demonstrated the lowest C_p^{conf} values due to the simple melt composition. Furthermore, Baasner et al. (2013a) suggested that the aluminium effect on the c_p^{conf} can be neglected.

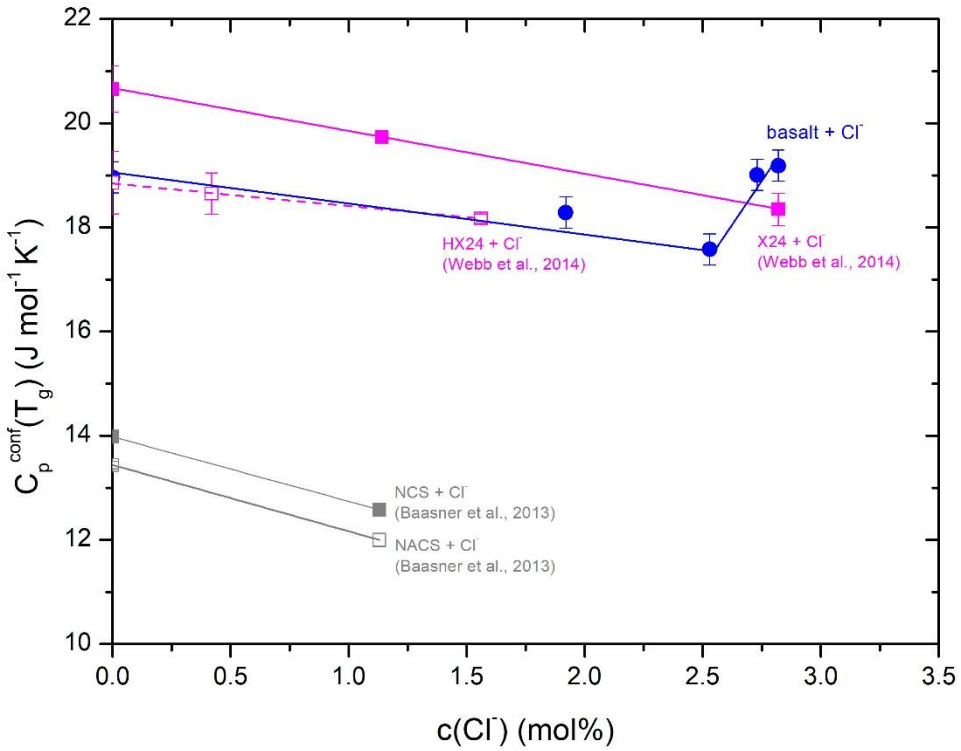

Figure 46: Comparison of configurational heat capacity C_p^{conf} as function of chlorine content of silicate melts. Literature data: Webb et al. (2014) – basaltic melts (pink open rectangles) and haplo-basaltic melts (pink close rectangles); Baasner et al. (2013a)- Na_2O-CaO-Al_2O_3-SiO_2 melts (NACS – grey open rectangles) and Na_2O-CaO-SiO_2 melts (NCS – grey close rectangles).

6.2.3. Effect of chlorine on the structure of peralkaline melt

The addition of chlorine to peralkaline melts modifies the network structure due to two different structural behaviours. Based on diverse melting systems, the incorporation mechanisms of chlorine in peralkaline melts are discussed in the literature. Evans et al. (2008) conducted XANES analysis and indicated that Cl^- prefers the bonding to divalent cations like Ca^{2+} and Mg^{2+} over monovalent ones such as Na^+ and K^+ in multi component alumina-silicate melts. Therefore, Baasner et al. (2013a) suggested that the increasing viscosity results in the formation of Na-Cl and Ca-Cl_2 complexes in peralkaline melts (NACS). These new bondings result in a decrease in NBO and an increase in BO due to the alkali loss of the structure. The formation of complexes by the addition of > 2.53 mol% chlorine explains the increasing viscosity. The presence of < 2.53 mol% Cl^- results in a decrease in viscosity due to the replacement of Si-O-Si bonds by Si-Cl bonds (Giordano et al. 2004). The chlorine disrupts the network structure, which leads to a depolymerisation. Due to that, the presence of chlorine in the basaltic glass results in a decrease in density by 2.69 to 2.66 g cm^{-3}.

The present glasses were analysed by Raman spectroscopy, whereby the structure of peralkaline melts can be discussed. The Raman spectra are sensitive for the variation of the iron speciation, which was caused by the addition of halogens to the present glasses. During the synthesis, the redox conditions are constant for all glasses at 1 atm. The results of the addition of halogens to the basaltic glasses are represented in figure 19. A difference is not visible between the halogens except for the iron speciation. In general the HF region shows an asymmetric peak near 935 cm^{-1}, which is enhanced by the addition of halogens accompanied by the iron speciation. This region indicates the interconnected three-dimensionally structure with Al and Si. The band near 935 cm^{-1} could reflect the Si-Cl stretch band similar to the Si-F bonding (Mysen and Virgo 1985b). Furthermore, the LF region reflects an increase in intensity of a shoulder around 530 cm^{-1} accompanied by the addition of halogens.

6.3. Comparison with recent models

6.3.1. Model for the calculation of Fe^{2+}/Fe_{total}

The model by Kress and Carmichael (1991) can be used to calculate the Fe^{2+}/Fe_{total} based on the microprobe data, melting temperature and oxygen fugacity (see section 4.3.3. Calculation of Fe^{2+}/Fe_{total} after Kress and Carmichael (1991)). For the halogen-free basaltic glass, the calculated Fe^{2+}/Fe_{total} gives a value of 0.18 after the calculation of Kress and Carmichael (1991). This value is in the same range to the measured data of 0.18 ± 0.01 by wet chemistry. Thus, the model works for halogen-free basaltic glass, but the calculation does not consider the addition of halogens. Thus, the calculated Fe^{2+}/Fe_{total} of halogen-bearing basaltic glass show a deviation from the measured values Fe^{2+}/Fe_{total}. Consequently, the model underestimates the Fe^{2+}/Fe_{total} of chlorine- and (Cl^- + F^-)-bearing glass, whereas the model overestimates the fluorine-bearing glasses. An exception is the BA-Cl-F-2 sample (1.96 mol% Cl^- & 5.25 mol% F^-), the model works well due to the balance of individual effects of Cl^- and F^-. As a consequence of our findings, the model works for basaltic glass with small amounts of halogens (figure 47), but the wet chemistry analysis cannot be replaced by the model of Kress and Carmichael (1991).

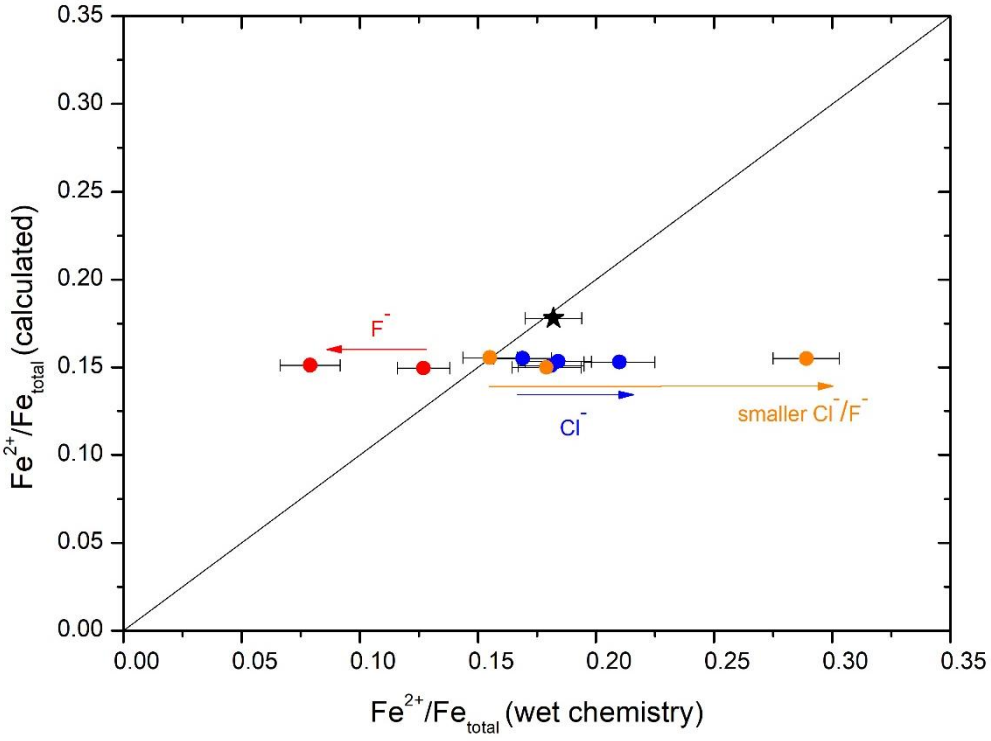

Figure 47: Comparison of the measured Fe^{2+}/Fe_{total} with the calculated data from model of Kress and Carmichael (1991).

6.3.2. Models for the calculation of viscosity

The following figure 48, 49 and 50 show a comparison of the measured viscosity with a model of calculated viscosity from Giordano et al. (2008), Duan (2014) and Sehlke and Whittington (2016). The solid line represents the 1 to 1 correlation. The models are based on the experimental temperature, the glass composition as well as the iron ratio, which were determined by microprobe analysis and wet chemistry. Giordano et al. (2008) developed a viscosity model of magmatic liquids based on the Vogel-Fulcher-Tamman equation. The special regards are on the consideration of water and fluorine. The model was tested on 257 viscosity measurements with rhyolite, phonolite, dacite, shoshonite, tephrit-phonolite and phono-teprhite. The temperature varied between 385 to 1640°C and the viscosity is in a range of $10^{0.7}$ to 10^{15} Pa s (Giordano et al. 2008). The results of the model after Giordano et al. (2008) is presented in figure 48 and show a good correlation between the measured and calculated viscosity for the halogen-free melt and melts with a small halogen content. The viscosity of 7.73 mol% fluorine (open red circles) and of 7.21 mol% of both halogens (light orange circles) to the present basaltic melts are overestimated by the model because of the high halogen contents. Furthermore, the model does not consider the chlorine, thus the viscosity of chlorine-bearing melts are underestimated by the model.

The second model of Duan (2014) is based on calculated viscosity of natural iron-bearing silicate melts (figure 49) and it describes a modification of the VFT equation. The model can be applied on ultramafic, mafic and silica glasses in a temperature range of 733 to 1873 K with a pressure of 0.001 to 15 kbar as well as a range of 0 to 12.30 wt% water content. The model focuses on the varied iron ratio by the oxygen fugacity (Duan 2014). The model does not work for the viscosity of halogen-free basalt (black circle). The increasing halogens show a better correlation of the viscosities by the model with the present viscosity data. All samples are underestimated by the model of Duan (2014) due to the fact of the halogens and the small variation in the iron ratio. Finally, the viscosity are better described by the model from Giordano et al. (2008) for the present melts with few halogens and the viscosity can be correlated well by the model after Duan (2014) for basaltic melts with a high halogen contents.

An additional viscosity model (Sehlke and Whittington 2016) is shown in figure 50. The model is based on the viscosity data of planetary tholeiitic melts with the focus on Fe^{2+}/Fe_{total}. The model shows a good correlation between the calculated and measured viscosities for the halogen-free, chlorine- and small fluorine-bearing basaltic melts. We observed that the increasing halogen content results in an overestimation of viscosities by the model. This is shown clearly by the increasing fluorine content (7.73 mol% F^-). Furthermore, the (Cl^- + F^-)-bearing melts show an overrestimation by the model with the exception of BA-Cl-F-3 (3.28 mol% Cl^- and 2.35 mol% F^-). BA-Cl-F-3 shows a good correlation by the model due to the high Cl^- content.

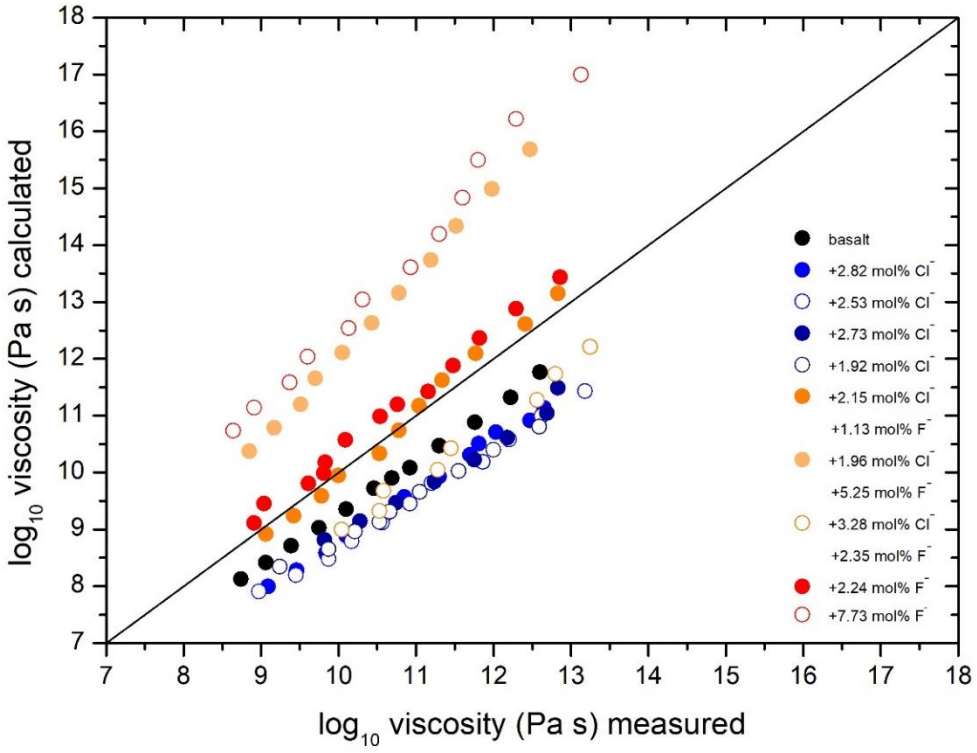

Figure 48: Comparison of the measured viscosity with the calculated data from model of Giordano et al. (2008). The error bars are smaller than the circles.

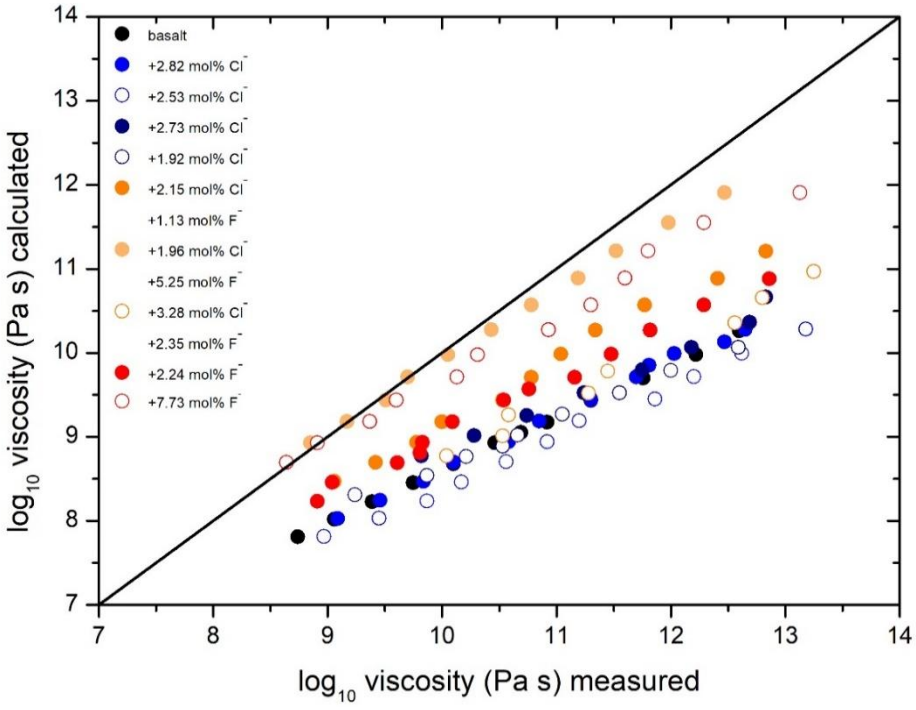

Figure 49: Comparison of the measured viscosity with the calculated data from model of Duan (2014). The error bars are smaller than the circles.

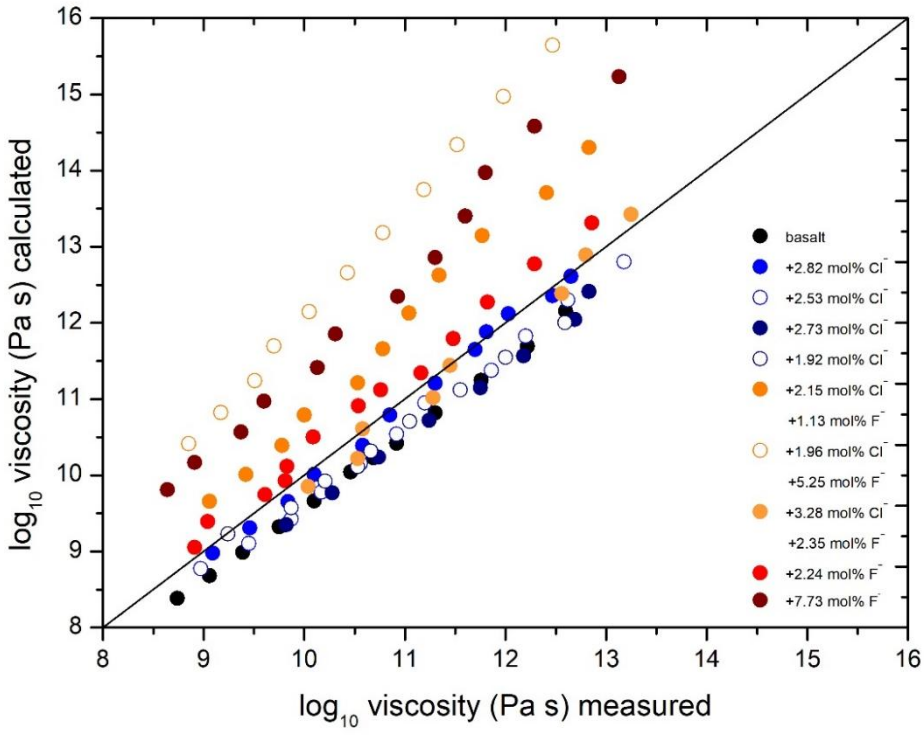

Figure 50: Comparison of the measured viscosity with the calculated data from model of Sehlke and Whittington (2016). The error bars are smaller than the circles.

6.3.3. Models for the calculation of heat capacity

Three models for the calculated liquid heat capacity (C_{pl}) of silicate melts (Stebbins et al. 1984; Richet and Bottinga 1984; Lange and Navrotsky 1992) and one model for the calculated glass heat capacity (C_{pg}) of silicate glasses (Richet, 1987) compared to the measured C_{pl} and C_{pg} are demonstrated in figure 51. The model by Stebbins et al. (1984) and Lange and Navrotsky (1992) are reproduced by the experimental data but the melts with increasing halogen contents are underestimated by the models. In contrast to that, the model from Richet and Bottinga (1984) does not work for the halogen-free as well as for the halogen-bearing basaltic melts. In consideration of the halogens, Richet (1987) proposes to use the C_{pg} from the literature for other oxides. The calculated glass heat capacity describes the model by Richet (1987) and correlates well for the halogen-free and the glasses with low halogen concentrations. Contrary, the increase in halogen concentration results in an underestimation of C_{pg} by the model.

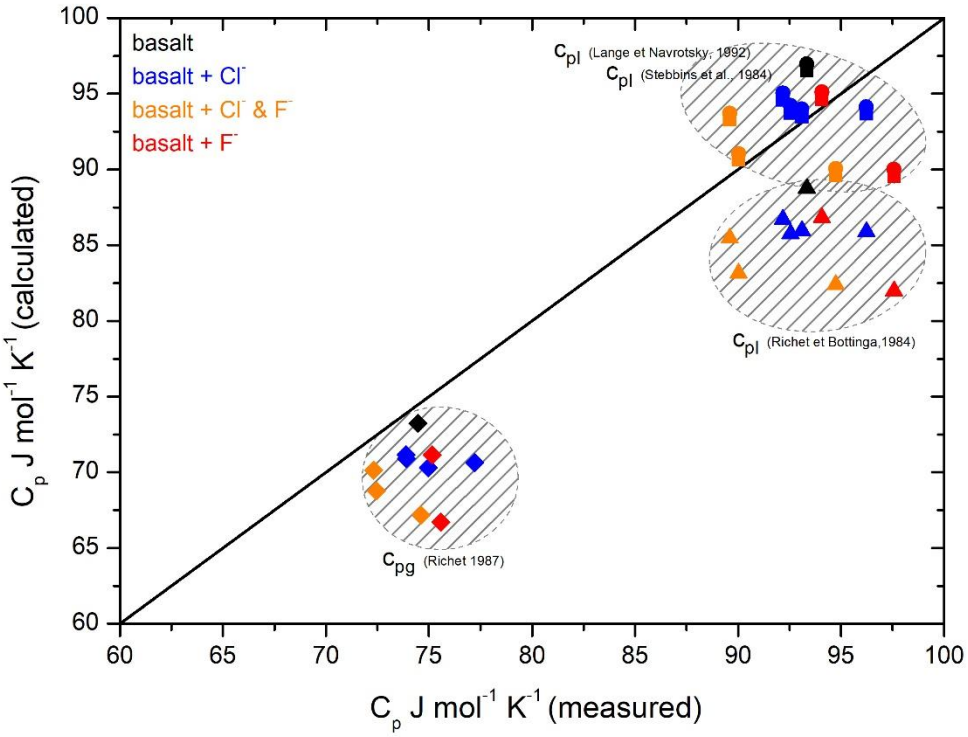

Figure 51: Comparison of calculated with measured heat capacity data of halogen-free and halogen-bearing basaltic melts. The symbols represents a comparison between the measured and the calculated data from Stebbins et al. (1984) model (rectangles), Lange and Navrotsky (1992) model (circles), Richet and Bottinga (1984) model (triangles) and Richet (1987) model (rhombus). The error bars are smaller than the symbols.

7. Conclusion

This study demonstrates the effect of halogens on the viscosity of basaltic melts. To enable an independent comparison, the T_g^{12} was calculated using the Arrhenian fits for the individual viscosity measurements. The presence of fluorine in peralkaline melts always results in a decrease in T_g^{12} and also in the viscosity due to the formation of Si-F bonds that depolymerise the structure. This effect on viscosity is more pronounced than the effect of the decreasing Fe^{2+}/Fe_{total}, which has a small increasing effect on the viscosity due to an increase of network formers (Fe^{3+}) and a decrease in network modifiers (Fe^{2+}). The addition of chlorine to the basaltic melt shows two trends due to the diverse incorporation mechanisms of chlorine. The addition of Cl^- up to 2.53 mol% results in an increase in T_g^{12} due to the formation of some Na-Cl and Ca-Cl_2 complexes (Baasner et al. 2013a). Further addition of < 2.53 mol% Cl^- shows a decrease in T_g^{12} due to the replacement of Si-O-Si bonds by Si-Cl bonds (Giordano et al. 2004). The hypothesis that the presence of Cl^- increases the Fe^{2+}/Fe_{total} by Webb et al. (2014) cannot be confirmed. In contrast, our research has shown that the addition of Cl^- does not show a significant effect on the Fe^{2+}/Fe_{total}. On the basis of the influence of fluorine and chlorine on viscosity data from this study, we conclude that a low Cl^-/F^- leads to a stronger decrease in viscosity, whereas a high Cl^-/F^- results in a slight decrease in viscosity. The addition of chlorine to fluorine-bearing glasses results in a weakened decrease in viscosity due the formation of complexes (Na-Cl and Ca-Cl_2).

Part B – The effect of redox on the viscosity of the present MORB composition

1. Abstract

The viscosity of basaltic magmas is not only a function of composition but oxygen fugacity and the halogen content. This study describes the decrease in viscosity of halogen-free and halogen-bearing basaltic glasses accompanied by the variation of Fe^{2+}/Fe_{total}. The experiments were conducted in a 1 atm gas mixing furnace at 1473 K using a varied CO_2 and H_2 mixture (log fO_2: -0.7 (air) to -9.0). All samples were quenched with a rate of 200 K min^{-1} in order to avoid the formation of quench crystals. The effect of fO_2 on the iron speciation results in an increase from 0.16 to 0.82 in Fe^{2+}/Fe_{total} due to decreasing log fO_2 from -0.7 to -9.0. This increase of network modifying Fe^{2+} results in a 0.5 log unit decrease in viscosity at 973.2 K. This effect on viscosity is enhanced by a further 0.5 log unit due to the addition of Cl^-, F^- as well as (Cl^- + F^-). The Raman spectra indicate a shoulder in the low-frequency region (LF) around 590 cm^{-1}. This shoulder decreases at reduced conditions. Furthermore, the Raman spectra show an isomer shift from 1100 to 950 cm^{-1} (HF) for glasses synthesised at increased oxidising conditions. The combination of the wet chemistry analysis and the Raman spectroscopy enables a specific calibration for unknown halogen-free and -bearing basaltic glasses.

2. Introduction

The effect of redox on the viscosity of silicate melts is discussed in the literature (Dingwell 1991; Liebske et al. 2002; Vetere et al. 2006; Duan 2014; Stabile et al. 2016). Several authors have shown that the increasing Fe^{2+}/Fe_{total} in silicate melt results in a decrease in viscosity. Kress and Carmichael (1988) suggested that the structural position of ferrous and ferric cations in silicate melts shows an effect on the viscosity, heat capacity and density. Mysen (1991) and Virgo and Mysen (1985) indicated that Fe^{2+} appears as a network modifier or charge compensator, whereas Fe^{3+} behaves as a network former. There is some literature data on the viscosity of silicate and basaltic melts with varying Fe^{2+}/Fe_{total}. Liebske et al. (2002) observed a 1.6 log units decrease in viscosity with decreasing Fe^{3+}/Fe_{total} from 0.58 to 0.34 for andesitic melts, whereas further reduced samples (Fe^{3+}/Fe_{total} ~ 0.2) do not show a stronger decrease in viscosity. Duan (2014) found that the increasing Fe^{3+}/Fe_{total} from 0.2 to 0.6 results in an increase in viscosity of 0.8 log units for andesitic melts, whereas the basaltic melts show an increase in viscosity of 0.9 log units.

Furthermore, Stabile et al. (2016) found that the viscosity decreases by 0.7 log units at 603°C due to increasing Fe^{2+}/Fe_{total} from 0.18 to 0.84 for Na-Si-Fe-O composition (Ebu-B) and a stronger decrease in viscosity by 1.34 log units due to increasing Fe^{2+}/Fe_{total} from 0.19 to 0.76 for Na-Si-Fe-O composition (Ebu-N – K_2O-free).

There is no data on the effect of redox on the viscosity of halogen-bearing basaltic glasses. Knowledge of Fe^{2+}/Fe_{total} ratio in natural samples is used to indicate the redox conditions of the source regions during the magma generation and volcanic eruptions. Furthermore, the iron speciation allows conclusions about melting and crystallisation histories (Christie et al. 1986). The aim of this study is to demonstrate the effect of the oxygen fugacity on the viscosity of halogen-free and –bearing basaltic glass.

3. Experimental and analytic methods

3.1. Starting materials

Before the redox equilibria experiments, four glasses were synthesised from a mixture of oxides, carbonates and halogens. The synthesis was performed at 1473 K for 4 to 9 h in a 1 atm $MoSi_2$ furnace. A detailed description can be found in Part A (section 3.1. Starting materials). The sample name represents the oxygen fugacity from NNO+3 (N3) to NNO-1 (N-1).

3.2. Redox equilibria experiments

Twelve samples were equilibrated in a vertical gas mixing furnace at 1473 K under a mixture of CO_2 and H_2 gases (table 13). The theoretical Fe^{2+}/Fe_{total} was calculated after Kress and Carmichael (1991) and the H_2/CO_2 mixture was adjusted after the temperatures-oxygen fugacity tables by Deines et al. (1974). The variation of oxygen fugacity (NNO+3 to NNO-1) results in an increase in Fe^{2+}/Fe_{total}. In order to avoid iron loss, the glass pieces were loaded into a wire-loop (Pressnall and Brenner 1974). The problem was that a large amount of halogens decomposed and degassed during the melting process. Therefore, the wire loop was modified with a small platinum plate (figure 52). Furthermore, the samples were quenched using a rapid-quench technique to minimise the formation of quench crystals. Initial kinetic experiments showed that a stable equilibrium between the melt and the gas atmosphere is reached after 12 h (figure 55). Thus, the 20 h melting regime was enough to create stable equilibrium. At increasing oxidising condition, the loss of halogens and iron was minimised by using a shorter duration time of 8 h.

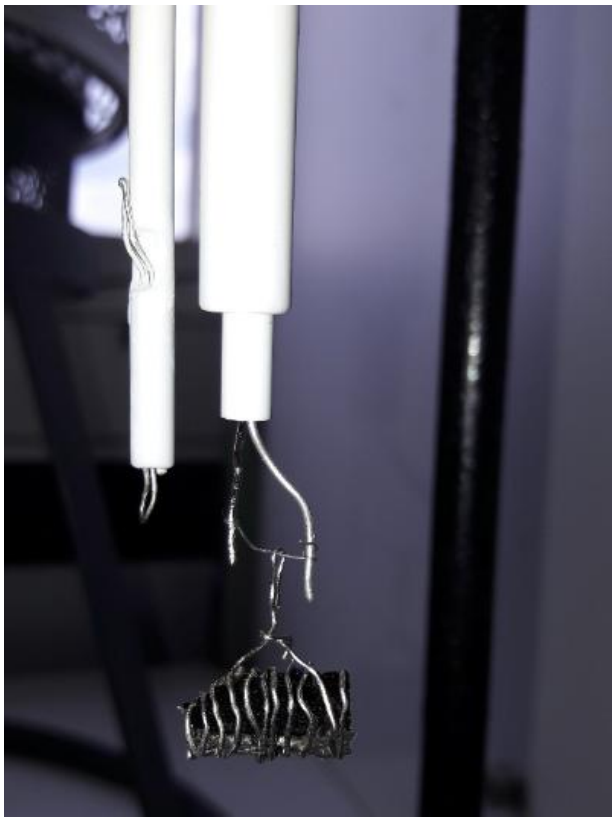

Figure 52: Glass sample in a modified wire-loop on a small platinum plate.

3.3. Optical spectroscopy

A dual channel broad band spectrometer (AvaSpec-UV/VIS/NIR) was used to measure the UV-VIS spectrum (6000 to 16000 cm^{-1}) of the halogen-free and –bearing basaltic glass. The glass samples were double polished to a thickness between 50 and 100 µm. Afterwards the samples were fixed with a small aperture (3 - 4 mm) on a microscope, which was connected with a fibre optic cable to the spectrometer. The optical absorption spectra enable the calculation of absorption coefficients. The absorption coefficient can be calculated with the Lambert-Beer-Law:

$$\varepsilon = \frac{M_{FeO} * A_{Fe2+}}{\rho * d * c_{FeO}} \qquad \textit{Equation 12}$$

where M_{FeO} describes the molar mass (g mol^{-1}), A_{Fe2+} represents the absorbance of the ferrous peak around 9000 cm^{-1} (a.u.), ρ is the density (g l^{-1}), d (cm) defines the thickness of the polished glass sample and c_{FeO} is the ferrous iron content of the wet chemistry method (wt%). This method enables the prediction of Fe^{2+}/Fe_{total} of silicate glass by means of one optical single measurement.

Table 13: Analysis of redox equilibrated halogen-free and -bearing glasses (electron microprobe). The measurement of each glass is based on average of 10 measurements with the standard deviation (σ). Standards were: albite (Na), sanidine (K), wollastonite (Ca, Si), titanium dioxide (Ti), rhodonite (Mn), hematite (Fe), sodium chloride (Cl), olivine (Mg), anorthite (Al) and topaz (F).

Oxides/ ions mol%	BA-0 _N3	BA-0 _N1	BA-0 _N-1	BA-Cl _N3	BA-Cl _N1	BA-Cl_N-1	BA-Cl-F_N3	BA-Cl-F_N1	BA-Cl-F_N-1	BA-F _N3	BA-F _N1	BA-F _N-1
ΔNNO	+3	+1	-1	+3	+1	-1	+3	+1	-1	+3	+1	-1
$\log_{10}(fO_2)$ gas mixing	-4.97	-6.97	-8.97	-4.39	-6.39	-8.39	-4.39	-6.39	-8.39	-4.97	-6.97	-8.97
SiO_2	54.42 ±0.30	54.57 ±0.24	54.39 ±0.30	55.53 ±0.30	54.88 ±0.20	54.70 ±0.28	54.45 ±0.32	54.09 ±0.30	54.12 ±0.22	53.36 ±0.30	53.05 ±0.26	53.21 ±0.26
Na_2O	4.40 ±0.10	4.48 ±0.12	4.50 ±0.06	3.73 ±0.08	3.61 ±0.04	3.51 ±0.02	3.51 ±0.10	4.04 ±0.12	3.72 ±0.12	4.57 ±0.10	4.55 ±0.18	4.37 ±0.08
K_2O	0.15 ±0.04	0.16 ±0.02	0.16 ±0.02	0.11 ±0.02	0.10 ±0.05	0.10 ±0.01	0.11 ±0.04	0.12 ±0.02	0.11 ±0.01	0.16 ±0.04	0.17 ±0.02	0.16 ±0.02
TiO_2	1.05 ±0.06	1.07 ±0.06	1.03 ±0.10	1.06 ±0.06	1.07 ±0.02	1.06 ±0.02	1.05 ±0.06	1.04 ±0.06	1.04 ±0.02	1.05 ±0.04	1.04 ±0.04	1.02 ±0.08
FeO_{total}	3.18 ±0.09	2.89 ±0.12	3.14 ±0.13	3.35 ±0.20	2.80 ±0.15	2.71 ±0.08	3.06 ±0.14	3.66 ±0.12	3.49 ±0.16	3.48 ±0.08	3.85 ±0.20	3.26 ±0.16
Al_2O_3	9.63 ±0.18	9.42 ±0.16	9.46 ±0.04	9.16 ±0.18	9.45 ±0.10	9.39 ±0.10	9.34 ±0.02	9.41 ±0.05	9.35 ±0.03	9.28 ±0.05	9.29 ±0.08	4.60 ±0.10
MgO	12.81 ±0.14	12.90 ±0.12	12.65 ±0.10	12.40 ±0.04	12.78 ±0.06	12.73 ±0.04	12.62 ±0.12	12.12 ±0.12	12.47 ±0.17	12.75±0.18	12.70 ±0.22	12.49 ±0.18
CaO	14.15 ±0.18	14.32 ±0.06	14.47 ±0.16	13.56 ±0.19	14.39 ±0.12	14.37 ±0.18	14.35 ±0.16	13.52 ±0.34	13.77 ±0.12	13.81 ±0.14	13.93 ±0.14	14.14 ±0.26
MnO	0.18 ±0.04	0.18 ±0.02	0.18 ±0.02	0.17 ±0.02	0.16 ±0.02	0.15 ±0.06	0.17 ±0.06	0.16 ±0.02	0.16 ±0.01	0.18 ±0.04	0.17 ±0.02	0.17 ±0.05
Cl^-	0.01 ±0.01	0.01 ±0.01	0.01 ±0.02	0.92 ±0.03	0.74 ±0.06	1.29 ±0.02	1.13 ±0.06	1.32 ±0.05	1.28 ±0.16	0.02 ±0.02	0.02 ±0.00	0.01 ±0.01
F^-	0.00 ±0.00	0.00 ±0.01	0.00 ±0.00	0.00 ±0.00	0.00 ±0.01	0.00 ±0.01	0.20 ±0.03	0.51 ±0.22	0.48 ±0.04	1.35 ±0.08	1.25 ±0.12	1.87 ±0.36
γ [1]	0.77	0.78	0.77	0.77	0.77	0.77	0.77	0.77	0.76	0.78	0.78	0.77
NBO/T [2]	0.49	0.52	0.54	0.45	0.48	0.49	0.45	0.48	0.51	0.49	0.53	0.53
NBO/T [3]	0.49	0.52	0.54	0.47	0.50	0.51	0.48	0.51	0.54	0.51	0.56	0.56

[1] γ is an indicator for the degree of polymerisation of the melt (Webb et al. 2014)

$\gamma = (Na_2O + K_2O + MnO + FeO + CaO + MgO) / (Na_2O + K_2O + MnO + FeO + CaO + MgO + Al_2O_3 + Fe_2O_3)$

[2] *NBO/T calculated without halogens (chlorine and fluorine)*

[3] *NBO/T calculated assuming NBO/T calculated assuming* $2Cl^- = 1O^{2-}$ *or* $2F^- = 1O^{2-}$

4. Results

4.1. Density

Table 14 lists the density and molar volume of the redox equilibrated basaltic glasses. Comparison of density as a function of iron speciation is represented in figure 53. The density of halogen-free basalt increases from 2.70 to 2.73 g cm^{-3} due to increasing Fe^{2+}/Fe_{total}, whereas the further increase of Fe^{2+}/Fe_{total} from 0.16 to 0.82 decreases the density from 2.73 to 2.60 g cm^{-3}. The addition of fluorine to the basaltic glass results in an increase in density from 2.70 to 2.79 cm^{-3} due to the increasing Fe^{2+}/Fe_{total} from 0.29 to 0.44. Further increasing Fe^{2+}/Fe_{total} results in a decrease in density from 2.79 to 2.60 g cm^{-3}. The chlorine-bearing glasses do not show a decrease in density by increasing Fe^{2+}/Fe_{total} from 0.54 to 0.81. The addition of both halogens results in an increase in density from 2.68 to 2.82 g cm^{-3} due to increasing Fe^{2+}/Fe_{total} (0.29 to 0.44). As a consequence, the variation of the density is not only a function of Fe^{2+}/Fe_{total} but also depending on the presence of halogens.

Figure 54 shows the molar volume as a function of Fe^{2+}/Fe_{total} for the redox equilibrated glasses. This diagram illustrates a strong decrease in molar volume by an increase in Fe^{2+}/Fe_{total} (0.4 to 0.6) for all halogen-free and –bearing glasses. Further increasing Fe^{2+}/Fe_{total} results in an increase in molar volume with up to 2.37 cm^3 mol^{-1}.

Table 14: Density ρ and molar volume of series II.

Sample	$(Cl^- + F^-)$ (mol%)	Fe^{2+}/Fe_{total}	ρ (g cm^{-3})	σ (g cm^{-3})	molar volume (cm^3 mol^{-1})
BA-0_II	0.00	0.16	2.704	0.021	23.41
BA-0_N3	0.00	0.50	2.730	0.036	22.91
BA-0_N1	0.00	0.65	2.635	0.015	23.53
BA-0_N-1	0.00	0.82	2.596	0.035	23.82
BA-Cl_II	1.50	0.19	2.679	0.018	23.36
BA-Cl_N3	0.92	0.54	2.699	0.023	22.98
BA-Cl_N1	0.74	0.70	2.677	0.007	23.05
BA-Cl_N-1	1.29	0.81	2.669	0.010	23.00
BA-Cl-F_II	2.15	0.29	2.681	0.001	22.93
BA-Cl-F_N3	1.33	0.44	2.821	0.007	21.29
BA-Cl-F_N1	1.83	0.61	2.702	0.014	22.92
BA-Cl-F_N-1	1.76	0.85	2.591	0.032	23.66
BA-F_II	2.33	0.11	2.701	0.002	22.71
BA-F_N3	1.35	0.41	2.790	0.008	22.32
BA-F_N1	1.25	0.66	2.715	0.010	22.74
BA-F_N-1	1.87	0.72	2.603	0.016	23.52

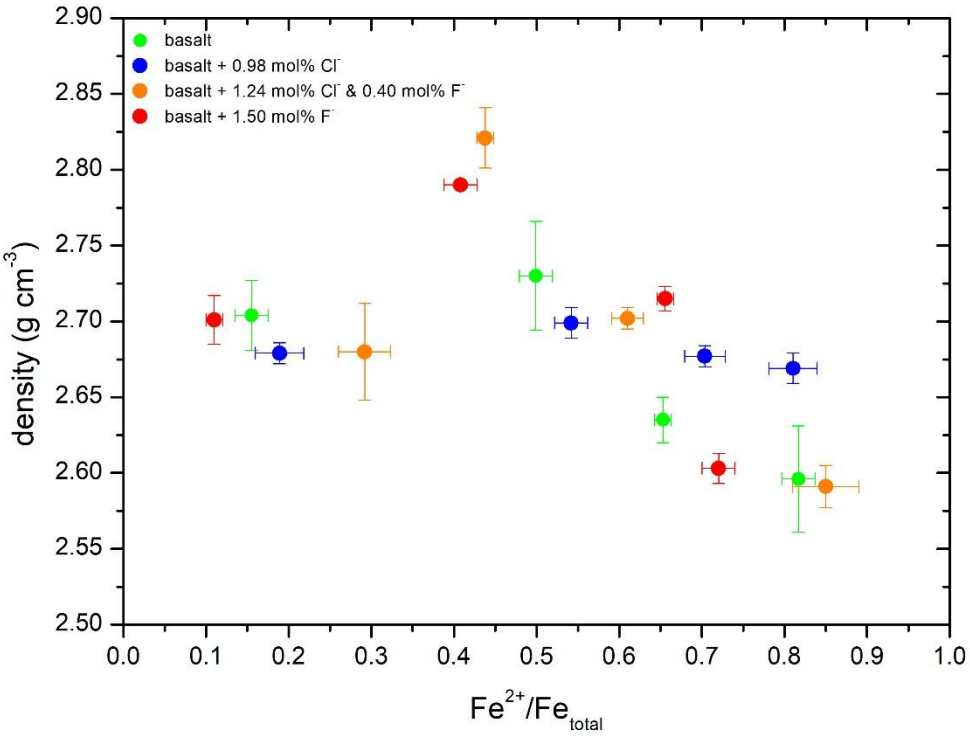

Figure 53: Glass density as a function of Fe^{2+}/Fe_{total} on halogen-free and -bearing basaltic glasses.

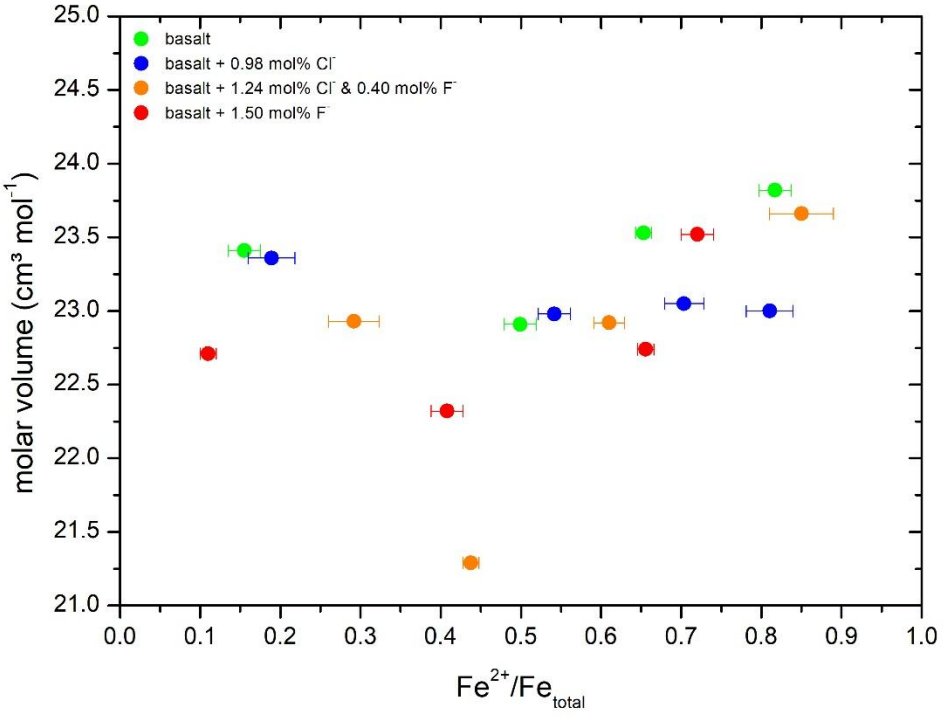

Figure 54: Molar volume of basaltic glasses of series II as a function of Fe^{2+}/Fe_{total}

4.2. Effect of iron

4.2.1. Total iron loss and evolution of Fe^{2+}/Fe_{total} as a function of duration time

The synthesis of redox equilibrated halogen-free glasses show a significant total iron loss to the platinum wire loop and the platinum sheet. Therefore, it is essential to use a saturated platinum wire and sheet (Pressnall and Brenner 1974). Furthermore, the redox equilibria experiments reflect a variation of Fe^{2+}/Fe_{total} as a function of duration time (figure 55). A duration time of 20 h shows the best results of a stable Fe^{2+}/Fe_{total}.

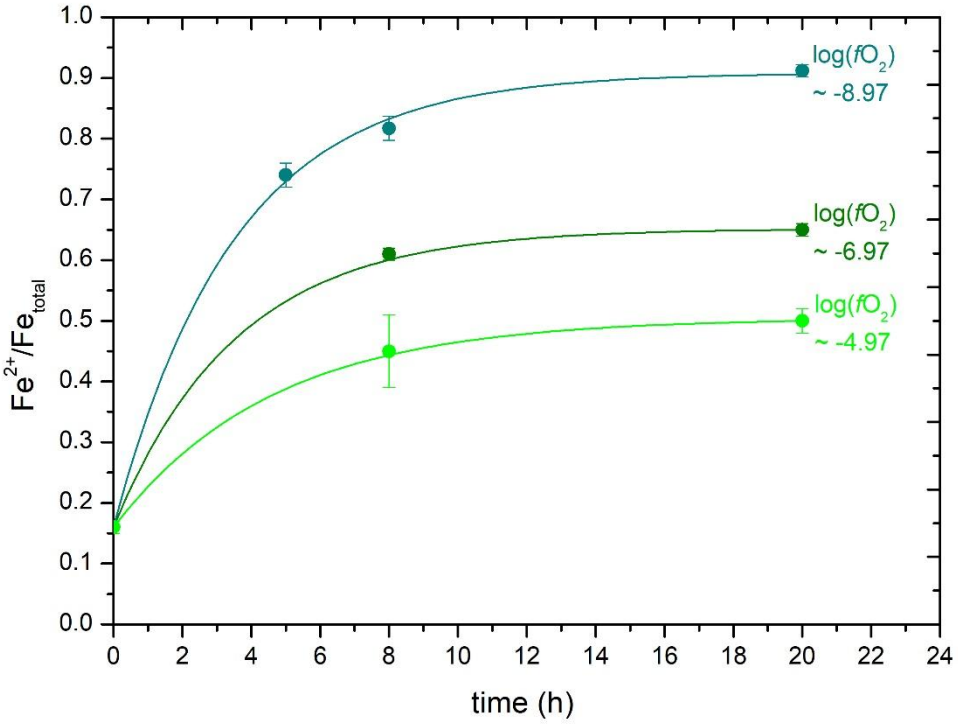

Figure 55: Evolution of Fe^{2+}/Fe_{total} in halogen-free basaltic glasses as a function of duration time.

4.2.2. Evolution of chlorine with duration time

The halogens in basaltic glasses are a critical factor due to the fast degassing during the synthesis. The high halogen loss can be controlled by the duration time and temperature. The synthesis temperature has to be fixed on 1473 K, because the present composition would tend to form crystals. Figure 56 shows a significance chlorine loss as a function of duration time. There was ~ 40 % loss of chlorine in this synthesis procedure. The study by Webb et al. (2014) describes the chlorine loss with up to 60 % in the synthesis procedure. The iron speciation requires a longer duration time in order to reach a stable equilibrium, but the Cl^- and FeO_{total} content decreases during synthesis.

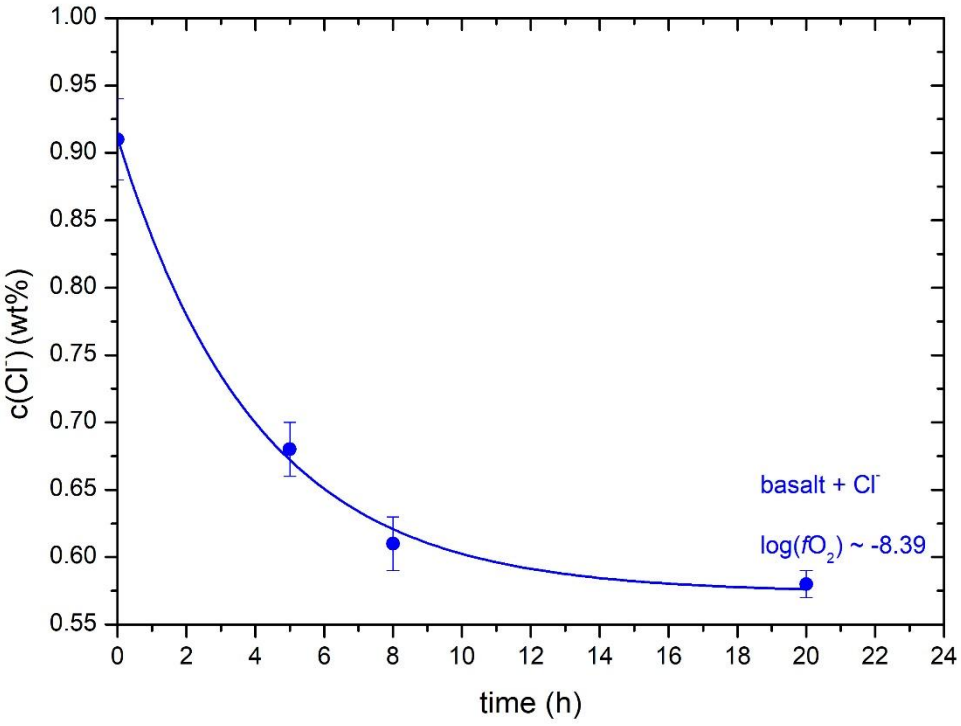

Figure 56: Evolution of chlorine in basaltic melts as a function of duration time.

4.2.3. Comparison of diverse iron analysis

Table 15 presents a comparison of diverse iron analysis and the fO_2 (gas mixing). The Fe^{2+}/Fe_{total} was changed by the variation of the fO_2. The accuracy of Fe^{2+}/Fe_{total} was checked by the analysis of FeO_{total} with external methods (electron microprobe and X-ray fluorescence). The halogen-free basaltic glass (BA-0-II) shows a stable iron total content of 5.46 - 5.55 wt% for the microprobe, X-ray fluorescence and wet chemistry methods. Furthermore, the FeO_{total} of the microprobe and wet chemistry correlate well, whereas sometimes the values of the XRF method differ from the results of the other methods. The variation of the CO_2 and H_2 atmosphere enables the manipulation of the fO_2 as well as the iron speciation. The significance deviation was obtained by the increase in Fe^{2+}/Fe_{total}.

Figure 57 presents the results of the FeO_{total} analysis of the three methods as well as 1:1 solid line. The microprobe results show a good correlation with the wet chemistry data (rectangles) and follow the 1:1 solid line. On the opposite of the wet chemistry, the FeO_{total} contents of X-ray fluorescence (circles) differ from the microprobe data and show an overestimation for most glasses.

Table 15: Results of FeO_{total} analysis of wet chemistry compared to microprobe and X-ray fluorescence. Furthermore, the results of Fe^{2+}/Fe_{total} of wet chemistry and the oxygen fugacity of the gas mixing.

Sample	Fe^{2+}/Fe_{total}	FeO_{total} (wt %)			FeO (wt%)	$log_{10}(fO_2)$
	wet chemistry	microprobe	XRF	wet chemistry	wet chemistry	gas mixing
BA-0-II	0.16	5.46	5.55	5.53	0.65	-0.68
BA-0_N3	0.50	5.12	5.68	5.18	2.55	-4.97
BA-0_N1	0.65	4.25	5.62	4.25	2.74	-6.97
BA-0_N-1	0.82	4.14	4.84	4.18	3.37	-8.97
BA-Cl-II	0.19	4.96	5.24	4.95	0.94	-0.68
BA-Cl_N3	0.54	5.40	5.39	5.35	2.90	-4.39
BA-Cl_N1	0.70	4.15	4.92	3.96	2.79	-6.39
BA-Cl_N-1	0.81	3.37	4.30	3.62	2.93	-8.39
BA-Cl-F-II	0.29	7.53	6.29	7.58	2.20	-0.68
BA-Cl-F_N3	0.44	5.34	5.64	5.18	2.27	-4.39
BA-Cl-F_N1	0.61	5.39	5.56	5.49	3.34	-6.39
BA-Cl-F_N-1	0.85	4.55	4.39	4.59	3.90	-8.39
BA-F-II	0.11	5.55	5.88	5.49	0.61	-0.68
BA-F_N3	0.41	5.98	5.92	6.10	2.49	-4.97
BA-F_N1	0.66	5.68	5.56	5.72	3.75	-6.97
BA-F_N-1	0.72	4.52	5.28	4.60	3.31	-8.97

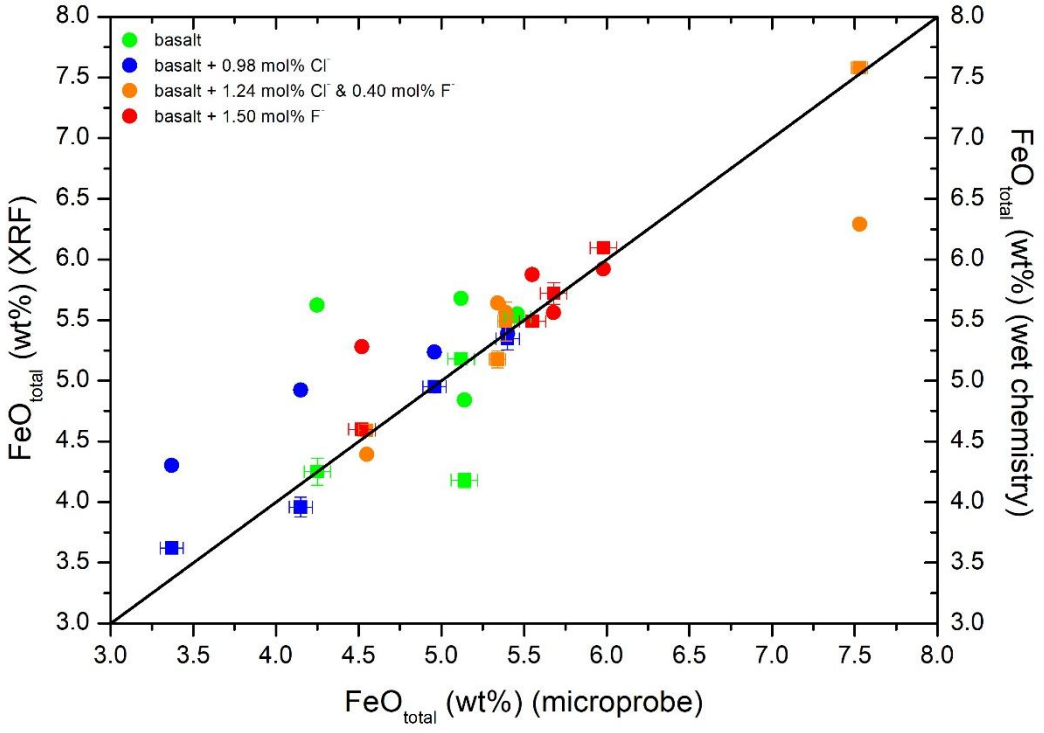

Figure 57: Comparison of the total iron FeO_{total} (wt%) determined by microprobe versus X-ray fluorescence (circles) and wet chemistry (rectangles). The solid line shows a 1:1 correlation.

Figure 58 compares the iron speciation with the fO_2 of gas mixing. The addition of halogens to the present peralkaline melts synthesised in air results in a 0.05 increase in Fe^{2+}/Fe_{total} for 0.98 mol% Cl^-, whereas the addition of 1.24 mol% F^- shows a 0.05 decrease by a constant oxygen fugacity. This effect is enhanced by the addition of (Cl^- + F^-) at high fO_2 and results in an increase in iron ratio by 0.15 for glasses synthesised in air at 1 atm. The stronger increase is explained by the higher halogen contents of BA-Cl-II and BA-F-II compared to an average of 1.24 mol% Cl^- and 0.40 mol% F^-. The reduced atmosphere results in a constant increase in Fe^{2+}/Fe_{total} for all halogen-bearing glasses due to decreasing oxygen fugacity.

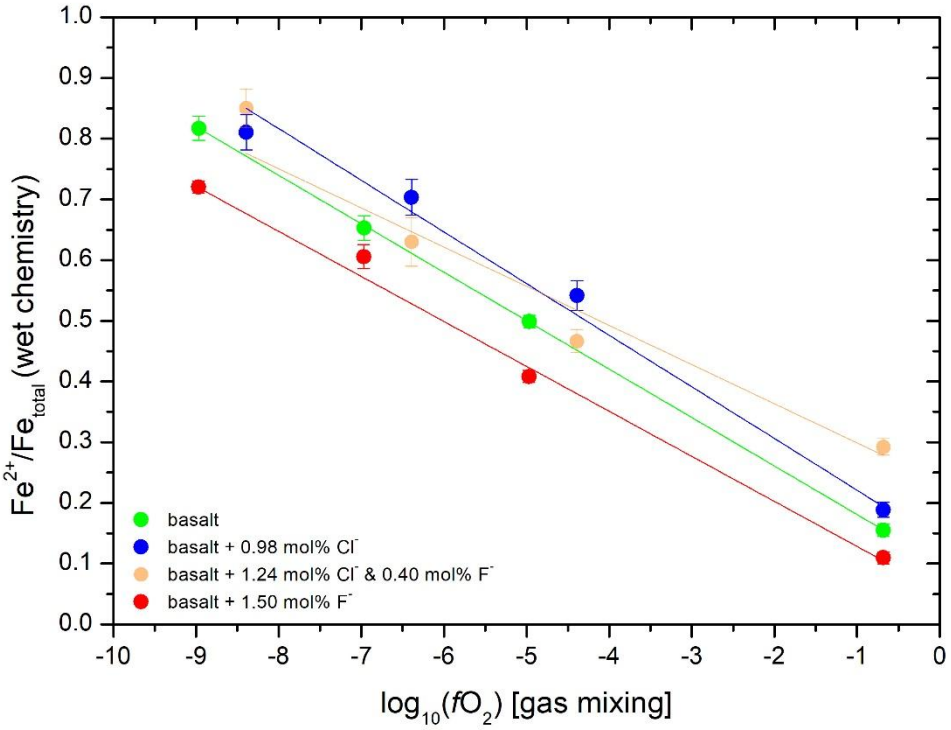

Figure 58: Iron speciation as a function of oxygen fugacity for glasses synthesised at increasing oxidising condition.

4.2.4. Raman-spectra: Effect of Fe^{2+}/Fe_{total} iron ratio on the structure

Figure 59 (a) demonstrates the raw data of the Raman measurements of the halogen-free basaltic glasses. The data (b) has experienced a frequency and temperature correction of Raman intensity after Long (1977). This correction modifies the intensity of the low frequency range (LF: 200 to 600 cm^{-1}).

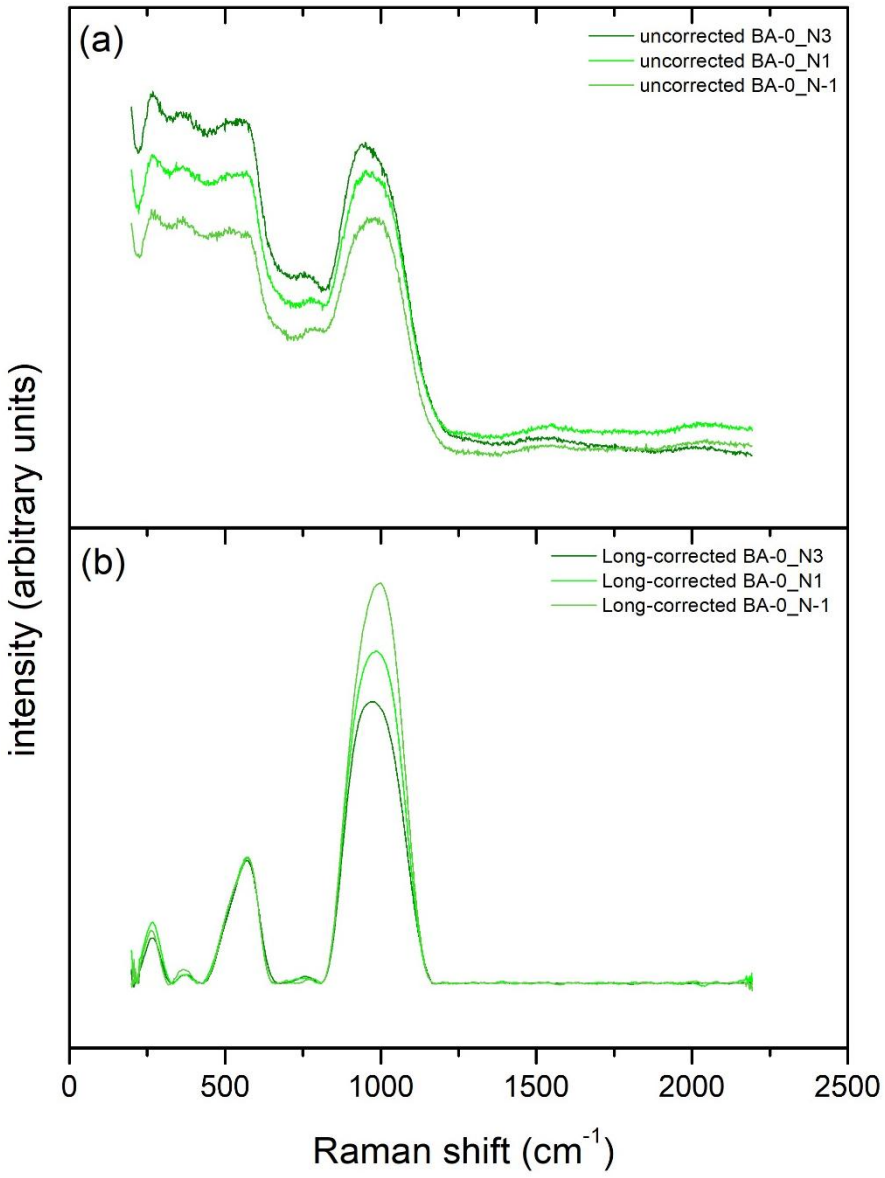

Figure 59: (a) Uncorrected Raman spectra for the redox equilibrated halogen-free basaltic glasses, (b) Long-corrected spectra for the redox equilibrated halogen-free basaltic glasses.

The halogen-free and -bearing basaltic glasses indicate two characteristic regions in the Raman spectra (figure 60). The low-frequency region (I) describes the wavenumbers between ~400 to 600 cm^{-1} and the high-frequency region (IIa & IIb) varies from ~ 800 to 1200 cm^{-1}. The mid-range region between 700 and 800 cm^{-1} shows only small intensity values and is thus not used for the interpretation of the present basaltic glasses (McMillian 1984).

The Raman spectra of halogen-free basaltic glass show a peak shift at the maximum from 950 (IIb) to 1020 cm^{-1} (IIa) with reducing conditions describing the increasing Fe^{2+}/Fe_{total} (figure 60 a). The Raman spectra of the halogen-bearing glasses show an identical trend compared to the halogen-free basalt and also demonstrate the peak shift to lower wavenumbers (figure 60 b-d).

Figure 61 indicates the overlap of Raman spectra for glasses synthesised in air (black line) and reduced atmosphere (green line) at 1 atm. The decrease in Fe^{2+}/Fe_{total} results in an increase in intensity of the peak in the low frequency region. These results correlate well with the data from Di Genova et al. (2016), where the relationship between the increasing intensity and the iron speciation was observed. Furukawa et al. (1981) described that the peak shift from 950 to 1050 cm^{-1} is associated with the polymerisation of the network structure. However, the authors showed that the peak around 590 cm^{-1} shifts to a lower frequency. This peak shift was not observed for the present basaltic composition.

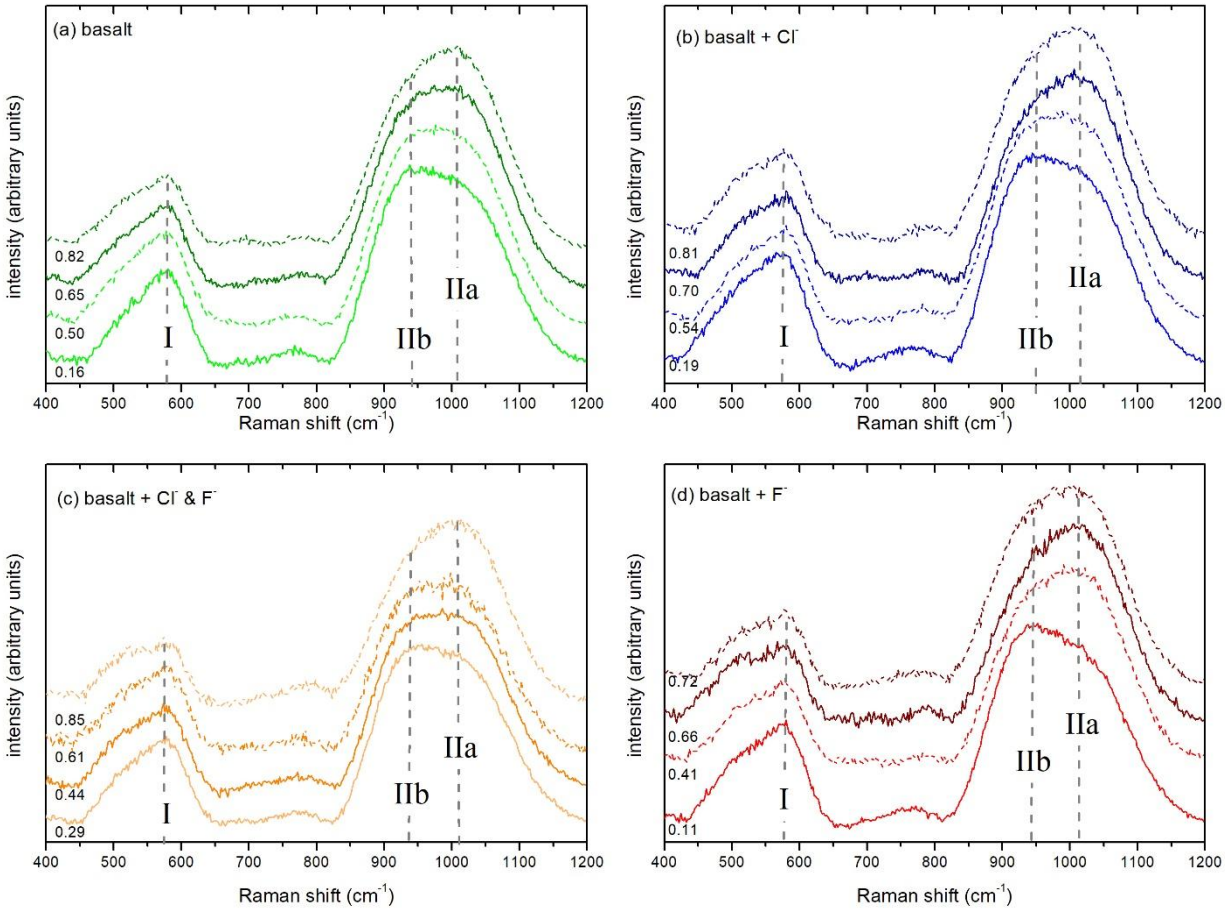

Figure 60: Raman spectra after baseline and Long correction of basaltic glasses. The numbers represent the Fe^{2+}/Fe_{total} of the halogen-free and –bearing basaltic glasses. The vertical dashed lines show the main peaks in the low-frequency region (I) and the high-frequency regions (IIa and IIb).

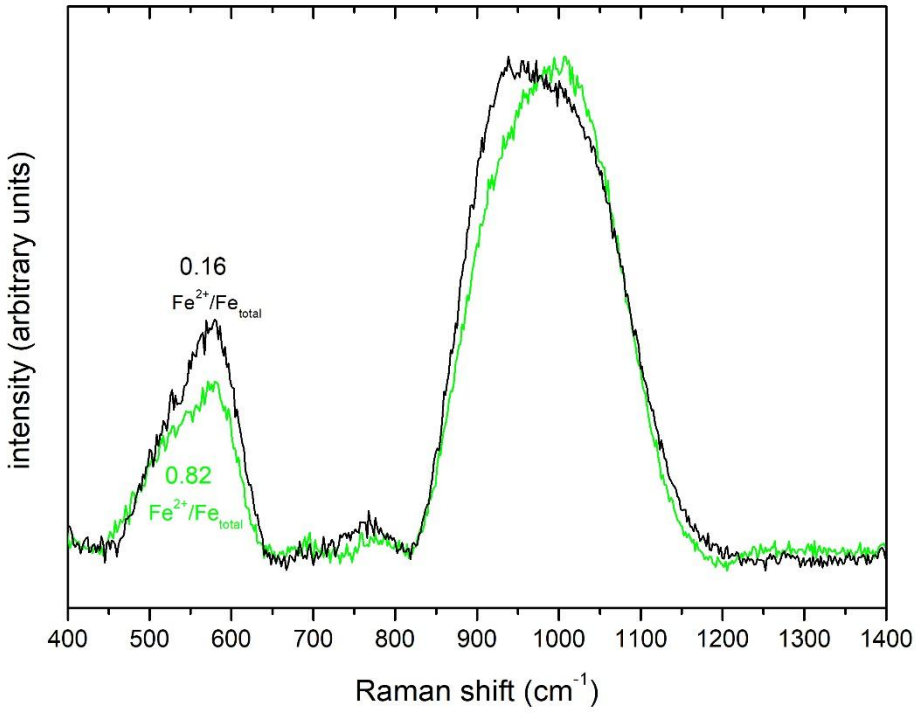

Figure 61: Comparison of the overlap of Raman spectra after a Long correction of basaltic glasses for glasses synthesised at increasing oxidising condition.

4.2.5. Correlation of Fe^{2+} content versus absorption

Figure 62 shows the Fe^{2+} peak depending on the thickness correlated absorption of the glass pieces. Knipping et al. (2015) described the increasing absorbance of the Fe^{2+} peak around 9000 cm^{-1} with reducing atmosphere. The halogen-free and halogen-bearing basaltic glasses show a peak around 9600 cm^{-1}, which are characterised as the Fe^{2+} peak. Figure 62 presents the typical increase of the Fe^{2+} peak due to the increasing Fe^{2+}/Fe_{total}. Figure 63 shows the increase in intensity of the ferrous peak with decreasing oxygen fugacity for the halogen-free basalt. This effect can be observed for the halogen-bearing glasses, whereby the intensity of the absorbance varies with the addition of halogens. The addition of fluorine to the present glass demonstrates the strongest effect on the Fe^{2+} peak (see figure 63 b and c). These results are consistent with figure 17, which describes the strong influence of halogens on the Fe^{2+}/Fe_{total}. Furthermore, figure 63 d indicates that the addition of chlorine does not show a strong effect on Fe^{2+} and this corresponds well with figure 17.

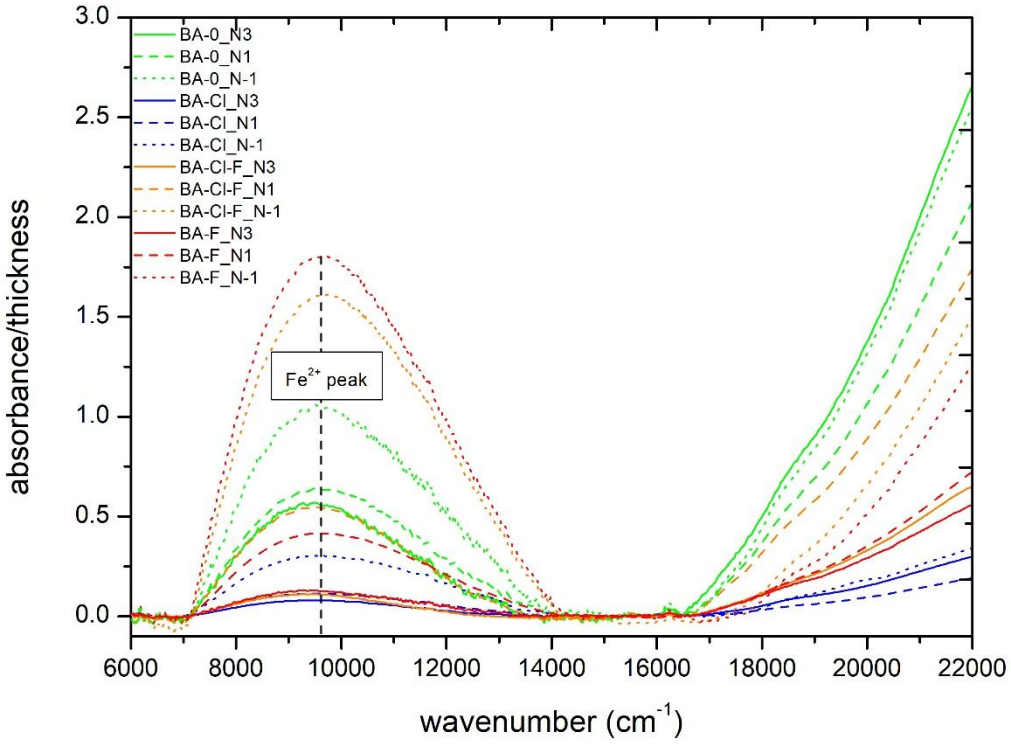

Figure 62: Comparison of the thickness corrected absorbance of halogen-free and halogen-bearing glasses in the range of 6000-22000 cm^{-1} by the Fe^{2+} peak.

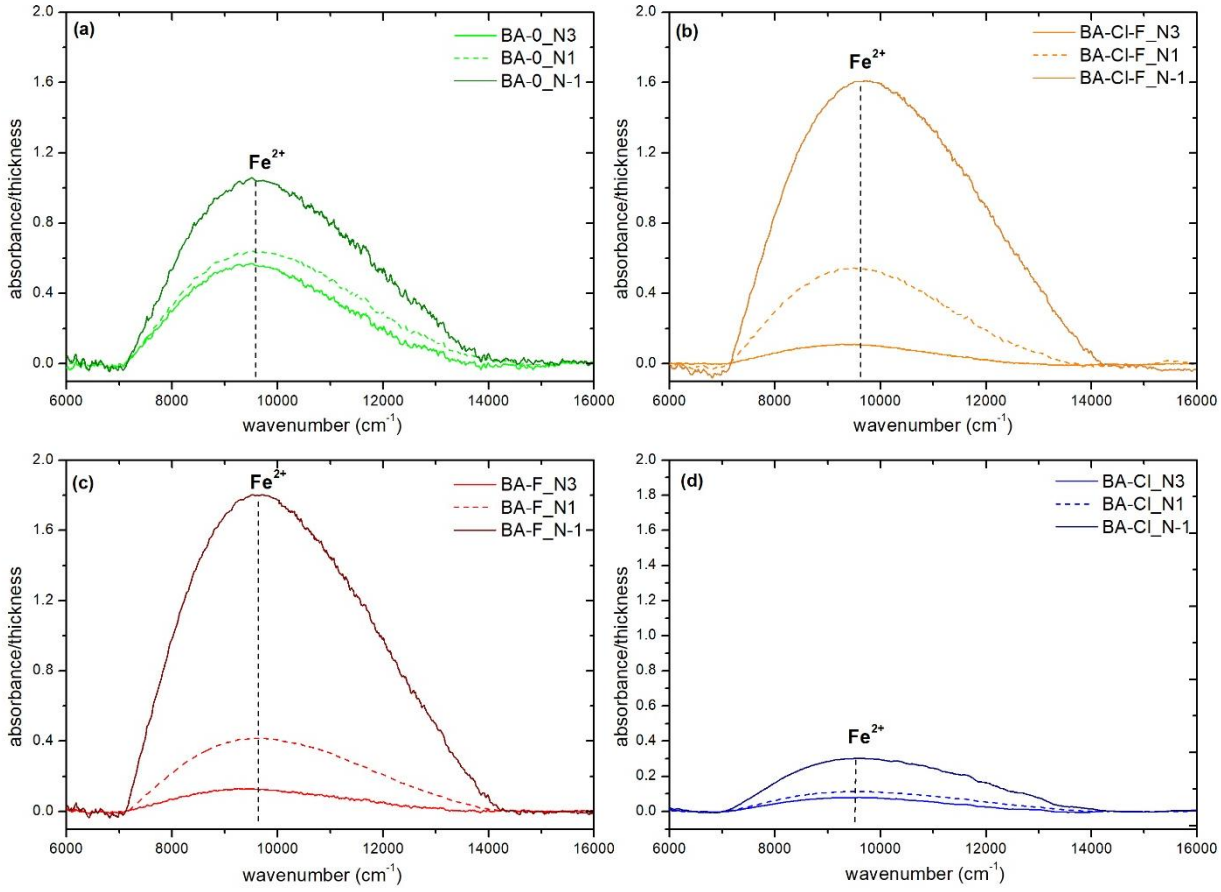

Figure 63: Corrected UV-Visible spectra of (a) halogen-free, (b) chlorine and fluorine, (c) fluorine and (d) chlorine bearing basaltic glasses in the range of ferrous iron bands.

4.3. Viscosity

4.3.1. Halogen dependence of viscosity for basaltic glasses

Figure 64 shows the viscosity as a function of temperature and the data is presented in table 16 for redox equilibrated glasses. Furthermore, the Arrhenian parameters *A* and *B* with the standard deviations are given in table 17. The error in temperature is 0.5 K and the viscosity shows an error of 0.06 $\log_{10}$ Pa s.

Table 16 a: Micropenetration viscosity data of halogen-free and halogen-bearing basaltic glasses with a varied oxidation state at diverse experimental temperatures.

BA-0-II		BA-0_N3		BA-0_N1		BA-0_N-1	
T (K)	$\log_{10}\eta$ (Pa s)	T (K)	$\log_{10}\eta$ (Pa s)	T (K)	$\log_{10}\eta$ (Pa s)	T (K)	$\log_{10}\eta$ (Pa s)
931.0	12.64	927.1	12.74	922.1	12.80	922.2	12.63
940.4	12.31	932.1	12.52	932.1	12.42	932.1	11.99
960.4	11.44	942.2	12.13	942.1	11.87	942.2	11.65
970.4	11.02	952.3	11.58	952.3	11.52	952.1	11.13
991.0	10.3	962.0	11.16	962.1	10.89	962.0	10.68
1000.4	10.11	972.3	10.72	972.1	10.56	972.0	10.32
1011.2	9.48	982.2	10.33	982.9	10.07	977.0	10.29
1018.3	9.26	992.4	9.97	992.8	9.75	982.2	9.98
		1001.9	9.65	1002.8	9.46	987.2	9.81
		1012.3	9.24	1012.8	9.08	993.0	9.60
BA-Cl-II		BA-Cl_N3		BA-Cl_N1		BA-Cl_N-1	
T (K)	$\log_{10}\eta$ (Pa s)	T (K)	$\log_{10}\eta$ (Pa s)	T (K)	$\log_{10}\eta$ (Pa s)	T (K)	$\log_{10}\eta$ (Pa s)
940.7	12.59	932.2	12.82	932.1	12.71	922.5	12.71
950.4	12.28	941.5	12.45	942.1	12.32	932.1	12.26
960.4	11.90	952.8	12.03	942.5	12.15	942.1	12.03
970.4	11.36	962.4	11.72	952.1	11.72	952.1	11.61
980.4	11.10	972.2	11.36	952.1	11.65	962.0	11.19
990.5	10.55	976.9	11.02	962.0	11.25	964.4	11.03
1000.5	10.27	982.4	10.93	972.3	10.86	977.0	10.65
1010.3	9.76	991.8	10.43	981.9	10.49	982.0	10.17
		1002.2	10.05	992.3	10.12	992.1	9.89
		1014.9	9.73	1002.2	9.78	1002.5	9.47
BA-Cl-F-II		BA-Cl-F_N3		BA-Cl-F_N1		BA-Cl-F_N-1	
T (K)	$\log_{10}\eta$ (Pa s)	T (K)	$\log_{10}\eta$ (Pa s)	T (K)	$\log_{10}\eta$ (Pa s)	T (K)	$\log_{10}\eta$ (Pa s)
940.3	12.57	922.2	13.06	922.2	12.69	912.3	12.57
950.4	12.28	932.1	12.73	932.6	12.26	922.2	12.15
960.4	12.08	942.1	12.13	942.1	11.98	932.5	11.74
970.6	11.36	952.1	11.63	952.6	11.43	942.1	11.27
975.4	11.27	972.0	11.21	962.1	11.03	952.1	10.88
988.5	10.87	962.0	11.14	972.0	10.74	962.0	10.68
1000.7	10.30	982.0	10.65	982.6	10.24	972.4	10.14
1011.5	10.03	992.1	10.05	987.2	9.93	977.3	9.95
		998.1	10.05	992.3	9.82	987.3	9.59
		1002.0	9.96	1002.1	9.47	991.9	9.55

Table 16 b: Micropenetration viscosity data of halogen-free and halogen-bearing basaltic glasses with a varied oxidation state at diverse experimental temperatures.

BA-F-II		BA-F_N3		BA-F_N1		BA-F_N-1	
T (K)	$\log_{10}\eta$ (Pa s)	T (K)	$\log_{10}\eta$ (Pa s)	T (K)	$\log_{10}\eta$ (Pa s)	T (K)	$\log_{10}\eta$ (Pa s)
930.3	12.82	922.2	12.82	911.4	12.98	912.2	11.80
940.6	12.40	931.2	12.39	917.4	12.72	922.7	11.50
950.8	11.97	942.1	11.71	922.5	12.51	932.1	11.30
962.1	11.56	962.6	10.91	932.2	12.04	942.6	10.93
970.4	11.23	972.7	10.51	952.1	11.31	952.2	10.31
980.4	10.94	981.5	10.16	962.2	10.67	972.0	9.88
1002.0	9.93	991.8	10.04	972.1	10.37	973.1	9.67
1011.9	9.67	1011.9	9.32	982.3	10.06	983.9	9.20
1035.0	8.91	1023.0	8.89	987.1	9.86	993.7	9.05
		1034.8	8.55	1011.8	9.10	1004.0	8.74

Table 17: Parameters for the Arrhenius fit to the micropenetration viscosity data.

Sample	A_{Arr} (log10 Pa s)	ΔA_{Arr} (log10 Pa s)	B_{Arr} (log10 Pa s K)	ΔB_{Arr} (log10 Pa s K)	T_g^{12} (K)	ΔT_g^{12} (K)	$\eta@ T_g^{12}$ (log10 Pa s)
BA-0_II	-26.43	0.89	3.63	0.06	944.8	0.3	12.00
BA-0_N3	-29.17	0.54	3.88	0.05	943.5	0.2	11.90
BA-0_N1	-29.52	0.91	3.90	0.09	939.6	0.3	11.77
BA-0_N-1	-28.80	1.12	3.81	0.11	933.5	0.4	11.52
BA-Cl_II	-31.20	0.54	4.12	0.15	952.7	0.4	12.00
BA-Cl_N3	-26.19	0.92	3.64	0.09	953.3	0.4	12.02
BA-Cl_N1	-29.23	1.23	3.90	0.11	946.4	0.4	11.73
BA-Cl_N-1	-27.99	1.25	3.76	0.12	940.5	0.5	11.49
BA-Cl-F_II	-28.05	0.95	3.80	0.07	948.7	0.3	12.00
BA-Cl-F_N3	-26.62	1.77	3.66	0.17	946.4	0.7	11.96
BA-Cl-F_N1	-28.47	0.80	3.80	0.08	939.3	0.3	11.60
BA-Cl-F_N-1	-25.86	0.76	3.50	0.07	925.6	0.3	11.08
BA-F_II	-25.23	1.25	3.51	0.09	942.1	0.5	12.00
BA-F_N3	-25.73	1.13	3.54	0.11	937.2	0.5	11.85
BA-F_N1	-27.12	0.82	3.65	0.08	933.6	0.3	11.65
BA-F_N-1	-23.19	1.22	3.20	0.12	910.0	0.6	10.80

Figure 64 (a) shows the viscosity data for the decrease of fO_2. The increasing 0.15 Fe^{2+}/Fe_{total} in the halogen-free basalt results in a decrease in viscosity by 0.3 log units. The addition of halogens to the present basaltic melts results in a larger decreasing effect on viscosity caused by the iron speciation. Thus, the decrease of viscosity is associated with redox state as well as the halogen content. The addition of 0.98 mol% chlorine to the present basalt results in a decrease in viscosity of 0.5 log units by decreasing fO_2 (figure 64 b). The addition of fluorine effects a decrease in viscosity by 0.5 log units (1.50 mol% F^-) respectively 1.5 log units (1.92 mol% F^-) due to the varied Fe^{2+}/Fe_{total} and fluorine content (figure 64 d). Furthermore, the addition of both halogens (c) with an average of 1.24 mol% Cl^- and 0.40 mol% F^- to the basaltic melt demonstrates a decrease in viscosity by 0.8 log units (figure 64 c).

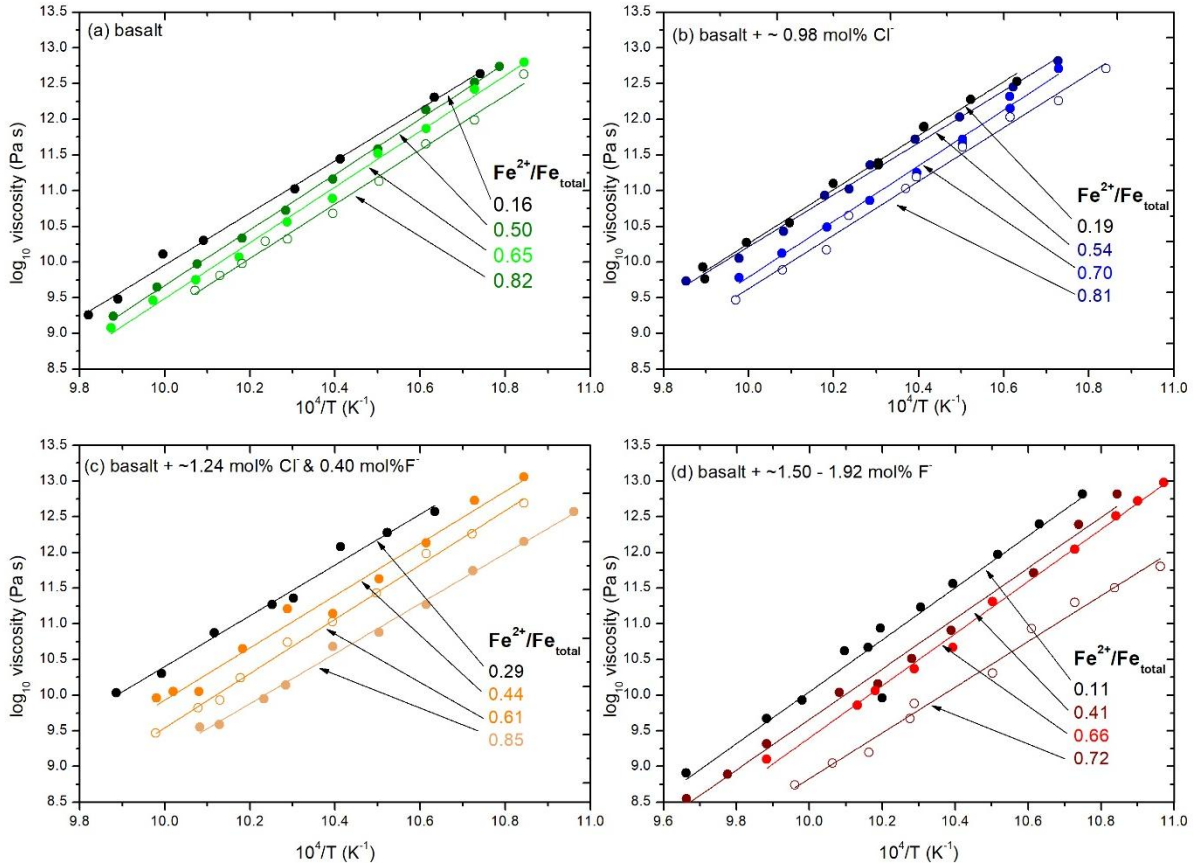

Figure 64: Effect of redox on the viscosity of the halogen-free and halogen-bearing basaltic glasses. The error bars are smaller than the circle. Viscosity data from micropenetration (a) halogen-free basalt, (b) basalt with chlorine, (c) basalt with chlorine and fluorine and (d) basalt with fluorine. The error bars are smaller than the circles

Figure 65 shows T_g^{12} as a function of the iron speciation for melts synthesised at decreasing oxygen fugacity. The T_g^{12} was calculated from the Arrhenian fit and describes the temperature at a viscosity of log 10^{12} Pa s. The increase of Fe^{2+}/Fe_{total} results in a decrease in T_g^{12} by 15 K in halogen-free basaltic melts. The addition of 0.98 mol% chlorine to the present

basalt synthesised in air increases the glass transition temperature by 5 K and the increase of Fe^{2+}/Fe_{total} due to decreasing fO_2 results in a decrease in the T_g^{12} by 15 K as well. In contrast to that, fluorine-bearing basaltic melts show a decrease in T_g^{12} by 10 K to the halogen-free basalt. The addition of fluorine to the present melts accompanied by the reduced atmosphere shows the largest decrease in T_g^{12} by 25 K. Furthermore, the addition of (Cl^- + F^-) has no significant effect on T_g^{12} compared to the starting composition but the decrease in fO_2 results in a decrease by 20 K. Consequently, the values plot between only chlorine and fluorine.

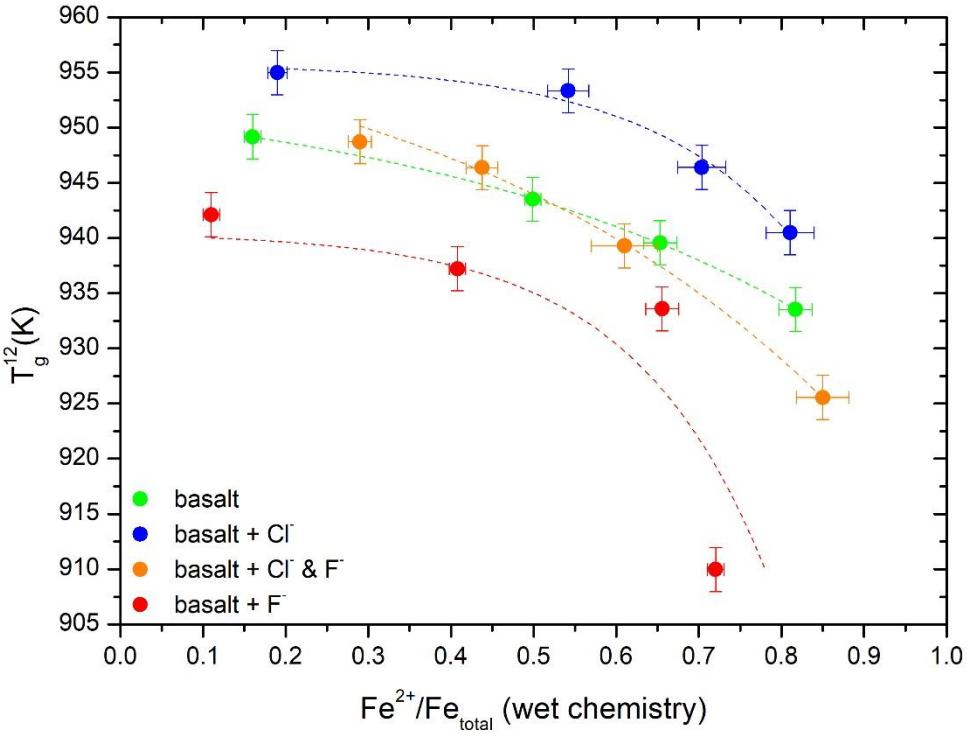

Figure 65: The glass transition temperature T_g^{12} as a function of Fe^{2+}/Fe_{total}. Exponential functions were fitted to the data (dashed lines).

Table 18 represents the parameter of the Vogel-Fulcher-Tamman fit (equation 8) as well as the corresponding glass transition temperature. The fit does not work with three free parameters, therefore the value of A_{VFT} has to be fixed on a constant number. The T_g^{12} of the halogen-free basaltic melts decreases by 10 K with reducing atmosphere. The addition of chlorine to the present basaltic melt results in a decrease in T_g^{12} by 12 K accompanied by a decreasing oxygen fugacity, whereas the addition of F^- and (Cl^- + F^-) results in a decrease in T_g^{12} by 27 and 20 K. The T_g^{12} values of the VFT equation correspond well with the data of the Arrhenius fit (table 17), but the VFT equation has a higher error than the Arrhenius fit cause of the curve regression.

Table 18: Parameters for the Vogel-Fulcher-Tamman fit (VFT) to the micropenetration viscosity data.

Sample	A_{VFT} (log10 Pa s)	B_{VFT} (log10 Pa s K)	ΔB_{VFT} (log10 Pa s K)	C_{VFT} (log10 Pa s K)	ΔC_{VFT} (log10 Pa s K)	T_g^{12} (K)	ΔT_g^{12} (K)
BA-0_II	-4.55	6169.16	266.55	572.33	17.22	945.1	23.6
BA-0_N3	-4.55	5809.02	63.22	592.14	3.98	943.1	5.5
BA-0_N1	-4.55	5674.59	102.58	596.46	6.51	939.3	9.0
BA-0_N-1	-4.55	5789.64	126.44	583.78	8.09	933.6	11.1
BA-Cl_II	-4.55	5894.26	216.54	595.33	13.82	951.5	19.0
BA-Cl_N3	-4.55	6527.87	199.08	558.35	12.40	952.8	17.3
BA-Cl_N1	-4.55	5875.79	123.94	591.23	7.69	946.3	10.7
BA-Cl_N-1	-4.55	6082.78	252.09	572.66	15.82	940.2	22.0
BA-Cl-F_II	-4.55	6430.43	196.15	567.41	10.05	956.0	15.5
BA-Cl-F_N3	-4.55	6396.62	279.64	559.31	17.37	945.8	24.2
BA-Cl-F_N1	-4.55	5958.91	163.81	578.54	10.36	938.6	14.3
BA-Cl-F_N-1	-4.55	6212.55	126.37	550.14	8.06	925.5	11.1
BA-F_II	-4.55	6430.43	196.15	567.41	9.05	946.0	14.9
BA-F_N3	-4.55	6094.83	132.40	569.89	8.54	938.1	11.7
BA-F_N1	-4.55	6102.47	101.77	564.11	6.33	932.8	8.8
BA-F_N-1	-4.55	6311.97	256.12	529.97	17.00	911.4	23.0

4.4. Heat capacity

The heat capacity measurements were performed in the temperature range of 400 to 1040 K with a cooling and heating rate of 20 K min^{-1} for all glasses. Figure 66 shows the heat capacity data as a function of temperature. The increasing fO_2 results in a shift of the glass transition peak of halogen-free basaltic melts and the onset temperature peak to lower temperatures (figure 66 a). Figure 66 b results in a shift of the glass transition peak of chlorine-bearing basaltic melts and the onset temperature peak to higher temperatures. The addition of fluorine and (Cl^- + F^-) to the present basaltic melts shows the same peak shift to lower temperatures, whereas the addition of chlorine results in a peak shift to higher temperatures (figure 66 c-d). Table 19 represents the fit parameters of the Maier-Kelley fit (equation 9) as well as the heat capacity of the glasses and the melts. The halogen-free and the halogen-bearing basaltic melts reflect a decrease in C_{pl} and C_{pg} with decreasing oxidising condition.

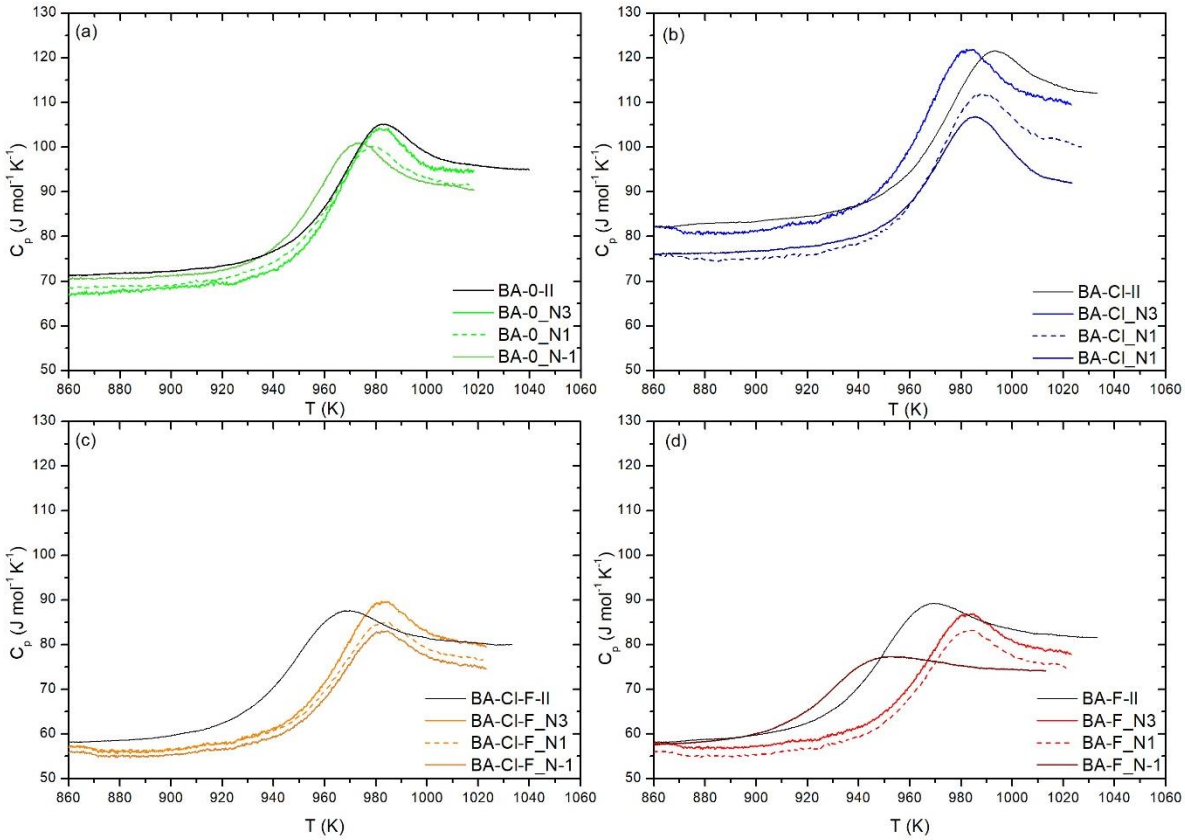

Figure 66: Heat capacity data as a function of temperature for halogen-free basalt melts and melts with chlorine, fluorine and (Cl^- + F^-) synthesised at increasing oxidising conditions.

Table 19: Parameters for Maier-Kelley-fit and C_{pl} and C_{pg} for melts synthesised at decreasing oxidising condition.

Sample	Maier-Kelley parameters						C_{pl}	C_{pg}
	a	Δa	b	Δb	c	Δc		
	($J\,g^{-1}K^{-1}$)	($J\,g^{-1}K^{-1}$)	($10^{-4}J\,g^{-1}K^{-1}$)	($10^{-4}J\,g^{-1}K^{-1}$)	($10^{-4}J\,g^{-1}K^{-1}$)	($10^{-4}J\,g^{-1}K^{-1}$)	($J\,mol^{-1}K^{-1}$)	($J\,mol^{-1}K^{-1}$)
BA-0_II	0.764	0.002	7.570	0.002	-1.369	0.024	94.85	75.99
BA-0_N3	0.495	0.002	6.876	0.002	-1.239	0.025	93.71	73.49
BA-0_N1	0.631	0.001	5.536	0.002	-1.576	0.015	91.08	73.69
BA-0_N-1	0.893	0.002	3.213	0.002	-1.831	0.016	90.83	74.63
BA-Cl_II	1.157	0.004	3.909	0.005	-1.794	0.055	112.82	94.54
BA-Cl_N3	1.152	0.005	2.338	0.005	-2.496	0.049	109.40	84.18
BA-Cl_N1	1.181	0.004	8.578	0.004	-2.491	0.043	100.11	77.51
BA-Cl_N-1	0.795	0.002	2.503	0.002	-1.858	0.022	91.09	76.16
BA-Cl-F_II	0.646	0.004	7.860	0.004	-4.149	0.041	79.86	62.59
BA-Cl-F_N3	0.189	0.003	7.128	0.004	-3.363	0.037	79.41	57.63
BA-Cl-F_N1	0.856	0.004	1.251	0.004	-2.988	0.052	76.47	59.21
BA-Cl-F_N-1	0.843	0.004	1.253	0.004	-2.923	0.052	74.59	57.70
BA-F_II	0.816	0.003	3.045	0.003	-1.068	0.031	80.32	64.09
BA-F_N3	0.830	0.003	1.715	0.003	-1.783	0.036	79.96	62.24
BA-F_N1	0.789	0.003	1.604	0.004	-1.709	0.034	75.22	58.57
BA-F_N-1	0.526	0.009	5.044	0.001	-0.816	0.011	73.69	61.59

Table 20 shows the parameters of C_p^{conf} and S_{conf} at T_g^{12}. A decrease in T_f^{20}, C_p^{conf} and S^{conf} is indicated accompanied by the decreasing fO_2. The decreasing iron ratio of the halogen-free basalt results in a decrease in the fictive temperature (T_f^{20}) by 10 K. This effect is enhanced by the addition of fluorine to the present melts. The addition of fluorine to the basaltic melt results in a decrease in T_f^{20} by 27 K, whereas the addition of chlorine shows a decrease in T_f^{20} by 12 K compared to the halogen-free basaltic melts. As a consequence, the addition of fluorine to the basaltic melt reflects an even stronger effect on the T_f^{20} accompanied by the varied oxygen fugacity. This is shown by the addition of both halogens, which results in a decrease in T_f^{20} by 20 K. Besides the fictive temperature, C_p^{conf} and S_{conf} demonstrate the same decreasing behaviour at decreasing oxidising condition.

Table 20: Parameters of C_p^{conf} and S_{conf} for the viscosity at T_g^{12}. The measurements were performed with a constant heating and cooling rate of 20 K min^{-1}.

Sample	T_f^{20} (K)	C_p^{conf} (J mol^{-1}K^{-1})	$S_{conf}(Tg^{12})$ (J mol^{-1}K^{-1})	$\Delta S_{conf}(Tg^{12})$ (J mol^{-1}K^{-1})	B_e (kJ mol^{-1})	ΔB_e (kJ mol^{-1})
BA-0_II	945	18.86	11.55	0.15	418.29	36.22
BA-0_N3	944	20.22	12.27	0.21	440.73	35.92
BA-0_N1	940	17.39	10.25	0.31	366.97	35.80
BA-0_N-1	934	16.20	9.94	0.39	353.75	35.59
BA-Cl_II	953	18.28	9.36	0.93	340.17	36.34
BA-Cl_N3	953	25.22	18.11	0.94	657.28	36.29
BA-Cl_N1	946	22.60	13.85	0.52	499.30	36.05
BA-Cl_N-1	941	17.28	11.29	0.78	404.53	35.83
BA-Cl-F_II	950	17.27	13.25	0.69	466.02	35.17
BA-Cl-F_N3	946	21.78	15.30	1.20	551.16	36.02
BA-Cl-F_N1	939	17.26	10.96	0.49	392.03	35.77
BA-Cl-F_N-1	926	16.88	11.82	0.43	416.91	35.28
BA-F_II	944	16.23	12.16	0.49	432.22	35.44
BA-F_N3	937	17.71	15.61	0.64	548.56	35.14
BA-F_N1	934	16.65	15.68	0.45	543.78	34.68
BA-F_N-1	910	12.10	9.09	0.69	316.27	34.79

In figure 67, the configurational heat capacity C_p^{conf} of the halogen-free and -bearing basaltic melts is plotted as a function of iron speciation. The increase of Fe^{2+}/Fe_{total} (up to 0.50) results in an increase in C_p^{conf} from 18.86 to 20.22 J mol^{-1} K^{-1} in halogen-free basaltic melts. This effect changes above a Fe^{2+}/Fe_{total} of 0.5 and results in a decrease in C_p^{conf} from 20.22 to 16.20 J mol^{-1} K^{-1}. The addition of chlorine to the present basaltic melts shows an increasing effect of C_p^{conf} up to 7 J mol^{-1} K^{-1} (18.52 to 25.22 J mol^{-1} K^{-1}) in due to the increasing Fe^{2+}/Fe_{total} from 0.19 ($\log_{10} fO_2$ -0.68) to 0.54 ($\log_{10} fO_2$ -4.97). The further increase of Fe^{2+}/Fe_{total} results in a decrease in C_p^{conf} from 25.22 to 17.28 J mol^{-1} K^{-1}. Furthermore, the addition of ($Cl^- + F^-$) to the present basaltic melts show an increase in C_p^{conf} up to 5 J mol^{-1} K^{-1}

(18.02 to 21.78 J mol^{-1} K^{-1}) due to the increasing Fe^{2+}/Fe_{total}. This effect changes above a Fe^{2+}/Fe_{total} of 0.44 and results in a decrease in C_p^{conf} from 21.78 to 16.88 J mol^{-1} K^{-1}. The fluorine-bearing melts follow the same trend but show the lowest C_p^{conf} values between 16.12 and 12.10 J mol^{-1} K^{-1}, which decrease by the reduced conditions.

The configurational entropies (S_{conf}) as a function of Fe^{2+}/Fe_{total} for glasses synthesised at increasing oxidising condition is shown in figure 68. The halogen-free basaltic melts show the smallest variation of S_{conf} between 12.27 and 9.94 J mol^{-1} K^{-1} due to the redox equilibration. The addition of chlorine to the present basaltic melts show an increasing effect of S_{conf} up to 4 J mol^{-1} K^{-1} (9.32 to 18.11 J mol^{-1} K^{-1}) due to the increasing Fe^{2+}/Fe_{total} from 0.19 ($\log_{10} fO_2$ -0.68) to 0.55 ($\log_{10} fO_2$ -4.97). This effect changes at Fe^{2+}/Fe_{total} of 0.54 and results in a decrease in S_{conf} from 18.11 to 11.29 J mol^{-1} K^{-1}. Furthermore, the addition of fluorine as well as (Cl^- + F^-) to the present basaltic melts show a similar increase in S_{conf} due to the increasing Fe^{2+}/Fe_{total} up to 0.45. The increasing effect of S_{conf} is removed by the reduced condition due to the increasing Fe^{2+}/Fe_{total}. As a consequence S_{conf} is not only a function of iron speciation but also halogen content.

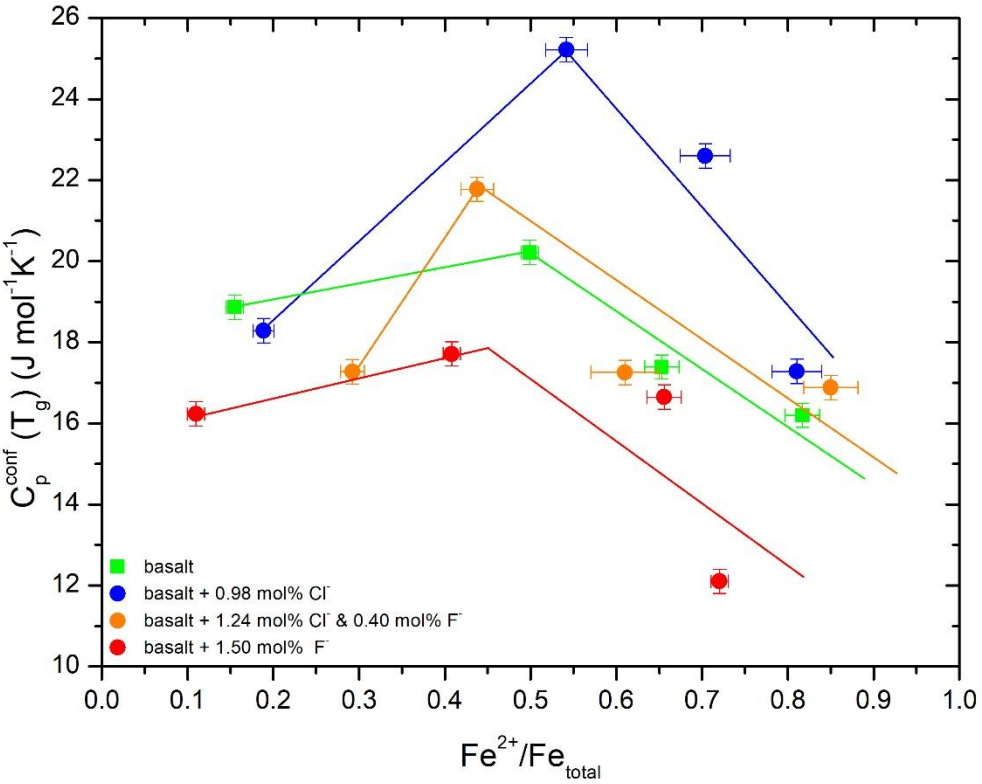

Figure 67: Configurational heat capacity C_p^{conf} as function of iron speciation of halogen-free and -bearing basaltic melts.

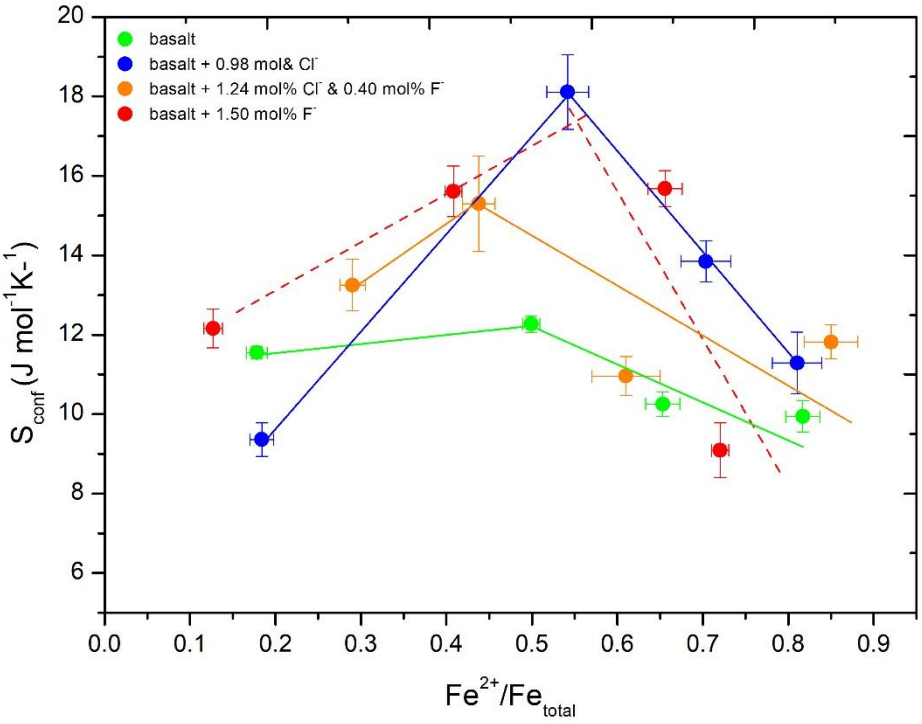

Figure 68: Configurational entropy S_{conf} as a function of iron speciation for basaltic melts.

Figure 69 demonstrates B_e as a function of Fe^{2+}/Fe_{total} for glasses synthesised at increasing oxidising condition. It is shown that the B_e values increase by reducing condition (Fe^{2+}/Fe_{total} > 0.54), whereas the further increase in Fe^{2+}/Fe_{total} results in a decrease in B_e values. This increase in B_e value shows an increasing polymerisation, whereas the decrease in B_e indicates a depolymerisation due to the decreasing Fe^{2+}/Fe_{total} (Richet 1984).

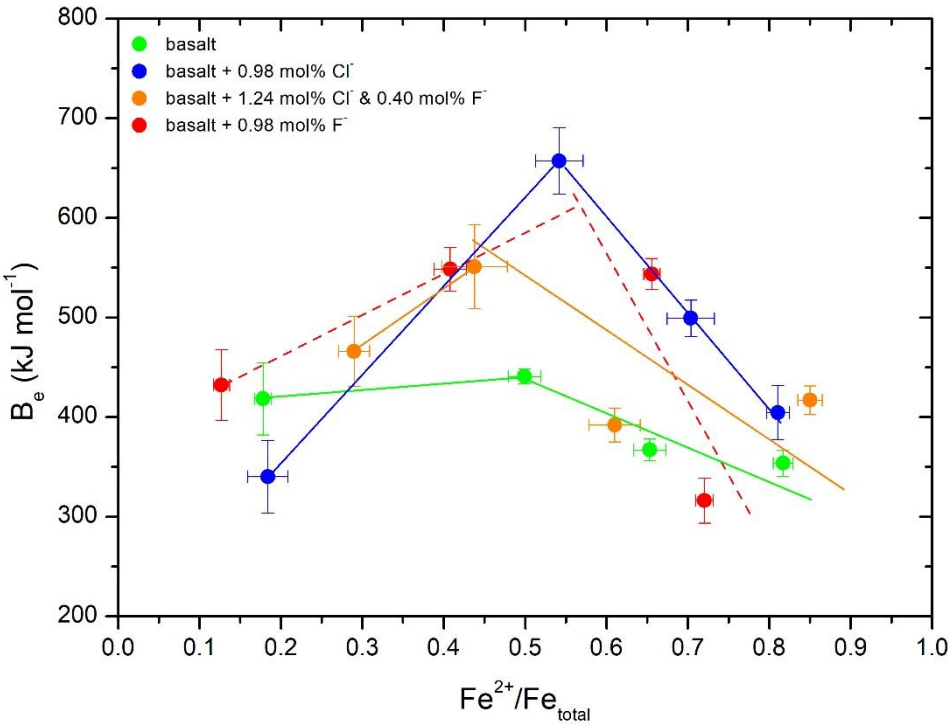

Figure 69: B_e as a function of iron speciation for basaltic melts.

The B_e values as a function of the configurational entropy (S^{conf}) for halogen-free and –bearing basaltic melts are represented in figure 70. The diagram shows a linear relation between S^{conf} and B_e for all halogen-free and -bearing melts. Figure 71 shows the dependence of B_e/S_{conf} on the iron speciation of the halogen-free and –bearing basaltic melts. The increasing Fe^{2+}/Fe_{total} in basaltic melts results in a linear decrease in B_e/S_{conf} from 36.25 to 35.59. The increasing Fe^{2+}/Fe_{total} (from 0.16 to 0.50) in basaltic melts shows a constant B_e/S_{conf} between 36.34 and 36.29, whereas the further reducing condition results in an exponential decrease in B_e/S_{conf} from 36.29 to 35.27. The fluorine-bearing basaltic melts results in a decrease in B_e/S_{conf} from 35.54 to 34.79 due to increasing Fe^{2+}/Fe_{total} and shows the lowest B_e/S_{conf} values. The increasing Fe^{2+}/Fe_{total} in (Cl^- + F^-)-bearing basaltic melts results in an exponential decrease in B_e/S_{conf} from 36.22 to 35.54 and this trend is located between the chlorine- and fluorine-bearing basaltic melts. Furthermore, the (Cl^- + F^-)-bearing basaltic melts follow a similar trend as the halogen-free basalt, this can be explained by a balance of the chlorine and fluorine effect on B_e/S_{conf}.

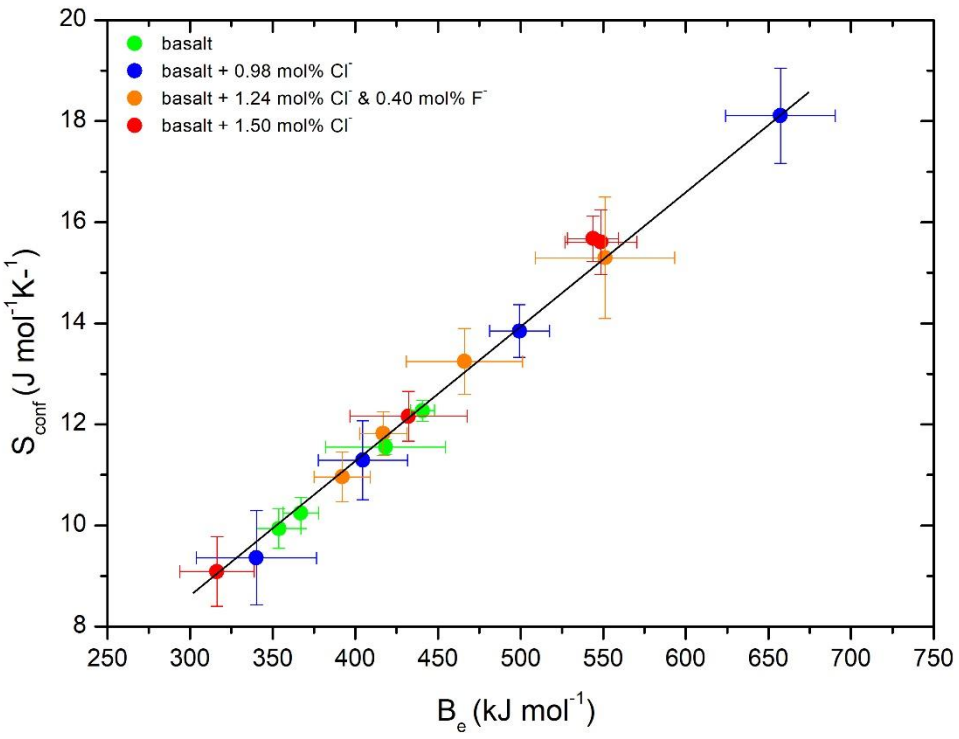

Figure 70: Configurational entropy S_{conf} as a function of B_e of basaltic melts.

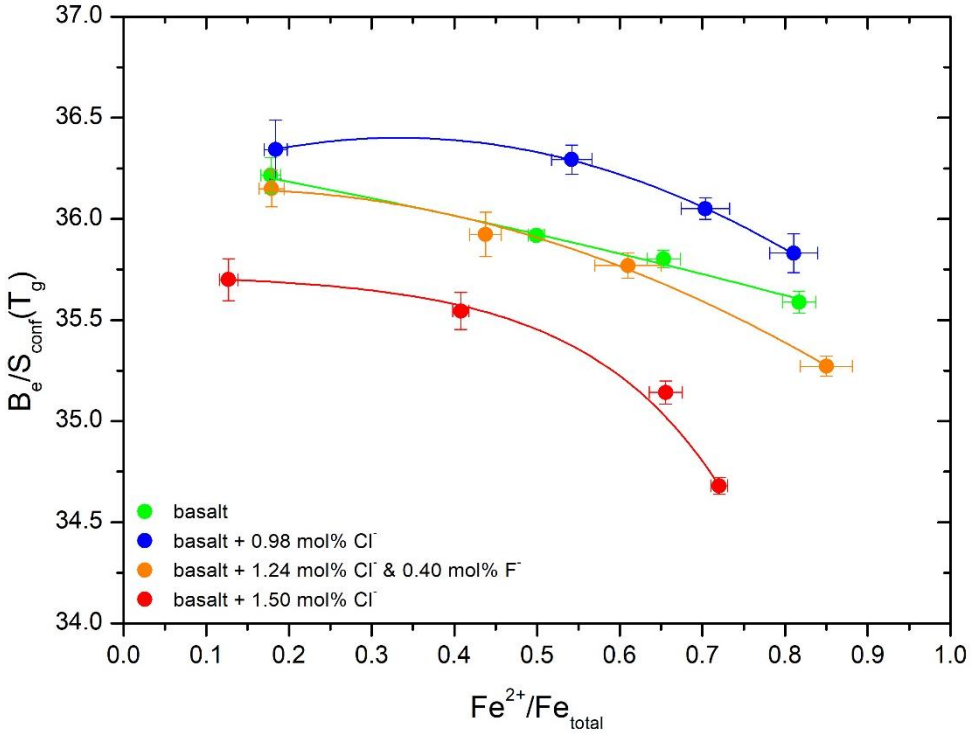

Figure 71: B_e/S_{conf} terms as a function of iron speciation for halogen-free and –bearing basaltic melts.

Figure 72 represents the heat capacity of the halogen-free basaltic melts at increasing oxidising conditions. The Dulong-Petit limit for the present glasses is not close to the heat capacity values. This overestimation is enhanced by the addition of halogens to the present basalt for example the BA-F_N3 (red lines).

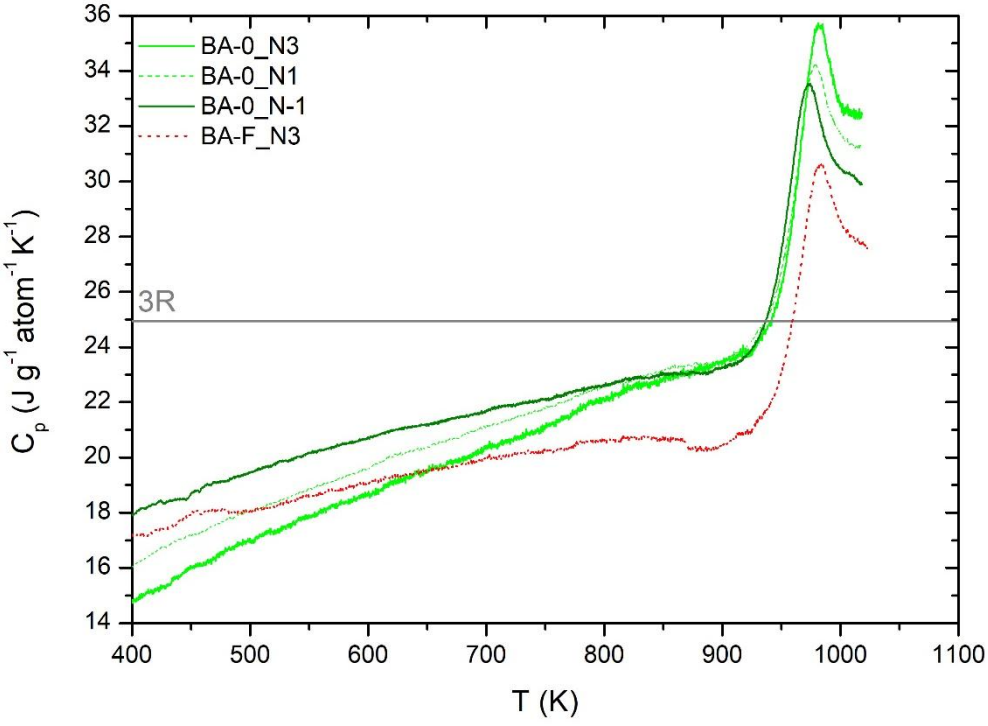

Figure 72: Heat capacity data of the halogen-free basaltic melts as a function of temperature with the plot of 3R (Dulong and Petit limit - for heat capacity calculated in mole per atoms).

5. Discussion

5.1. Influence of halogens on the iron ratio

Our experiments indicated that the increasing Fe^{2+}/Fe_{total} change the melt structure. Figure 73 highlights the calculated absorption coefficients as a function of the Fe^{2+}/Fe_{total} for the present oxidised and reduced sample. The absorption coefficient of halogen-free basaltic glasses increases logarithmically with reducing atmosphere, whereas the halogen-bearing glasses follow an exponential trend. Furthermore, figure 73 shows that fluorine has a stronger influence on the ferrous iron than the chlorine. In this context, the data correlate well with figure 17, where the dependence of fluorine on the iron ratio is discussed. This diagram can be used to predict the Fe^{2+}/Fe_{total} for unknown silicate glass without the time-consuming wet-chemistry method.

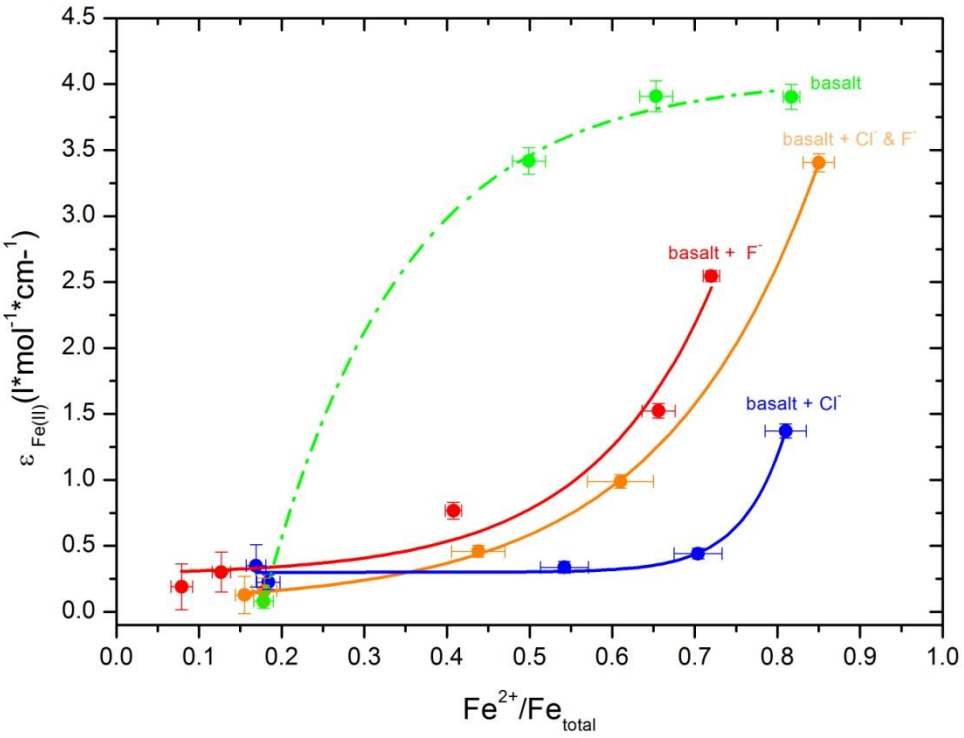

Figure 73: The $\varepsilon_{Fe(II)}$ for the ferrous iron peak (9000 cm^{-1}) versus the Fe^{2+}/Fe_{total} iron ratio of halogen-free and halogen-bearing basaltic glasses.

5.2. Influence of the iron ratio on the structure

The presence of Fe^{2+} in peralkaline melts modifies the network structure and can be observed in the Raman spectra. Figure 74 represents the Raman spectra after a frequency and temperature correction of the Raman intensity after Long (1977) for halogen-free basaltic glasses with a log fO_2 of -0.68 (Fe^{2+}/Fe_{total} of 0.16) and -8.97 (Fe^{2+}/Fe_{total} of 0.82). The low frequency range describes the degree of depolymerisation of glass network and the peak shift at the maximum to higher frequency due to increasing depolymerisation of the structure (Di Muro et al. 2009). This diagram shows the increase in intensity of the low frequency peak as well as the shift of the high frequency peak to a higher Raman shift. The increasing Fe^{2+}/Fe_{total} (0.16 to 0.80) results in a decrease in low frequency peak by 25 % and the high frequency peak shifts from 950 to 1020 cm^{-1}. Di Muro et al. (2009) proposed a relationship between the peak intensity and the iron speciation in the glass. The comparison of diverse measurements is performed by the integrated area or the normalised peak intensity (black dashed line) as a function of the iron speciation by an independent method (colorimetric micro determination). The LF/HF (integrated area) is presented as a function of the iron speciation (figure 75). The halogen-free and -bearing glasses show a linear decrease in the LF/HF (integrated areas) due to increasing Fe^{2+}/Fe_{total}. A clear differentiation between the halogen-free and –bearing basaltic glasses does not appear.

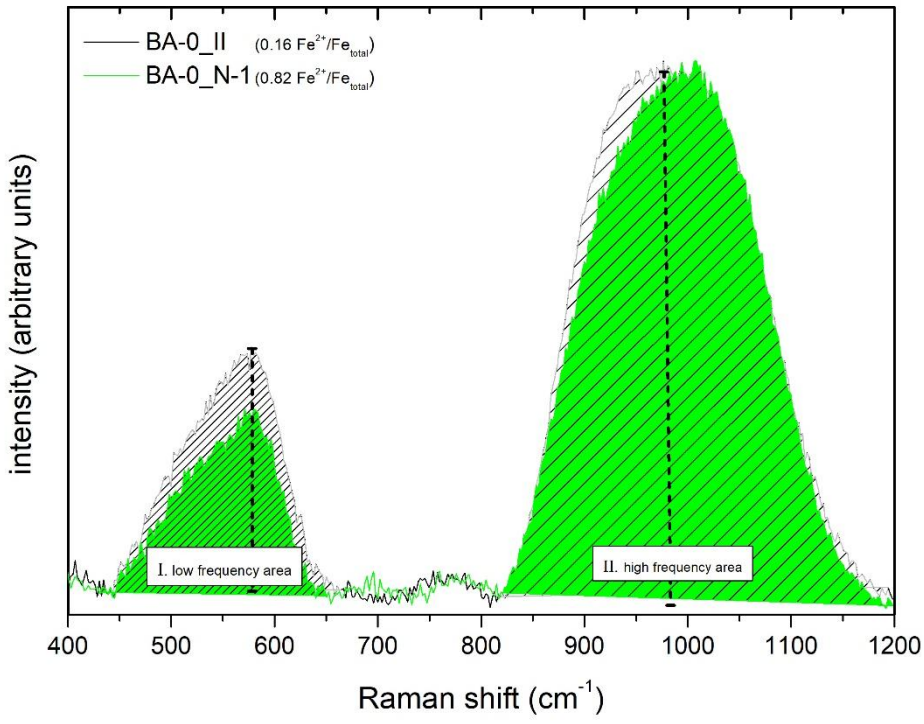

Figure 74: Raman spectra after a baseline and Long correction of halogen-free basaltic glass with a logarithmic oxygen fugacity of -4.97 (_N3) and -8.97 (_N-1). The vertical dashed lines show the low-frequency area (I) and the high-frequency area (II) as well as the peak height.

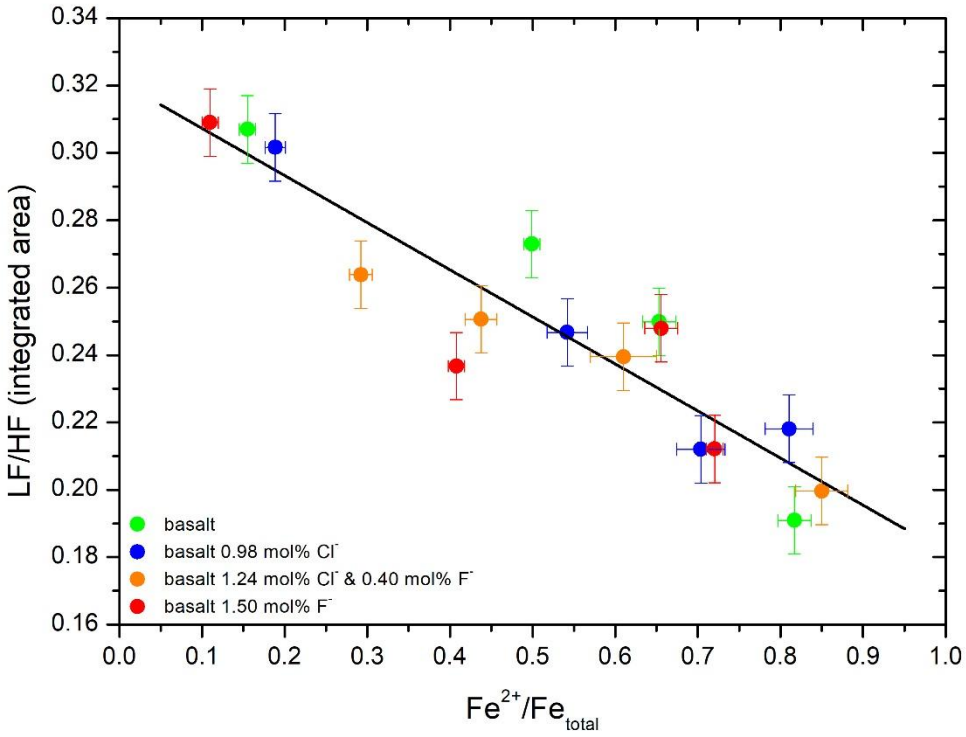

Figure 75: Effect of redox state on the LF/HF (integrated area) of halogen-free and halogen-bearing basaltic glasses.

In addition to the integrated areas, the normalised intensity ratios (LF/HF) decrease with increasing iron speciation (figure 76). The plot demonstrates that the present basaltic glasses follow a linear regression. The halogen-bearing basaltic glasses show a decrease in the intensity ratio, whereby a specific regression can be created for each composition. These linear regressions enable an estimation of iron speciation in unknown samples by means of non-destructive Raman analysis. The addition of chlorine and (Cl^- + F^-) to basaltic glasses results in an increase in LF/HF due to decreasing NBO/T (0.37), whereas the presence of fluorine results in a decrease in LF/HF (NBO/T ~ 0.40) compared to halogen-free basaltic glasses (NBO/T ~ 0.38).

In this context, the present basaltic glasses were compared to natural basalts like samples from Etna and Stromboli (Di Muro et al. 2009). In figure 77, the Etna basalts shows a similar slope as the present basaltic glasses, whereas the Stromboli basalts does not reflected a decrease in intensity ratio as a function of the iron speciation. The natural samples show a higher iron content (~ 7-10 wt%) compared to the present basaltic glasses (~ 5 wt%). The Stromboli samples show a smaller intensity ratio (LF/HF) due to a higher Fe/Al effect compared to the present basaltic glass (Di Muro et al. 2009). To conclude, the iron total content affects the intensity ratio (LF/HF) as well as the Fe/Al ratio.

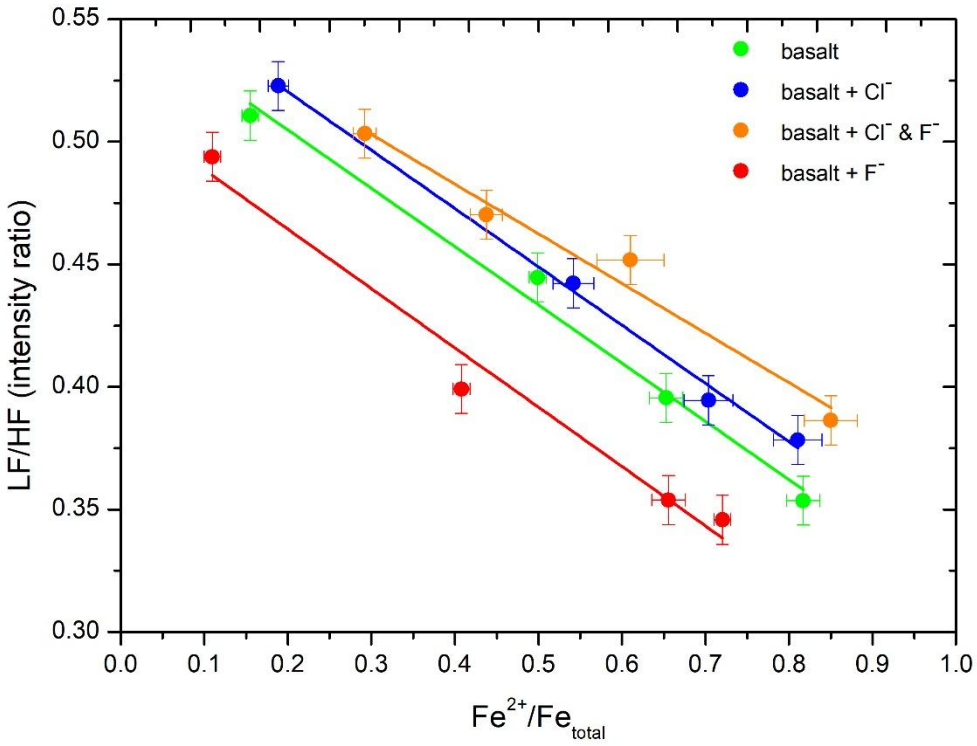

Figure 76: Effect of iron speciation on the LF/HF intensity ratio of halogen-free and halogen-bearing basaltic glasses.

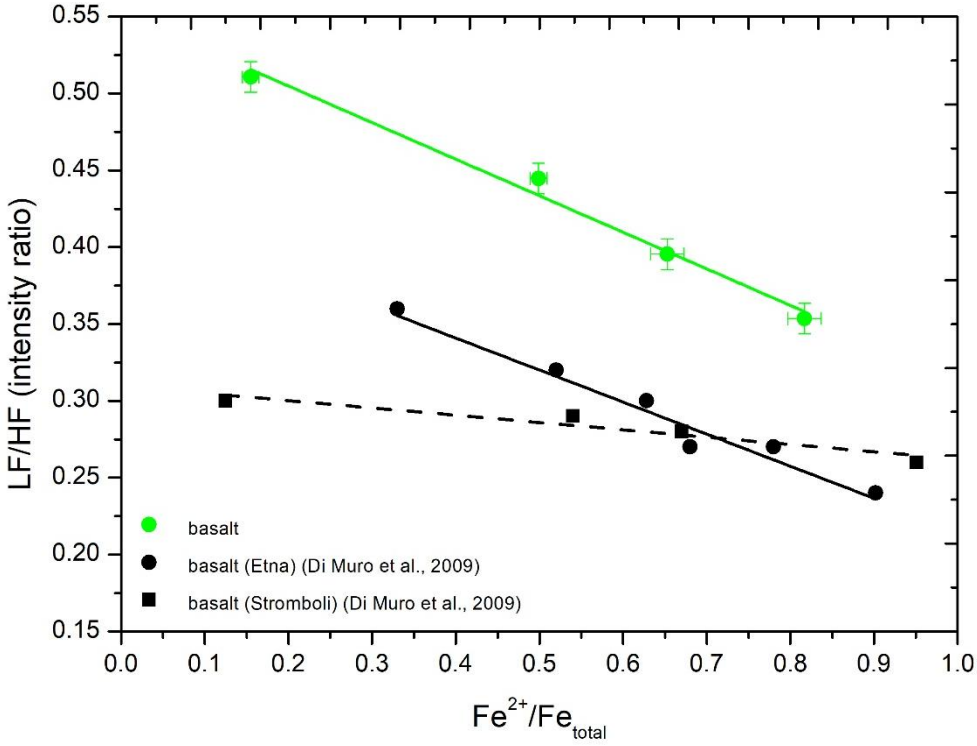

Figure 77: Comparison of the present data (green circles) with the calibration lines from (Di Muro et al. 2009) to natural samples from the Etna and the Stromboli (black symbols).

The HF band of Raman spectra can be analysed in detail with the Gauss curve-fitting model. The bands can be classified as individual species compared to the literature data (McMillian 1984; Mysen 1999; Di Muro et al. 2009; Rossano and Mysen 2012). Figure 78 represents the most reduced halogen-free basaltic glasses (BA-0_N-1) with the classification in five species using the literature description (Furukawa et al. 1981; Mysen 1999, 2007; Di Muro et al. 2009). Di Muro et al. (2009) indicated the bands II to VII as the Q^n units, where *n* is the number of bridging oxygens (BO). The band VII around 1150 cm^{-1} does not occur due to an over-fitting as well as the negative effect of other bands. The BOs compounds by the symmetric T-O stretching vibrations (Furukawa et al. 1981). Wang et al. (1993) describe the symmetric stretching band from Q^1 species as the band II (~894 cm^{-1}), the Q^2 species as the band III and IV (~942 and 985 cm^{-1}) as well as the Q^3 species as the band V and VI (~1035 and 1097 cm^{-1}). The peak shift in the high frequency range is induced by the increase of band III as well as a decrease of band V due to the iron speciation (figure 61). Di Muro et al. (2009) proposed that the band III around ~ 935 cm^{-1} is sensitive by increasing Fe^{3+}/Fe_{total}. This is shown by the comparison of the most oxidised and reduced basaltic glasses, which reflects a peak shift at the maximum from 950 cm^{-1} (oxidised glass) to 1020 cm^{-1} (reduced glass). Figure 79 reflects the most oxidised basaltic glasses with the classification in four species using the literature description (Furukawa et al. 1981; Mysen 1999, 2007; Di Muro et al. 2009). The IV around 985 cm^{-1} and the VI peak around 1097 cm^{-1} is overlapped by the V peak (1025 cm^{-1}). Thus, the IV and VI peaks will not be displayed for the oxidised basaltic glass in figure 79. The band III (~942 – 945 cm^{-1}) shows an increase in intensity due to increasing Fe^{2+}/Fe_{total}. The band I and II of the oxidised basaltic glass are combined to the band II in the reduced glass, whereas no intensity change can be discussed. Therefore, the band III around 942 to 945 cm^{-1} can be used to introduce a distinction between oxidised and reduced basaltic glass.

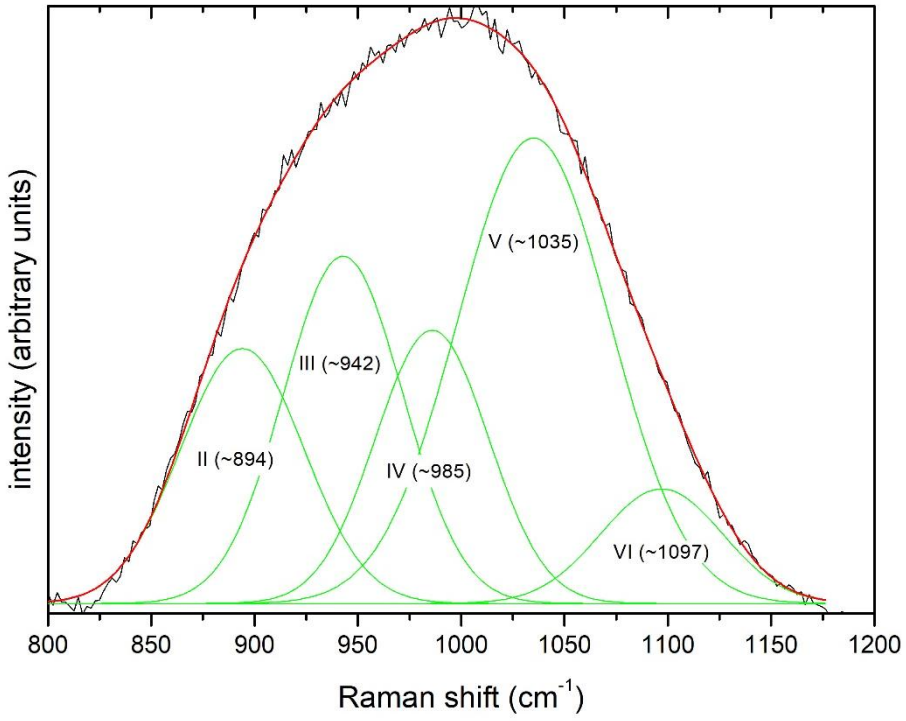

Figure 78: Curve-fitted Long-corrected Raman spectra of the most reduced basaltic glasses BA-0_N-1 with five typical bands (green line) in the high frequency area.

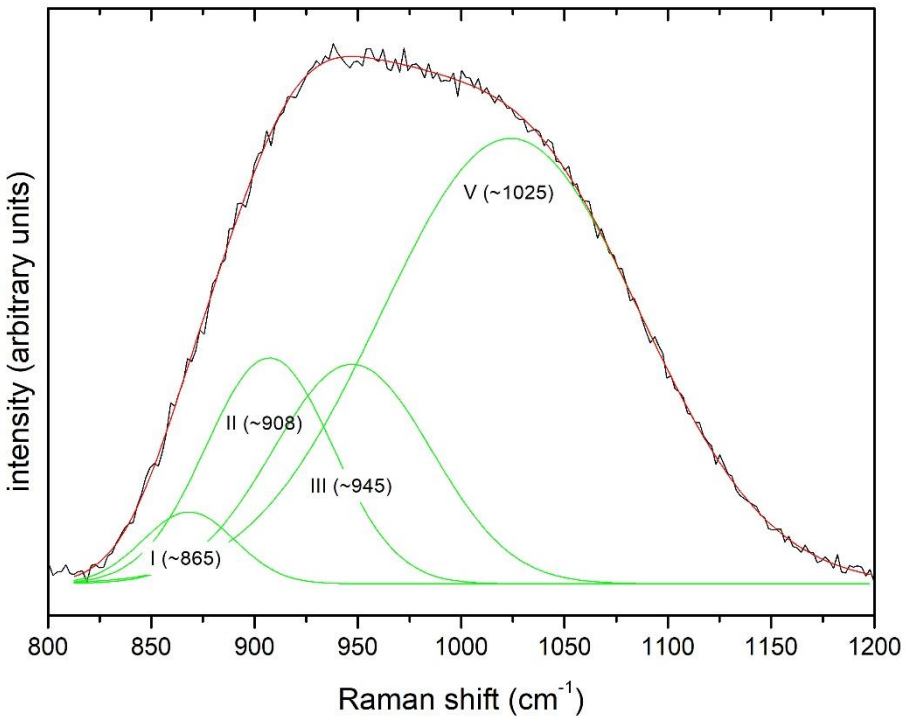

Figure 79: Curve-fitted Long-corrected Raman spectra of the most oxidised basaltic glasses BA-0_II with four bands (green line) in the high frequency area.

5.3. Effect of iron redox condition on the viscosity

Liebske et al. (2002) discussed the influence of iron redox condition on the viscosity of andesitic melt. The authors have investigated the transformation of ferric to ferrous iron due to the reducing condition. The decreasing fO_2 results in a decrease in viscosity by 0.3 log units for halogen-bearing basaltic melts investigated in this study (figure 64). This decreasing viscosity results from the conversion of a network-building Fe^{3+} to a network-modifying Fe^{2+}, whereby the network structure is depolymerised. This decreasing viscosity is enhanced by 0.8 to 1.0 log units due to the presence of halogens in basaltic melts. To conclude, the increasing Fe^{2+}/Fe_{total} in basaltic melts decreases the viscosity by 0.3 log units in the high viscosity regions from $10^{8.5}$ to $10^{13.5}$ Pa s.

5.4 Comparison with recent models

5.4.1. Model for the calculation of Fe^{2+}/Fe_{total}

A comparison of diverse iron analysis and the calculated Fe^{2+}/Fe_{total} after Kress and Carmichael (1991) is presented in table 21 and figure 80. The calculation is based on the part A section 4.3.3. (Calculation of Fe^{2+}/Fe_{total} after Kress and Carmichael (1991)). The calculated Fe^{2+}/Fe_{total} (0.15) for halogen-free basaltic glass synthesised in air at 1 atmosphere correlates well with the measured iron speciation of 0.16 ± 0.01 by wet chemistry. The calculated Fe^{2+}/Fe_{total} of halogen-bearing glasses show a lager deviation from the measured Fe^{2+}/Fe_{total} (wet chemistry). Thus, the model cannot be applied to halogen-bearing basaltic glasses, because the model does not consider Cl^- and F^-.

Table 21: Comparison of the Fe^{2+}/Fe_{total} from wet chemistry method and the calculated values after Kress and Carmichael (1991).

Sample	Fe^{2+}/Fe_{total}	
	calculated [a]	wet chemistry
BA-0-II	0.15	0.16
BA-0_N3	0.56	0.50
BA-0_N1	0.76	0.65
BA-0_N-1	0.88	0.82
BA-Cl-II	0.15	0.19
BA-Cl_N3	0.49	0.54
BA-Cl_N1	0.70	0.70
BA-Cl_N-1	0.84	0.81
BA-Cl-F-II	0.15	0.29
BA-Cl-F_N3	0.49	0.44
BA-Cl-F_N1	0.70	0.61
BA-Cl-F_N-1	0.85	0.85
BA-F-II	0.15	0.11
BA-F_N3	0.49	0.41
BA-F_N1	0.71	0.66
BA-F_N-1	0.85	0.72

[a] calculated from Kress and Carmichael (1991)

Figure 80 shows a comparison of the Fe^{2+}/Fe_{total} iron ratios of wet chemistry data versus calculated values. The iron ratios of the halogen-free and halogen-bearing basaltic glasses follow the 1:1 solid line, but some values show a large deviation from this line. The model of Kress and Carmichael (1991) does not consider all components and especially the halogens. Therefore some measured values indicate an overestimation or underestimation by the model. The halogen-free basaltic glasses with a Fe^{2+}/Fe_{total} of 0.16 (wet chemistry) and 0.15 (calculation) shows the best results. The increasing Fe^{2+}/Fe_{total} of wet chemistry reflects an overestimation for the halogen-free basalt as well as the fluorine and (Cl^- + F^-)-bearing glasses. An exception indicates the chlorine-bearing basaltic glasses, which show a good correlation with the model.

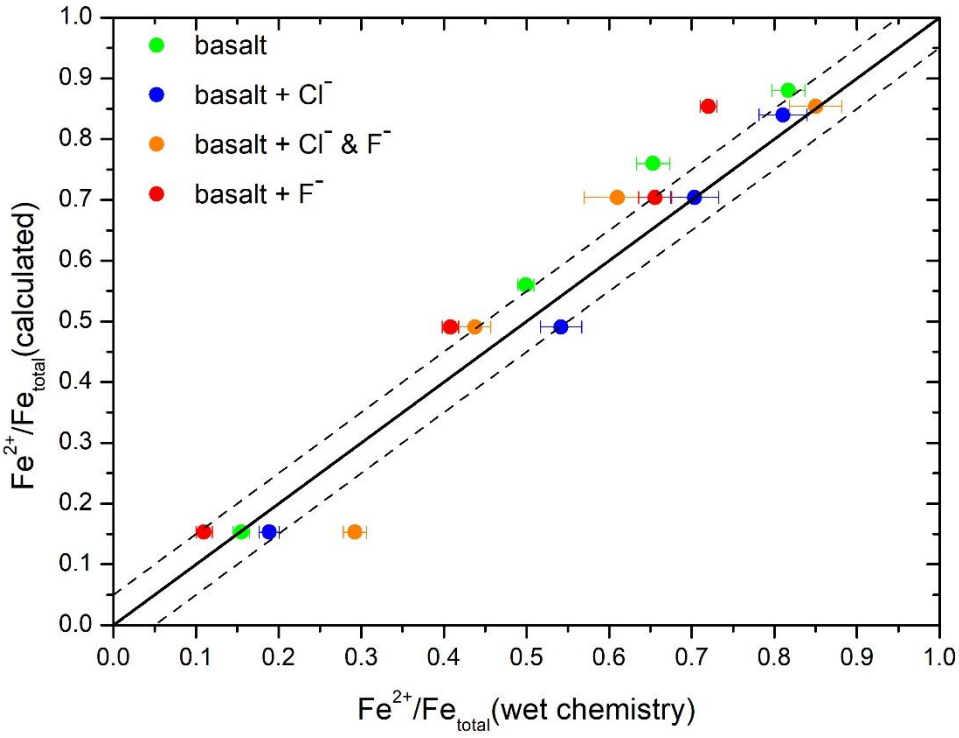

Figure 80: Fe^{2+}/Fe_{total} by wet chemistry versus data calculated from Kress and Carmichael (1991). Solid line represents 1:1 ratios, whereas the dashed lines indicate the interval ± 0.05.

5.4.2. Models for the calculation of viscosity

The comparison of the present experimental viscosity data with literature models enables an estimation of the influence of diverse parameters on the viscosity of melts. Generally, the largest effect on the viscosity results from the glass composition, whereas the model does not consider all elements like the halogens. Figure 81 represents a comparison of the measured viscosity with calculated viscosity values from a model after Giordano et al. (2008). The model shows a good correlation with the halogen-free basaltic melt accompanied by the varied Fe^{2+}/Fe_{total}. Furthermore, the addition of halogens to the present basaltic melts is partially in accordance with the model by Giordano et al. (2008). We observed differences between measured and calculated viscosities of the most reduced fluorine-bearing melts (BA-F_N-1) and the most oxidised chlorine-bearing melts (BA-Cl_N3). Consequently, the viscosity is not only a function of fluorine and water content but also Fe^{2+}/Fe_{total} and chlorine content. Therefore, the deviation results by not respect of chlorine and iron speciation.

Furthermore, the viscosity model by Duan (2014) is demonstrated the figure 82. This model represents the iron speciation in melt but it neglects the halogen contents. The model does not work for the viscosity of halogen-free and –bearing melts despite the iron ratio in the glasses. All samples are significantly underestimated by the model of Duan (2014). A

particularly conspicuous aspect is the higher viscosity of reduced samples (rectangles) compared to the oxidised ones (circles).

Sehlke and Whittington (2016) proposed a viscosity model with the focus on Fe^{2+}/Fe_{total}. Figure 83 represents a comparison of the measured viscosity with calculated viscosity values from a model after Sehlke and Whittington (2016). The model shows a good correlation with all redox equilibrated melts of series II. Therefore, the model can be used for our redox equilibrated samples for a viscosity range between 10^7 and 10^{14} Pa s.

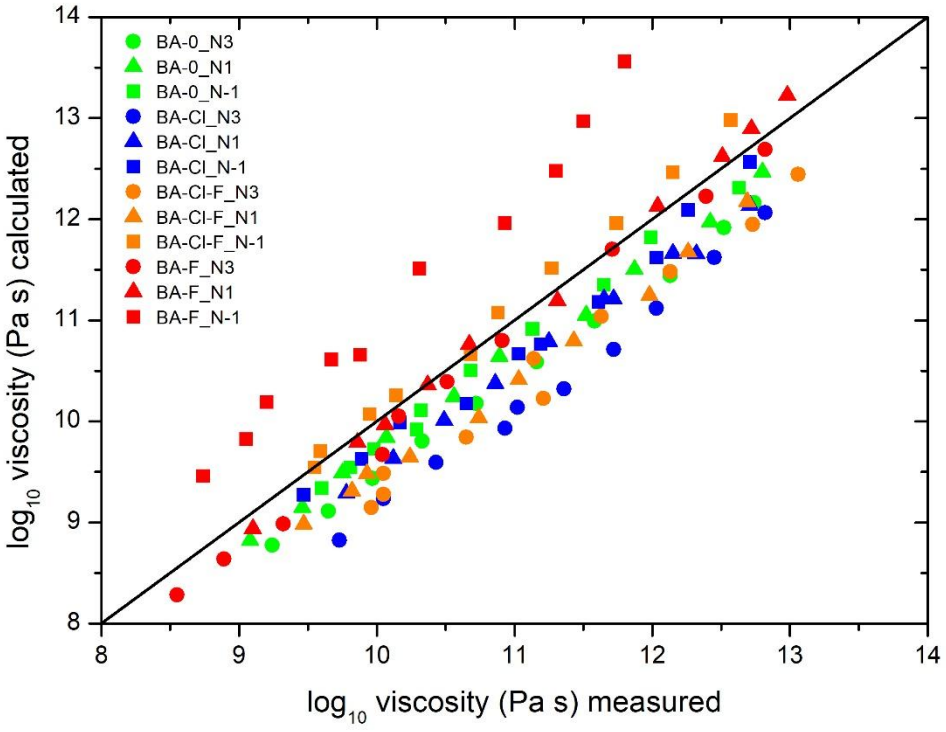

Figure 81: Comparison of the measured viscosity with the calculated data from model of Giordano et al. (2008). The error bars are smaller than the circles.

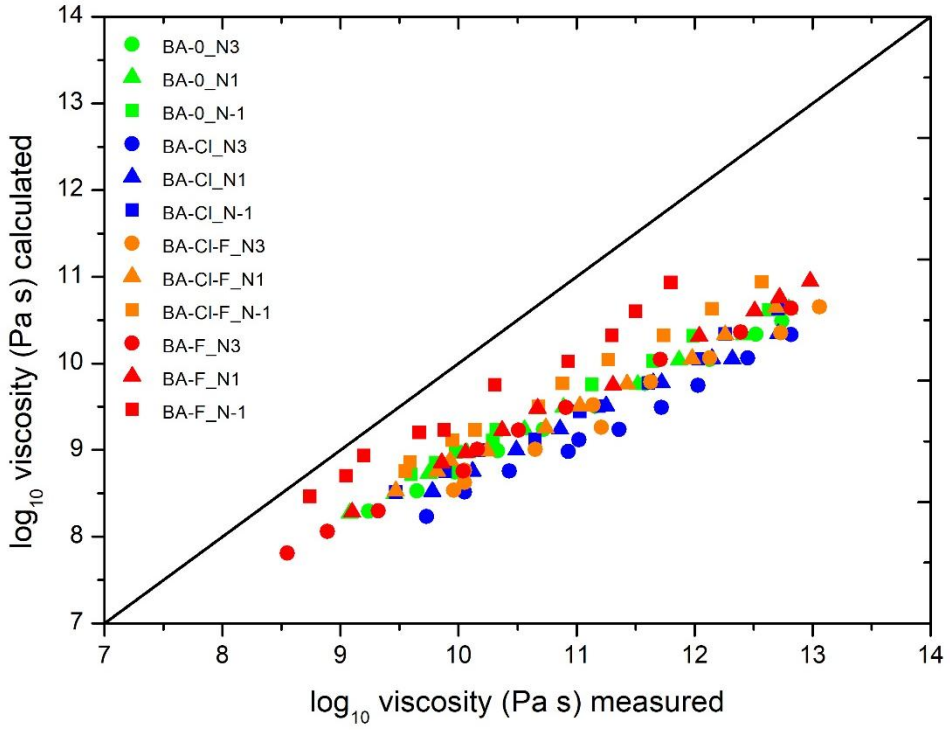

Figure 82: Comparison of the measured viscosity with the calculated data from model of Duan (2014). The error bars are smaller than the circles.

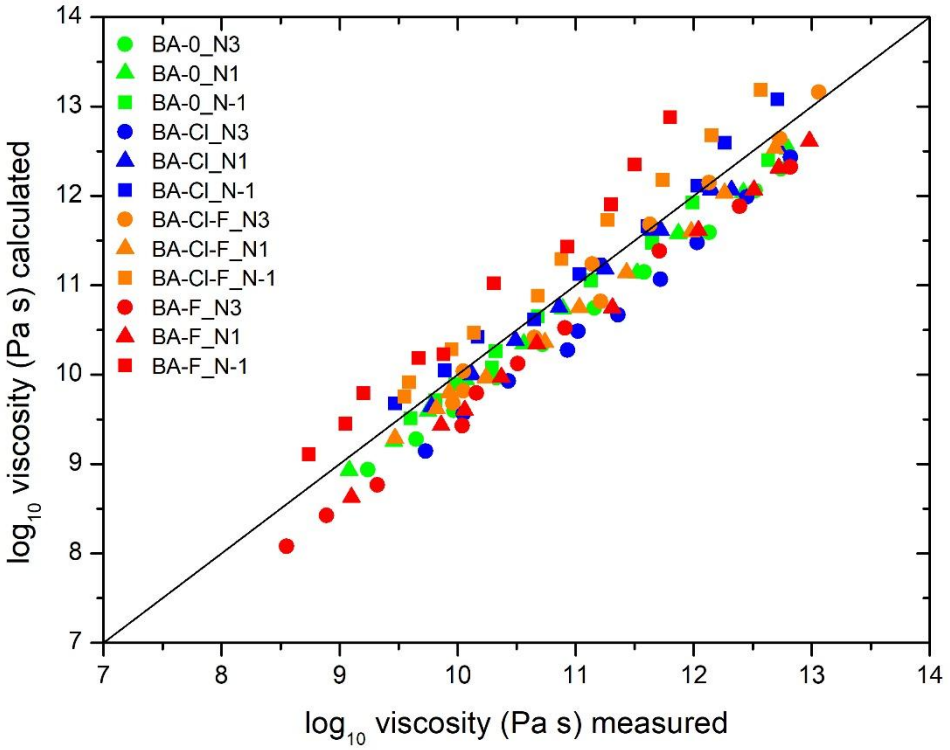

Figure 83: Comparison of the measured viscosity with the calculated data from model of Sehlke and Whittington (2016). The error bars are smaller than the circles.

5.4.3. Models for the calculation of heat capacity

Figure 84 shows a comparison of the measured and calculated heat capacities (Stebbins et al. 1984; Richet and Bottinga 1984; Lange and Navrotsky 1992; Richet 1987) for basaltic melts synthesised at increasing oxidising condition. The halogen-free basaltic melt correlates well with the calculated C_{pg} (rhombus symbols - Richet 1987). Furthermore, the model for C_{pl} (Stebbins et al. 1984; Lange and Navrotsky 1992; Richet and Bottinga 1984) is consistent with the measured heat capacities. Compared to the halogen-bearing melts, the calculation of C_{pg} are overestimated by the model from Richet (1987) for all composition with the exception of BA-Cl_N1 (blue rhombus). Furthermore, the C_{pl} of fluorine-bearing basaltic melts are overestimated by the models (Stebbins et al. 1984; Lange and Navrotsky 1992; Richet and Bottinga 1984). The C_{pl} of chlorine-bearing melts is preferably underestimated by the models with the exception of BA-Cl_N1 due to higher chlorine content (blue circles, triangles and rectangles). Particularly, the C_{pl} of (Cl^- + F^-)-bearing melt corresponds well with the measured data, which results from the balancing effect of both halogens (orange circles, triangles and rectangles).

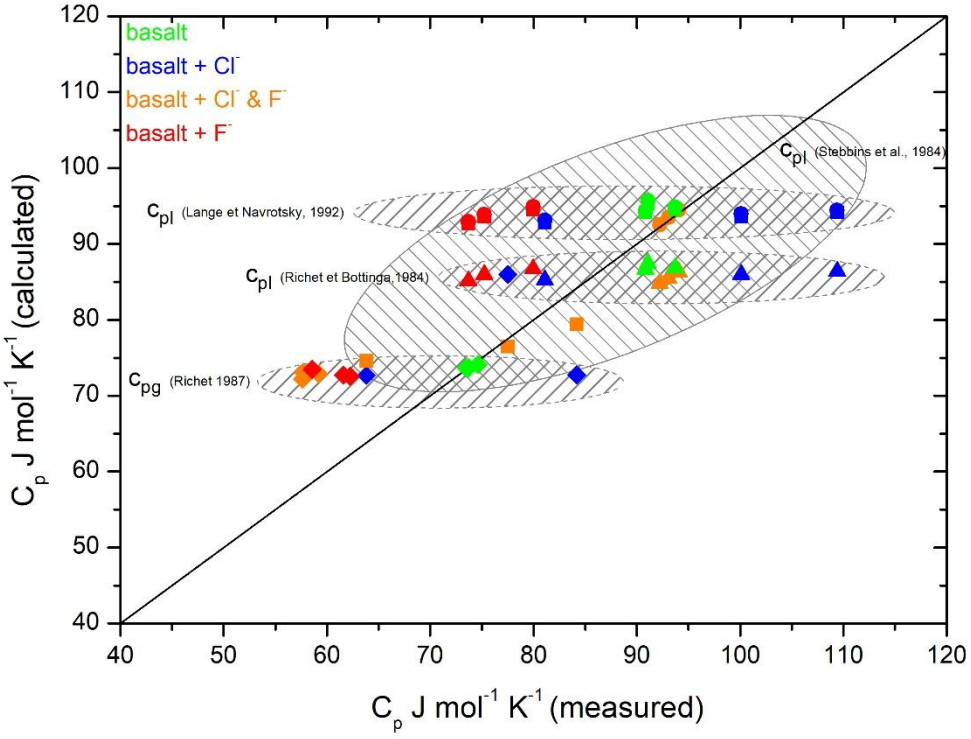

Figure 84: Comparison of calculated and measured heat capacity data of halogen-free and halogen-bearing basaltic glasses. The symbols represent a comparison between the measured and the calculated data from Stebbins et al. (1984) model (rectangles), Lange and Navrotsky (1992) model (circles), Richet and Bottinga (1984) model (triangles) and Richet (1987) model (rhombus). The error bars are smaller than the symbols.

6. Conclusion

This study illustrates the effect of the oxygen fugacity on the viscosity of halogen-free and -bearing basaltic melts. The experimental viscosity data as a function of redox for this basaltic melt confirms the literature data for simple melt compositions (Dingwell 1991; Liebske et al. 2002; Vetere et al. 2006; Duan 2014; Stabile et al. 2016). The increasing Fe^{2+}/Fe_{total} (0.16 to 0.82) results in a decrease in viscosity by 0.3 log units for a halogen-free basaltic melt at these high viscosity conditions. The addition of halogens to the present basaltic melts results in a larger decreasing effect by the iron speciation on the viscosity. The decreasing fO_2 results in an increase in Fe^{2+}/Fe_{total} due to the increase of network-modifying Fe^{2+} and decrease of network-building Fe^{3+} for halogen-free and –bearing basaltic glasses. On the basis of the conversion of Fe^{3+} to Fe^{2+}, we deduce a depolymerisation of the melt structure. These results are in close agreement with the Raman measurements, which show a decrease in intensity in the low frequency region due to increasing Fe^{2+}/Fe_{total}. Furthermore, the LF/HF intensity ratio as a function of the Fe^{2+}/Fe_{total} enables the understanding of different NBO/T, FeO_{total} content and Fe/Al on the melt structure. Our viscosity measurements suggest that the varied Fe^{2+}/Fe_{total} should be included in future viscosity models. This effect is included in viscosity model for basalt of Sehlke and Whittington (2016), whereas the model of Giordano et al. (2008) includes the effect of halogens.

The Fe^{2+}/Fe_{total} of natural melts reflect a combination of fO_2 and melting temperature at the source of the magma as well as the composition of the melt. If the melting temperature is known, the oxygen fugacity can be calculated by the Fe^{2+}/Fe_{total} of the magma source. On the basis of the viscosity data, a precise estimation of fO_2 of natural melts is difficult due to the effect of melt composition. Generally, the viscosity data is observed in comparison with the 1 atm or volatile-free melts. Thus, a small amount of the natural melts can be synthesised in a 1 atm furnace, whereby the viscosity can be determined and set in relation to the primal natural melts. As a result, this decrease in viscosity implies the oxygen fugacity at the source of the magma using the information that an increase in Fe^{2+}/Fe_{total} of 0.2 results in a decrease in viscosity by 0.1 log units.

Part C - The effect of combined volatiles on viscosity of the present MORB composition for glasses synthesised at constant redox conditions

1. Abstract

All glasses discussed in this chapter were synthesised in the Internally-heated pressure vessel (IHPV) at constant oxygen fugacity of log (fO_2) -3.56 to -2.56. Besides the halogen content and oxygen fugacity, the viscosity of basaltic melts also decreases by the presence of H_2O and CO_2. This range of values is set by the environment with in the IHPV. The experiments were conducted in IHPV at 1550 ± 10 K and 300 ± 5 MPa for 24 h. All samples were quenched with a 150 K/min quenching rate (rapid quench) in order to avoid the formation of quench crystals. This study illustrates the decrease in viscosity by 3.4 log units in H_2O-bearing basaltic melts (3.47 wt% H_2O) despite of the accompanying decrease in Fe^{2+}/Fe_{total} from 0.60 to 0.19. In comparison to the presence of H_2O, the increasing CO_2 content (2199 ppm CO_2) in basaltic melts produces a smaller decrease in viscosity by 0.7 log units. But no evidence for a dependency of viscosity change on CO_2 and Fe^{2+}/Fe_{total} was detected. Compared to the 1 atm basalt (0 wt% H_2O), the *dry* basalt (~ 0.10 wt% H_2O) synthesised at 3 kbar shows a decrease in viscosity by 2.0 log units. A further point to note is that the samples synthesised in IHPV always contain small water contents around 0.10 wt% H_2O, which results in a decrease in viscosity by 0.2 log units. This difference on viscosity between the melt synthesised in air and in the IHPV is a result of changing Fe^{2+} speciation. Furthermore, the normalised intensity ratio (LF/HF) as a function of Fe^{2+}/Fe_{total} of the Raman spectroscopy enables a differentiation between hydrous and redox equilibrated halogen-free and –bearing basaltic melts.

2. Introduction

We have studied the effect of water on rheology and structure of halogen-free and –bearing basaltic melts. The rheology of basaltic magmas is not only a function of water content but also iron speciation as well as the halogen content. The viscosity of melts controls magma degassing and eruption styles of volcanoes (Black et al. 2012). Besides halogens, natural basaltic magmas contain water and carbon dioxide. Danyushevsky (2001) observed water contents from 0.1 to 1.0 wt% in basaltic magmas from mid-ocean ridge. The highest H_2O concentration (up to 6 wt%) is found in basalts from Island Arc (Wanless et al. 2011). Cartigny et al. (2008) measured CO_2 contents up to 57 000 ppm in MORB samples from mid-Atlantic ridge.

There is extensive literature concerning the role of water and fluorine on the viscosity of silicate melts (Dingwell and Mysen 1985; Giordano et al. 2004; Vetere et al. 2006; Giordano et al. 2008; Bartels et al. 2013; Baasner et al. 2013b; Robert et al. 2015). These authors have demonstrated that the addition of H_2O and F^- to silicate melts results in a strong decrease in viscosity. Some studies have examined the role of CO_2 on the viscosity of silicate melts (Brearley and Montana 1989; White and Art; Bourgue and Richet 2001; Morizet et al. 2007; Di Genova et al. 2014; Robert et al. 2015). These earlier studies have reported different viscosity results. The addition of CO_2 to latitic melts results in a small decrease in viscosity (Di Genova et al. 2014). Robert et al. (2015) suggested that the addition of CO_2 to silicate melts does not clearly affect the viscosity. This study was conducted in order to measure the viscosity of H_2O and CO_2-bearing halogen-free and –bearing basaltic glasses. If carbon © exists in silica-rich melts as CO_2, it is not part of the melt structure and will not affect the viscosity. In basaltic melts, C exist as CO_3 and is incorporated in the melt structure (Fine and Stolper 1985; Ni and Keppler 2013). Thus, the effect of CO_2 on the viscosity depends on the melt composition.

3. Experimental methods

3.1. Starting materials

Four glasses were prepared from a mixture of oxides, carbonates and halogens for the synthesis of hydrous glasses. The dry glasses were melted for 4 to 9 h at 1473 K in a Pt crucible in 1 atm $MoSi_2$ furnace. The chapter A section (3.1. Starting materials) shows a detailed description of the synthesis procedure. Table 22 represents the chemical composition of the dry starting materials.

Table 22: Chemical composition of the starting glasses of series III analysed by electron microprobe. The analysis of each glass is based on the average of 10 measurements.

Oxides/ions mol%	BA-0-III	BA-Cl-III	BA-Cl-F-III	BA-F-III
SiO_2	55.25 ±0.15	53.72 ±0.15	52.02 ±0.14	52.49 ±0.16
Na_2O	4.53 ±0.05	3.59 ±0.04	3.79 ±0.04	4.36 ±0.05
K_2O	0.17 ±0.02	0.10 ±0.01	0.12 ±0.02	0.16 ±0.02
TiO_2	1.06 ± 0.03	1.04 ±0.03	1.00 ±0.02	0.99 ±0.03
FeO	2.44 ±0.06	2.33 ±0.06	2.49 ±0.08	2.29 ±0.06
Al_2O_3	9.45 ±0.09	9.20 ±0.08	8.89 ±0.10	8.99 ±0.09
MgO	12.71 ±0.07	12.22 ±0.07	11.96 ±0.05	12.13 ±0.06
CaO	14.21 ±0.09	13.99 ±0.08	13.50 ±0.09	13.51 ±0.09
MnO	0.17 ±0.02	0.15 ±0.03	0.16 ±0.03	0.16 ±0.02
Cl^-	0.01 ±0.01	3.65 ±0.04	3.90 ±0.02	0.01 ±0.01
F^-	0.00 ±0.01	0.00 ±0.01	2.18 ±0.03	4.90 ±0.04
γ [1]	0.78	0.77	0.78	0.78
NBO/T [2]	0.315	0.314	0.326	0.315
NBO/T [3]	0.316	0.370	0.422	0.392

[1] *γ is an indicator for the degree of polymerisation of the melt (Webb et al. 2014)*

$\gamma = (Na_2O + K_2O + MnO + FeO + CaO + MgO) / (Na_2O + K_2O + MnO + FeO + CaO + MgO + Al_2O_3 + Fe_2O_3)$

[2] *NBO/T calculated without halogens (chlorine and fluorine)*

[3] *NBO/T calculated assuming NBO/T calculated assuming* $2Cl^- = 1O^{2-}$ *or* $2F^- = 1O^{2-}$

3.2. Synthesis of H_2O-CO_2-bearing glasses

The aim was to produce halogen-free and –bearing basaltic glasses with the addition of 1000 to 2500 ppm of CO_2 and 0.50 to 3.50 wt% of H_2O. For synthesis of carbon-bearing and hydrous glasses, 200 mg of basaltic glass powder with specific amounts of silver oxalate ($Ag_2C_2O_4$) or distilled water were loaded into $Au_{75}Pd_{25}$ capsules (20 mm length, 4 mm diameter, 0.2 mm wall thickness). The capsules were closed with a PUK welding device from Lampert GmbH. Furthermore, the capsules were heated up to 383 K in a drying furnace for

test of weight loss (leak test). The experiments were performed into the Internally-heated pressure vessel (IHPV) at 1550 ± 10 K and 300 ± 5 MPa for 24 h using argon as pressure medium.

The sample temperature was checked by three thermocouples, which are located at the top of the samples as well as below and above the capsules (limitation of heating zone). For each experiment, six capsules were placed into two Pt crucible and hung on a thin Pt wire, which was melted with a current pulse. This method allows an isobarically cooling process with a rapid 150 K/min quenching rate (rapid quench). Berndt et al. (2002) described the apparatus with the rapid-quench device in detail.

4. Analytical methods

4.1. Water content determination

4.1.1. Thermogravimetry

Determination of the water content in the present CO_2-free glasses was performed using the Setaram TGA 92. The method is based on the weight loss of the glasses as a consequence of the sample heating with 10 K/min to 1473 K (Schmidt and Behrens 2008). 15 to 30 mg glass powder is filled in a platinum crucible and hung up on the thermos-balance (figure 85). The weight of the water-bearing glasses were measured as a function of temperature in air. The buoyancy effect of air at high temperature was corrected by a blank measurement. The precision of the analysis was checked by a double measurement. This method can be used to produce a calibration of the extinction coefficient for the determination of water speciation, which is measured by the infrared spectroscopy.

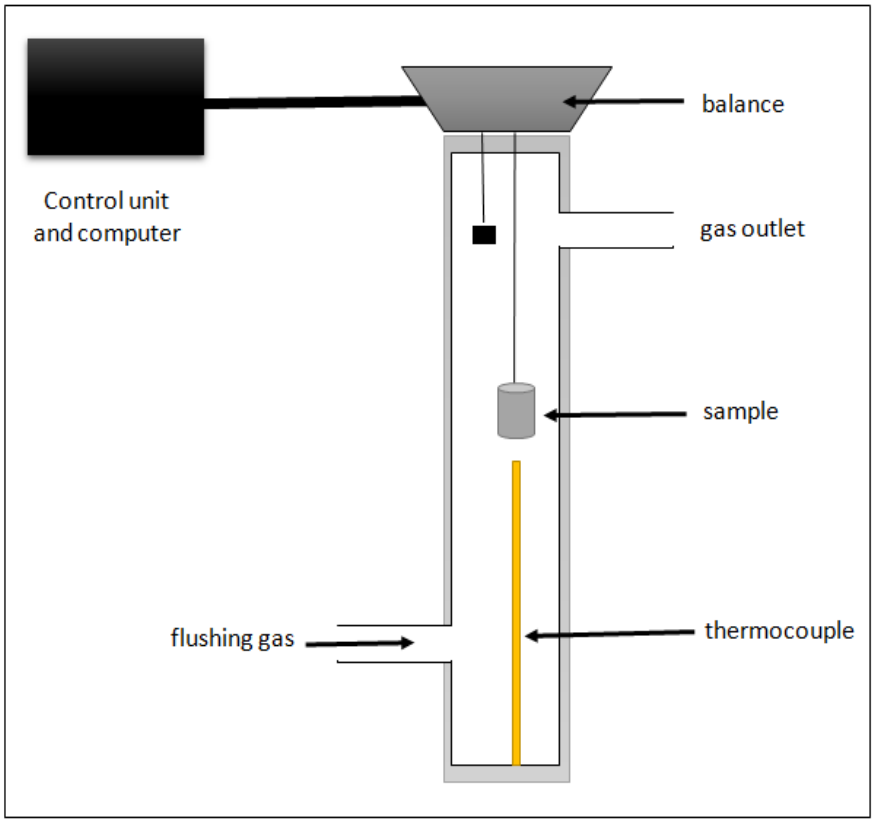

Figure 85: Schematic illustration of Setaram TGA 92, modified after Yang et al. (2012).

4.1.2. Infrared spectroscopy – Near-infrared spectra (NIR)

The Fourier Transform Infrared Spectroscopy (FTIR) enables a qualitative indication of molecular structures by means of the position and intensity of substance-specific absorption bands. Furthermore, the combination of the near-infrared spectra with thermogravimetry (an extern method) allows the calculation of the water speciation in glasses. The NIR spectra were measured using a Fourier Transform Infrared spectrometer (type Bruker Vertex 70) (figure 86) and IR microscope (Hyperion 3000). The samples were double polished and have a thickness of 300 µm, which was determined by a digital micrometer (type Mitutoyo) with a precession of 3 µm. Each three NIR spectra were acquired with 100 scans and a spectral resolution of 2 cm^{-1}. The near infrared spectra were collected in the range of 4000 to 12500 cm^{-1}, which describes the fundamental vibrations. The triatomic and angled water molecule has three fundamental vibrations like the deformation vibration as well as the symmetric and asymmetric valence vibrations. The band at 4500 cm^{-1} describes the OH groups related by tetrahedral cations and the band around 5200 cm^{-1} reflects the H_2O molecules (Stolper 1982a, 1982b; Behrens et al. 1996). The determination of absorbance A_λ is based on the Beer-Lambert Law, which describes the relation of extinction coefficient ε_λ, water concentration c and sample thickness d (Behrens et al. 1996).

$$A_\lambda = \varepsilon_\lambda * c * d \qquad \textit{Equation 13}$$

The ε_λ can be calculated with the following equation:

$$\varepsilon_\lambda = \frac{M_{H2O} * A_\lambda}{d * \rho * c_t} \qquad \textit{Equation 14}$$

where M_{H2O} describes the molar mass of H_2O, ρ is the glass density and c_t represents the water content of the thermogravimetry measurements (on the CO_2-free glasses). The calculated extinction coefficients of the OH groups against H_2O molecules represent a calibration line. The axis intercept enables the calculation of the water speciation with the following equation (Behrens et al. 1996; Yamashita et al. 2008).

$$c_{OH\ or\ H_2O} = \frac{M_{H2O} * A_\lambda}{d * \rho * \varepsilon_\lambda} \qquad \textit{Equation 15}$$

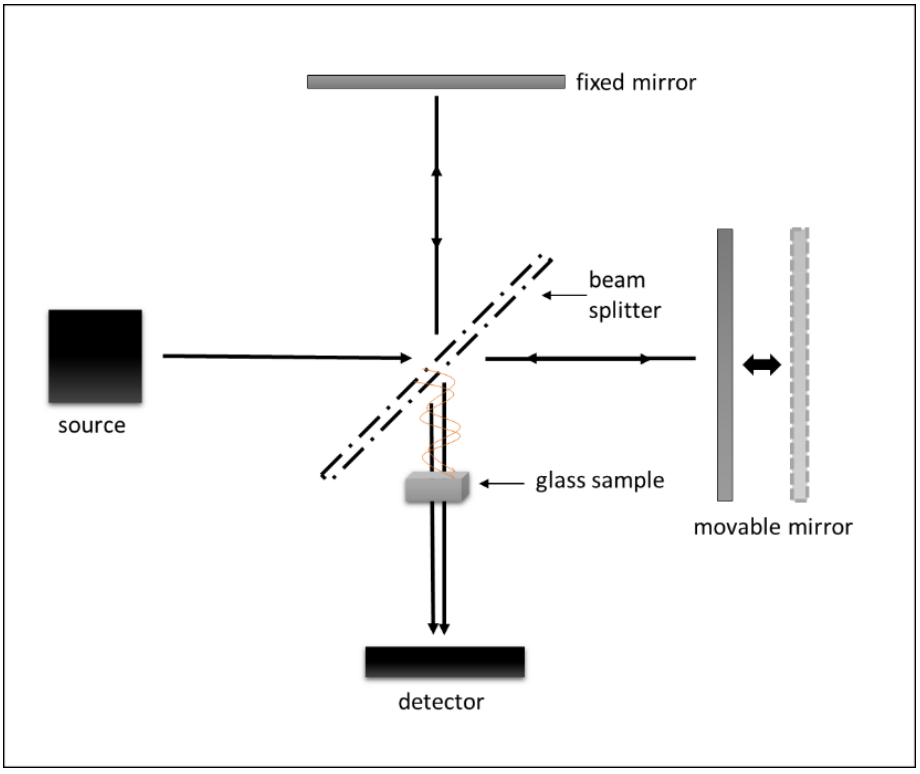

Figure 86: Schematic illustration of Michelson interferometer, modified after Harris (2014).

4.2. Carbon determination

4.2.1. CS Analysis

The carbon contents were measured using the carbon and sulphur analyser from Elementar (figure 87). The glass powders were weighed into a ceramic crucible together with the two accelerators (Fe and W-Sn), which support the melting and oxidizing of the glass samples. The samples were heated up to 2273 K in an oxygen atmosphere, whereby the carbon and sulphur is oxidised. The gases are purified to determine the intensities of CO_2 and SO_3 by two infrared detectors. The signals are converted into the concentration of CO_2 and SO_3. For

each measurement session a “day factor” machine sensitivity is determined and a calibration with five standards was conducted. The standards have a concentration of carbon of 43, 154, 262, 489 and 4240 ppm. The CS data are used to determine the extinction coefficient for the calculation of the carbon speciation by the infrared spectroscopy.

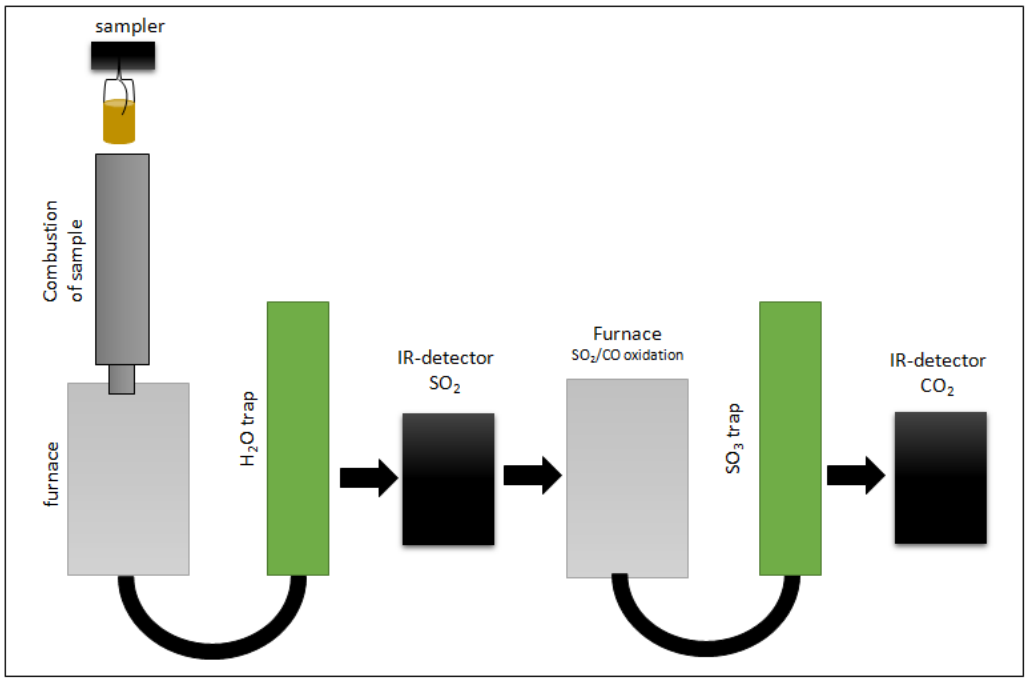

Figure 87: Schematic illustration of carbon and sulphur analyser based on the description of Elementar Analysensysteme GmbH (2016).

4.2.2. Infrared spectroscopy – Mid-infrared spectra (MIR)

The mid-infrared spectra were recorded in the range of 400 to 4000 cm^{-1} using a FTIR spectrometer and IR microscope. The glass pieces are double polished on a thickness of 150 µm, which was measured by a digital micrometer. The spectra were acquired with 100 scans as well as a spectral resolution of 2 cm^{-1}. Ni and Keppler (2013) described the occurrence of a carbon peak around 2350 cm^{-1} for molecular CO_2 and a double band in the range of 1350 – 1650 cm^{-1} for CO_3^{2-}. The MIR method is based on the Beer-Lambert Law (see section 4.1.2. Infrared spectroscopy – Near-infrared spectra (NIR)). The CO_2 content can be determined by the following equation, where M_{CO2} describes the molar mass of CO_2:

$$c_{CO_2} = \frac{M_{CO2} * A_\lambda}{d * \rho * \varepsilon_\lambda} \qquad \textit{Equation 16}$$

5. Results

5.1. Quantification of H_2O and CO_2 in the present basaltic glasses

5.1.1. Evaluation of H_2O spectra

The NIR spectroscopy was used for the quantification of H_2O in basaltic glasses. All glass pieces have been measured three times to check the reproducibility of each spectra. Furthermore, the homogeneity of the H_2O distribution was checked for individual glasses (figure 88). For this purpose, glass pieces (top, middle and bottom) were double polished with a thickness of 300 µm and measured with the NIR spectroscopy. The determination of water species is based on the peak height. The main absorption bands of molecular water are located around 5200 cm^{-1} and the OH groups are observed around 4500 cm^{-1} in the near-infrared (Scholze 1960; Stolper 1982a, 1982b). All glasses show a homogeneous H_2O distribution.

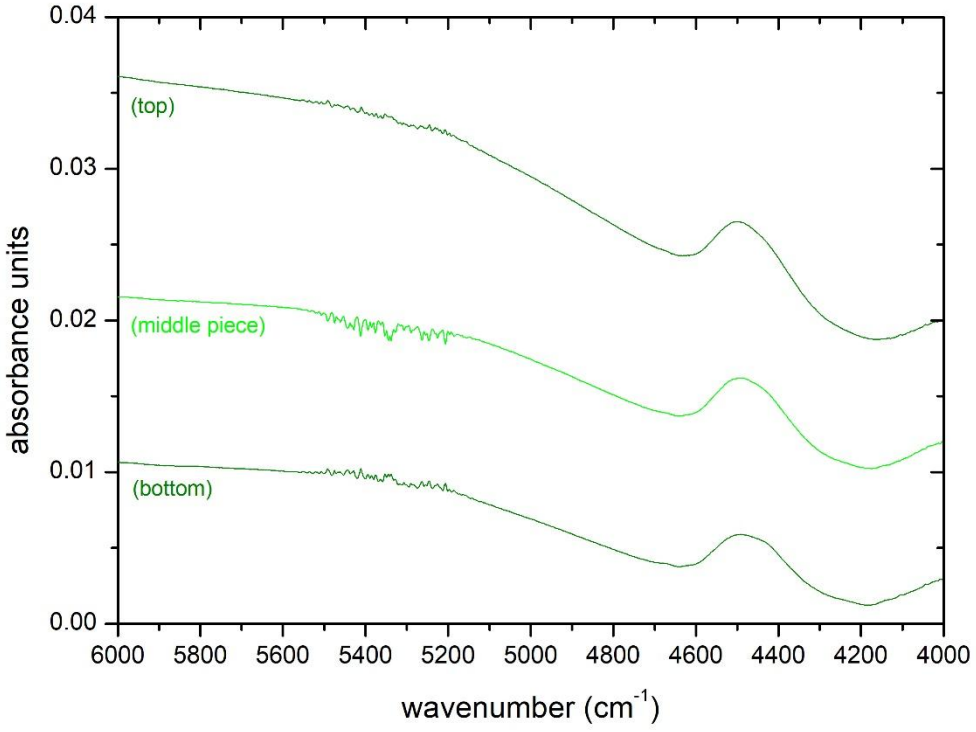

Figure 88: Three NIR-spectra of halogen-free basaltic glasses with the addition of 0.75 wt% H_2O (thickness between 305 and 298 µm).

NIR spectra of H_2O-free and -bearing basaltic glasses are shown in figure 89. The spectra experience a thickness correction as well as a subtraction of H_2O-free spectrum to highlight the differences. Furthermore, the spectra are corrected by a linear baseline in order to compare the diverse compositions. The addition of 0.73 wt% water to the present basaltic glasses results in an increase in peak intensities of OH groups around 4500 cm^{-1} and small

peaks form around 5200 cm^{-1}. The intensities of these peaks become stronger with increasing water content (1.29 and 3.47 wt% H_2O), which reflects the formation of molecular water. Furthermore, the increase of water results in an increase in peak intensities of hydroxyl groups (OH). Stolper (1982a, 1982b) and Behrens et al. (1996) suggested that the OH groups are associated by tetrahedral cations (Al, Si).

Figure 90 shows a comparison of the NIR spectra of the halogen-free and halogen-bearing basaltic glasses accompanied by the addition of water. The synthesis conditions are similar for all compositions (3 kbar, 1550 K, 24h). The spectra demonstrate that the strengths of the incorporation mechanism of water vary with the addition of halogens to the present basaltic glasses. Especially, the fluorine-bearing glass (BA-F_4.04H) shows a high intensity of the OH groups as well as the molecular water, whereas the glasses with combined halogens demonstrate the smallest intensities. This effect can be explained by the variation of density, which is not considered in the spectra.

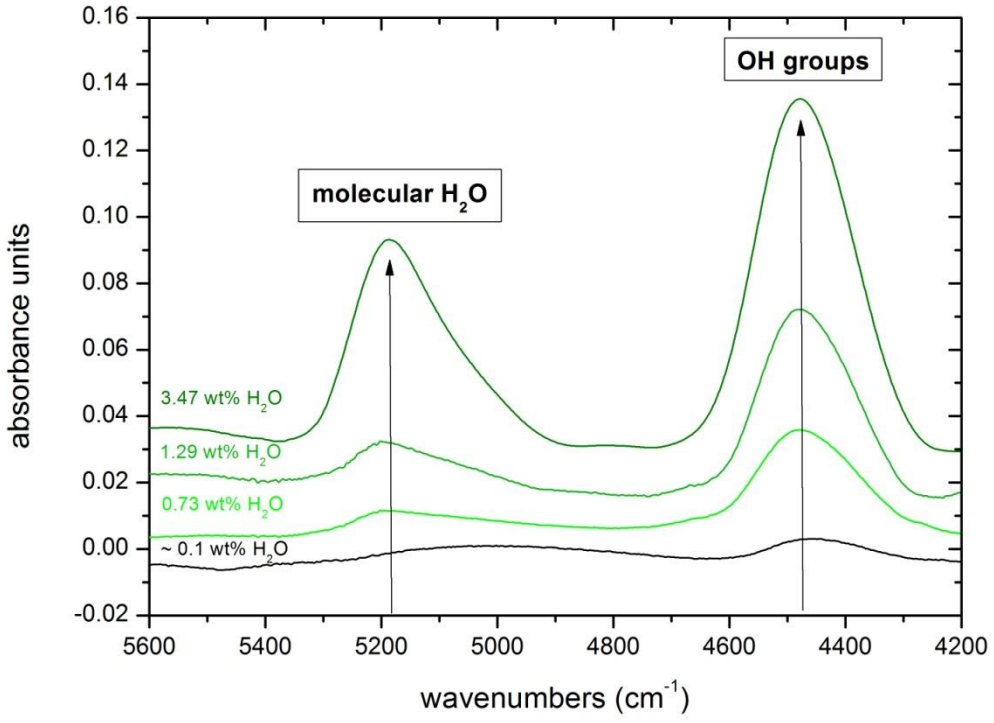

Figure 89: Near-infrared spectra (NIR) of H_2O-free and H_2O -bearing basaltic glasses. The spectra are normalised to the thickness and experienced a subtraction of the H_2O -free spectrum. The spectra are vertically shifted in order to clearly show the differences in peak height.

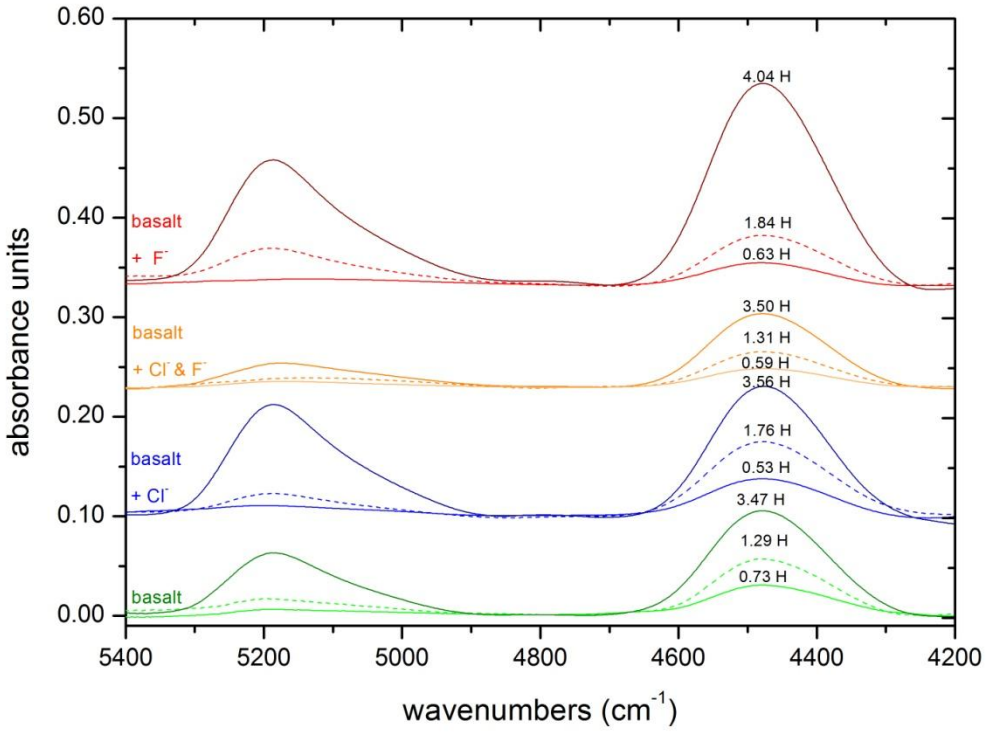

Figure 90: Comparison of NIR spectra of H_2O- and halogen-bearing basaltic glasses. The spectra are normalised to the thickness and experienced a subtraction of the H_2O -free spectrum. The spectra are vertically shifted in order to illustrate the changes in peak size.

5.1.2. Evaluation of CO_2 spectra

Konschak and Keppler (2014) described the two bands at 1520 cm^{-1} and 1430 cm^{-1} as antisymmetric stretching bands of the carbonate group. Figure 91 represents the mid-infrared spectra of the CO_2-free as well as the CO_2-bearing basaltic glasses. After a thickness correction, the spectra experienced a subtraction of the CO_2-free spectrum to highlight the differences. The 0.15 and 0.23 wt% CO_2-bearing basaltic glasses reflect the characteristic double peak. The peak intensities increase with increasing CO_2 content. Furthermore, the small peak at 2320 cm^{-1} in spectra of the CO_2-bearing glasses shows the presence of CO_2-molecules (Brey 1976). The solubility of CO_2 in silicate melts depends on pressure and temperature and is two orders of magnitude lower than the H_2O solubility (e.g. Shishkina et al. 2010).

Comparison of NIR spectra of halogen-free and –bearing basaltic glasses with the addition of CO_2 can be observed in figure 92. All glasses (including the CO_2-free) were synthesised at 3 kbar and 1550 K over 24 h. The addition of CO_2 to the halogen-bearing glasses show that carbonate is incorporated in the structure. Precise discussions can be made on the basis of the CS analysis combined with the MIR spectra (5.1.4. Determination of carbonate in the present glasses).

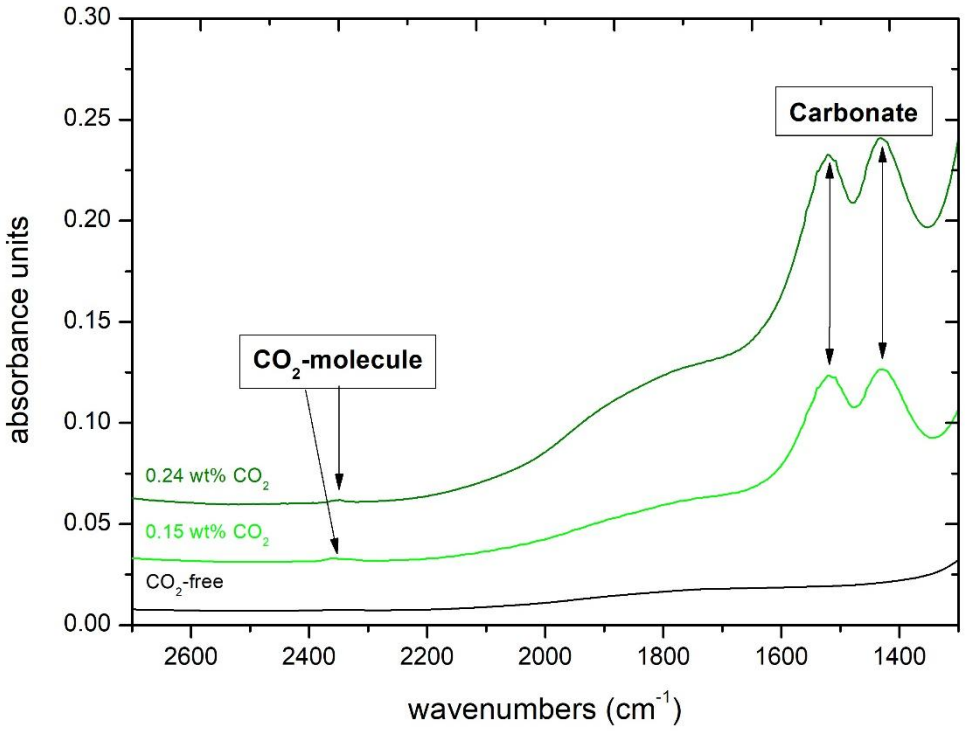

Figure 91: Mid-infrared spectra (MIR) of CO_2-free and CO_2-bearing basaltic glasses. The spectra are normalised to the thickness and experienced a subtraction of the CO_2-free spectrum. The spectra are vertically shifted in order to clearly show the differences in peak height.

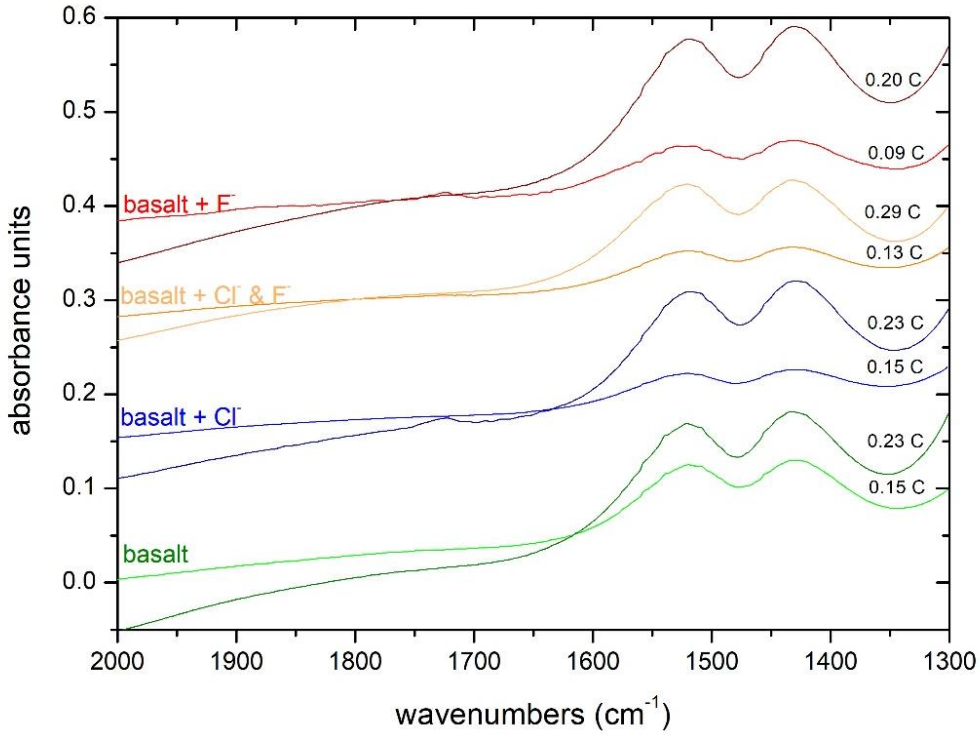

Figure 92: Comparison of MIR spectra of CO_2- and halogen-bearing basaltic glasses. The spectra are normalised to the thickness and experienced a subtraction of the CO_2 -free spectrum. The spectra are vertically shifted in order to illustrate the changes in peak size.

5.1.3. Determination of water species in the present glasses

The calculation is based on Beer-Lambert Law by means of the peak intensities and the total water content. The H_2O_{total} content was determined by the thermogravimetry measurement. The peak intensities are required for the determination of the absorption coefficients (equation 14). The calculated extinction coefficients of the OH groups and molecular H_2O band are represented in figure 93. The intercepts of linear regression with x- and y-axes enable the calculation of the absorption coefficients (ε) of OH and H_2O for the halogen-free and –bearing basaltic glasses in table 23. These coefficients allow the determination of the water species in glasses. The calculation was done with equation 15 and the results of the water species are given in table 24. Figure 94 demonstrates that the incorporation of water starts by the formation of OH-groups by the addition of 0.73 wt% H_2O to the halogen-free basaltic glass. The further addition of up to 3.47 wt% H_2O to the halogen-free basaltic glass enhances the formation of molecular water in the structure. The addition of 4.70 wt% H_2O results in an equal concentration of OH groups and molecular H_2O. In comparison, the halogen-bearing basaltic glasses show a shift of this equilibrium of the water speciation. Figure 94 c shows that the equilibrium shifts to 4.34 wt% H_2O due to the addition of 4.90 mol% F^- to basaltic glasses. This shift of the equilibrium is lowered by the addition of 3.65 mol% Cl^- to the basaltic glasses. The equal concentration of OH groups and molecular H_2O arise at 3.37 wt% H_2O (figure 94 d). On the results of the addition of fluorine or chlorine, it is assumed that the addition of (Cl^- + F^-) results in an average decrease of the equilibrium, but the addition of both halogens increases the equilibrium to 6.54 wt% H_2O (figure 94 b). Okrusch and Matthes (2009) reported that the increase of alkali and alkaline metals in the structure results in a decrease in bridging oxygens of the network formers, whereby water preferably exists as molecular water. It is possible to conclude from the incorporation mechanism of water how the addition of halogens changes the structure of basaltic glasses.

Table 23: Molar absorption coefficient (ε) of the halogen-free and –bearing basaltic glasses were determined by the intercepts of linear regression with x- and y-axes in figure 93 after equation 15.

Sample	ε_{H2O} ($l*mol^{-1}*cm^{-1}$)	$\Delta\varepsilon_{H2O}$ ($l*mol^{-1}*cm^{-1}$)	ε_{OH} ($l*mol^{-1}*cm^{-1}$)	$\Delta\varepsilon_{OH}$ ($l*mol^{-1}*cm^{-1}$)
BA-0	0.63	0.05	0.78	0.07
BA-Cl	0.68	0.07	0.76	0.06
BA-Cl-F	0.47	0.01	0.69	0.04
BA-F	0.79	0.05	0.81	0.06

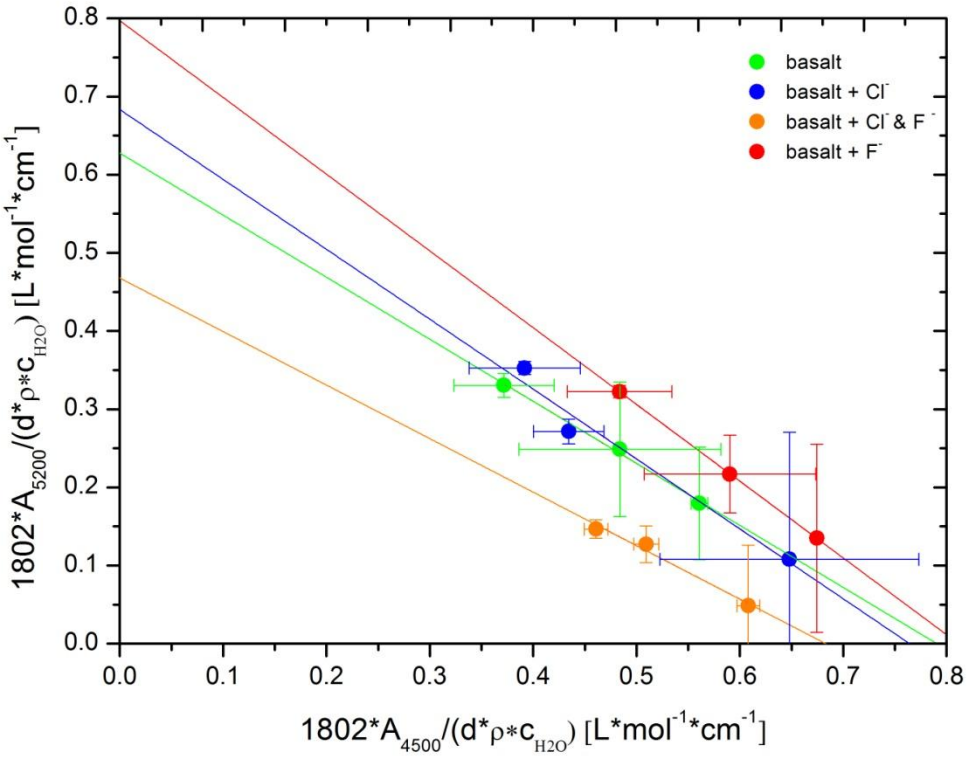

Figure 93: Normalised absorbance of OH groups and molecular H_2O bands for the present basaltic glasses with a weighted regression. The absorption coefficients ε_{OH} and ε_{H2O} result from the intercepts of linear regression with the x- and y-axes. The results are given in table 23.

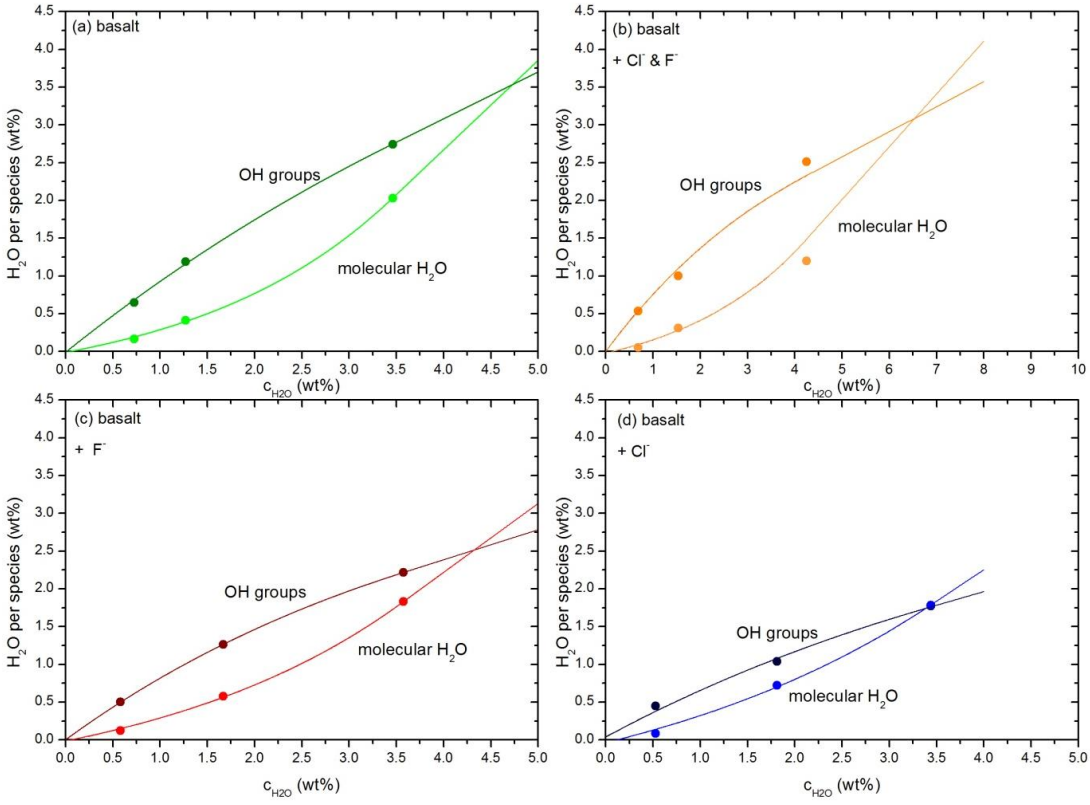

Figure 94: Water specification of OH groups (circles) and molecular H_2O (rectangles) as a function of total water content in halogen-free and -bearing basaltic glasses. The error bars are smaller than the symbols.

5.1.4. Determination of carbonate in the present glasses

The absorption coefficient (ε_{1430}) for the carbonate peaks can be determined by the calibration plot (figure 95). This diagram shows the $CO_{2\ (total)}$ content as a function of the absorption, density and thickness of the glass pieces. The halogen-free and –bearing basaltic glasses follow a linear regression with the normalised slope of 321 ± 16 L mol^{-1} cm^{-1}, which describes the absorption coefficient of the composition. Our absorption coefficient is in accordance with the ε_{1430} from Shishkina et al. (2010), who reported a ε_{1430} of 316 ± 12 L mol^{-1} cm^{-1} for tholeiitic basalts. The amount of carbonate in the present glasses can be determined by the Beer-Lambert law (equation 16) by means of the absorption coefficients.

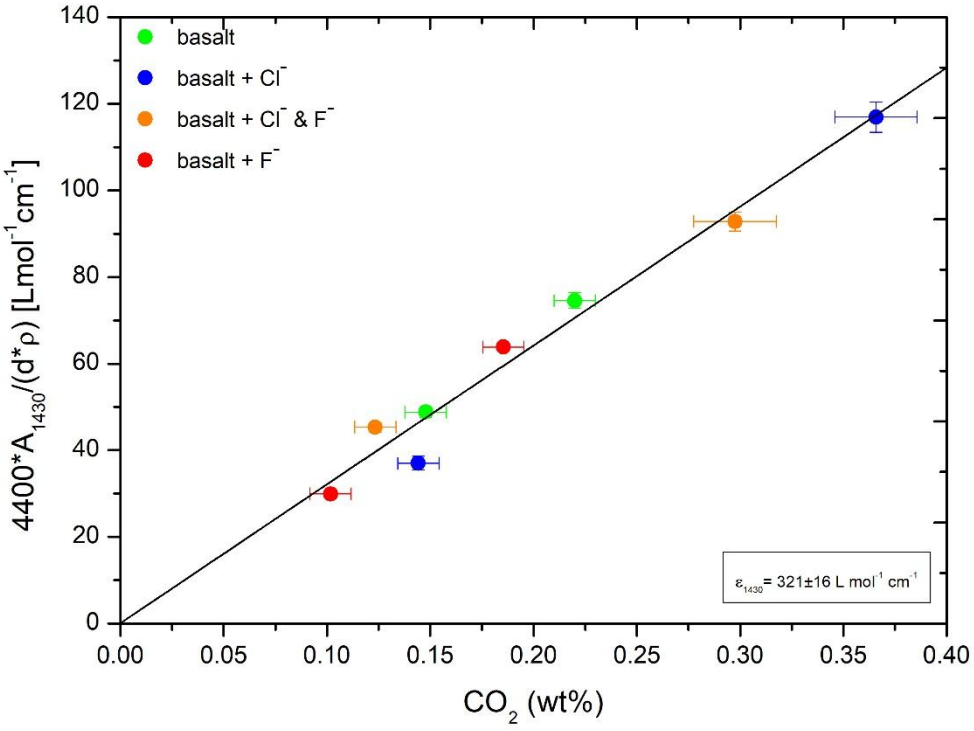

Figure 95: Calibration plot for the determination of the ε_{1430} for the carbonate bands at 1430 cm^{-1} for halogen-free and –bearing basaltic glasses. The $CO_{2\ (total)}$ contents are analysed with the CS analyser.

Table 24: Spectroscopic data of NIR and thermogravimetry measurements. The dry samples synthesised in IHPV have a water content ~ 0.10 wt% H_2O.

Sample	H_2O_{TGA} (wt%)	ΔH_2O_{TGA} (wt%)	ρ (g cm^{-3})	σ (g cm^{-3})	d[a] (mm)	A_{5200}[b] (mm^{-1})	A_{4500}[b] (mm^{-1})	H_2O_{NIR} (wt%)	OH_{NIR} (wt%)	H_2O_{total} (wt%)
BA-0_0.73H	0.73	0.02	2.708	0.015	0.311	0.006	0.019	0.21	0.52	0.73
BA-0_1.29H	1.27	0.05	2.678	0.013	0.292	0.014	0.027	0.50	0.79	1.29
BA-0_3.47H	3.46	0.03	2.669	0.027	0.260	0.061	0.069	1.82	1.65	3.47
BA-Cl_0.53H	0.53	0.05	2.661	0.009	0.272	0.002	0.014	0.08	0.45	0.53
BA-Cl_1.76H	1.81	0.02	2.644	0.015	0.264	0.019	0.031	0.72	1.04	1.76
BA-Cl_3.56H	3.44	0.02	2.635	0.025	0.270	0.069	0.076	1.78	1.77	3.56
BA-Cl-F_0.59H	0.69	0.03	2.681	0.010	0.307	0.002	0.019	0.05	0.54	0.59
BA-Cl-F_1.31H	1.53	0.02	2.649	0.009	0.266	0.008	0.031	0.31	1.00	1.31
BA-Cl-F_3.50H	4.25	0.04	2.622	0.019	0.294	0.027	0.084	0.99	2.51	3.50
BA-F_0.63H	0.58	0.02	2.692	0.014	0.250	0.004	0.019	0.12	0.50	0.63
BA-F_1.84H	1.67	0.03	2.686	0.015	0.253	0.019	0.052	0.58	1.26	1.84
BA-F_4.04H	3.57	0.02	2.674	0.008	0.286	0.076	0.114	1.83	2.22	4.04

Table 25: Spectroscopic data of MIR and CS measurements. The CO_2-bearing samples and dry samples synthesised in IHPV have a water content ~ 0.10 wt% H_2O.

Sample	$CO_{2\ CS}$ (ppm)	$\Delta CO_{2\ CS}$ (ppm)	ρ (g cm^{-3})	σ (g cm^{-3})	d[a] (mm)	A_{1500}[b] (mm^{-1})	$CO_{2\ MIR}$ (ppm)	$\Delta CO_{2\ MIR}$ (ppm)	H_2O_{MIR}[c] (wt%)	ΔH_2O_{MIR} (wt%)
BA-0_0.15C	1479	14	2.695	0.018	0.098	0.033	1523	8	0.04	0.01
BA-0_0.23C	2199	185	2.646	0.015	0.097	0.069	2326	13	0.08	0.01
BA-Cl_0.12C	1442	164	2.686	0.012	0.103	0.021	1154	6	0.02	0.01
BA-Cl_0.37C	3658	35	2.567	0.008	0.100	0.063	3649	20	0.07	0.01
BA-Cl-F_0.14C	1234	211	2.708	0.019	0.072	0.018	1414	8	0.03	0.02
BA-Cl-F_0.29C	2975	180	2.676	0.013	0.103	0.042	2896	16	0.04	0.01
BA-F_0.09C	1018	21	2.737	0.013	0.053	0.011	933	6	0.02	0.02
BA-F_0.20C	1853	34	2.697	0.017	0.143	0.067	1992	10	0.05	0.01

[a] Errors are ± 0.002 mm of thickness
[b] Errors are ± 0.003 mm^{-1} for the normalised absorbance
[c] The total H_2O content were calculated from IR spectra using the molar absorbance coefficient from Mandeville et al. (2002)

5.2. Density

5.2.1. Effect of H_2O on the density of basaltic glasses

Table 26 represents the influence of water on the density and the molar volume for hydrous halogen-free and –bearing basaltic glasses. Figure 96 shows that the density increases due to the synthesis in IHPV (300 MPa) for all halogen-free and –bearing basaltic glasses (pressure effect). An increasing water content in the basaltic glass results in a decrease in density (figure 96). The addition of 3.47 wt% H_2O to the halogen-free basaltic glass results in a decrease in density from 2.72 to 2.67 g cm^{-3}. The presence of 4.04 wt% H_2O in fluorine-bearing basaltic glasses shows a similar decrease in density from 2.72 to 2.67 g cm^{-3}. These results correlate well with the addition of 3.56 wt% H_2O to chlorine-bearing basaltic glasses (2.69 to 2.64 g cm^{-3}). The addition of 3.50 wt% H_2O to the (Cl^- + F-)-bearing basaltic glasses results in the strongest decrease in density by 0.09 g cm^{-1} (2.71 to 2.62 g cm^{-3}). In conclusion, the addition of H_2O to halogen-free and –bearing basaltic glasses results in a significant decrease in density especially for chlorine-bearing melts.

Figure 97 illustrates the effect of H_2O on the molar volume of halogen-free and –bearing basaltic glasses. The halogen-free and –bearing basaltic glasses shows a decrease in molar volume due to the synthesis in IHPV (300 MPa) for all glasses (pressure effect).The presence of water in basaltic glasses results in an increase in molar volume. The addition of 3.47 wt% H_2O to the halogen-free basaltic glasses results in an increase in molar volume from 23.22 to 23.66 cm^3 mol^{-1}. The presence of water in fluorine-bearing basaltic glasses shows the smallest increase in molar volume from 22.43 to 22.81 cm^3 mol^{-1}, whereas the presence of H_2O in chlorine-bearing glasses results in an increase in molar volume from 22.97 to 23.46 cm^3 mol^{-1}. The addition of H_2O to (Cl^- + F^-)-bearing basaltic glasses results in an increase in molar volume from 22.41 to 23.18 cm^3 mol^{-1} and the trend is located between the fluorine- and chlorine-bearing glasses. Thus, the effect of H_2O on the molar volume is weakened by the presence of halogens in basaltic glass.

Besides the total water content, the hydroxyl groups (OH groups) describe the water speciation, that is incorporated in the melt structure (Stolper 1982a, 1982b). At low total water content, the authors observed a strong effect of OH groups on the partial molar volume. In figure 98, the molar volume is demonstrated as a function of OH groups, whereby the exponential regression of the halogen-free basalt cannot be improved to a linear regression.

Table 26: Density ρ and molar volume of the hydrous glasses.

Sample	ρ (g cm^{-3})	σ (g cm^{-3})	molar volume (cm^3 mol^{-1})
BA-0_1atm	2.693	0.009	23.45
BA-0-III	2.719	0.015	23.22
BA-0_0.73H	2.708	0.015	23.32
BA-0_1.29H	2.678	0.013	23.58
BA-0_3.47H	2.669	0.027	23.66
BA-Cl_1atm	2.673	0.006	23.29
BA-Cl-III	2.692	0.013	22.97
BA-Cl_0.53H	2.661	0.009	23.23
BA-Cl_1.76H	2.644	0.015	23.38
BA-Cl_3.56H	2.635	0.025	23.46
BA-Cl-F_1atm	2.678	0.020	23.15
BA-Cl-F-III	2.712	0.027	22.41
BA-Cl-F_0.59H	2.681	0.010	22.67
BA-Cl-F_1.31H	2.649	0.009	22.94
BA-Cl-F_3.50H	2.622	0.019	23.18
BA-F_1atm	2.695	0.007	23.14
BA-F-III	2.720	0.009	22.43
BA-F_0.63H	2.692	0.014	22.66
BA-F_1.84H	2.686	0.015	22.71
BA-F_4.04H	2.674	0.008	22.81

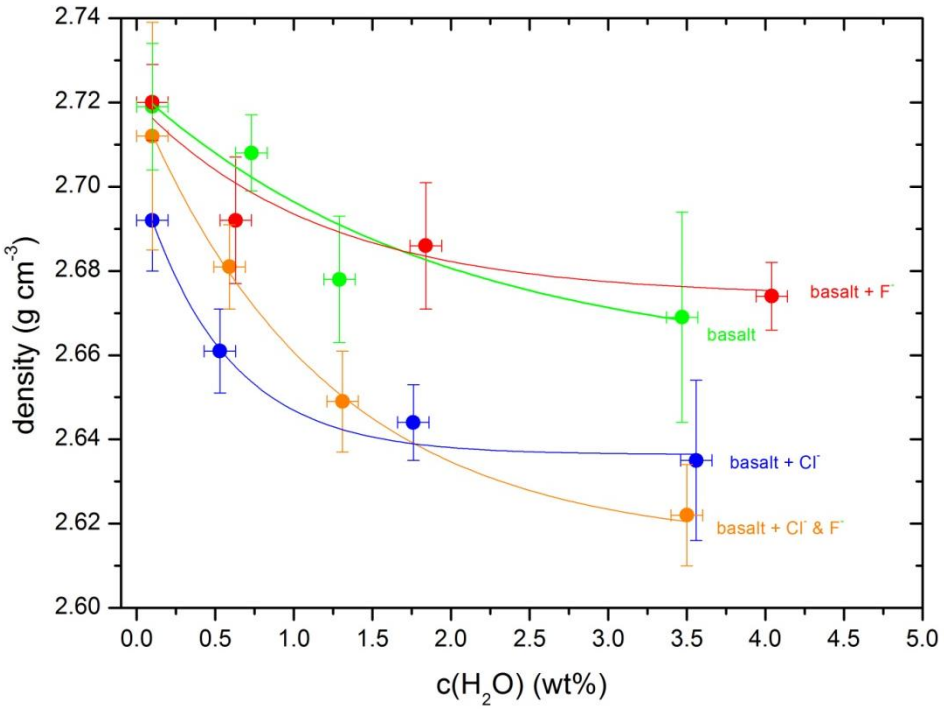

Figure 96: Effect of water on the density of halogen-free and -bearing basaltic glasses.

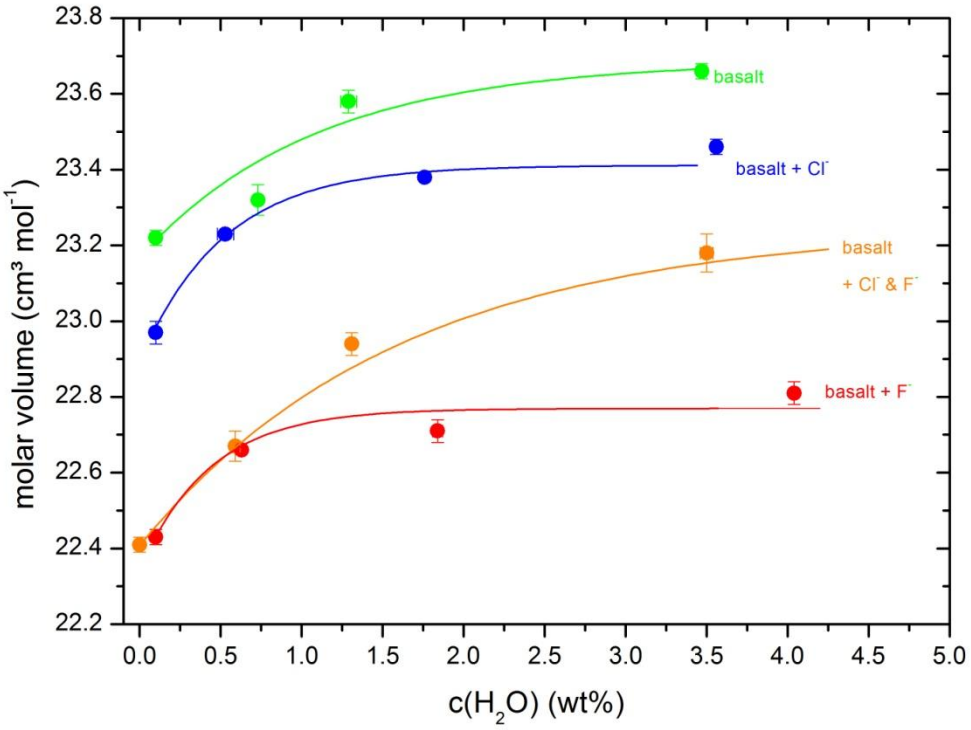

Figure 97: Effect of water on the molar volume of halogen-free and -bearing basaltic glasses.

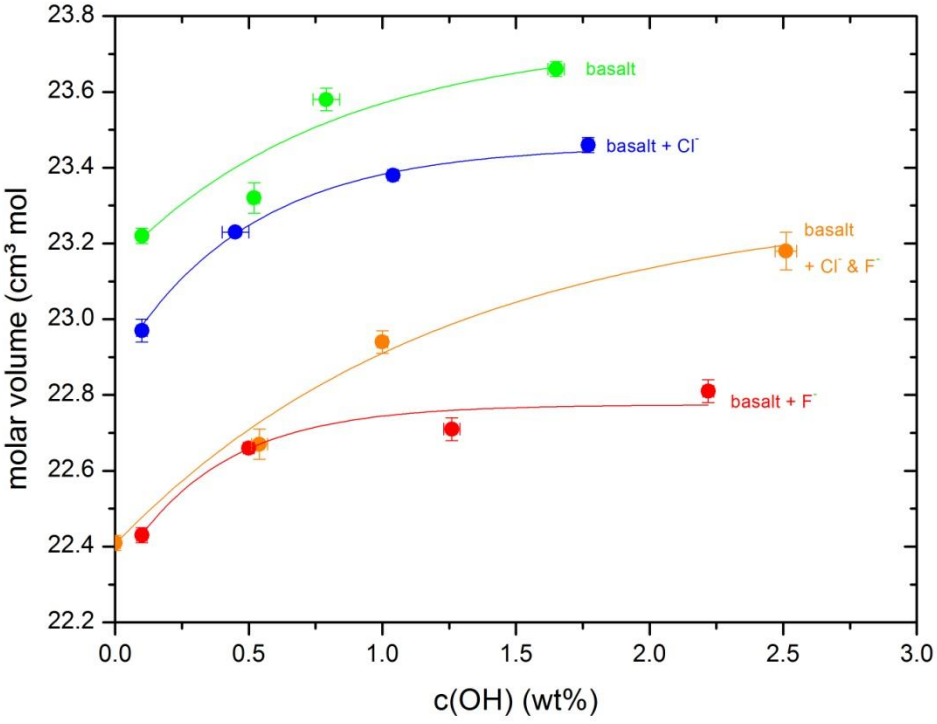

Figure 98: Effect of OH on the molar volume of halogen-free and -bearing basaltic glasses.

5.2.2. Effect of CO_2 on the density of basaltic glasses

The effect of CO_2 in halogen-free and –bearing basaltic glasses on density and molar volume is reported in table 27 represents the density as a function of CO_2 content on the present halogen-free and –bearing basaltic glasses. The addition of 2199 ppm CO_2 to the basaltic glasses results in a decrease in density from 2.72 to 2.65 g cm^{-3} (figure 99). The presence of 3658 ppm CO_2 in chlorine-bearing basaltic glasses results in a strong decrease in density from 2.69 to 2.57 g cm^{-3}, whereas the addition of 1853 ppm CO_2 to the fluorine-bearing basaltic glasses results in the smallest decrease in density from 2.72 to 2.70 g cm^{-3}. The addition of 2928 ppm CO_2 to the (Cl^- + F^-)-bearing basaltic glasses results in a decrease in density from 2.71 to 2.68 g cm^{-3}.

Figure 100 illustrates the effect of CO_2 on the molar volume of halogen-free and –bearing basaltic glasses. The presence of CO_2 in basaltic glasses results in an increase in molar volume. The addition of 2199 ppm CO_2 to the halogen-free basaltic glasses results in an increase in molar volume from 23.22 to 23.86 cm^3 mol^{-1}. The presence of 1853 ppm CO_2 in fluorine-bearing basaltic glasses shows the smallest increase in molar volume from 22.43 to 22.62 cm^3 mol^{-1}, whereas the presence of 3658 ppm CO_2 in chlorine-bearing glasses results in an increase in molar volume from 22.97 to 24.08 cm^3 mol^{-1}. The addition of CO_2 to (Cl^- + F^-)-bearing basaltic glasses results in an increase in molar volume from 22.41 to 22.71 cm^3 mol^{-1}. In conclusion, the effect of CO_2 on the density and molar volume of halogen-free basaltic glasses is stronger than the effect of H_2O. Furthermore, the molar volume of H_2O bearing glasses experiences a strong initial increase that is lowered afterwards and in contrast to the molar volume of CO_2 bearing glasses increases exponentially. But the concentration of CO_2 is much lower than H_2O.

Table 27: Density ρ and molar volume of the CO_2-bearing basaltic glasses.

Sample	ρ (g cm^{-3})	σ (g cm^{-3})	molar volume (cm^3 mol^{-1})
BA-0-III	2.719	0.015	23.22
BA-0_0.15C	2.695	0.018	23.43
BA-0_0.23C	2.646	0.015	23.86
BA-Cl-III	2.692	0.013	22.97
BA-Cl_0.12C	2.686	0.012	23.02
BA-Cl_0.37C	2.567	0.008	24.08
BA-Cl-F-III	2.712	0.027	22.41
BA-Cl-F_0.14C	2.708	0.019	22.44
BA-Cl-F_0.29C	2.676	0.013	22.71
BA-F-III	2.720	0.009	22.43
BA-F_0.09C	2.737	0.013	22.29
BA-F_0.20C	2.697	0.017	22.62

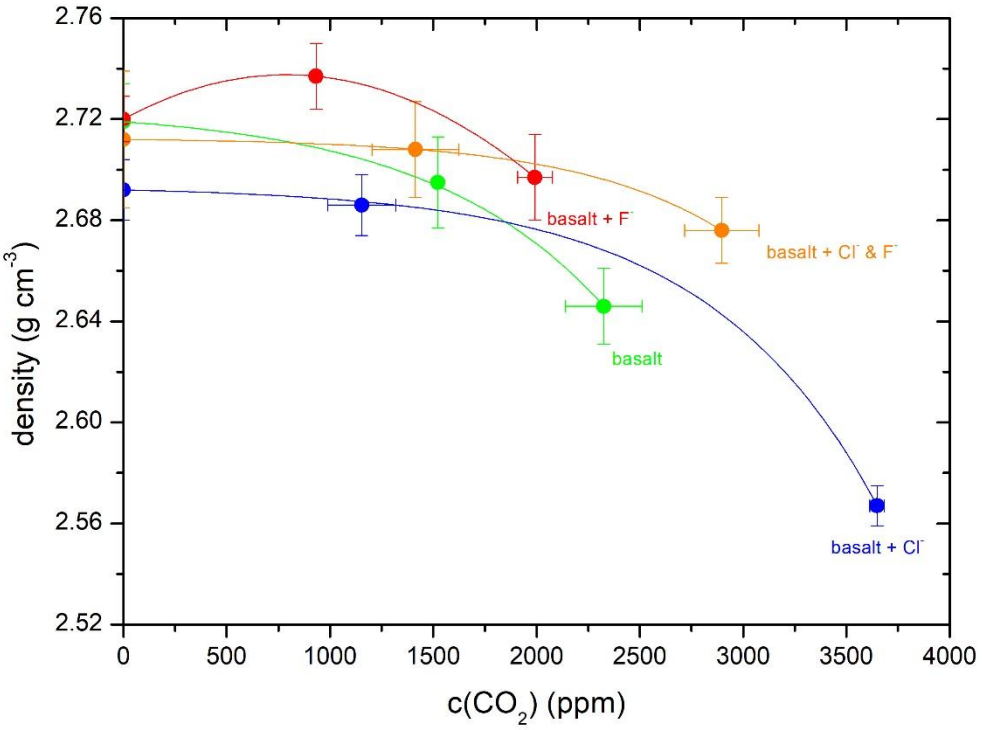

Figure 99: Effect of carbon dioxide on the density of halogen-free and -bearing basaltic glasses.

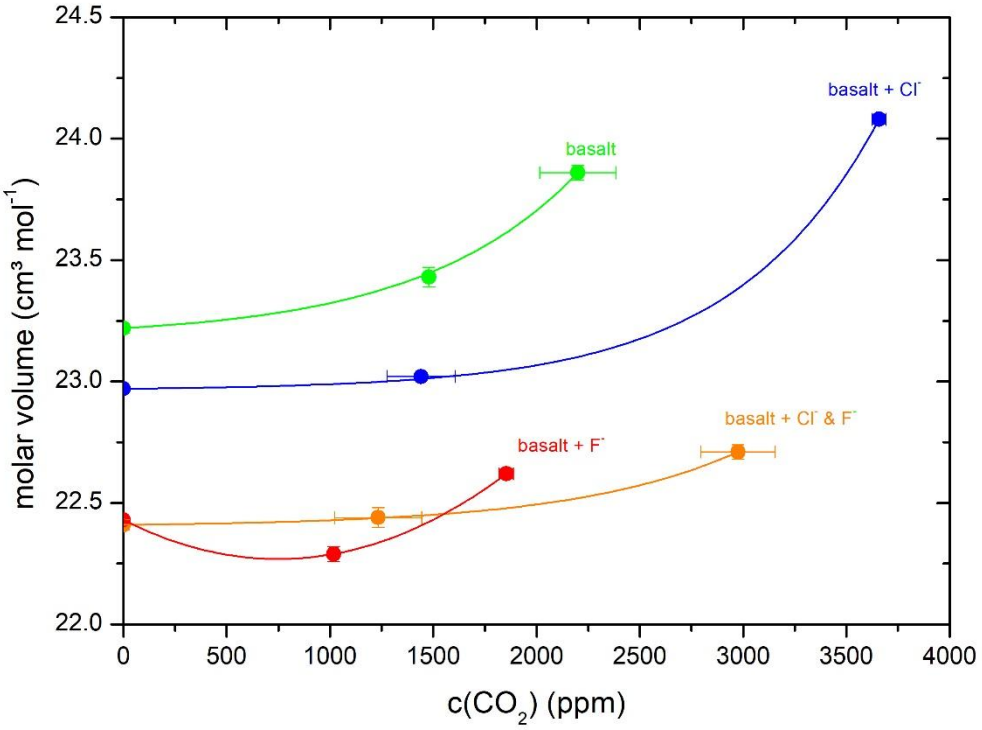

Figure 100: Effect of carbon dioxide on the molar volume of halogen-free and -bearing basaltic glasses.

5.3. Effect of iron

5.3.1. Effect of H_2O on the Fe^{2+}/Fe_{total} of basaltic glasses

The results of XRF analysis and colorimetric micro-determination are represented in table 28. Furthermore, table 28 shows the Fe^{2+}/Fe_{total} calculated after Kress and Carmichael (1991) as well as the prevailing oxygen fugacity. The range of calculated Fe^{2+}/Fe_{total} results from the calculation, which does not consider the water content. The results of measured iron speciation indicate that the addition of water results in a decrease in Fe^{2+}/Fe_{total}. The addition of 3.47 wt% H_2O to the halogen-free basaltic glasses shows a decrease from 0.60 to 0.19 in Fe^{2+}/Fe_{total}. This decreasing effect is similar by the addition of fluorine and (Cl^- + F^-) to the basaltic glasses. Furthermore, the addition of 3.56 wt% H_2O to the chlorine-bearing basaltic glasses results in weaker decrease by 0.34 in Fe^{2+}/Fe_{total}. In summary, figure 101 reflects that the addition of water to the halogen-free and –bearing basaltic glasses results in a significant decrease in Fe^{2+}/Fe_{total}. In addition to the total water content, figure 102 represents the Fe^{2+}/Fe_{total} as a function of OH groups. The halogen-free basalt demonstrates a linear decrease in Fe^{2+}/Fe_{total} due to increasing OH groups. This linear decrease is also evident for the fluorine- and (Cl^- + F^-)-bearing glasses. The addition of 0.65 wt% OH to chlorine-bearing glasses shows a linear regression, whereas the increasing OH content results in an exponential decrease. Thus, the presence of OH groups in chlorine-bearing glasses affects the Fe^{2+}/Fe_{total} in other ways than the halogen-free and fluorine-bearing glasses. Furthermore, the effect of water on the Fe^{2+}/Fe_{total} results from the constant fH_2 in IHPV and capsules as well as the variation of the water activity.

Table 28: Results of Fe^{2+}/Fe_{total} and a comparison of the FeO_{total} wet chemistry method and X-ray fluorescence (XRF) analysis for hydrous basaltic glasses. All glasses were synthesised in IHPV at constant oxygen fugacity of log (fO_2) -3.56 to -2.56.

Sample	Fe^{2+}/Fe_{total}	FeO_{total} (wt %)		FeO (wt%)
	wet chemistry	XRF	wet chemistry	wet chemistry
BA-0-III	0.60	5.81	5.06	2.54
BA-0_0.73H	0.52	5.85	5.18	2.71
BA-0_1.29H	0.29	5.78	5.08	1.45
BA-0_3.47H	0.19	5.49	5.21	0.99
BA-Cl-III	0.60	5.09	5.55	2.72
BA-Cl_0.53H	0.40	5.08	5.33	2.11
BA-Cl_1.76H	0.32	5.02	4.93	1.56
BA-Cl_3.56H	0.26	4.88	4.90	1.30
BA-Cl-F-III	0.61	5.32	5.19	3.15
BA-Cl-F_0.59H	0.50	5.13	5.18	2.59
BA-Cl-F_1.31H	0.27	5.11	4.91	1.73
BA-Cl-F_3.50H	0.21	4.79	4.47	0.95
BA-F-III	0.58	6.06	5.49	3.20
BA-F_0.63H	0.39	5.58	5.31	2.05
BA-F_1.84H	0.27	5.26	5.30	1.43
BA-F_4.04H	0.22	5.23	5.51	1.21

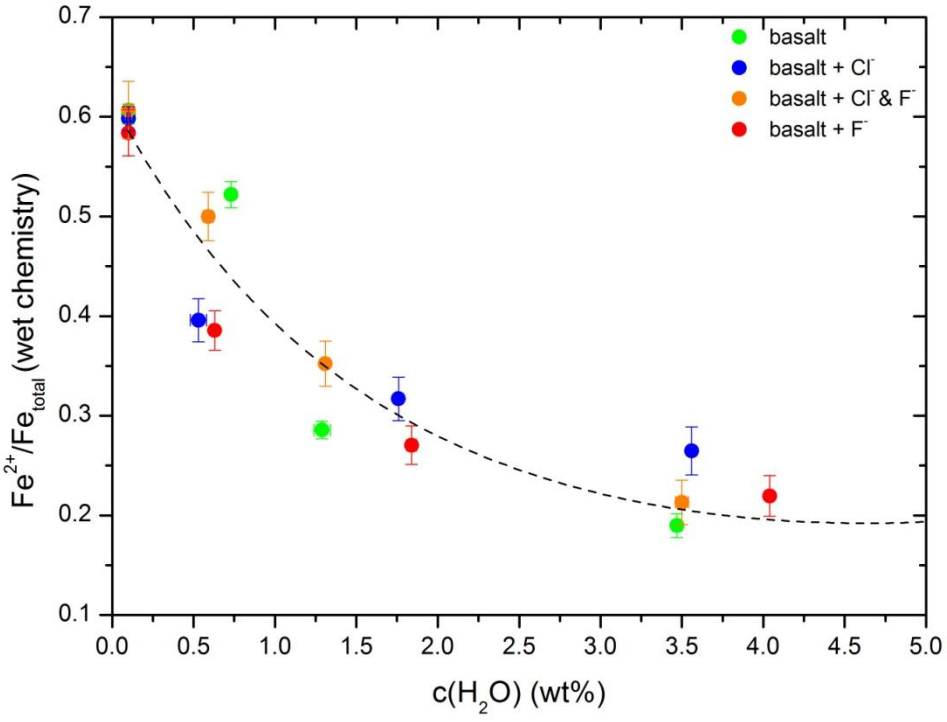

Figure 101: Fe^{2+}/Fe_{total} of the glasses as a function of the water content. The dashed line represents exponential regression for all glasses.

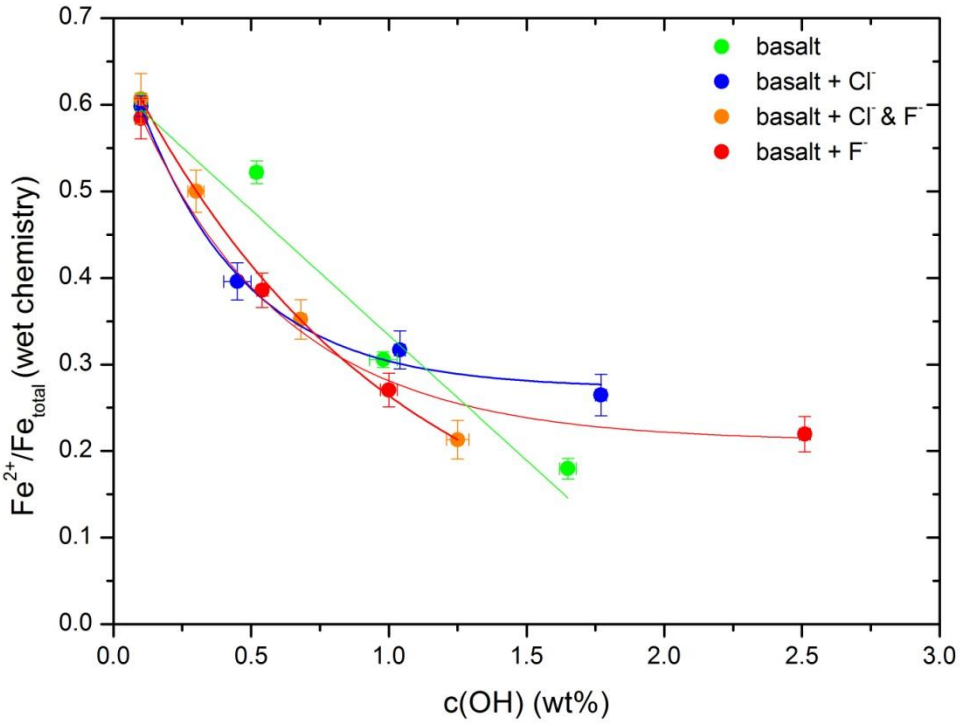

Figure 102: Fe^{2+}/Fe_{total} of the glasses as a function of the OH content.

5.3.2. Effect of CO_2 on the Fe^{2+}/Fe_{total} of basaltic glasses

The dependence of CO_2 on the Fe^{2+}/Fe_{total} of the present glasses is illustrated in figure 103 as well as the related data for each of the glasses is represented in table 29. The addition of 1479 ppm CO_2 to the halogen-free basaltic glasses results in an increase from 0.60 to 0.66 of Fe^{2+}/Fe_{total}, whereas the further addition of 2199 ppm CO_2 shows a decrease by 0.02 of Fe^{2+}/Fe_{total}. The measurements do not provide clear results due to the variation that lie within the range of errors. Therefore, the change of Fe^{2+}/Fe_{total} of the halogen-bearing basaltic glasses is not only affected by the addition of CO_2 but also by halogen contents.

Figure 103 shows the slight decrease in Fe^{2+}/Fe_{total} by the addition of fluorine to the halogen-free basaltic melt and this effect is enhanced by the addition of CO_2. In comparison, the addition of chlorine and CO_2 results in a slight increase from 0.60 to 0.83 in Fe^{2+}/Fe_{total}. The effect of the addition of both halogens and 1234 ppm CO_2 on the iron speciation results in an increase from 0.61 to 0.76 in Fe^{2+}/Fe_{total}, whereas the further addition of 2975 ppm CO_2 results in a decrease from 0.76 to 0.63 in Fe^{2+}/Fe_{total}.

Table 29: Results of Fe^{2+}/Fe_{total} and a comparison of the FeO_{total} wet chemistry method and X-ray fluorescence (XRF) analysis for CO_2-bearing basaltic glasses.

Sample	Fe^{2+}/Fe_{total}	FeO_{total} (wt %)		FeO (wt%)
	wet chemistry	XRF	wet chemistry	wet chemistry
BA-0_III	0.60	5.81	5.06	2.54
BA-0_0.15C	0.66	5.86	5.26	3.47
BA-0_0.23C	0.64	5.83	4.22	2.68
BA-Cl-III	0.60	5.09	5.55	2.72
BA-Cl_0.12C	0.76	5.11	4.20	3.17
BA-Cl_0.37C	0.83	5.12	5.16	4.28
BA-Cl-F-III	0.61	5.32	5.19	3.15
BA-Cl-F_0.14C	0.76	5.32	5.68	4.31
BA-Cl-F_0.29C	0.63	5.35	5.07	3.19
BA-F-III	0.58	6.06	5.49	3.20
BA-F_0.09C	0.57	5.88	5.11	2.89
BA-F_0.20C	0.37	5.92	5.50	2.01

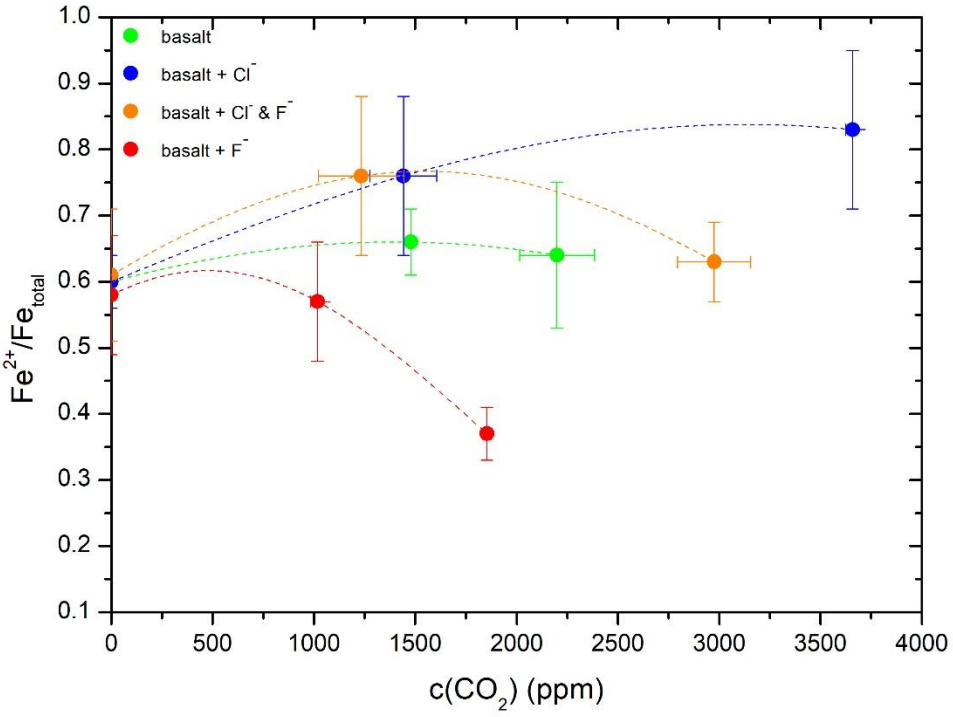

Figure 103: The effect of CO_2 on the iron speciation of halogen-free and –bearing basaltic glasses. The dashed line represents exponential regression for the glasses.

5.3.3. Raman-spectra: Effect of Fe^{2+}/Fe_{total} iron ratio on the structure of hydrous basaltic glasses

The Raman spectra of the hydrous basaltic glasses are shown in figure 104. The spectra indicate a peak at the wavenumbers between 495 to 520 cm^{-1} (I) as well as a peak around 930 to 1005 cm^{-1} (IIa and IIb). Furthermore, the mid-range region between 700 and 800 cm^{-1} does not experience an effect of the addition of water to the present basaltic glasses. The addition of water to the halogen-free basaltic glasses shows the peak shift of a shoulder from 979 (IIa) to 943 cm^{-1} (IIb). This peak shift can be explained by the addition of water as well as the increasing Fe^{3+} content (see section 4.2.4. Raman-spectra: Effect of Fe^{2+}/Fe_{total} iron ratio on the structure). The chlorine-bearing basaltic glass shows a significant shoulder around 1002 cm^{-1}, which is shifted to 935 cm^{-1} due to the addition of water. The addition of fluorine and (Cl^- + F^-) to the basaltic glasses reflects a weaker shoulder around 990 cm^{-1}. This shoulder shifts to a lower frequency as an effect of the increasing water content.

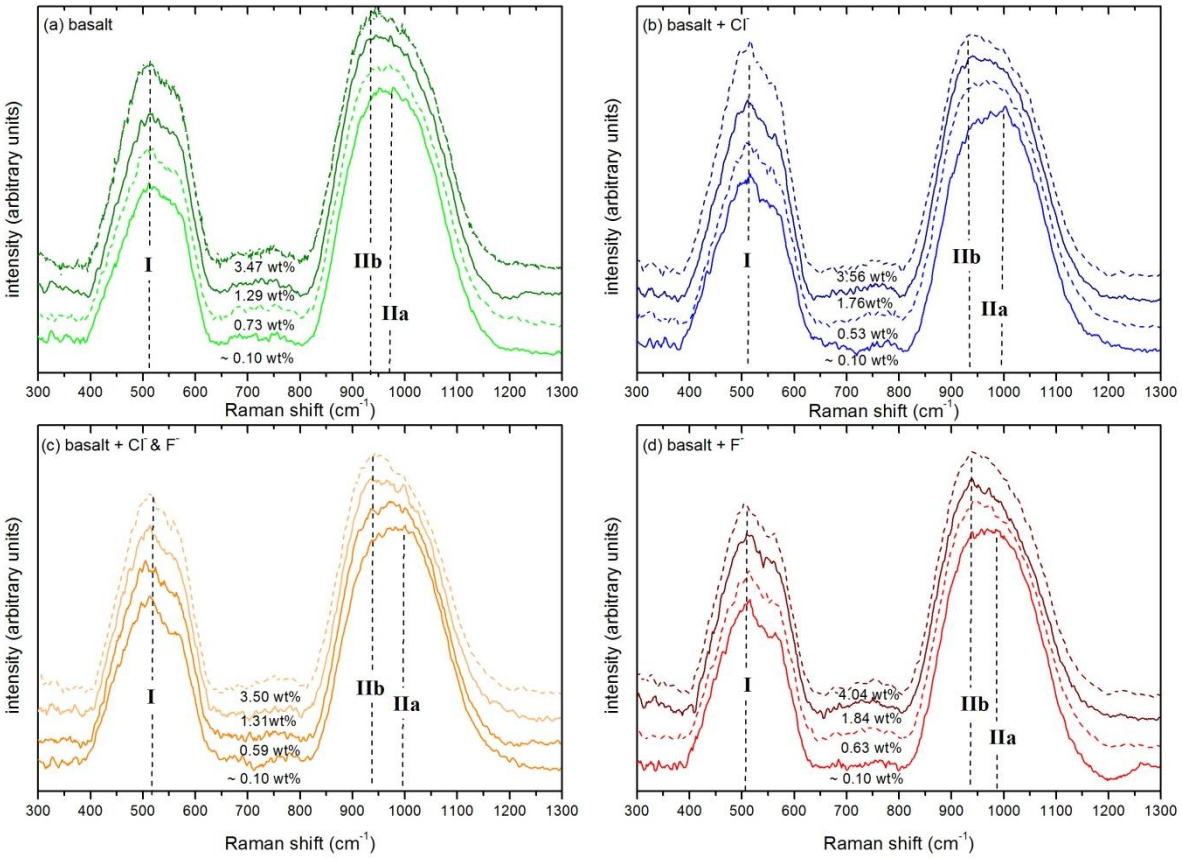

Figure 104: Raman spectra of hydrous basaltic glasses after a Long correction. The numbers represent the water contents of the halogen-free and –bearing basaltic glasses. The vertical dashed lines show the main peak in the low-frequency region (I) and the shift of the peak in high-frequency region (IIa and IIb).

A precise observation of the low frequency region is illustrated in figure 105. The overlapping spectra of the dry and basaltic glass with 3.47 wt% H_2O show an increase in intensity accompanied by the addition of water. This effect is not only a function of increasing water content but also iron speciation. The decreasing Fe^{2+}/Fe_{total} from 0.60 to 0.19 result in an increase in intensity of the peak in the low frequency region. This effect has been described by Di Muro et al. (2009) and Di Genova et al. (2016). The authors suggested the increase in intensity of the LF peak due to an increase in glass polymerisation by the formation of Q^2 units. This is also evident by the decrease in Fe^{2+}/Fe_{total} due to increasing H_2O content.

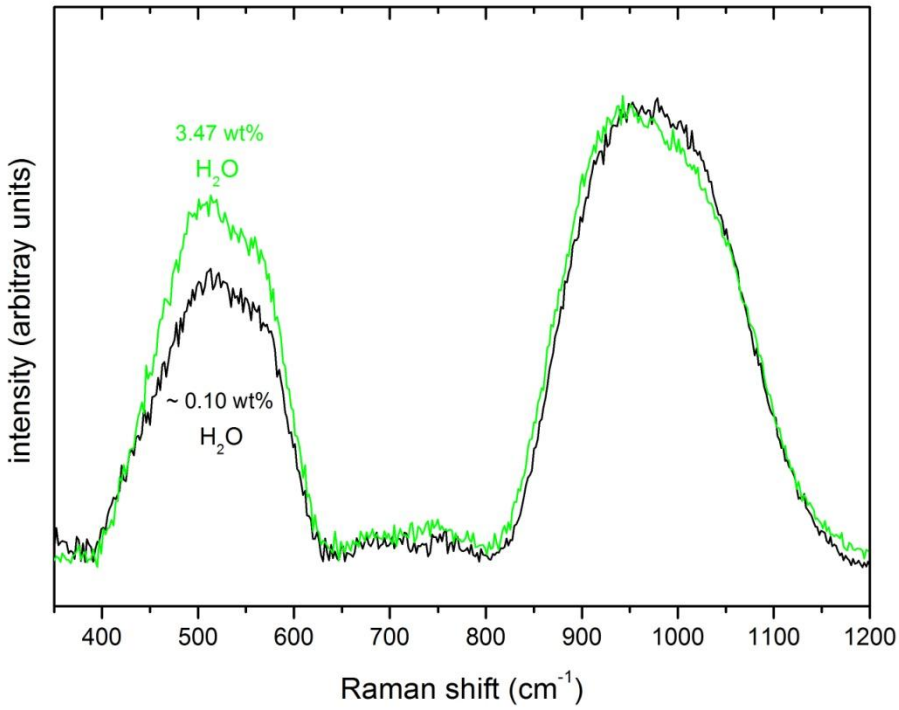

Figure 105: Comparison of Long-corrected Raman spectra of halogen-free basaltic glasses with ~0.10 and 3.41 wt% H_2O.

5.3.4. Raman-spectra: Effect of Fe^{2+}/Fe_{total} iron ratio on the structure of CO_2-bearing basaltic glasses

Figure 106 shows the Raman spectra of halogen-free and –bearing basaltic glasses doped with CO_2. The characteristic peak is indicated in the low (I) frequency region between 495 and 520 cm^{-1} and the high frequency peak (II) is shown between 935 and 1005 cm^{-1}. The mid-range region between 700 and 800 cm^{-1} can be neglected due to no visible changes of intensity or peak shift accompanied by increasing CO_2 content. The addition of CO_2 to halogen-free basaltic glasses does not show a shoulder in the high frequency region (II) and no peak shift.

The fluorine-bearing basaltic glasses represent a slight shoulder at 938 cm^{-1} (IIb) due to the addition of CO_2, whereas the chlorine and (Cl^- + F^-)-bearing glasses do not show a significant shoulder or peak shift in the high frequency region. Figure 107 represents the halogen-free basaltic glasses with 0 and 2199 ppm CO_2. The addition of CO_2 does not affect the intensity in the low frequency region. These results are similar to the halogen-bearing basaltic glasses doped with CO_2. There is no visible significant change of the intensity as well as a peak shift in the low and high frequency regions.

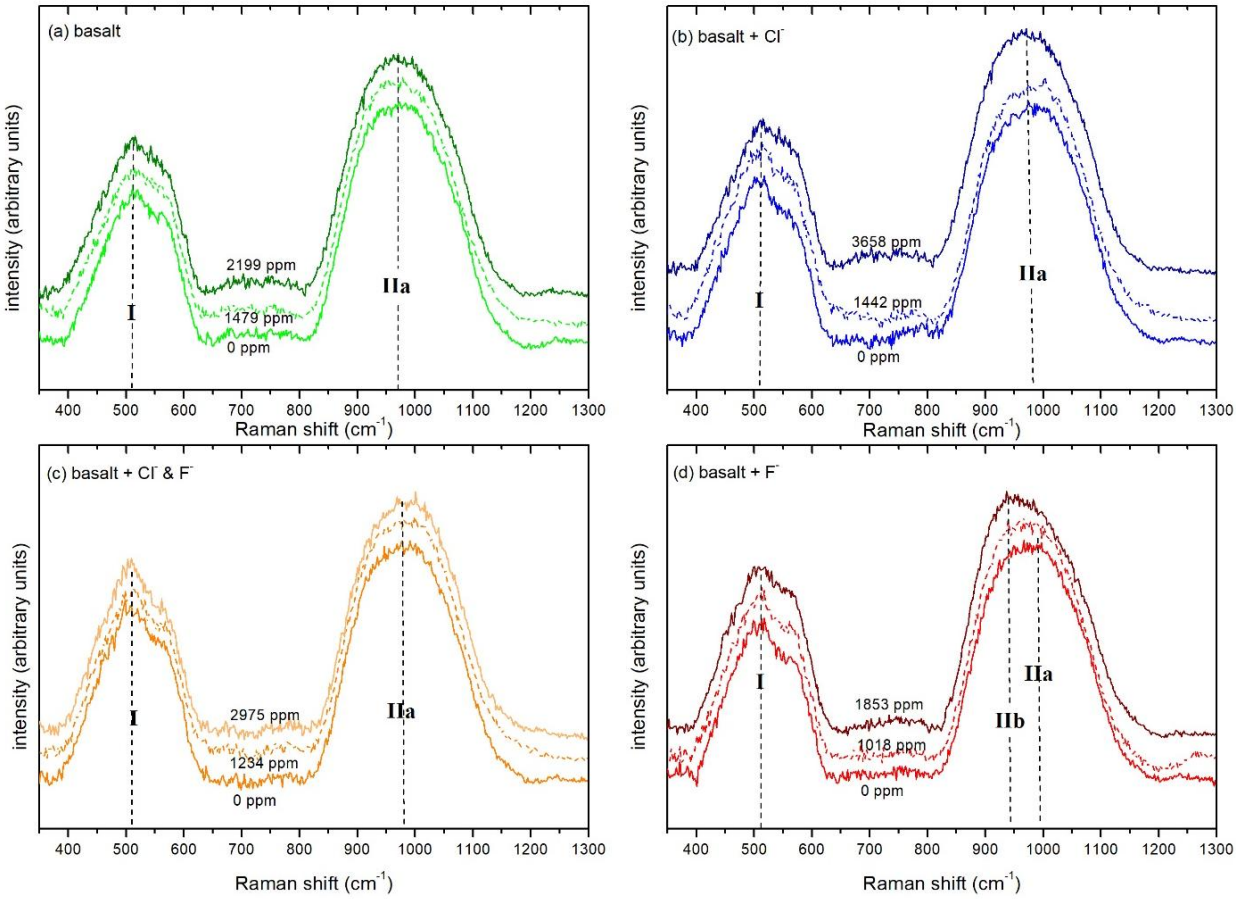

Figure 106: Long-corrected Raman spectra of basaltic glasses doped with CO_2. The numbers represent the CO_2 content of the halogen-free and –bearing basaltic glasses. The vertical dashed lines show the main peak in the low-frequency region (I) and the shift of the peak in high-frequency region (IIa and IIb).

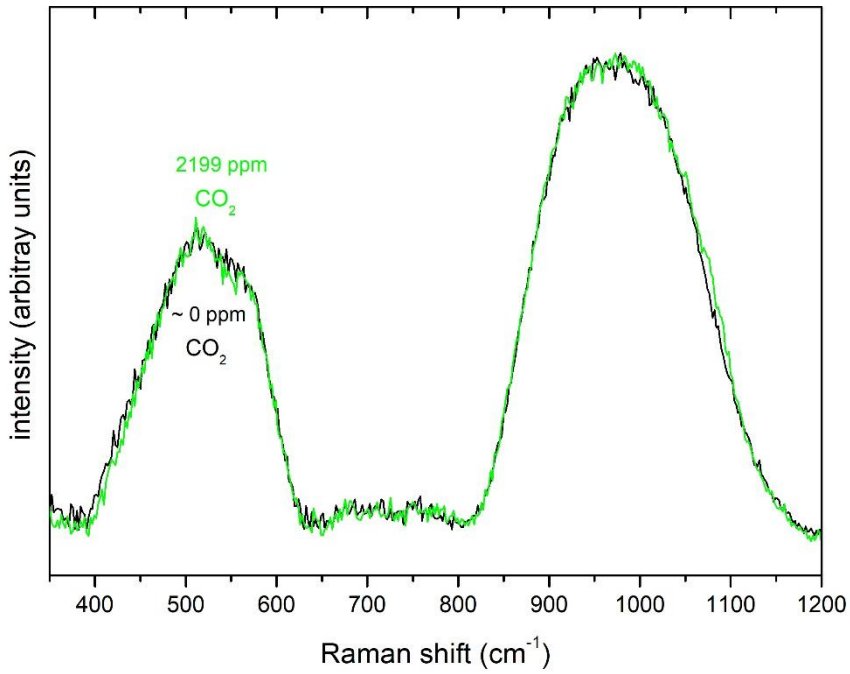

Figure 107: Comparison of Long-corrected Raman spectra of halogen-free basaltic glasses.

5.4. Viscosity

5.4.1. Effect of H_2O on the viscosity of basaltic glasses

The presence of water in basaltic melts results in a decrease in viscosity due to the depolymerisation of the melts. Table 30 shows the micropenetration viscosity data with the related experimental temperature. The error in temperature is 0.5 K and the viscosity shows an error of 0.06 $\log_{10}$ Pa s. Table 31 lists the parameters for the Arrhenian fit of the viscosity data as well as the glass transition temperature (T_g^{12}). This temperature describes the viscosity at 10^{12} Pa s, whereby it is possible to compare the viscosity with literature data. The addition of 0.73 wt% H_2O to the basaltic melt results in a decrease in viscosity by 1.0 log units as well as the further addition of 3.47 wt% H_2O shows a decrease in viscosity by 5.5 log units (figure 108 a). The combined effect of water and halogens is represented in figure 108 b – d. The addition of 0.53 wt% H_2O to chlorine-bearing basaltic melt shows a decrease in viscosity by 1.5 log units. The presence of 3.47 wt% H_2O in basaltic melt results in a decrease in viscosity by 6.5 log units (figure 108 b). In comparison to the chlorine-bearing basaltic melt, the addition of 0.63 wt% H_2O to basaltic melt with fluorine resulted in a decrease in viscosity by 1.3 log units, whereas the addition of 4.04 wt% H_2O shows a decrease in viscosity by 5.8 log units (figure 108 d). Figure 108 c represents the presence of water in (Cl^- + F^-) basaltic melts. The addition of 0.59 wt% H_2O to the basaltic melt with both halogens results in a decrease in viscosity by 1.4 log units as well as the further addition of 3.50 wt% H_2O shows a decrease in viscosity by 4.0 log units. The largest effect on the viscosity is shown by the combined volatiles chlorine and water.

Table 30: Micropenetration viscosity data of halogen-free and -bearing basaltic melts at diverse experimental temperatures.

BA-0-III		BA-0_0.73H		BA-0_1.29H		BA-0_3.47H	
T (K)	$\log_{10}\eta$ (Pa s)	T (K)	$\log_{10}\eta$ (Pa s)	T (K)	$\log_{10}\eta$ (Pa s)	T (K)	$\log_{10}\eta$ (Pa s)
880.5	12.65	840.3	12.92	810.3	12.40	710.6	13.90
890.4	12.16	850.7	12.62	820.5	11.80	720.8	13.08
902.3	11.55	860.5	12.07	840.8	11.32	730.8	12.69
930.6	10.56	870.3	11.57	850.5	11.03	740.8	12.33
951.3	10.23	880.4	11.18	870.3	10.51	760.8	11.43
962.6	9.44	891.0	10.73	890.6	9.51	780.8	10.74
981.0	9.01	924.6	9.95	898.4	9.06	790.7	10.03
992.7	8.87	945.1	9.07	910.4	8.50	820.8	9.35
BA-Cl-III		BA-Cl_0.53H		BA-Cl_1.76H		BA-Cl_3.56H	
T (K)	$\log_{10}\eta$ (Pa s)	T (K)	$\log_{10}\eta$ (Pa s)	T (K)	$\log_{10}\eta$ (Pa s)	T (K)	$\log_{10}\eta$ (Pa s)
882.4	12.76	850.3	12.60	780.3	12.88	720.2	13.07
891.9	12.36	860.3	12.10	800.3	12.14	730.5	12.83
902.3	11.75	870.9	11.70	810.3	11.63	740.3	12.18
922.3	11.34	880.7	11.31	820.5	11.26	750.4	11.79
932.2	10.81	890.3	10.82	830.3	10.79	760.2	11.55
950.7	10.18	900.9	10.57	840.6	10.40	770.3	11.18
962.5	9.87	911.1	10.18	850.5	10.04	780.3	10.87
972.1	9.34	920.4	9.65	861,0	9.62	792.8	10.20
BA-Cl-F-III		BA-Cl-F_0.59H		BA-Cl-F_1.31H		BA-Cl-F_3.50H	
T (K)	$\log_{10}\eta$ (Pa s)	T (K)	$\log_{10}\eta$ (Pa s)	T (K)	$\log_{10}\eta$ (Pa s)	T (K)	$\log_{10}\eta$ (Pa s)
860.8	12.52	830.3	13.16	770.3	12.96	740.2	13.02
880.4	11.86	840.3	12.33	780.4	12.26	750.3	12.29
890.4	11.59	850.4	11.83	790.7	11.99	760.2	11.77
900.3	11.15	860.3	11.29	800.3	11.42	770.3	11.62
920.6	10.42	870.3	11.04	810.8	10.91	780.3	11.01
940.4	9.72	880.3	10.65	823.0	10.50	790.4	10.91
954.5	9.24	890.4	10.25	830.9	10.47	802.8	10.36
962.3	9.05	900.7	9.92	841.2	9.92	820.6	10.10
BA-F-III		BA-F_0.63H		BA-F_1.84H		BA-F_4.04H	
T (K)	$\log_{10}\eta$ (Pa s)	T (K)	$\log_{10}\eta$ (Pa s)	T (K)	$\log_{10}\eta$ (Pa s)	T (K)	$\log_{10}\eta$ (Pa s)
882.4	12.85	840.6	13.07	800.5	12.60	750.3	12.49
887.6	12.64	850.6	12.41	810.3	12.31	760.4	12.20
902.3	12.12	860.4	12.17	821.6	11.69	770.3	11.71
907.7	11.89	870.6	12.01	830.3	11.42	780.4	11.31
921.9	11.45	880.4	11.35	840.4	11.15	790.3	10.89
932.2	11.02	890.4	11.30	841.8	11.02	800.3	10.29
942.3	10.86	900.4	11.03	850.3	10.80	820.3	9.44
962.8	10.32	910.4	10.64	860.4	10.42	830.3	9.32

Table 31: Parameters for the Arrhenian fit of micropenetration viscosity data.

Sample	A_{Arr} (log10 Pa s)	ΔA_{Arr} (log10 Pa s)	B_{Arr} (log10 Pa s K)	ΔB_{Arr} (log10 Pa s K)	T_g^{12} (K)	ΔT_g^{12} (K)	$\eta @ T_g^{12}$ (log10 Pa s)
BA-0-III	-21.04	1.45	2.95	0.14	894.0	0.3	12.00
BA-0_0.73H	-21.36	1.44	2.88	0.13	862.1	0.2	10.81
BA-0_1.29H	-21.16	2.02	2.72	0.17	821.6	0.2	9.32
BA-0_3.47H	-19.93	1.27	2.39	0.10	748.1	0.2	6.79
BA-Cl-III	-22.67	1.25	3.12	0.12	900.7	0.2	12.00
BA-Cl_0.53H	-24.67	1.00	3.17	0.09	863.7	0.2	10.49
BA-Cl_1.76H	-22.30	0.55	2.75	0.05	801.7	0.1	8.23
BA-Cl_3.56H	-17.56	1.27	2.21	0.10	747.5	0.2	6.97
BA-Cl-F-III	-21.21	0.58	2.91	0.05	876.5	0.1	12.00
BA-Cl-F_0.59H	-26.64	2.21	3.28	0.19	849.3	0.2	10.80
BA-Cl-F_1.31H	-21.88	1.71	2.67	0.14	788.7	0.2	8.61
BA-Cl-F_3.50H	-16.45	2.17	2.16	0.17	759.3	0.2	8.20
BA-F-III	-17.94	0.93	2.71	0.09	905.8	0.3	12.00
BA-F_0.63H	-16.68	1.96	2.49	0.17	867.2	0.2	10.78
BA-F_1.84H	-25.37	1.61	3.05	0.13	815.6	0.2	8.28
BA-F_4.04H	-22.61	1.20	2.64	0.10	763.2	0.2	6.55

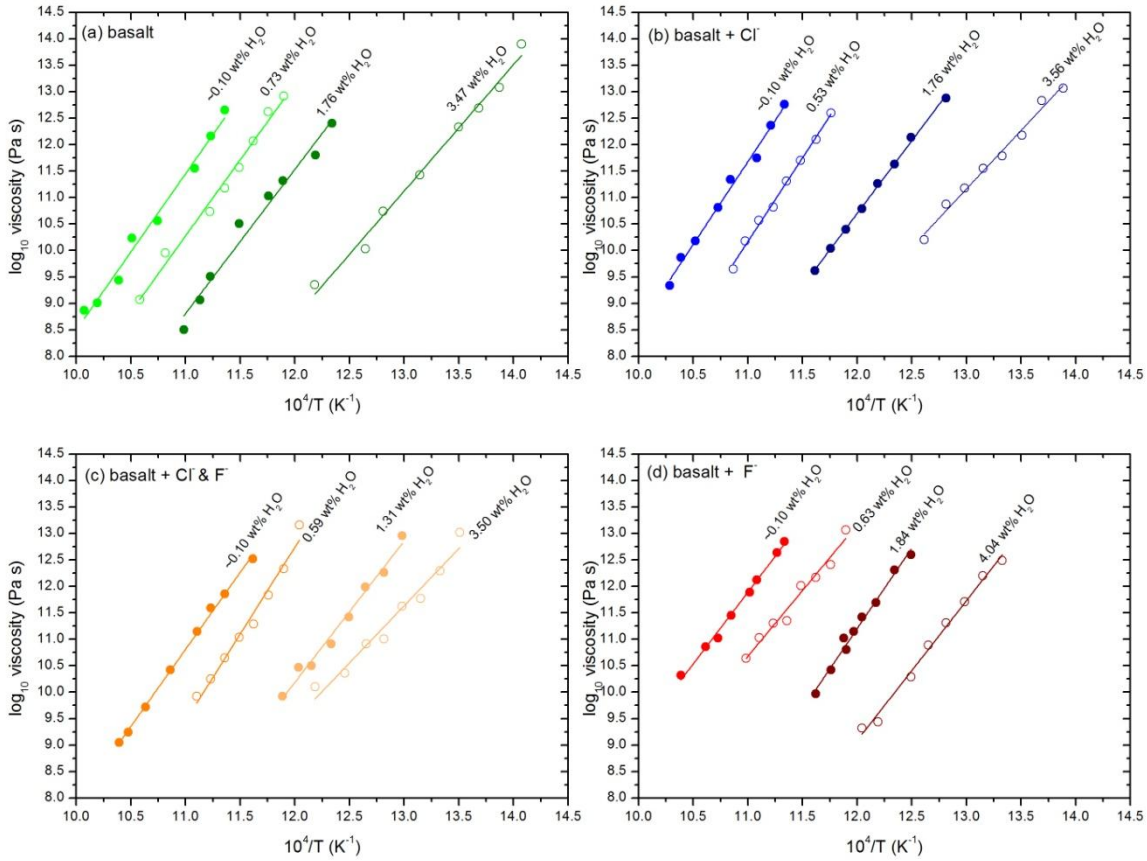

Figure 108: Effect of water on the viscosity of the halogen-free and –bearing basaltic melts. The lines through the data are Arrhenian fits. The error bars are smaller than the symbols.

In figure 109, the temperature of T_g^{12} of halogen-free and –bearing basaltic melts is shown as a function of water content. The addition of 0.73 wt% water to the halogen-free basaltic melt results in a decrease in T_g^{12} by 30 K. Further addition of 3.47 wt% H_2O resulted in a decrease in T_g^{12} by 145 K. In comparison to halogen-free basaltic melts, the presence of water and halogens show a similar decrease in T_g^{12}. The addition of 3.56 wt% H_2O to chlorine-bearing melt results in the decrease in T_g^{12} by 153 K compared to halogen-free basalt. The presence of 4.04 wt% H_2O in fluorine-bearing basaltic melts shows a lower decrease in T_g^{12} by 140 K than the halogen-free basalt. The addition of 3.50 wt% H_2O to the (Cl^- + F^-)-bearing melt results in a decrease in T_g^{12} by 117 K. In conclusion, the addition of H_2O to halogen-free and –bearing basaltic melts results in a decrease in T_g^{12}.

Figure 110 illustrates T_g^{12} as a function of OH groups, whereby the effect of the individual water speciation on T_g^{12} can be observed. The increasing OH groups show a linear decrease of T_g^{12} for the halogen-free basalt. This deviation between total water content and OH groups on T_g^{12} is strong and gave to be considering for the present basaltic melts. The decrease in T_g^{12} of the halogen-bearing basalt is enhanced due to the combined effect of halogens and OH groups. This linear decreasing effect can also observed for the halogen-bearing basaltic melts. It is shown, that the decreasing T_g^{12} of halogen-free and -bearing basaltic melts is influenced by the dominant water species (OH groups).

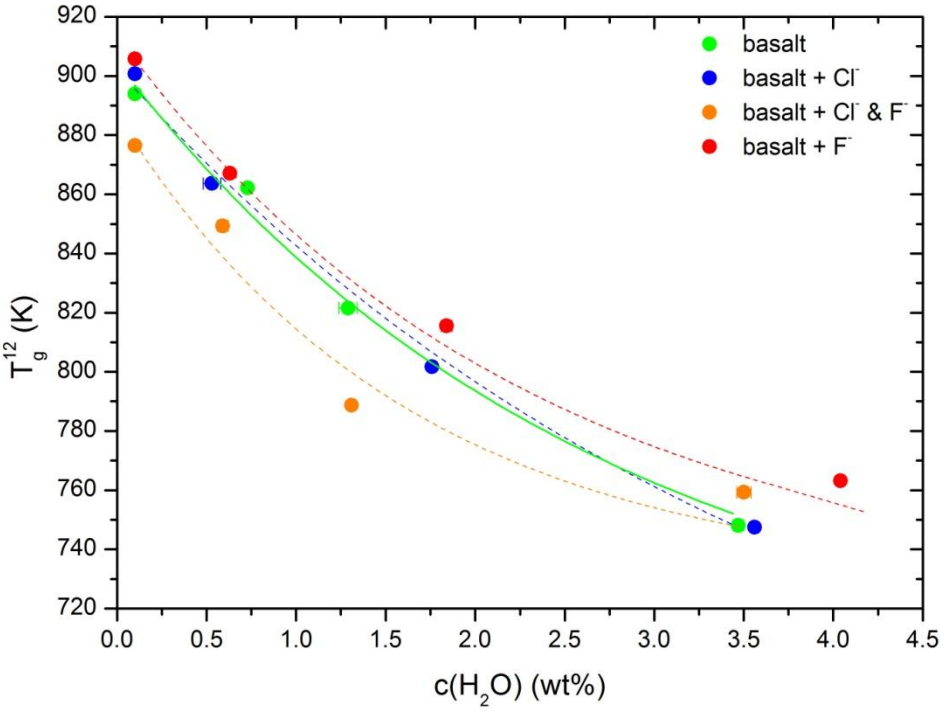

Figure 109: The glass transition temperature T_g^{12} as a function of water content. The error bars are smaller than the symbols.

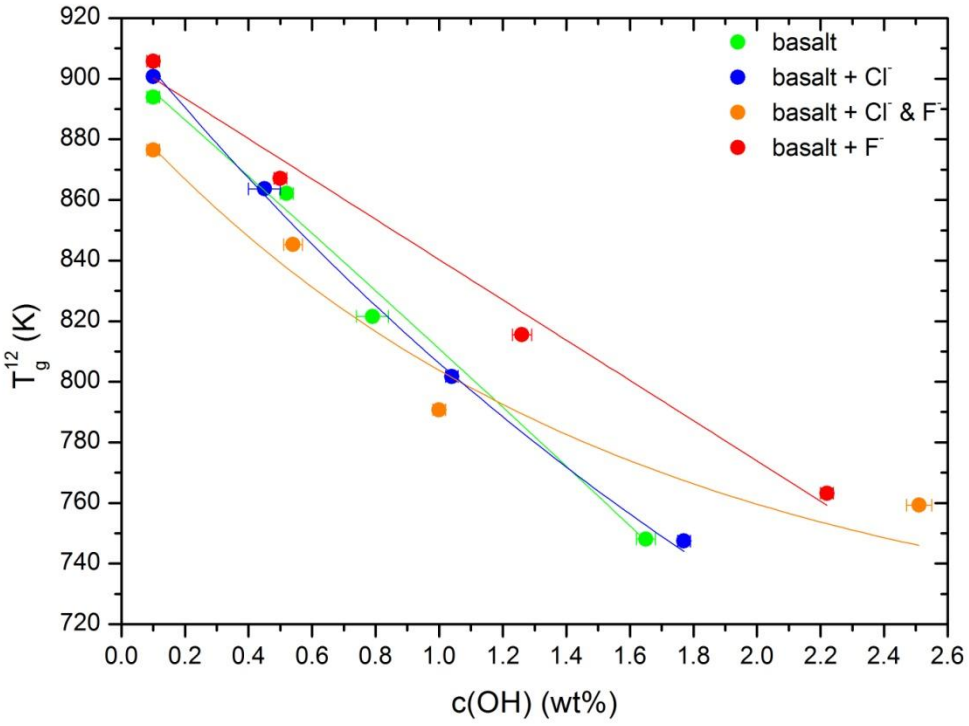

Figure 110: The glass transition temperature T_g^{12} as a function of OH content. The error bars of T_g^{12} are smaller than the circles

5.4.2. Effect of CO_2 on the viscosity of basaltic glasses

The viscosity data with the related experimental temperature are represented in table 32. The parameters for the Arrhenian fit of the viscosity data as well as the glass transition temperature (T_g^{12}) is shown in table 33. Figure 111 plots the logarithmic viscosity versus temperature for different CO_2 contents in halogen-free and –bearing basaltic melts. For all present basaltic melts the viscosity decreases with increasing temperature. The addition of 1479 ppm CO_2 to the halogen-free basalt results in a decrease in viscosity by 0.5 log units. Further addition of 2199 ppm CO_2 results in a decrease in viscosity by 0.2 log units (figure 111 a). Figure 111 b-d represents the combined effect of CO_2 and halogens on the viscosity. The addition of 1442 ppm CO_2 to the chlorine-bearing basaltic melts does not show a decrease in viscosity, but the further addition of 3658 ppm CO_2 to the chlorine-bearing melts results in a decrease in viscosity by 0.5 log units (figure 111 b). The addition of 1018 ppm CO_2 to the fluorine-bearing basaltic melts results in a decrease in viscosity by 0.5 log units, further addition of 1853 ppm CO_2 to the fluorine-bearing basaltic melts shows a decrease in viscosity by 1.5 log units (figure 111 d). The addition of 1234 ppm CO_2 to the (Cl^- + F^-)-bearing basaltic melts shows a decrease in viscosity by 0.5 log units and further addition of 2975 ppm CO_2 results in a decrease in viscosity by 0.3 log units (figure 111 c).

Table 32: Viscosity data for CO_2-bearing basaltic melts. The error in temperature is 0.5 K and the error in viscosity is 0.06 log_{10} Pa s.

BA-0_0.15C		BA-0_0.23C		BA-Cl_0.12C		BA-Cl_0.37C	
T (K)	$log_{10}\eta$ (Pa s)	T (K)	$log_{10}\eta$ (Pa s)	T (K)	$log_{10}\eta$ (Pa s)	T (K)	$log_{10}\eta$ (Pa s)
872.5	12.51	870.5	12.55	862.5	13.67	851.5	13.67
881.8	12.12	880.4	11.64	882.4	12.86	871.5	12.75
912.4	10.85	900.4	11.54	890.3	12.43	892.3	11.90
920.6	10.76	900.4	11.30	897.4	12.12	902.3	11.42
930.5	10.17	920.4	10.48	912.4	11.49	912.4	11.05
942.1	9.89	940.4	9.76	922.2	10.98	922.2	10.62
950.4	9.82	952.1	9.41	932.2	10.72	932.2	10.34
955.5	9.50	961.1	9.14	952.8	10.17	943.1	9.93
BA-Cl-F_0.14C		BA-Cl-F_0.29C		BA-F_0.09C		BA-Cl_0.20C	
T (K)	$log_{10}\eta$ (Pa s)	T (K)	$log_{10}\eta$ (Pa s)	T (K)	$log_{10}\eta$ (Pa s)	T (K)	$log_{10}\eta$ (Pa s)
872.4	12.62	872.4	12.23	850.3	13.46	831.5	13.32
882.7	12.19	882.4	11.92	870.5	12.69	840.3	12.95
890.5	11.72	892.3	11.40	890.3	12.07	850.5	12.55
901.8	11.36	902.3	11.11	900.5	11.67	860.4	11.92
912.4	11.05	912.3	10.63	9118	11.19	870.5	11.53
930.3	10.80	922.2	10.32	921.2	11.00	881.2	11.11
940.4	10.06	927.7	10.27	930.4	10.78	890.4	10.64
952.2	9.65	942.2	9.72	942.9	10.27	900.7	10.24

Table 33: Parameters for the Arrhenius fit to the micropenetration viscosity data.

Sample	A_{Arr} (log10 Pa s)	ΔA_{Arr} (log10 Pa s)	B_{Arr} (log10 Pa s K)	ΔB_{Arr} (log10 Pa s K)	T_g^{12} (K)	ΔT_g^{12} (K)	$\eta@ T_g^{12}$ (log10 Pa s)
BA-0-III	-21.04	1.45	2.95	0.14	894.0	0.3	12.00
BA-0_0.15C	-21.74	1.27	2.98	0.12	884.4	0.2	11.64
BA-0_0.23C	-21.78	1.63	2.97	0.15	879.0	0.3	11.43
BA-Cl-III	-22.67	1.25	3.12	0.12	900.7	0.2	12.00
BA-Cl_0.12C	-24.76	2.29	3.31	0.12	900.9	0.3	12.01
BA-Cl_0.37C	-25.01	0.47	3.29	0.04	889.3	0.1	11.53
BA-Cl-F-III	-21.21	0.58	2.91	0.05	876.5	0.1	12.00
BA-Cl-F_0.14C	-21.87	0.91	3.00	0.08	886.5	0.2	12.39
BA-Cl-F_0.29C	-22.03	1.05	2.99	0.09	878.2	0.2	12.07
BA-F-III	-17.94	0.93	2.71	0.09	905.8	0.3	12.00
BA-F_0.09C	-18.62	0.67	2.73	0.06	890.7	0.2	11.49
BA-F_0.20C	-27.33	0.77	3.38	0.07	860.3	0.1	10.03

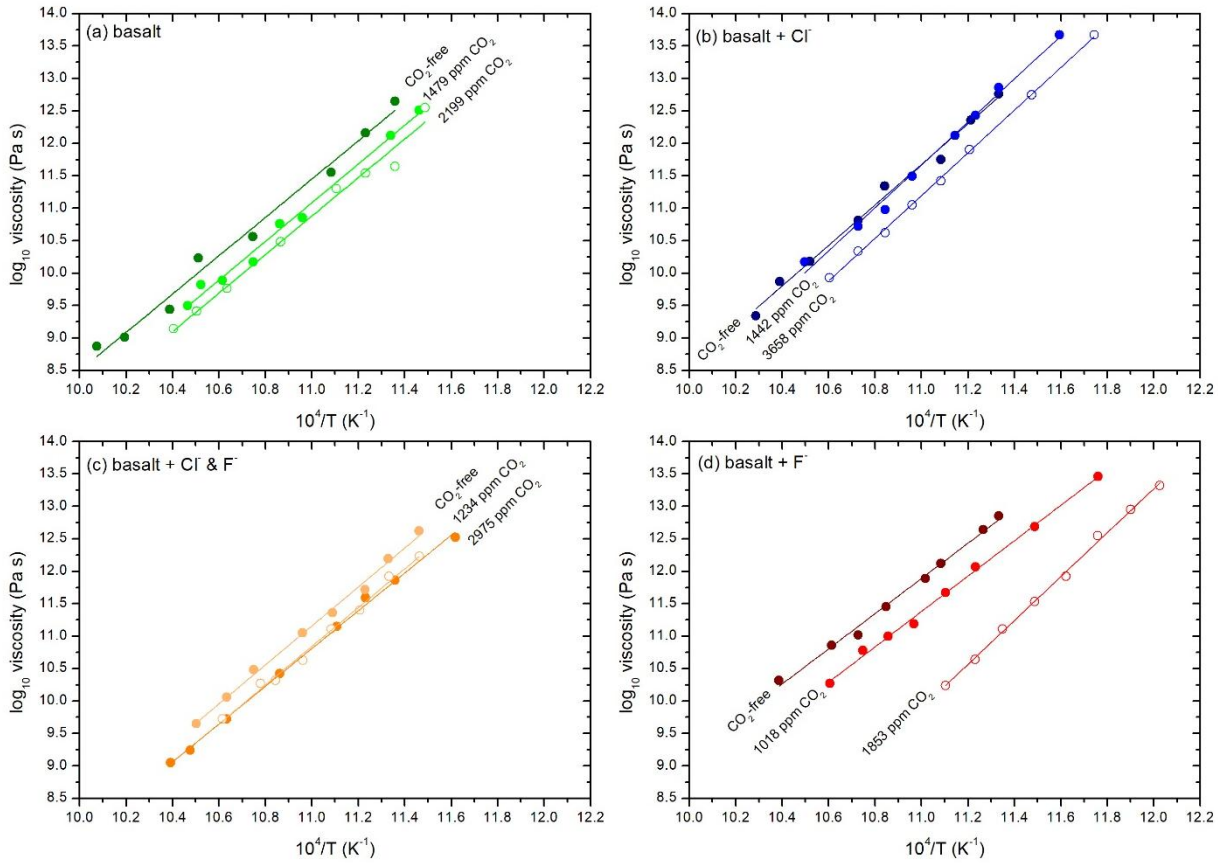

Figure 111: Effect of CO_2 on the viscosity of the halogen-free and –bearing basaltic melts. The lines through the data are Arrhenian fits. The error bars are smaller than the symbols.

Figure 112 shows the glass transition temperature (T_g^{12}) as a function of increasing CO_2 content for all halogen-free and –bearing basaltic melts. The addition of 2199 ppm CO_2 to the halogen-free basaltic melts results in a decrease in T_g^{12} by 15 K. In comparison to halogen-free basaltic melts, the presence of 3658 ppm CO_2 and chlorine show a similar decrease in T_g^{12} from 900 to 889 K. The presence of 1853 ppm CO_2 to the fluorine-bearing basaltic melts results in a decrease in T_g^{12} by 45 K. The addition of 1234 ppm CO_2 to the (Cl^- + F^-)-bearing melts results in an increase in T_g^{12} by 10 K, but the further addition of 2975 ppm CO_2 shows a decrease in T_g^{12} by 8 K. In conclusion, the addition of H_2O to halogen-free and –bearing basaltic melts results in a stronger decrease in T_g^{12} due to the higher solubility in basaltic melts (under the present synthesis properties).

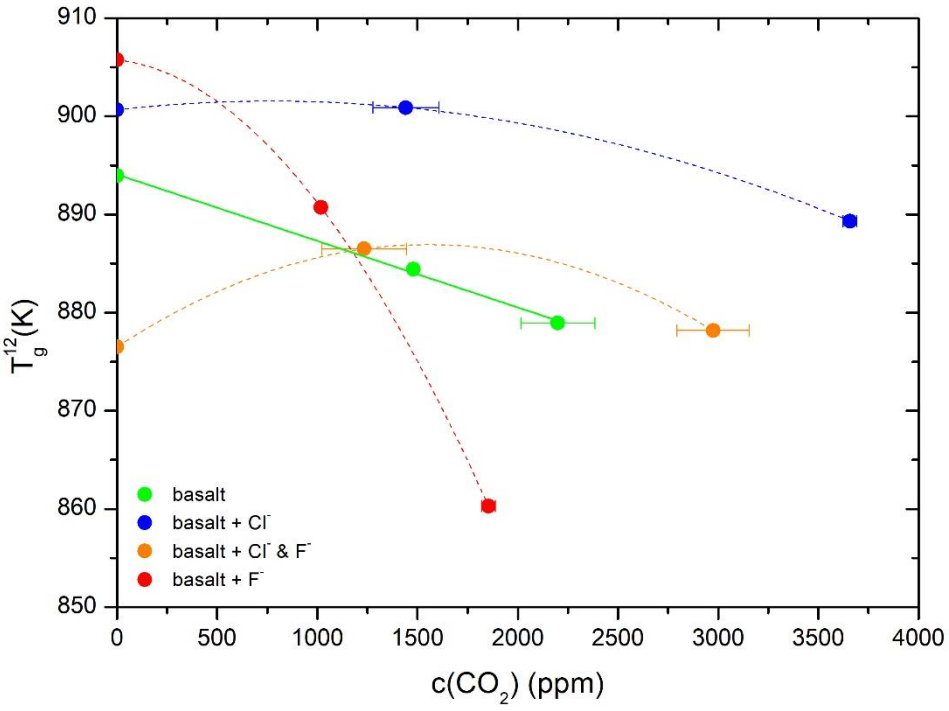

Figure 112: The glass transition temperature T_g^{12} as a function of CO_2 (ppm). The error bars of T_g^{12} are smaller than the symbols.

5.5. Heat Capacity

5.5.1. Effect of H_2O on the heat capacity of basaltic melts

Figure 113 illustatres the measurements of the heat capacities of the glasses C_{pg} and melts C_{pl} as a function of temperature. The heat capacity was measured with a constant cooling and heating rate of 20 K min^{-1}. The addition of 1.29 wt% H_2O to the present basaltic melt shows a shift of the onset temperature of the glass transition peak to higher temperature as a function of composition (figure 113 a). The addition of 3.47 wt% H_2O to the basaltic melt results in a decrease of the glass transition peak and a shift of T_g^{12} from 1010 to 910 K. This observation can result from a crystallisation during the measurements. The addition of 1.76 and 1.31 wt% H_2O to the (Cl^- + F^-)- and chlorine-bearing basaltic melt does not show a shift in glass transition peak to higher temperature, but the addition of H_2O results in a decrease in intensity (figure 113 b-c). In contrast to that, the further addition of 3.56 wt% H_2O to the chlorine-bearing basaltic melt shows a decrease in glass transition peak to lower temperature from 1100 to 890 K. This decreasing effect is similar to the addition of 3.50 wt% H_2O to the (Cl^- + F^-)-bearing basaltic melt, which can be explained by the crystallisation of the hydrous melts. The strongest crystallisation is observed by the hydrous fluorine-bearing basaltic melts (figure 113 d). Only, the H_2O-free melt shows the typical glass transition peak. The addition of H_2O to the fluorine-bearing basaltic melts results in a crystallisation of the glass samples during the measurements. Due to these crystallisation effects, the results of the further calculation (C_p^{conf}, S_{conf} and B_e) might be affected.

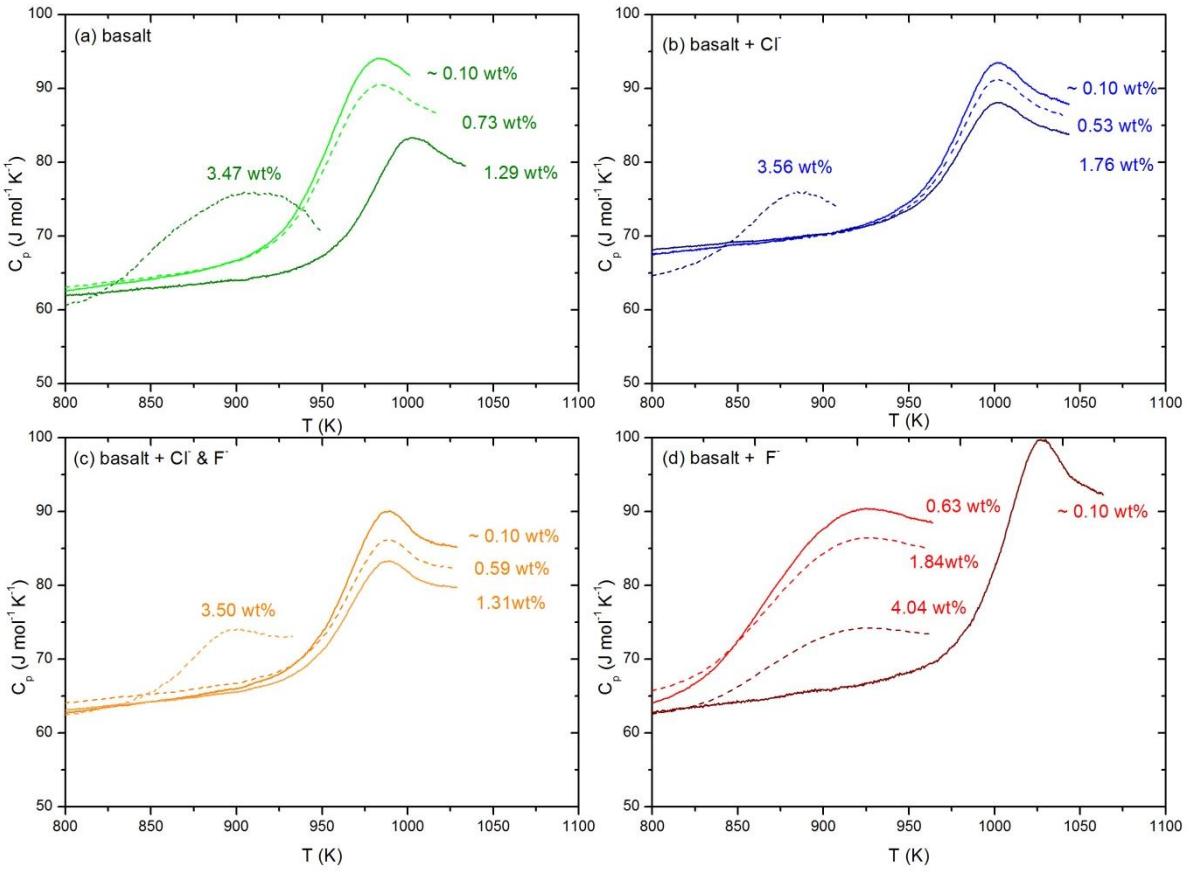

Figure 113: Heat capacity data as a function of temperature for hydrous halogen-free and -bearing basaltic melts.

Table 34 lists the fit parameters of the Maier-Kelley fit (equation 9) as well as the measured C_{pl} and C_{pg}. The addition of water to the halogen-free and the halogen-bearing basaltic melts reflects a decrease in C_{pl} and C_{pg}. Table 35 lists the parameters of C_p^{conf} and S_{conf} for a viscosity at T_g^{12} as well as T_f^{20} and B_e. The addition of H_2O to the basaltic melts decreases all parameters. The addition of 3.41 wt% H_2O to halogen-free basalt results in a decrease in the fictive temperature (T_f^{20}) by 146 K. This decreasing effect is similar to the addition of H_2O to chlorine- and fluorine-bearing basaltic melts, which results in a decrease in T_f^{20} by ~ 145 K. The addition of H_2O to (Cl^- + F^-)-bearing basaltic melt decreases the T_f^{20} by 118 K due to the lower water content. Besides the fictive temperature, C_p^{conf} and S_{conf} demonstrate a similar decreasing effect due to the addition of water, which is represented in the following illustration (figure 114 and 116).

Table 34: Parameters for the Maier-Kelley fit and the heat capacity of the glasses and melts for hydrous basaltic melts.

Sample	Maier-Kelley parameters						C_{pl}	C_{pg}
	a	Δa	b	Δb	c	Δc		
	($J\ g^{-1}K^{-1}$)	($J\ g^{-1}K^{-1}$)	($10^{-4}J\ g^{-1}K^{-1}$)	($10^{-4}J\ g^{-1}K^{-1}$)	($10^{-4}J\ g^{-1}K^{-1}$)	($10^{-4}J\ g^{-1}K^{-1}$)	($J\ mol^{-1}K^{-1}$)	($J\ mol^{-1}K^{-1}$)
BA-0-III	0.439	0.007	2.429	0.008	-4.674	0.076	91.69	68.56
BA-0_0.73H	0.464	0.007	2.164	0.001	-3.750	0.071	87.04	67.98
BA-0_1.29H	0.192	0.009	5.108	0.002	-2.660	0.010	79.38	65.58
BA-0_3.47H	0.642	0.008	6.695	0.009	-2.982	0.096	70.36	61.65
BA-Cl-III	0.515	0.009	2.142	0.001	-6.838	0.010	87.87	72.38
BA-Cl_0.53H	0.525	0.009	2.001	0.009	-5.755	0.098	86.05	71.51
BA-Cl_1.76H	0.557	0.070	1.670	0.008	-5.028	0.080	83.76	70.89
BA-Cl_3.56H	0.588	0.024	0.853	0.003	-9.682	0.023	73.80	64.94
BA-Cl-F-III	0.438	0.018	2.471	0.002	-3.549	0.022	85.21	65.89
BA-Cl-F_0.59H	0.496	0.002	1.903	0.001	-3.754	0.016	82.24	67.46
BA-Cl-F_1.31H	0.499	0.001	1.741	0.001	-3.362	0.015	79.63	67.09
BA-Cl-F_3.50H	0.580	0.002	0.805	0.003	-1.283	0.003	72.98	65.16
BA-F-III	0.473	0.001	2.122	0.002	-6.756	0.017	92.34	68.12
BA-F_0.63H	0.428	0.001	2.647	0.001	-4.179	0.011	88.58	67.02
BA-F_1.84H	0.472	0.002	2.304	0.001	-1.883	0.012	84.94	68.57
BA-F_4.04H	0.517	0.008	1.351	0.009	-6.741	0.078	73.32	65.91

Table 35: Parameters of C_p^{conf} and S_{conf} for the viscosity at T_g^{12}. The measurements were performed with a constant heating and cooling rate of 20 K min^{-1}.

Sample	T_f^{20}	C_p^{conf}	$S_{conf}(Tg^{12})$	$\Delta S_{conf}(Tg^{12})$	B_e	Δ B_e
	(K)	($J\ mol^{-1}K^{-1}$)	($J\ mol^{-1}K^{-1}$)	($J\ mol^{-1}K^{-1}$)	($kJ\ mol^{-1}$)	($kJ\ mol^{-1}$)
BA-0-III	894	23.13	20.17	1.71	687.30	55.74
BA-0_0.73H	862	19.06	16.81	1.32	551.16	42.51
BA-0_1.29H	822	13.80	11.64	1.74	364.24	51.92
BA-0_3.47H	748	8.71	8.86	0.66	251.97	18.59
BA-Cl-III	901	15.49	12.98	0.99	445.28	33.10
BA-Cl_0.53H	864	14.54	11.04	0.62	363.14	19.86
BA-Cl_1.76H	802	12.87	11.25	0.52	343.36	15.38
BA-Cl_3.56H	747	8.96	10.90	1.20	310.23	31.57
BA-Cl-F-III	877	19.32	17.09	0.91	570.81	29.29
BA-Cl-F_0.59H	849	14.78	9.95	0.87	321.80	27.34
BA-Cl-F_1.31H	789	12.54	11.51	1.06	345.74	30.99
BA-Cl-F_3.50H	759	7.82	10.02	1.72	290.01	48.74
BA-F-III	906	24.22	22.22	1.15	715.58	36.73
BA-F_0.63H	867	21.56	15.37	1.30	482.48	40.99
BA-F_1.84H	816	16.37	15.11	1.34	437.39	39.21
BA-F_4.04H	763	7.41	9.54	1.63	274.80	46.19

Figure 114 illustrates the configurational heat capacity C_p^{conf} as a function of water content of halogen-free and -bearing basaltic melts. The addition of H_2O to the halogen-free basaltic melts results in an exponential decrease in C_p^{conf} from 23.13 to 8.71 J mol^{-1} K^{-1}. The increasing water content in chlorine-bearing basaltic melt results in a slight linear decrease in C_p^{conf} from 15.49 to 8.86 J mol^{-1} K^{-1}, whereas the addition of H_2O to fluorine-bearing basaltic melts shows a similar decrease in C_p^{conf} from 24.22 to 7.41 J mol^{-1} K^{-1} as the halogen-free basaltic melt. Furthermore, the presence of H_2O in (Cl^- + F^-)-bearing basaltic melts results in an exponential decrease in C_p^{conf} from 19.32 to 7.82 J mol^{-1} K^{-1}, which reflects a similar decrease in C_p^{conf} as the halogen-free basalt.

Figure 115 illustrates the effect of OH groups on C_p^{conf} for halogen-free and –bearing basaltic melts. This diagram clearly shows the linear decrease in C_p^{conf} due to increasing OH groups for halogen-free basaltic melts. Previously in figure 114, the increase in H_2O results in linear decrease of C_p^{conf}, which is affected by increasing molecular water content in the halogen-free basaltic melts. The effect of OH groups has a strong influence on C_p^{conf} in fluorine-bearing basaltic melts, whereas the effect of OH groups on C_p^{conf} in chlorine-bearing basaltic melts results in a slight linear decrease. Furthermore, the effect of OH groups on C_p^{conf} in (Cl^- + F^-)-bearing basaltic melts results in a linear decrease due to the high Cl^-/F^-. Thus, figure 115 reflects the strong influence of the water species (OH groups) on C_p^{conf}.

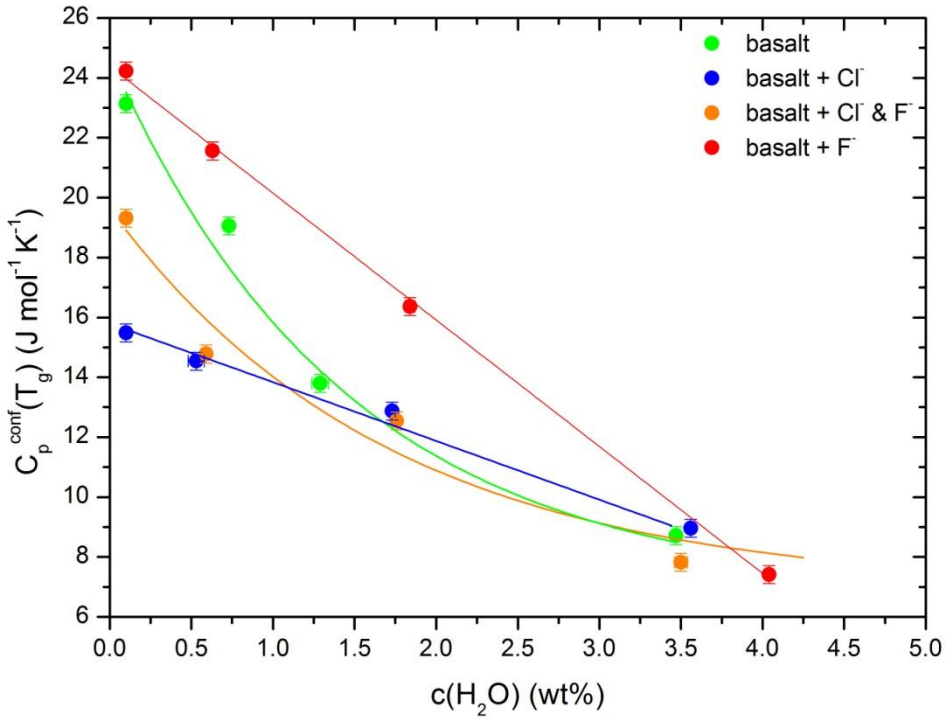

Figure 114: Configurational heat capacity C_p^{conf} as a function of water content for halogen-free and -bearing basaltic melts.

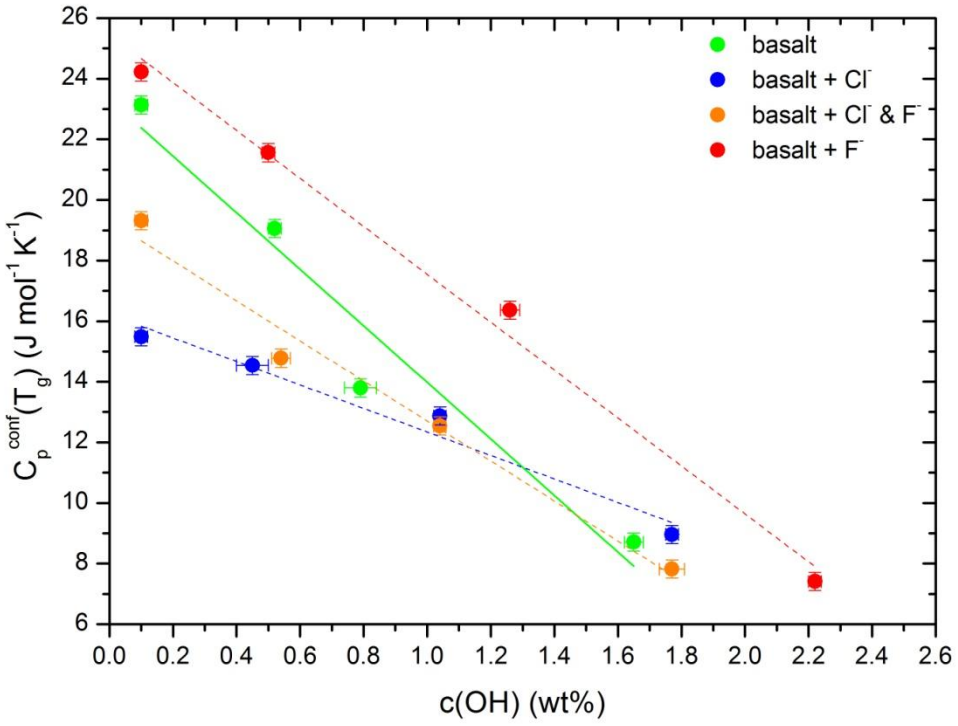

Figure 115: Configurational heat capacity C_p^{conf} as a function of OH content for halogen-free and -bearing basaltic melts.

The S_{conf} values as a function of water content for halogen-free and –bearing basaltic glass are illustrated in figure 116. The increasing H_2O content in halogen-free basaltic melt results in a decrease in S_{conf} from 20.17 to 8.86 J mol^{-1} K^{-1}. The addition of H_2O to the chlorine-bearing basaltic melt shows the smallest decrease in S_{conf} from 12.98 to 10.90 J mol^{-1} K^{-1}, whereas the presence of H_2O in fluorine-bearing basaltic melt decreases S_{conf} by 12.68 J mol^{-1} K^{-1} (from 22.22 to 9.54 J mol^{-1} K^{-1}). The addition of H_2O to (Cl^- + F^-)-bearing basaltic melts shows a similar exponential decrease in S_{conf} from 17.08 to 10.02 J mol^{-1} K^{-1} than the halogen-free basaltic melts. As a consequence S_{conf} is not only a function of water content but also halogen content.

Figure 117 represents the effect of OH groups on S_{conf} for halogen-free and –bearing basaltic melts. The effect is particularly obvious in halogen-free basalt, where the increasing amount of OH groups results in a nearly linear decrease in S_{conf}. The chlorine-bearing basalt does also not show changes in S_{conf} as shown in figure 116. Furthermore, the effect of OH groups on S_{conf} shows a similar exponential decrease compared to figure 116 for fluorine- and (Cl^- + F^-)-bearing melts. Excepted from fluorine-bearing basaltic melts, the high water content does not show a difference in OH groups.

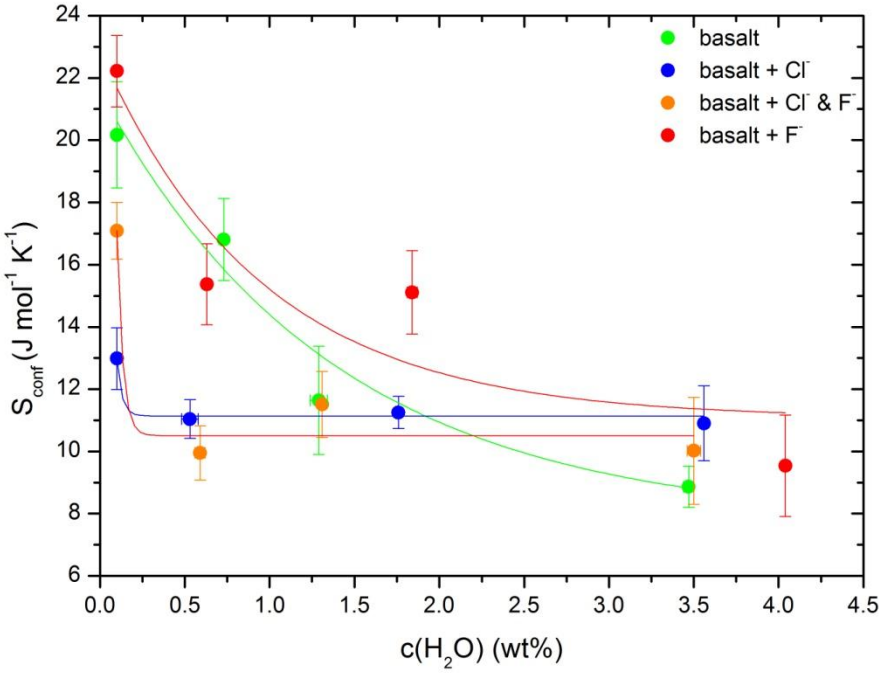

Figure 116: Configurational entropy S_{conf} as a function of water content for halogen-free and -bearing basaltic melts.

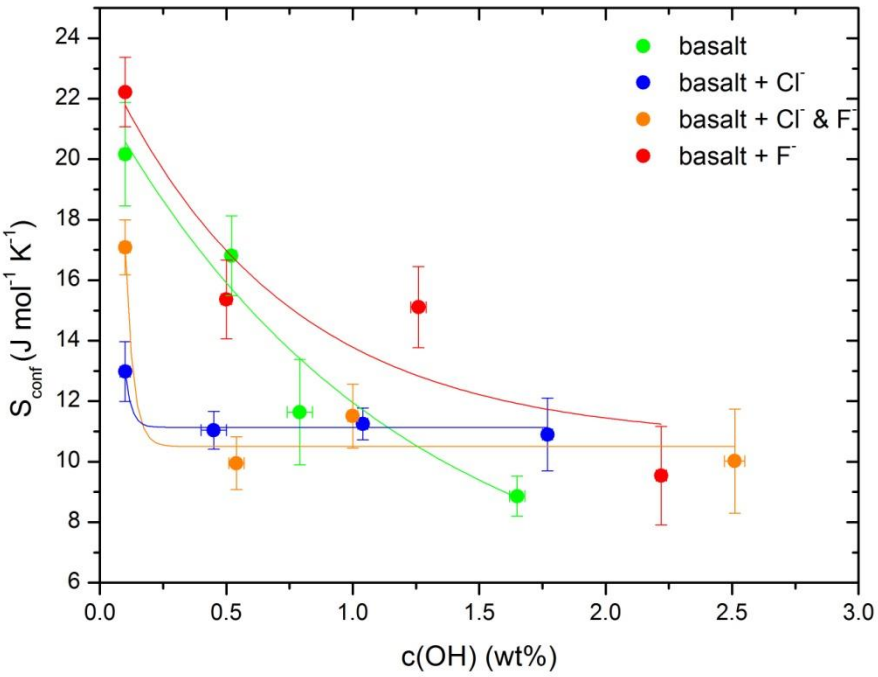

Figure 117: Configurational entropy S_{conf} as a function of OH content for halogen-free and -bearing basaltic melts.

Figure 118 illustrates B_e as a function of H_2O content for the halogen-free and –bearing basaltic melts. The addition of 3.47 wt% H_2O to the halogen-free basaltic melt results in a decrease in B_e from 687.30 to 251.97 kJ mol^{-1}. The presence of water in fluorine-bearing basaltic melts results in a similar decreasing trend than the halogen-free basaltic melt. The hydrous chlorine-bearing basaltic melts show the smallest variation of B_e from 445.28 to 338.23 kJ mol^{-1}. The strong decreasing effect of B_e in hydrous fluorine-bearing basaltic melt is dampened by the addition of Cl^-. This results in a decrease in B_e from 570.81 to 290.01 kJ mol^{-1}.

The B_e values as a function of OH groups for halogen-free and –bearing basaltic melts are illustrated in figure 119. The increasing OH content in halogen-free basalt results in nearly linear decrease in B_e compared to the exponential decrease in figure 118. In comparison to halogen-free basalt, the increase of OH groups in halogen-bearing basaltic melts does not show any difference in exponential decreasing trend.

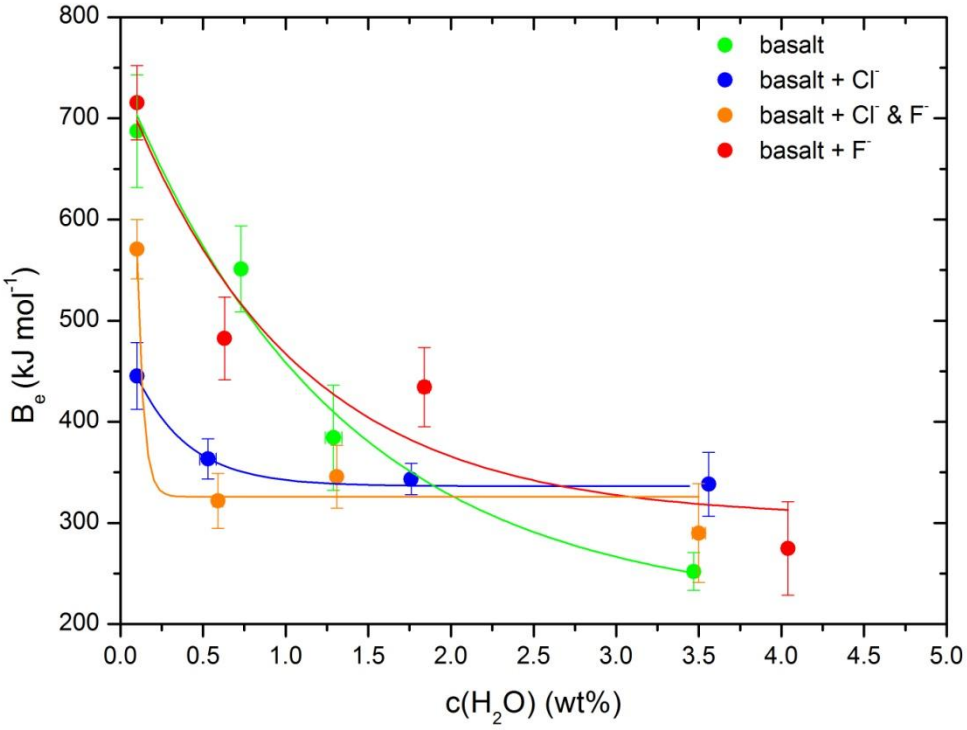

Figure 118: B_e as a function of water content for halogen-free and -bearing basaltic melts.

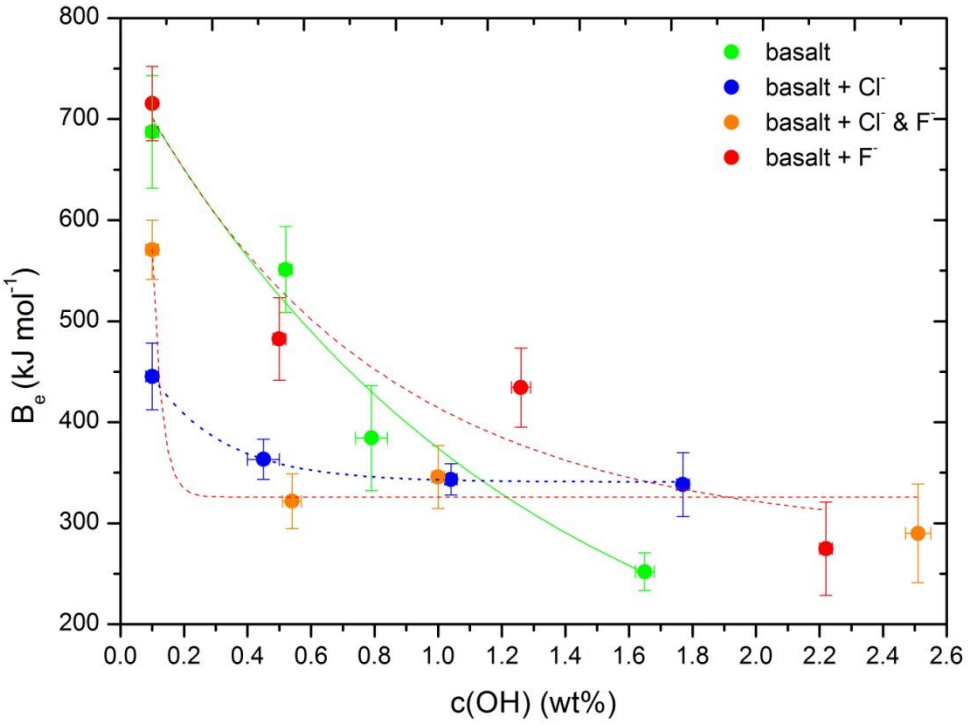

Figure 119: B_e as a function of OH content for halogen-free and -bearing basaltic melts.

The dependence between B_e and S_{conf} is represented in in figure 120. All hydrous halogen-free and –bearing basaltic melts follow a linear trend, whereby the relation between S_{conf} and B_e is confirmed. Webb (2005) suggested that the B_e/S_{conf} term reflects the flow mechanism, which results of a dependence between B_e/S_{conf} term and composition. This dependence of B_e/S_{conf} on the H_2O content of basaltic melts is illustrated in figure 121. The increasing H_2O content (up to 3.47 wt%) in basaltic melts results in a strong decrease in B_e/S_{conf} from 34 to 28. The addition of 3.56 wt% H_2O to the chlorine-bearing melts shows a decrease in B_e/S_{conf} from 34 to 31, whereas the presence of 4.04 wt% H_2O in fluorine-bearing basaltic melts results in a decrease in B_e/S_{conf} from 32 to 29. The (Cl^- + F^-)-bearing basaltic melt decreases B_e/S_{conf} from 33 to 29 due to the addition of H_2O. To sum up, the presence of H_2O in halogen-bearing basaltic melts results in an exponential decrease in B_e/S_{conf}. The further increasing water content (above 3 wt%) results in a slight increase in B_e/S_{conf}, which can result of the formation of crystallisation nuclei. Figure 122 represents the B_e/S_{conf} as a function of OH groups for the halogen-free and –bearing basalt. The previous linear trend disappears by the described water specification and the increasing OH groups result in exponential decrease in B_e/S_{conf}. All halogen-bearing melts can be described by a linear regression, which indicates a stronger influence of OH groups on halogen-bearing melt than halogen-free basalt.

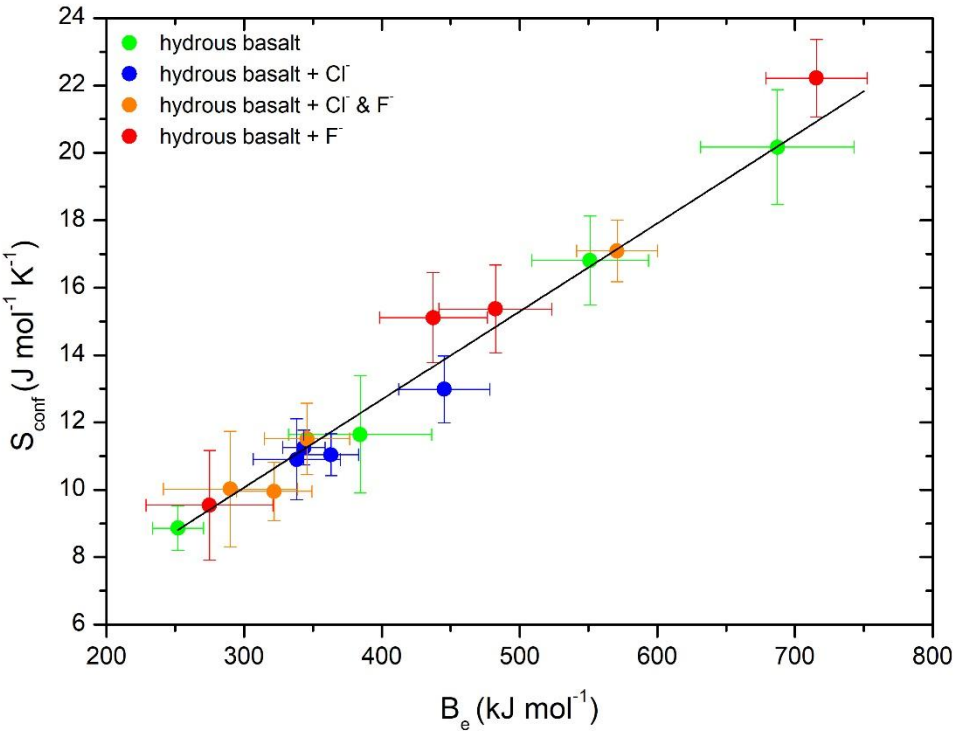

Figure 120: Configurational entropy S_{conf} as a function of B_e of basaltic melts.

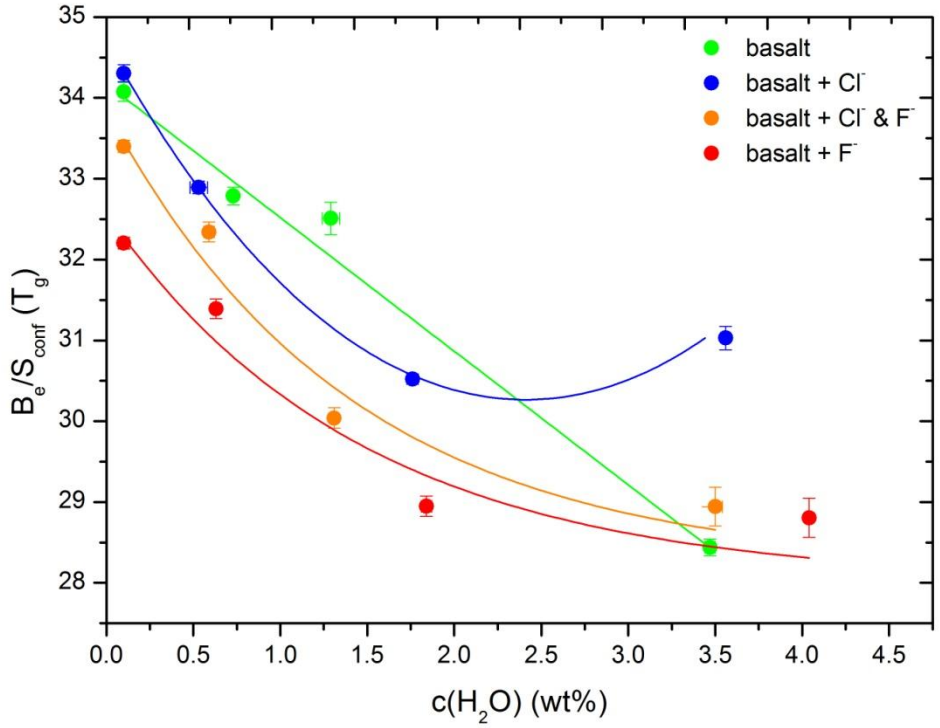

Figure 121: B_e/S_{conf} terms as a function of H_2O content for halogen-free and –bearing basaltic melts.

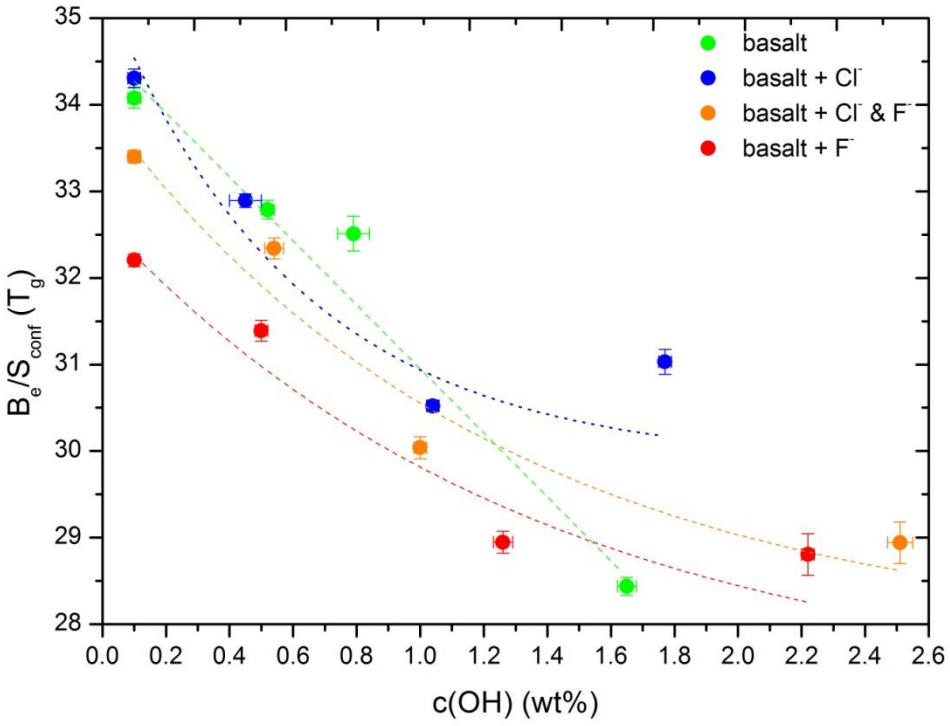

Figure 122: B_e/S_{conf} terms as a function of OH content for halogen-free and –bearing basaltic melts.

5.5.2. Effect of CO_2 on the heat capacity of basaltic melts

The heat capacity data as a function of temperature is shown in figure 123. The addition of 1479 ppm CO_2 to the present basaltic melt results in a slight shift of the onset temperature of the glass transition peak to higher temperature. Further addition of 2199 ppm CO_2 to the present basaltic melt shows a decrease of the glass transition peak and a shift of T_g[12] from 1020 to 970 K (figure 123 a). In comparison to the hydrous basaltic melts, the CO_2-bearing basaltic melts tends to crystallise during the cooling and heating rate at a 20 K min^{-1}. The addition of 1442 and 3658 ppm CO_2 to chlorine-bearing basaltic melt result in a shift in glass transition peak to higher temperature from 1000 to 1025 K and a decrease in intensity of the glass transition peak (figure 123 b). A crystallisation effect is not observed for the addition of CO_2 to chlorine-bearing basaltic melt. The addition of ~1000 ppm CO_2 to (Cl^- + F^-) and fluorine-bearing basaltic melts results in a slight shift of the onset temperature of the glass transition peak to higher temperature, whereas the further addition of CO_2 shows a shift of T_g[12] from 980 to 890 K (figure 123 c – basalt + Cl^- & F^-) and from 990 to 930 K (figure 123 d – basalt + F^-). This reflects a crystallisation of the samples during the measurements, which was reflected by a consistently discoloration of the samples. The fit parameters of the Maier-Kelley fit (equation 9) as well as the heat capacity of the glasses and the melts are given in table 36.

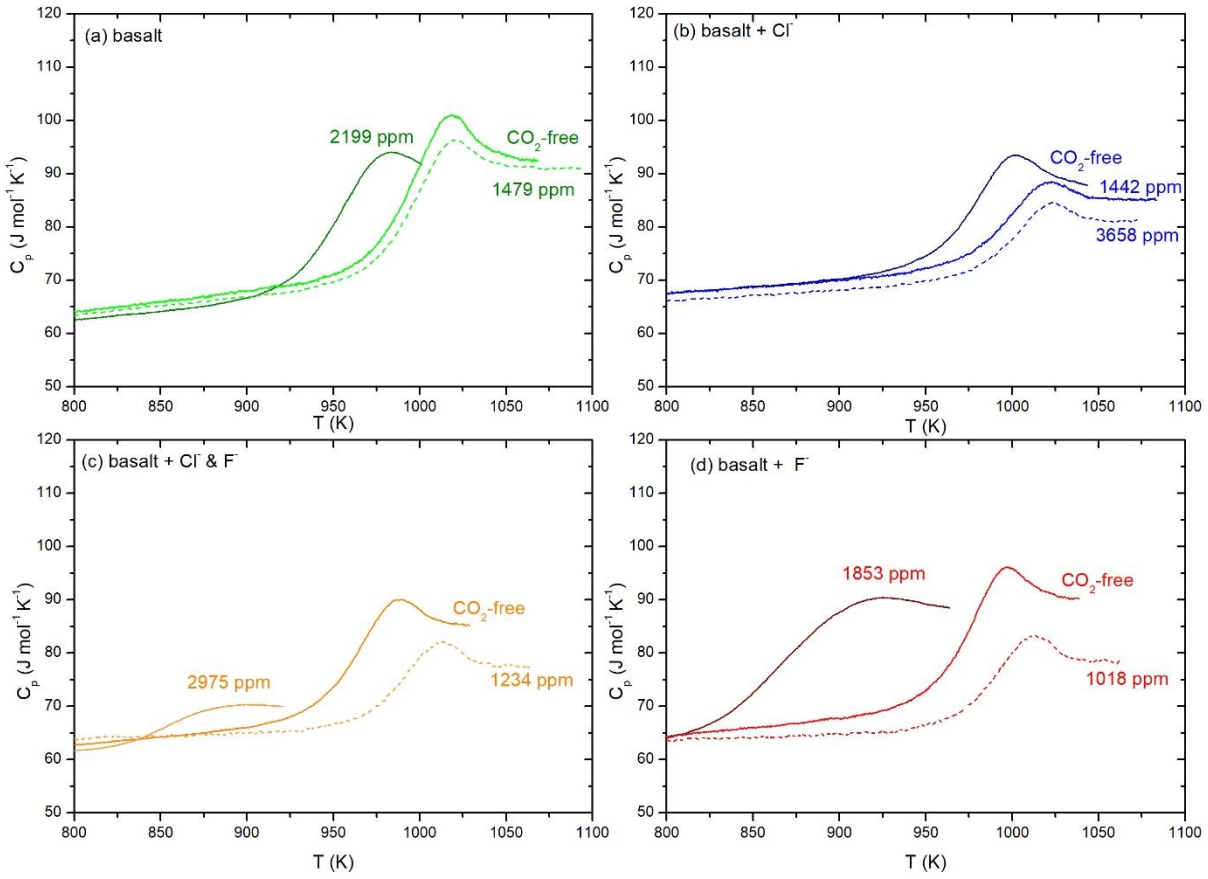

Figure 123: Heat capacity data as a function of temperature for halogen-free and -bearing basaltic melts with CO_2.

Table 36: Parameters for the Maier-Kelley fit and the heat capacity of the glasses and melts for CO_2-bearing basaltic melts.

Sample	Maier-Kelley parameters						C_{pl}	C_{pg}
	a	Δa	b	Δb	c	Δc		
	($J\,g^{-1}K^{-1}$)	($J\,g^{-1}K^{-1}$)	($10^{-4}J\,g^{-1}K^{-1}$)	($10^{-4}J\,g^{-1}K^{-1}$)	($10^{-4}J\,g^{-1}K^{-1}$)	($10^{-4}J\,g^{-1}K^{-1}$)	($J\,mol^{-1}K^{-1}$)	($J\,mol^{-1}K^{-1}$)
BA-0-III	0.439	0.007	2.429	0.008	-4.674	0.076	91.69	68.56
BA-0_0.15C	0.325	0.003	3.789	0.003	-1.117	0.050	92.52	73.24
BA-0_0.23C	0.354	0.002	3.420	0.002	-5.835	0.027	91.38	71.99
BA-Cl-III	0.515	0.009	2.142	0.001	-6.838	0.010	87.87	72.38
BA-Cl_0.12C	0.551	0.001	1.705	0.001	-5.395	0.001	85.09	73.73
BA-Cl_0.37C	0.575	0.001	1.274	0.001	-8.093	0.013	80.91	71.20
BA-Cl-F-III	0.438	0.018	2.471	0.002	-3.549	0.022	85.21	65.89
BA-Cl-F_0.14C	0.584	0.001	0.759	0.001	-2.648	0.013	77.23	65.48
BA-Cl-F_0.29C	0.643	0.007	0.151	0.008	-7.824	0.063	70.17	61.76
BA-F-III	0.473	0.001	2.122	0.002	-6.756	0.017	92.34	68.12
BA-F_0.09C	0.481	0.002	2.249	0.002	-8.698	0.017	90.25	71.36
BA-F_0.20C	0.578	0.001	0.803	0.001	-3.014	0.015	78.39	66.03

The fictive temperature (T_f^{20}), configurational heat capacity (C_p^{conf}) and fit parameter S_{conf} and B_e are given in table 37. The addition of 2199 ppm CO_2 to the halogen-free basaltic melt results in a decrease in T_f^{20} from 894 to 879 K. This effect is enhanced by the addition of H_2O to the fluorine-bearing basaltic melt. The addition of H_2O to the fluorine-bearing basaltic melt shows a decrease in T_f^{20} from 906 to 860 K, whereas the increasing water content in chlorine-bearing basaltic melt results in a decrease in T_f^{20} by 12 K. The addition of 1234 ppm CO_2 to (Cl^- + F^-)-bearing basaltic melts shows an increase in T_f^{20} from 877 to 886 K, but the further addition of 2975 ppm CO_2 results in a decrease in T_f^{20} by 8 K.

Table 37: Parameters of C_p^{conf} and S_{conf} for the viscosity at T_g^{12}. The measurements were performed at constant heating and cooling rate of 20 K min^{-1}.

Sample	T_f^{20} (K)	C_p^{conf} (J mol^{-1}K^{-1})	$S_{conf}(T_g^{12})$ (J mol^{-1}K^{-1})	$\Delta S_{conf}(T_g^{12})$ (J mol^{-1}K^{-1})	B_e (kJ mol^{-1})	ΔB_e (kJ mol^{-1})
BA-0-III	894	23.13	20.17	1.71	687.30	55.74
BA-0_0.15C	884	19.28	16.76	1.17	564.67	37.73
BA-0_0.23C	879	19.39	16.34	1.60	547.68	51.57
BA-Cl-III	901	15.49	12.98	0.99	445.28	33.10
BA-Cl_0.12C	901	11.36	9.09	0.48	311.38	16.39
BA-Cl_0.37C	889	9.71	7.68	0.16	259.62	5.32
BA-Cl-F-III	877	19.32	17.09	0.91	570.81	29.29
BA-Cl-F_0.14C	886	11.75	10.27	0.53	346.97	17.28
BA-Cl-F_0.29C	878	8.41	7.20	0.41	240.99	13.38
BA-F-III	906	24.22	22.22	1.15	715.58	36.73
BA-F_0.09C	891	18.89	16.00	1.12	537.86	37.55
BA-F_0.20C	860	12.36	8.84	0.36	289.23	11.81

In figure 124, the configurational heat capacity (C_p^{conf}) is represented as a function of CO_2 content for halogen-free and –bearing basaltic melts. The addition of CO_2 to the halogen-free basaltic melts results in a decrease in C_p^{conf} from 23.13 to 19.39 J mol^{-1} K^{-1}. A similar decreasing trend in C_p^{conf} is shown for the chlorine-bearing basaltic melts with CO_2. The presence of CO_2 in fluorine-bearing basaltic melts results in a strong decrease in C_p^{conf} from 24.22 to 12.36 J mol^{-1} K^{-1}. Furthermore, the addition of 2928 ppm CO_2 to (Cl^- + F^-)-bearing basaltic melts shows a decrease in C_p^{conf} by 10.91 J mol^{-1} K^{-1} (from 19.32 to 8.41 J mol^{-1} K^{-1}).

The configurational entropy (S_{conf}) is illustrated in figure 125. The increasing CO_2 content in basaltic melts results in a decrease in S_{conf}. This decreasing trend is similar to the decreasing trend of C_p^{conf} (figure 124). The addition of 2199 ppm CO_2 to the halogen-free basaltic glass shows a decrease in S_{conf} from 20.17 to 16.34 J mol^{-1} K^{-1}. This decreasing trend is similar to the presence of CO_2 in chlorine-bearing basaltic melts. The fluorine-bearing basaltic melts show the strongest effect of CO_2 on the S_{conf} values. The addition of 1853 ppm CO_2 to the fluorine-bearing basaltic melts results in a linear decrease in S_{conf} from 22.22 to

8.84 J mol^{-1} K^{-1}, whereas the addition of 2975 ppm CO_2 to the (Cl^- + F^-)-bearing basaltic melts results in an exponential decrease in S_{conf} by 9.89 J mol^{-1} K^{-1} (from 17.09 to 7.20 J mol^{-1} K^{-1}). As a consequence, the presence of chlorine in basaltic melts dampens the decreasing effect on S_{conf} and the linear decreasing trend of the fluorine-bearing melt with CO_2 can results in an exponential trend due to increasing CO_2 content.

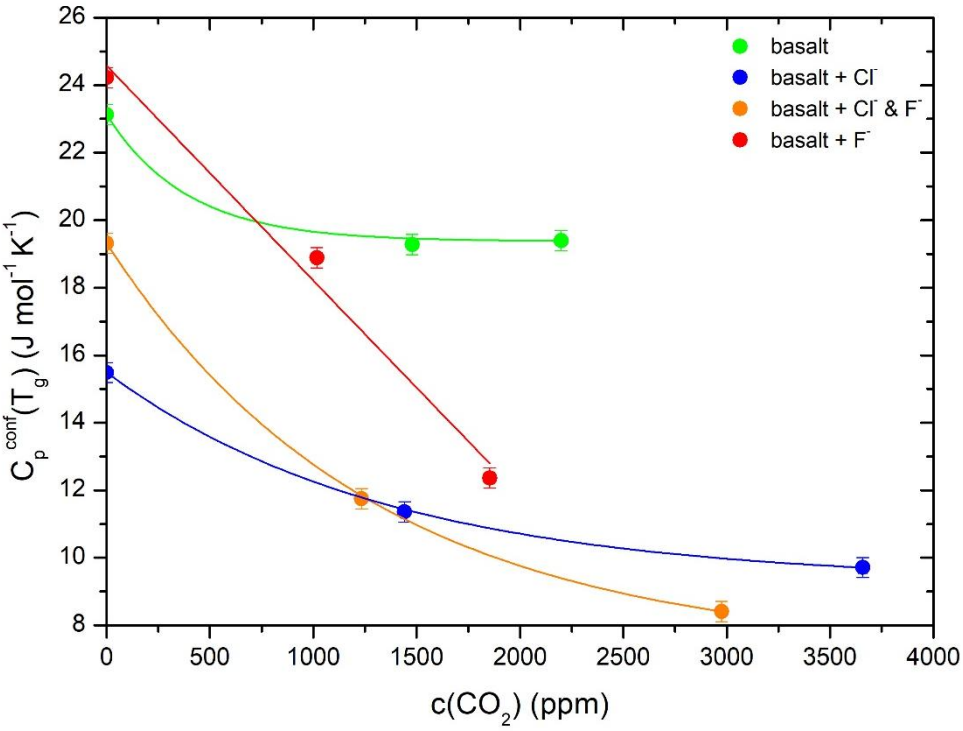

Figure 124: Configurational heat capacity C_p^{conr} as function of CO_2 content for halogen-free and -bearing melts.

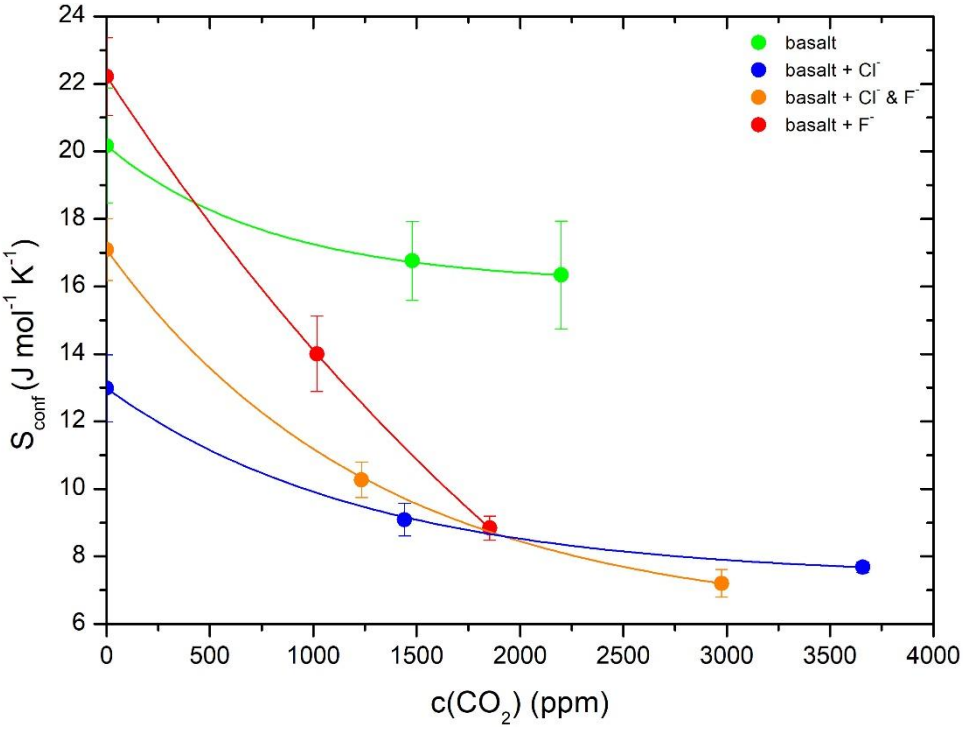

Figure 125: Configurational entropy S_{conf} as a function of CO_2 content for halogen-free and -bearing melts.

Figure 126 represents the B_e value as a function of CO_2 content for halogen-free and –bearing basaltic melts. It is shown that the B_e values decrease by the increasing CO_2 content. The addition of CO_2 to the halogen-free and chlorine-bearing basaltic melts results in a slight decrease in B_e with up to 185 kJ mol^{-1}, whereas the presence of CO_2 in fluorine- and (Cl^- + F^-) -bearing basaltic melts shows a strong decrease in B_e with up to 425 kJ mol^{-1}. This decrease in B_e reflects a depolymerisation due to the decreasing CO_2 content.

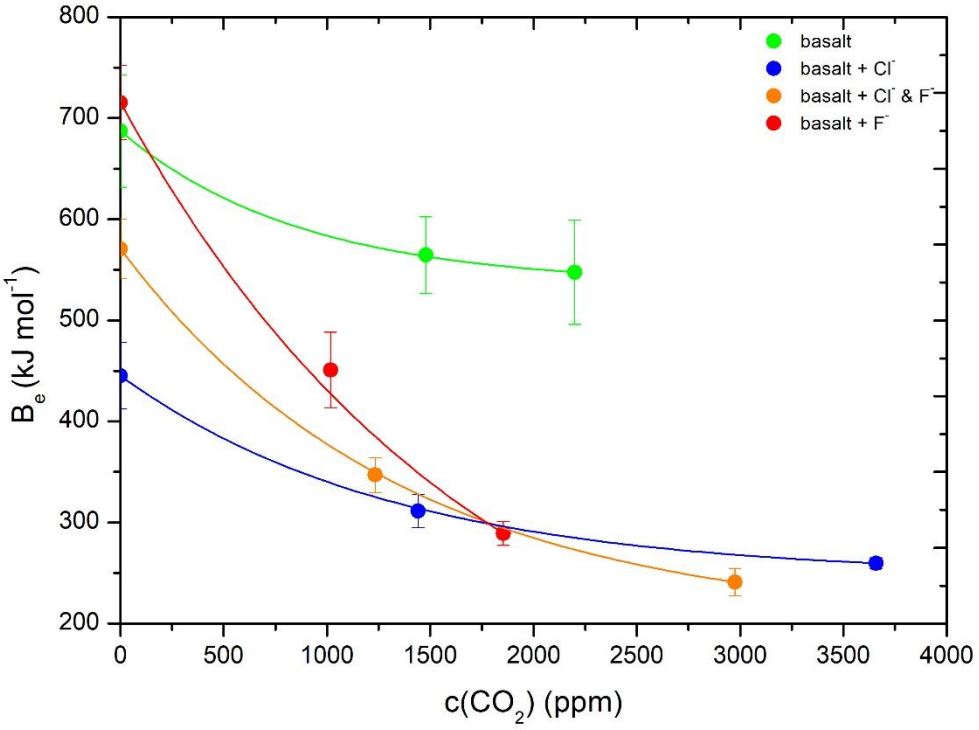

Figure 126: B_e as a function of CO_2 content for halogen-free and -bearing basaltic glasses.

In figure 127, S_{conf} is represented as a function of B_e value for halogen-free and –bearing basaltic melts with CO_2. The results show a linear increase in B_e/S_{conf} (T_g) for all CO_2-bearing basaltic melts. The B_e/S_{conf} term is plotted as a function of CO_2 content in figure 128. The addition of 2199 ppm CO_2 to halogen-free basaltic melts results in a decrease in B_e/S_{conf} from 34.08 to 33.52. The presence of 3658 ppm CO_2 in chlorine-bearing basaltic melt shows a similar decrease in B_e/S_{conf} from 34.31 to 33.81. An increasing effect of B_e/S_{conf} can be observed for the fluorine-bearing basaltic melt with CO_2. The increasing CO_2 content (1853 ppm) in the fluorine-bearing melt results in an increase in B_e/S_{conf} from 32.20 to 37.72. This increasing effect of CO_2 on the B_e/S_{conf} of fluorine-bearing basaltic melts becomes apparent for the (Cl^- + F^-)-bearing basaltic melts. The addition of 1234 ppm CO_2 results in an increase in B_e/S_{conf} from 33.40 to 33.79, but further addition of 2975 ppm CO_2 shows a decrease in CO_2 up to 33.47. As a consequence, the presence of CO_2 in fluorine-bearing

basaltic melts changes the flow mechanism in a different way than the CO_2 in chlorine-bearing basaltic melts. Furthermore, a high CO_2 content (> 1800 ppm) in fluorine-bearing basaltic melts leads to an earlier crystallisation during heating experiments (e.g. differential scanning calorimetry and micropenetration viscometry measurements).

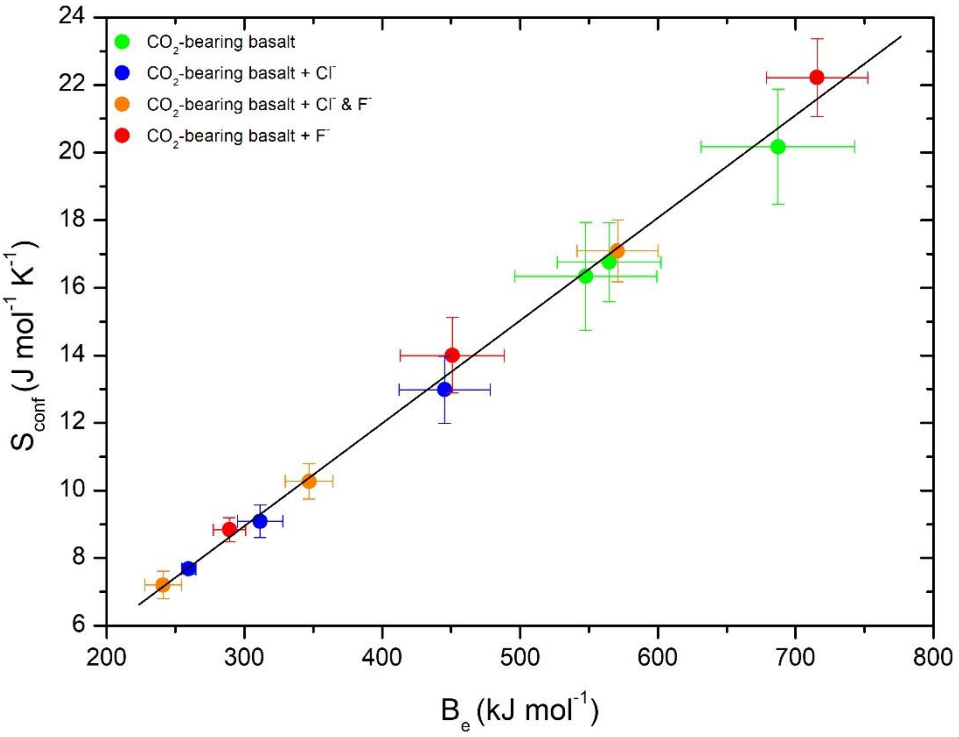

Figure 127: Configurational entropy S_{conf} as a function of B_e of basaltic melts.

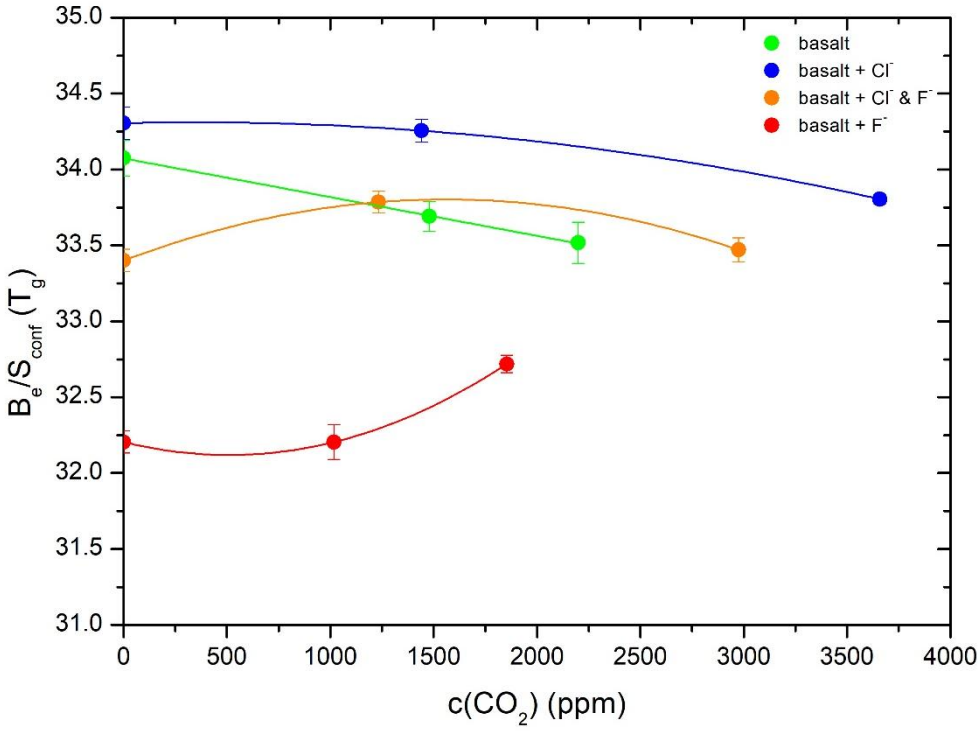

Figure 128: B_e/S_{conf} terms as a function of CO_2 content for halogen-free and –bearing basaltic melts.

6. Discussion

6.1. H_2O-bearing basaltic glasses

6.1.1. Influence of H_2O on the viscosity of basaltic melts

Figure 129 illustrates a comparison of the viscosity of the present basaltic melts as a function of water content with literature data (Baasner et al. 2013b; Robert et al. 2015). The first incorporation of 0.73 wt% H_2O results in a decrease in viscosity by 1.0 log units, whereas the increasing water content (1.29 wt% H_2O) shows a further decrease in viscosity by 1.8 log units. The most significant decrease in viscosity results from the addition of 3.47 wt% H_2O to the basaltic melt and shows a decreasing viscosity effect from 9.2 to 6.8 Pa s. Consequently, the increasing H_2O content in basaltic melts results in an decrease in viscosity (green circles). These results are consistent with those reported by Stolper (1982a). The author described that the melt viscosity is dependent on the degree of polymerisation. At low H_2O content, the water has the form of hydroxyl groups, which results in a strong depolymerisation of the melt. In contrast to the OH groups, the molecular water results in a less extensive depolymerisation of the melt structure (Stolper 1982a). These results correlate well with the exponential decrease in viscosity of the present basalt due to the addition of H_2O.

In figure 129, Robert et al. (2015) observed a stronger decrease in viscosity by 7.0 log units by the addition of 2.70 wt% H_2O to basaltic melts (grey circles). The authors synthesised Fuego basalt (fu06) and synthetic basalt (sb) with varying water content. An essential difference is the absence of iron in the synthetic basalt (sb), whereas the magnesium content was doubled (14.87 wt%). Therefore, the fu06 represents an iron-bearing basaltic melt with a similar composition as the sb melt without iron. The two basaltic melts fu06 (grey circles) and sb (rose circles) are consistent with the exponential trend despite the differences in FeO_{total} and MgO contents. Our findings differ from the previously recorded data by Robert et al. (2015) and show a slighter decreasing trend of viscosity at increasing water contents. This deviation in viscosity trends can result from differences in the melt composition or incorporation mechanisms of water in the structure. Al_2O_3 content of 9.45 mol% (present basalt) compared to 11.05 mol% (fu06) is essentially different. Furthermore, the present basalt shows a higher CaO content of 14.21 mol% (present basalt) than 10.25 mol% in fu06.

To verify this thesis, hydrous peralkaline (NACS – turquoise circles) melt from Baasner et al. (2013b) is plotted with the present data. The peralkaline melt (NACS) show a strongest decreasing trend of viscosity compared to the present basalt and the data by Robert et al. (2015). The peralkaline melt exhibit Al_2O_3 content of 11.28 mol%. Consequently, the Al_2O_3 content does not change the viscosity trends. In contrast to Al_2O_3 content, the peralkaline

melt shows the lowest value of 5.23 mol%. Thus, the increasing CaO content results in a stronger decrease in viscosity from present basalt (12.37 mol%) to NACS (5.23 mol%).

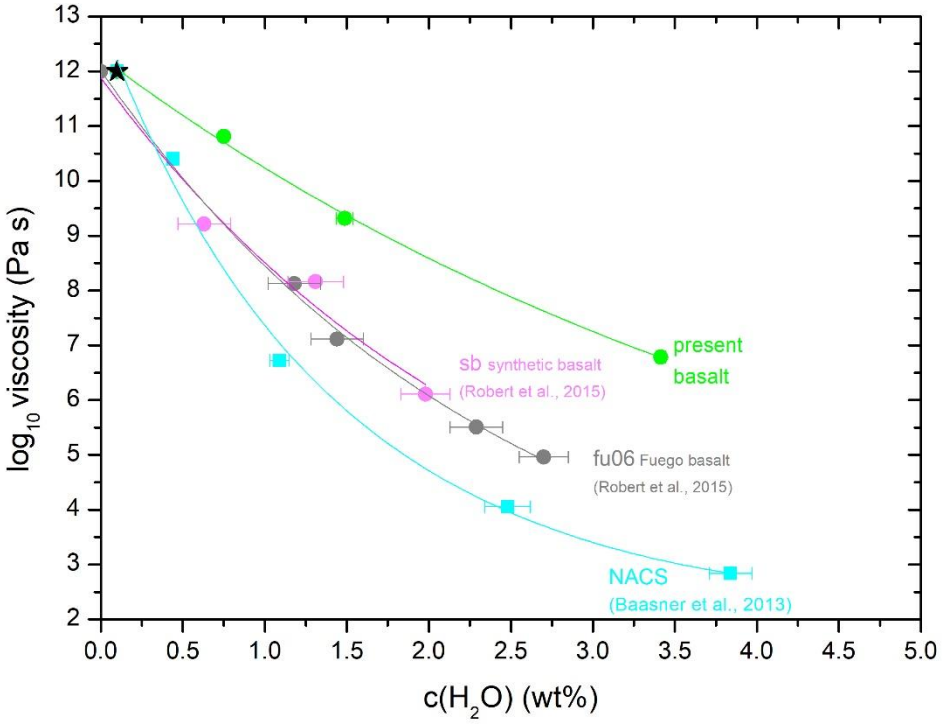

Figure 129: The change in viscosity due to the addition of H_2O at the same temperature (894 K) as the original melt at 10^{12} Pa s. Literature data: Robert et al. (2015) - fu06 (grey circles) and sb (rose circles); Baasner et al. (2013a) – NACS (turquoise rectangles). The error bars of log_{10} viscosity are smaller than the symbols.

Figure 130 demonstrates a comparison of the viscosity of present basaltic melts as a function of water content for halogen-free and –bearing basaltic melts. The addition of 3.47 wt% H_2O results in a decrease in viscosity by 5 log units. The addition of H_2O to the chlorine- and fluorine-bearing melts shows a similar decrease in viscosity by 5 log units as the halogen-free basaltic melts, whereas the presence of H_2O in (Cl^- + F^-)-bearing melts shows a smaller decrease in viscosity by 4 log units due to the mixed effect of both halogens and H_2O. Generally, the presence of H_2O in halogen-free and –bearing basaltic melts results in a strong decrease in viscosity.

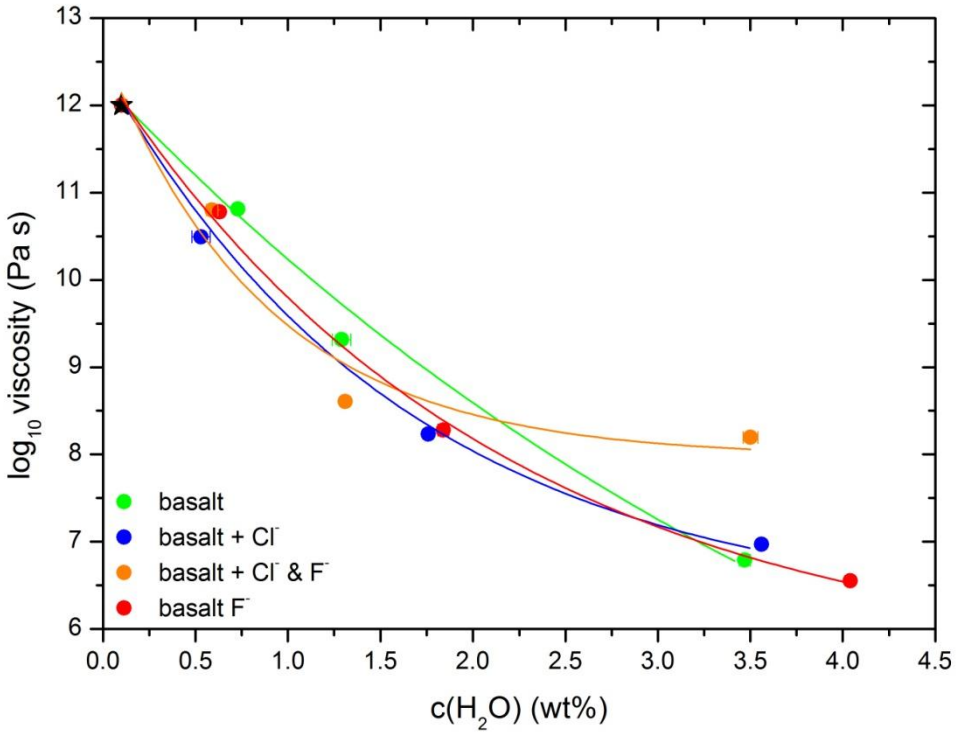

Figure 130: The change in viscosity due to the addition of H_2O at the same temperature as the original glass at 10^{12} Pa s for halogen-free and –bearing basaltic melts. The error bars of log_{10} viscosity are smaller than the symbols.

Previous studies proposed that Fe^{2+}/Fe_{total} in melts does not change during the high viscosity measurements due to the slow redox kinetics (Stabile et al. 2016 reference there in). The formations of cluster have to be check. This is consistent with the experiments of evolution of Fe^{2+}/Fe_{total} as a function of duration time and shows an equilibrated melt after 20 h, whereas an analysis time up to 2 h does not change the Fe^{2+}/Fe_{total} (figure 55). Figure 131 illustrates the pressure effect on the viscosity of hydrous basaltic melts. The change in viscosity is described at the same temperature as the original melt (1 atm basalt - green asterisk) at a viscosity of 10^{12} Pa s. The synthesis of the *dry* basalt (~0.10 wt% H_2O) at 3 kbar results in a decrease in viscosity by 2 log units.

As a consequence, a qualitative statement about the viscosity effect of H_2O and CO_2-bearing silicate melts requires a *dry* starting sample (up to 0.10 wt% H_2O). In chapter B (4.3.1. Halogen dependence of viscosity for basaltic glasses) the decreasing viscosity is described as a function of increasing Fe^{2+}/Fe_{total}. The increasing Fe^{2+}/Fe_{total} in halogen-free basalt by 0.15 results in a decrease in viscosity by 0.3 log units (figure 131). The Fe^{2+}/Fe_{total} increases from 0.19 (1 atm basalt) to 0.60 (3 kbar basalt) due to the synthesis in IHPV. Consequently, the Fe^{2+}/Fe_{total} in 3 kbar basalt increases by 0.41 during the synthesis in IHPV, whereby a decrease in viscosity up to 1.2 log units can be observed.

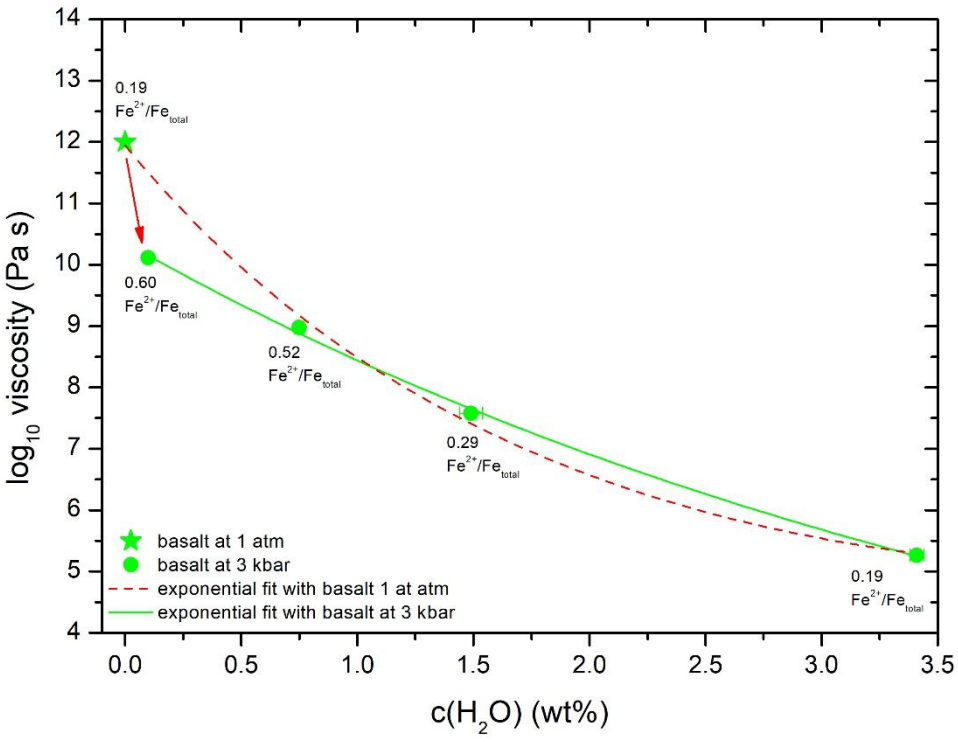

Figure 131: Change of viscosity as a function of H_2O content with the focus on pressure effect for halogen-free basaltic melts. The red dashed line represents the exponential fit with 1 atm basalt (data presented in chapter A: table 16) and disregard of the pressure effect. The green line describes the real exponential fit with 3 kbar basalt. The error bars of log_{10} viscosity are smaller than the symbols.

Thus, further parameters effect the additional decreasing viscosity effect of 0.8 log units. It is obvious that the increasing H_2O content (0.10 wt%) effects the viscosity. The *dry* basalt (0.10 wt% H_2O) has to be compared with a real dry basalt (0 wt% H_2O), which cannot be synthesised in IHPV. The IHPV generates a small water content due to argon as pressure medium. Therefore, the theoretical viscosity of a dry basaltic melt is calculated by means of ~ 0.10 and 0.73 wt% H_2O halogen-free basaltic melts (figure 132). Figure 132 represents the viscosity of the H_2O-free basaltic melt (red circles), whereby the addition 0.10 wt% H_2O results only in a small decrease in viscosity by 0.1 to 0.2 log units. Thus, the decreasing viscosity effect by 2.0 log units is not only a function of the increasing Fe^{2+}/Fe_{total} and the 0.10 wt% H_2O but an effect of composition.

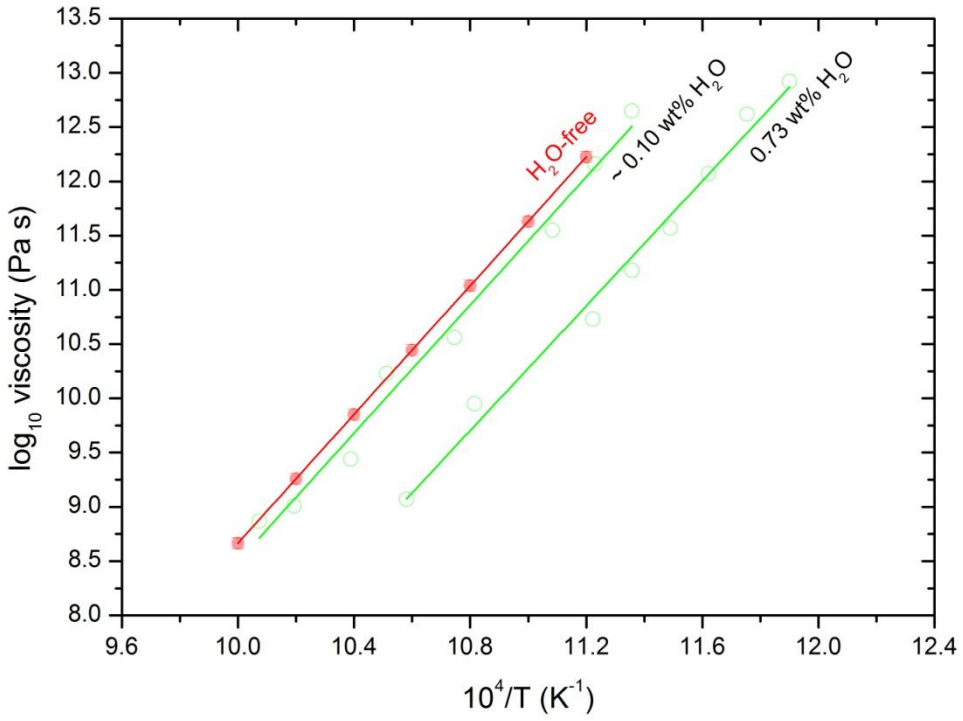

Figure 132: Effect of H_2O on viscosity of basaltic melts. The red circles represent the theoretical viscosity for real H_2O-free basalt. The error bars of log_{10} viscosity are smaller than the symbols.

6.1.2. Effect of H_2O on the iron ratio of basaltic melts

The presence of H_2O in basaltic glasses decreases the Fe^{2+}/Fe_{total} due to the increasing number of network formers Fe^{3+} (see figure 101). For this reason, the polymerisation of melt structure increases due to the conversion of ferrous to ferric iron. Robert et al. (2015) described the effect of water on the iron speciation by the reaction $Fe_2O_3 + H_2 \leftrightarrows 2FeO + H_2O$. The authors observed a decrease in Fe^{2+}/Fe_{total} from ~ 0.8 to 0.6 due to the increasing water content. In agreement with this observation, we found that the Fe^{2+}/Fe_{total} decreases from 0.60 (dry) to 0.19 (3.41 wt% H_2O). This decreasing effect is weaker for the addition of H_2O to halogen-bearing basaltic glasses. The polymerisation effect of the halogens is overlaid by depolymerisation due to the increasing water content. Furthermore, the effect of water on the normalised LF/HF (Raman spectra) is demonstrated as a function of iron speciation in figure 133. The normalised intensity ratios decrease with increasing iron speciation by 0.15 LF/HF for the halogen-free basaltic glasses. The addition of halogens to the present peralkaline melts results in a 0.15 increase in LF/HF for 3.65 mol% Cl^- and a 0.03 increase for 4.90 mol% F^- by a constant oxygen fugacity. Furthermore, the addition of (Cl^- + F^-) to the basaltic glass results in an increase in 0.12 LF/HF (intermediate of chlorine and fluorine for the 1 atm samples).

Figure 134 illustrates the normalised LF/HF as a function of OH groups for halogen-free and –bearing basaltic glasses. This diagram reflects the effect of OH groups on the LF/HF intensity ratio. The halogen-free basalt shows the lowest LF/HF intensity ratios, whereas the addition of chlorine to the basaltic glasses results in the highest LF/HF intensity ratio. Compared to figure 133 it becomes apparent that the increasing OH content results in a decreasing Fe^{2+}/Fe_{total}, whereby the LF/HF intensity ratios show a contrary trend.

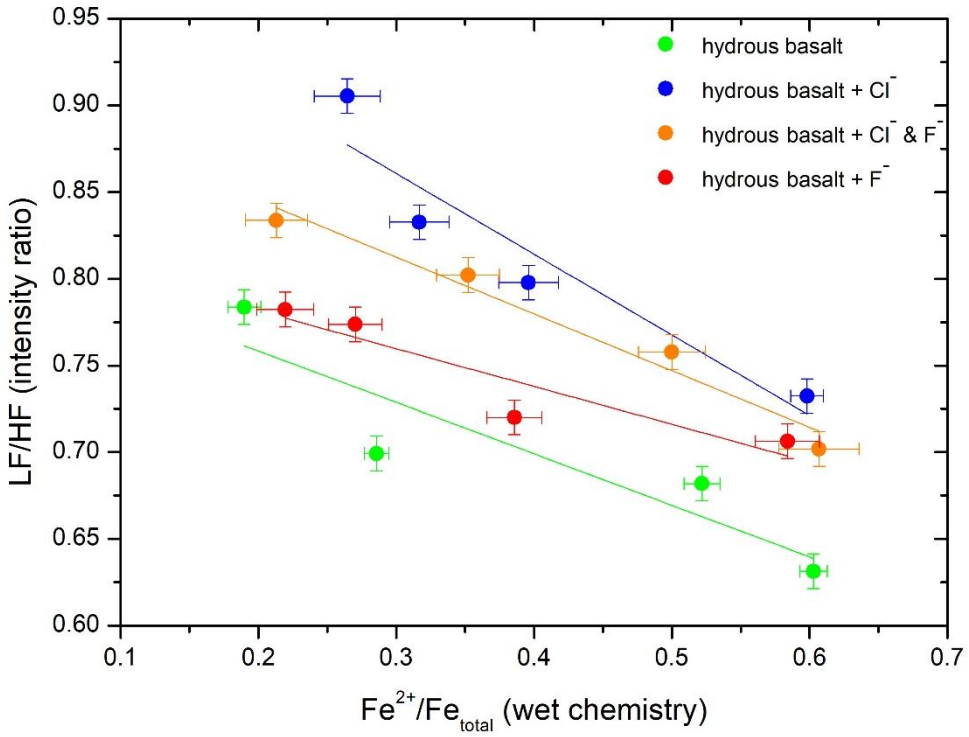

Figure 133: Effect of iron speciation on the LF/HF intensity ratio of halogen-free and halogen-bearing basaltic glasses.

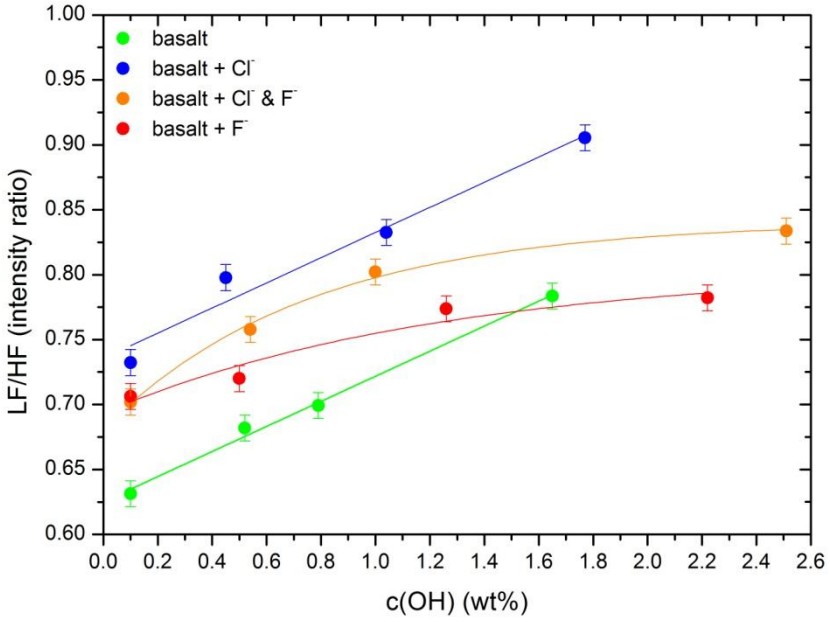

Figure 134: Effect of OH groups on the LF/HF intensity ratio of halogen-free and halogen-bearing basaltic glasses.

Figure 135 shows a comparison of the Long-corrected Raman spectra of halogen-free basaltic glasses without H_2O (black line), 0.10 wt% H_2O (green line) and 0.10 wt% H_2O after tempering at T_g[9] for 2 h (brown line). The synthesis of glasses in IHPV results in an increase in Fe^{2+}/Fe_{total} from 0.19 to 0.60 and the presence of 0.10 wt% H_2O in glass. This can be seen in the peak shift at the maximum from 950 (black line) to 1020 cm^{-1} (green line). The peak in the low frequency region (400 to 600 cm^{-1}) results in a strong increase in intensity due to the synthesis in IHPV. This increase in intensity can be explained by tempering of the 0.10 wt% H_2O basalt (red line), whereby the increasing effect disappears and thus can be described by a pressure effect. This effect is consistent with the results of molar volume of the glass, where also a difference between the H_2O-free basalt (1 atm) and 0.10 wt% H_2O basalt can be observed (figure 97).

To improve comparison, figure 136 illustrates the normalised intensity ratios (LF/HF) as a function of Fe^{2+}/Fe_{total}. All glasses show a decrease in LF/HF intensity ratio due to increasing Fe^{2+}/Fe_{total} and follow a linear regression. The redox equilibrated glasses are differentiated from the hydrous basalts which are characterised by a higher LF/HF ratio. This difference results from the addition of H_2O as well as the resulting decrease in Fe^{2+}/Fe_{total}. Furthermore, the addition of H_2O to basaltic glasses results in an increase in LF/HF due to decreasing NBO/T from 0.5 to 0.4.

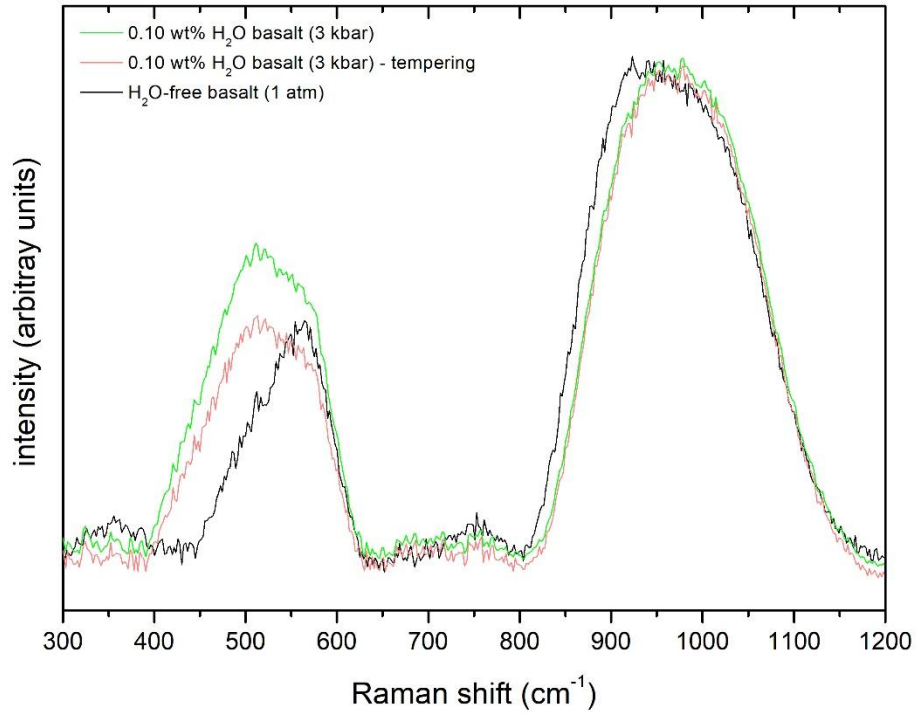

Figure 135: Comparison of the Long-corrected Raman spectra of halogen-free basaltic glasses without H_2O (1 atm) as well as 0.10 wt% H_2O (3 kbar) and 0.10 wt% H_2O (3 kbar) after tempering for 2 h.

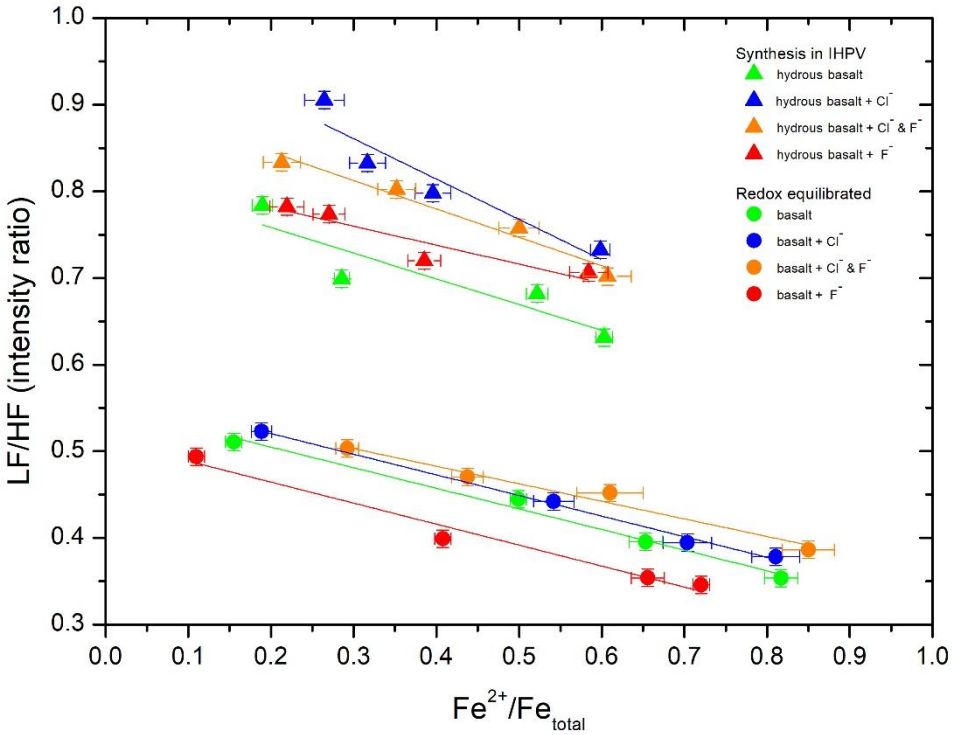

Figure 136: Effect of H_2O on Fe^{2+}/Fe_{total} of redox equilibrated basaltic glasses and basalts synthesised in IHPV.

6.1.3. Effect of H_2O on the structure of peralkaline melts

The addition of H_2O to peralkaline melts modifies the network structure due to two different structural incorporation mechanisms. The incorporation of water is in form of OH groups and molecular H_2O in silicate melts (Scholze 1960; Stolper 1982a). Kohn et al. (1989) and Kohn (2000) suggested different dissolution mechanisms for water in silicate melts. The simplest case is the replacement of a Si-O-Si + H_2O by a 2 Si-OH bond. In comparison to this simple reaction, Kohn (2000) suggested a replacement of Na^+ $(Al\text{-}O\text{-}Si)^-$ + H_2O by Al^{VI} + NaOH + $Si\text{-}O^-$ or rather $Al^{VI}(OH)_3$ + $Si\text{-}O^-$ Na^+ for more complex melts. As a result, the dissolution of water in silicate melts is depending on the melt composition.

6.2. CO_2-bearing basaltic glasses

6.2.1. Influence of CO_2 on the viscosity of basaltic melts

The effect of CO_2 on the viscosity of halogen-free basaltic melts is represented in figure 137. The measured viscosity data is described by open symbols fitted with an Arrhenian equation (dashed line). One important aspect to mention is that the synthesised samples in IHPV generate low water contents. The presence of 0.10 wt% H_2O in silicate melts results in a decrease in viscosity by 0.2 log units (see 6.1.1. Influence of H_2O on the viscosity of basaltic melts). Therefore, this decreasing viscosity effect has to be calculated out of the viscosity of CO_2-bearing silicate melts. This calculation is represented as close symbols with Arrhenius plot (line). Besides the CO_2-bearing basaltic melts, the CO_2-free basaltic melts show 0.10 wt% H_2O content as well and thus all CO_2-bearing samples have a higher viscosity by 0.2 log units. Therefore, the relationship between these three melts remains constant.

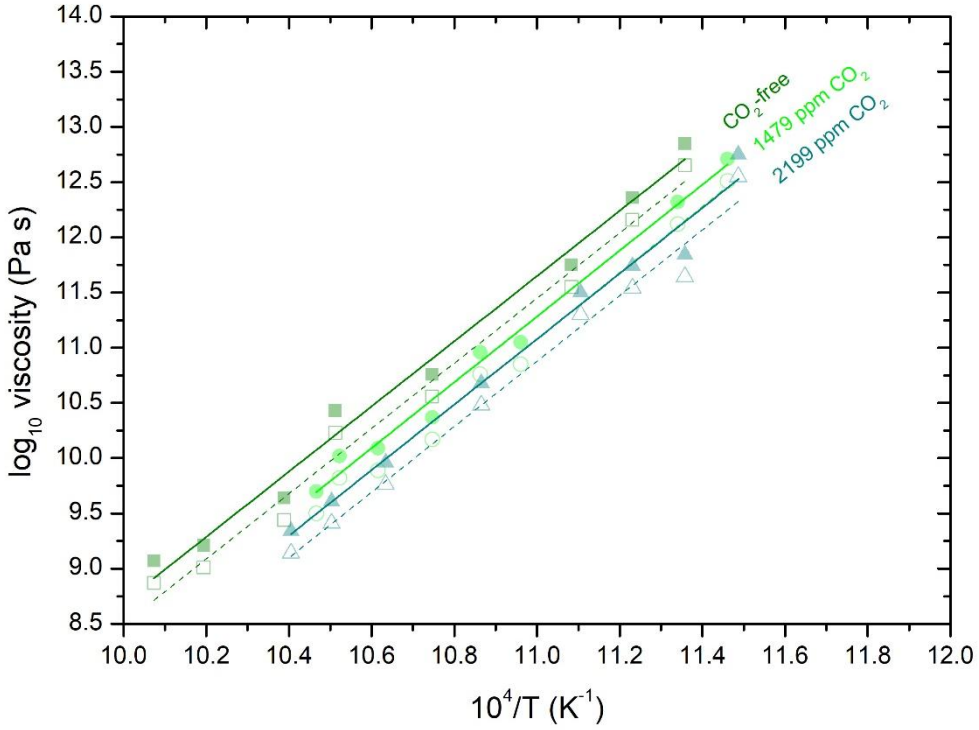

Figure 137: Effect of CO_2 on viscosity of halogen-free basaltic melts with 0.10 wt% H_2O. The original viscosity data is represented as open symbols with the Arrhenius plot (dashed line). The solid symbols demonstrate the water-corrected viscosity data (line). Rectangles shows the CO_2-free melt, circles represents the 1479 ppm CO_2 melt and triangles is the 2199 ppm CO_2 melt. The error bars are smaller than the circles and rectangles.

In figure 138, the viscosity data of the present basaltic melt is plotted as a function of CO_2 content (wt%) and compared with the viscosity data of Bourgue and Richet (2001). The addition of 0.23 wt% CO_2 to the present basaltic melts results in a decrease in viscosity by 0.6 log units (green circles). This basaltic melts have 0.10 wt% H_2O content. Previous studies have focused on the combined effect of H_2O and CO_2 on the viscosity of silicate melts.

That is the reason why a qualitative comparison with literature data does not work well. Bourgue and Richet (2001) synthesised diverse H_2O- and CO_2-bearing silicate melts with the focus on SiO_2/K_2O ratio. Figure 138 shows the associated viscosity data (brown circles). The addition of 1.99 wt% CO_2 to the silicate melt results in a decrease in viscosity by 2.0 log units. It is important to note that the H_2O content varies between 0.20 and 0.39 wt%. The complex melt structure of the present basalt results in the strong decrease in viscosity. Precise statement about the CO_2 effect on silicate melts requires more measurements with glasses of varying CO_2-content without H_2O.

The effect of CO_2 on the viscosity of halogen-free and –bearing basaltic melts is shown in figure 139. The presence of 2199 ppm CO_2 in the present basalt shows the above mentioned decreasing effect on viscosity of 0.7 log units. The addition of 1853 ppm CO_2 to the fluorine-bearing basaltic melts results in the strongest decrease in viscosity by 2.0 log units, whereas

the presence of 3658 ppm CO_2 in chlorine-bearing basalt shows a slighter decrease in viscosity by 0.5 log units. The addition of 2975 ppm CO_2 to (Cl^- + F^-)-bearing basaltic melts results in a mixed effect. The viscosity increases due to the addition of 1234 ppm CO_2 and further addition of 2975 ppm CO_2 results in a decrease in viscosity by 0.3 log units. Thus, the presence of CO_2 to halogen-free and –bearing basaltic melts results in a decrease in viscosity.

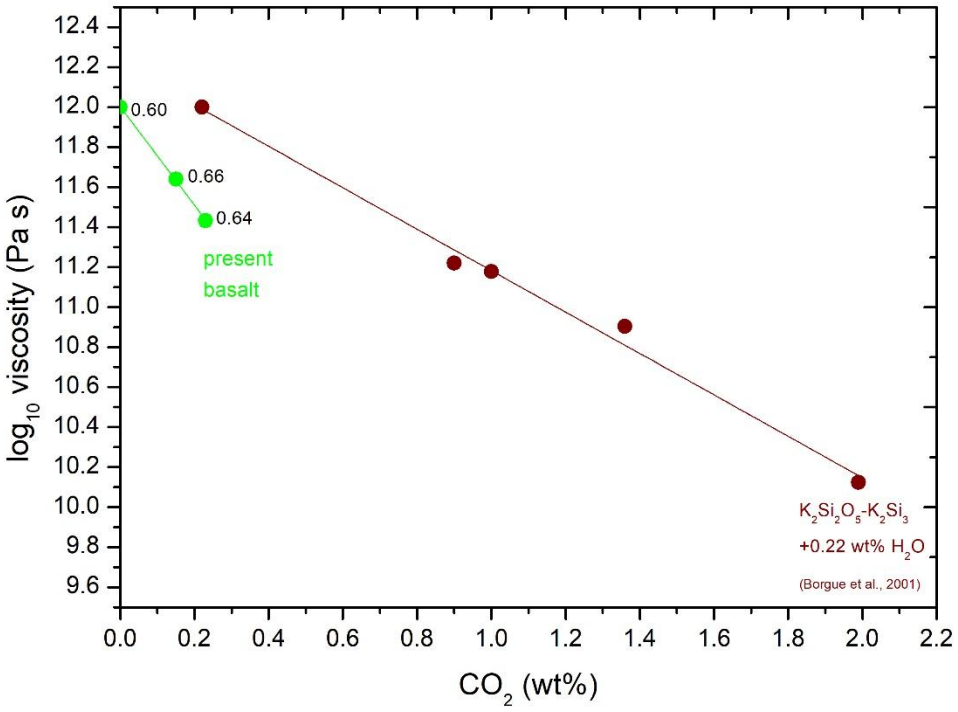

Figure 138: The change in viscosity due to the addition of CO_2 at the same temperature as the original melt at 10^{12} Pa s for present basalt (~ 0.10 wt% H_2O). Literature data: Bourgue and Richet (2001) – $K_2Si_2O_5$-K_2Si_3 + 0.22 wt% H_2O. The numbers represent the Fe^{2+}/Fe_{total}. The error bars are smaller than the symbols.

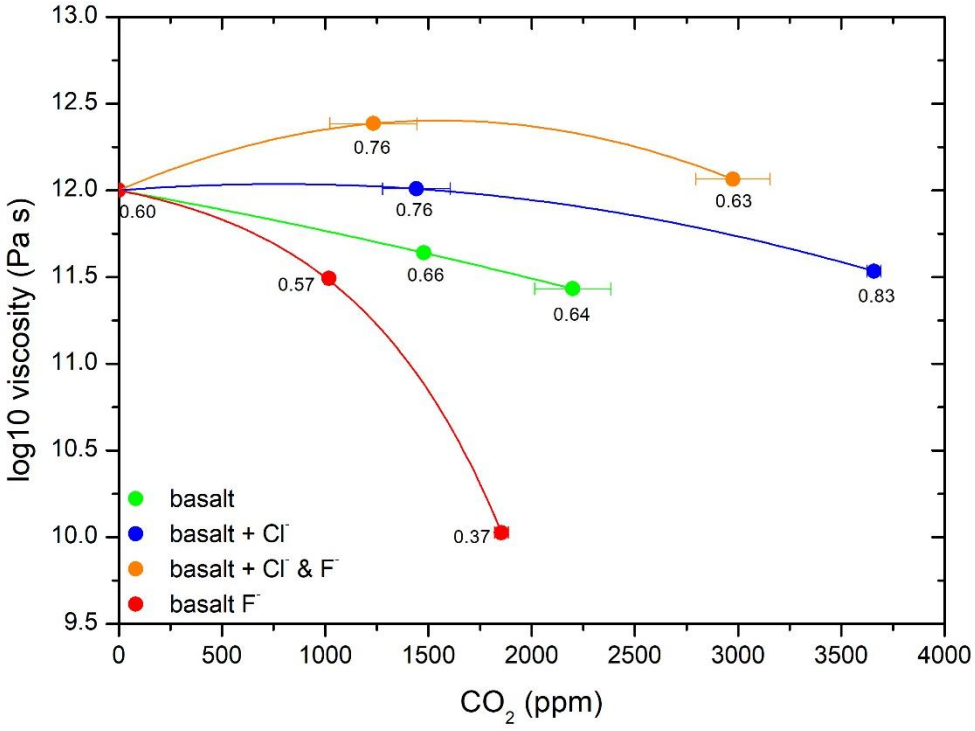

Figure 139: The change in viscosity due to the addition of CO_2 at the same temperature as the original glass at 10^{12} Pa s for halogen-free and –bearing basaltic glasses. The numbers represent the Fe^{2+}/Fe_{total}. The error bars of log_{10} viscosity are smaller than the symbols.

6.2.2. Effect of CO_2 on the iron ratio of basaltic melts

The presence of 1579 ppm CO_2 in halogen-free basaltic glasses increases the Fe^{2+}/Fe_{total} from 0.60 to 0.66, but the further addition of 2199 ppm CO_2 shows a decrease in Fe^{2+}/Fe_{total} from 0.66 to 0.64. There is no clear dependence between Fe^{2+}/Fe_{total} and CO_2 content. Furthermore, the addition of CO_2 to chlorine-bearing basaltic glasses results in a decrease in Fe^{2+}/Fe_{total}, whereas the presence of CO_2 in fluorine-bearing basaltic glasses increases the Fe^{2+}/Fe_{total}. This variation of Fe^{2+}/Fe_{total} in halogen-bearing basaltic glasses is not only effected by the addition of CO_2 but also halogens.

Figure 140 illustrates the effect of iron speciation on the normalised LF/HF (Raman spectra), whereas figure 141 shows the CO_2 content as a function of normalised LF/HF. The normalised LF/HF intensity ratios of halogen-free basaltic glasses increase with increasing Fe^{2+}/Fe_{total} as well as with increasing CO_2 content. The addition of CO_2 to chlorine-bearing basaltic glasses results in a strong decrease in LF/HF intensity ratio due to increasing Fe^{2+}/Fe_{total} and increasing CO_2 content. The increasing Fe^{2+}/Fe_{total} in fluorine-bearing basaltic glasses shows a slight increase in LF/HF intensity ratio accompanied by a decreasing CO_2 content.

Thus, the addition of 1234 ppm CO_2 to (Cl^- + F^-)-bearing basaltic melts increases the LF/HF intensity ratio as a function of increasing Fe^{2+}/Fe_{total}, whereas the further addition of 2975 ppm CO_2 decreases the LF/HF intensity ratio due to increasing Fe^{2+}/Fe_{total}. The increasing CO_2 content results in an increase in LF/HF intensity ratio regardless of the iron speciation. As a consequence, the Raman spectroscopy does not allow an observation of the structural change by the addition of CO_2 to basaltic melts due to varied iron speciation.

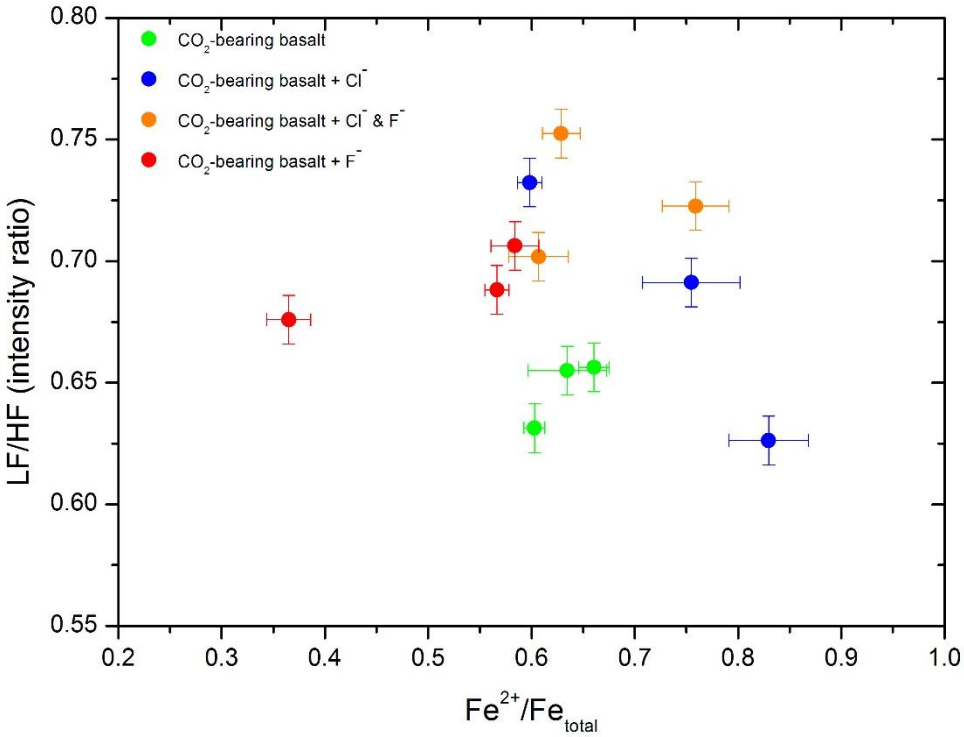

Figure 140: Effect of iron speciation on the intensity ratio LF/HF of halogen-free and halogen-bearing basaltic glasses with CO_2.

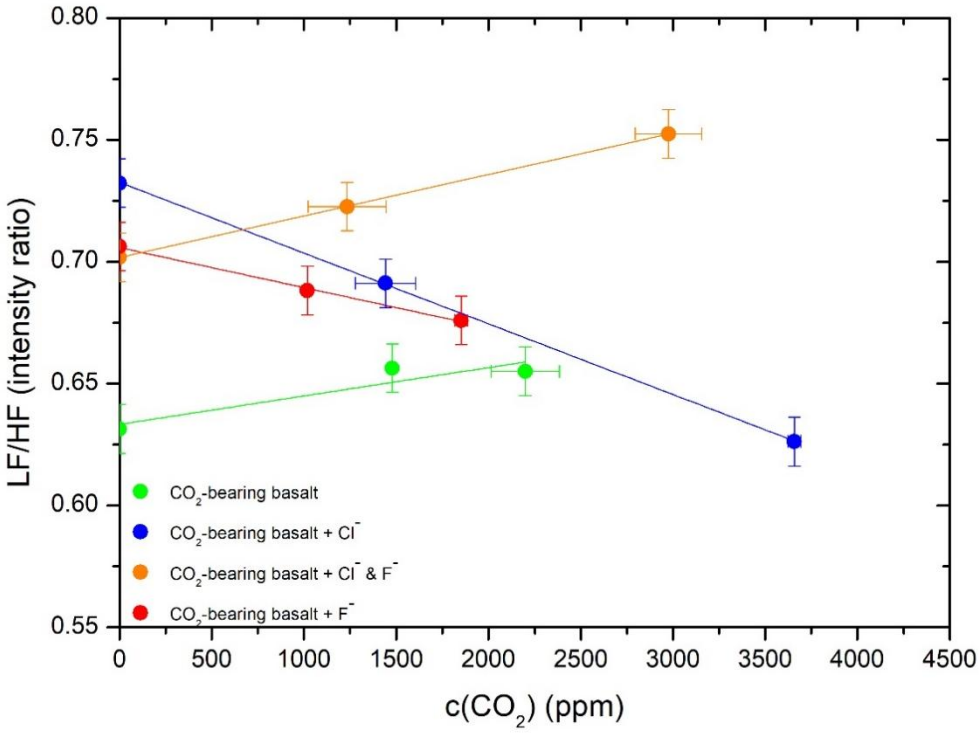

Figure 141: Effect of iron speciation on the intensity ratio LF/HF of halogen-free and halogen-bearing basaltic glasses with CO_2.

6.2.3. Effect of CO_2 on the structure of peralkaline melts

The solubility of CO_2 to peralkaline melts depends on the melting temperature and pressure (Brey 1976). Fine and Stolper (1985) suggested that the molecular CO_2 to carbonate ratio changes by the silicate composition in the glass. In basaltic glasses, all CO_2 is dissolved in form of carbonate (Brey 1976; Fine and Stolper 1985), whereas high silica content results in the formation of molecular CO_2. The carbonate groups prefer the bonding to non-bridging oxygen atoms. The splitting of carbonate peak in infrared spectroscopy describes the asymmetric stretching vibrations, which are characterised for most natural glass (Ni and Keppler 2013).

6.3. Models

6.3.1. Model for the calculation of Fe^{2+}/Fe_{total}

Table 38 and table 39 represent the measured Fe^{2+}/Fe_{total} (wet chemistry) and the calculated Fe^{2+}/Fe_{total} after Kress and Carmichael (1991). The model does not consider the H_2O and CO_2 content in the present composition. Therefore, the calculation cannot describe the real Fe^{2+}/Fe_{total} for the hydrous and CO_2-bearing basaltic glasses. The halogen-free basaltic glasses show a calculated Fe^{2+}/Fe_{total} of 0.33 to 0.44, whereby the characteristic decreasing effect of Fe^{2+}/Fe_{total} not considered. As a result, the model (Kress and Carmichael 1991) cannot be used for halogen-, H_2O- and CO_2-bearing basaltic glasses. The model after Kress and Carmichael (1991) should be improved, because the model considers only Al_2O_3,

FeO_{total}, CaO, Na_2O and K_2O. The model should include all relevant elements especially the halogens, H_2O and CO_2 content due to the effect on explosive behaviour. Therefore, a modified model can be applied for natural glasses. The oxygen fugacity in IHPV was calculated by means of measurement of nickel palladium sensor with the microprobe. This nickel palladium sensor was always located close to the samples during the IHPV synthesis, whereby the material provides insights about the oxygen fugacity.

Table 38: Comparison of the Fe^{2+}/Fe_{total} from wet chemistry method and the calculated values Kress and Carmichael (1991). All glasses were synthesised in IHPV at constant oxygen fugacity of $log_{10}(fO_2)$ -3.56 to -2.56.

Sample	Fe^{2+}/Fe_{total}	
	calculated [a]	wet chemistry
BA-0-III	0.44 - 0.33	0.60
BA-0_0.73H		0.52
BA-0_1.29H		0.29
BA-0_3.47H		0.19
BA-Cl-III	0.45 - 0.34	0.60
BA-Cl_0.53H		0.40
BA-Cl_1.76H		0.32
BA-Cl_3.56H		0.26
BA-Cl-F-III	0.45 - 0.34	0.61
BA-Cl-F_0.59H		0.50
BA-Cl-F_1.31H		0.27
BA-Cl-F_3.50H		0.21
BA-F-III	0.44 -0.34	0.58
BA-F_0.63H		0.39
BA-F_1.84H		0.27
BA-F_4.04H		0.22

[a] calculated from Kress and Carmichael (1991)

Table 39: Comparison of the Fe^{2+}/Fe_{total} from wet chemistry method and the calculated values Kress and Carmichael (1991). All glasses were synthesised in IHPV at constant oxygen fugacity of log (fO_2) -3.56 to -2.56.

Sample	Fe^{2+}/Fe_{total}	
	calculated [a]	wet chemistry
BA-0-III	0.44 - 0.33	0.60
BA-0_0.15C		0.66
BA-0_0.23C		0.64
BA-Cl-III	0.45 - 0.34	0.60
BA-Cl_0.12C		0.76
BA-Cl_0.37C		0.83
BA-Cl-F-III	0.45 - 0.34	0.61
BA-Cl-F_0.14C		0.76
BA-Cl-F_0.29C		0.63
BA-F-III	0.44 -0.34	0.58
BA-F_0.09C		0.57
BA-F_0.20C		0.37

[a] calculated from Kress and Carmichael (1991)

6.3.2. Models for the calculation of viscosity

6.3.2.1. Models for the calculation of viscosity for H_2O-bearing melts

Comparison of measured viscosities with literature models enables the illustration of the effect of melt composition on the viscosity of melts. Giordano et al. (2008) proposed a model for the viscosity of magmatic liquids with a focus on P_2O_5, H_2O and F_2O^{-1}. Figure 142 represents a comparison of the measured viscosity with calculated viscosity values from a model after Giordano et al. (2008). The model shows a relative good correlation with the H_2O-free basaltic melts. Furthermore, the additions of H_2O to the present basaltic melts show a significant overestimation of the viscosity by the model. This is shown clearly by the increasing H_2O content. The addition of H_2O to the present basaltic melts results in a decrease in the Fe^{2+}/Fe_{total}, but the varied Fe^{2+}/Fe_{total} is not considered by the model. The deviation results by the chlorine content (Section A (6.3.2. Models for the calculation of viscosity)) and the iron speciation (Section B (5.4.2. Models for the calculation of viscosity)).

An additional viscosity model (Duan, 2014) is shown in figure 143. This model characterises the viscosity of natural iron-bearing silicate melts with a focus on the Fe^{2+}/Fe_{total} and the H_2O content. The model shows a good correlation with the dry halogen-free and –bearing basaltic melts, but the increasing water content results in a significant overestimation of the viscosity by the model after Duan (2014) for all halogen-free and –bearing basaltic melts. In conclusion, the model works for the dry halogen-free and bearing melts.

Furthermore, the viscosity model by Sehlke and Whittington (2016) of planetary tholeiitic melts is demonstrated in figure 144. The model includes the iron speciation in melts but it neglects the H_2O content. Our viscosity results of dry halogen-free and –bearing basaltic melts are consistent with the calculated data after the model from Sehlke and Whittington (2016). In contrast to the dry melts, we observe that the increasing H_2O content results in an overestimation of the viscosity by the model. Therefore, the model should include the water content as well as the halogens (Cl^- and F^-).

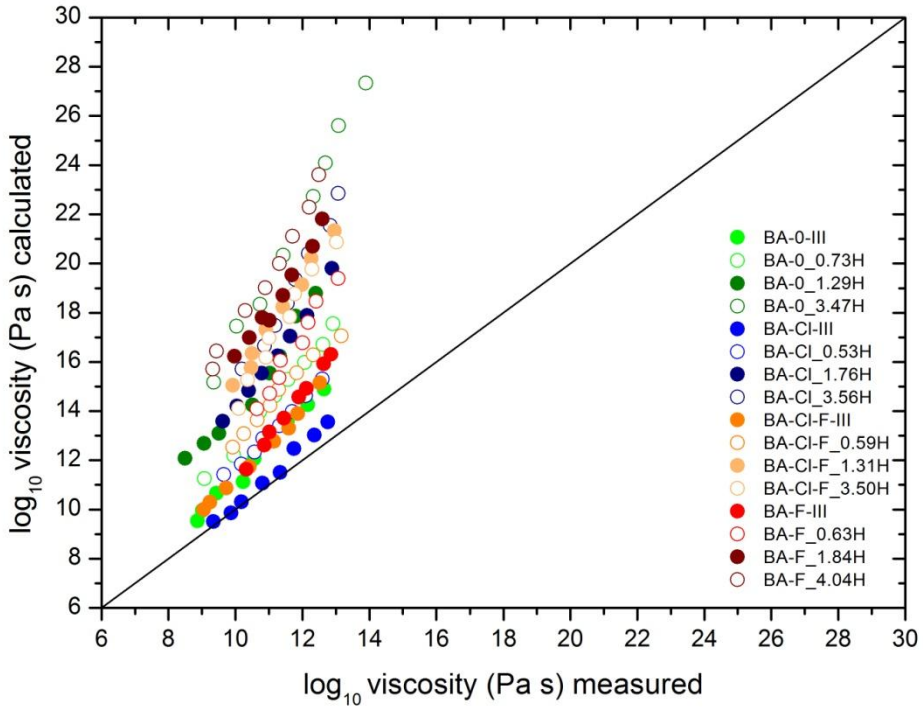

Figure 142: Comparison of the measured viscosity with the calculated data from model of Giordano et al. (2008). The error bars are smaller than the symbols.

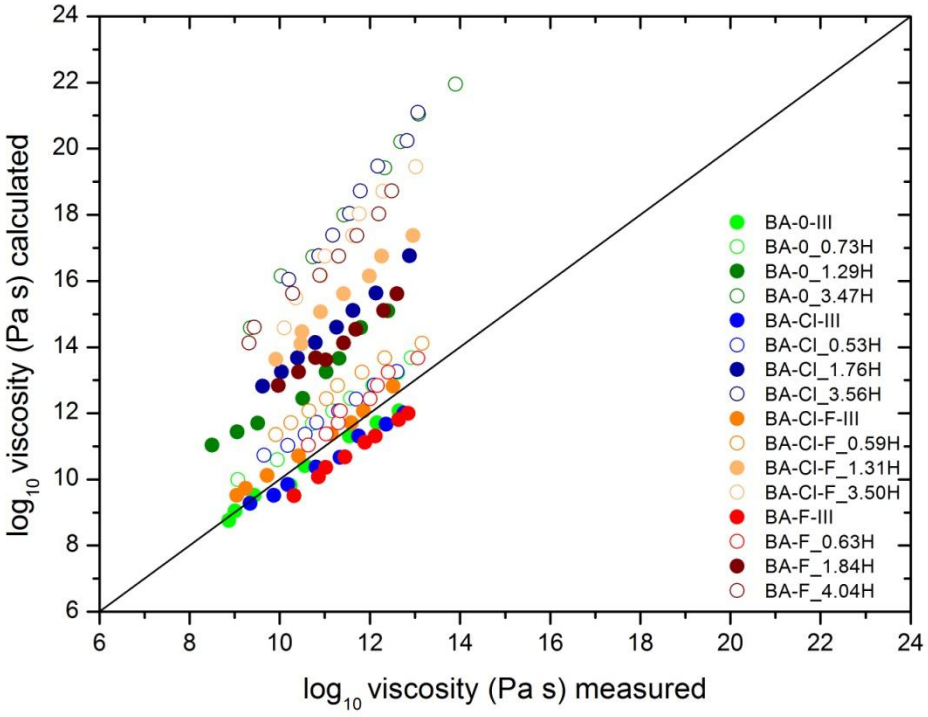

Figure 143: Comparison of the measured viscosity with the calculated data from model of Duan (2014). The error bars are smaller than the symbols.

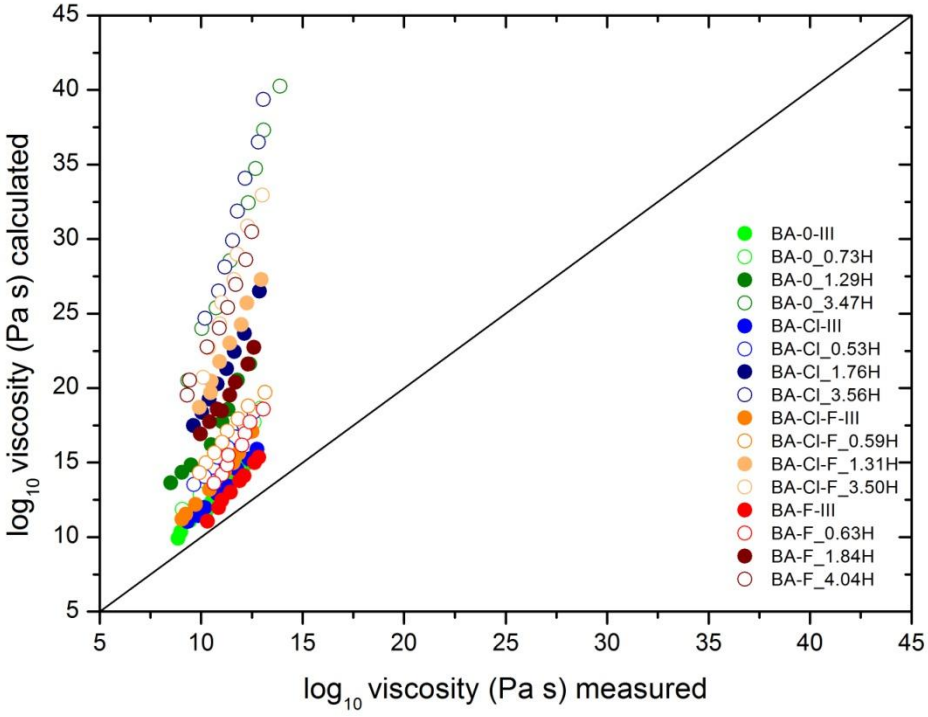

Figure 144: Comparison of the measured viscosity with the calculated data from model of Sehlke and Whittington (2016). The error bars are smaller than the symbols.

6.3.2.1. Models for the calculation of viscosity for CO_2-bearing melts

The effect of CO_2 on the viscosity is discussed in the literature (Brearley and Montana 1989; White and Art; Bourgue and Richet 2001; Morizet et al. 2007; Di Genova et al. 2014; Robert et al. 2015), but these earlier studies have reported different viscosity results. Therefore, there are no present models, which include the CO_2 content. Despite everything, the following models were tested on the functionality with CO_2-bearing basaltic melts.

Figure 145 illustrates the measured viscosity as a function of the calculated viscosity after the model from Giordano et al. (2008). The model shows a good correlation with CO_2-free and ~1000 ppm CO_2 of halogen-free and chlorine-bearing basaltic melts. The increasing CO_2 content results in a overestimation of the viscosity by the model after Giordano et al. (2008). Particularly, the model overestimates the fluorine and (Cl^- + F^-)-bearing basaltic melts despite the inclusion of F^- in the model. Furthermore, the model does not consider the iron speciation, whereas the overestimation of the calculated viscosity of fluorine-bearing glasses with a high CO_2 content results.

In figure 146, the measured viscosities for CO_2-bearing basaltic melts are compared with the values predicted by the Duan (2014) model. The model does not work for the CO_2-free and high CO_2 contents in basaltic melts. Only, the viscosities of the chlorine- and fluorine-bearing basaltic melts with ~1000 ppm CO_2 follows the 1:1 solid line and can be described by the model.

Further model of Sehlke and Whittington (2016) describes the calculated viscosity of natural iron-bearing silicate melts. Figure 147 shows that the model does not work for all CO_2-free and –bearing basaltic melts. The viscosity are significantly overestimated by the model of Sehlke and Whittington (2016). The increasing CO_2 content results in a stronger overestimation by the model.

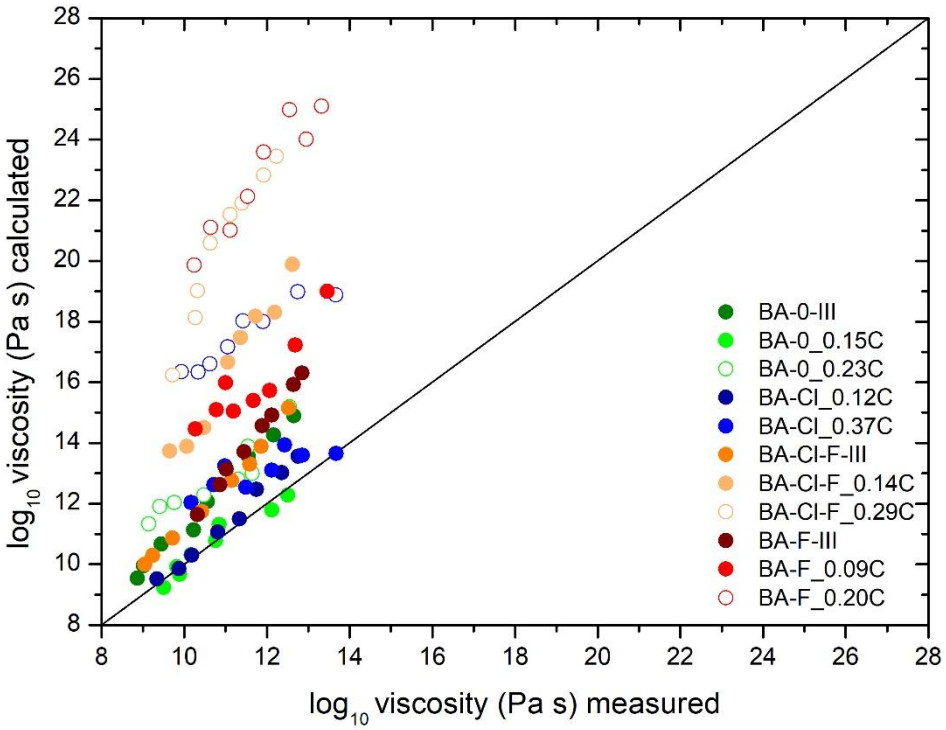

Figure 145: Comparison of the measured viscosity with the calculated data from model of Giordano et al. (2008). The error bars are smaller than the symbols.

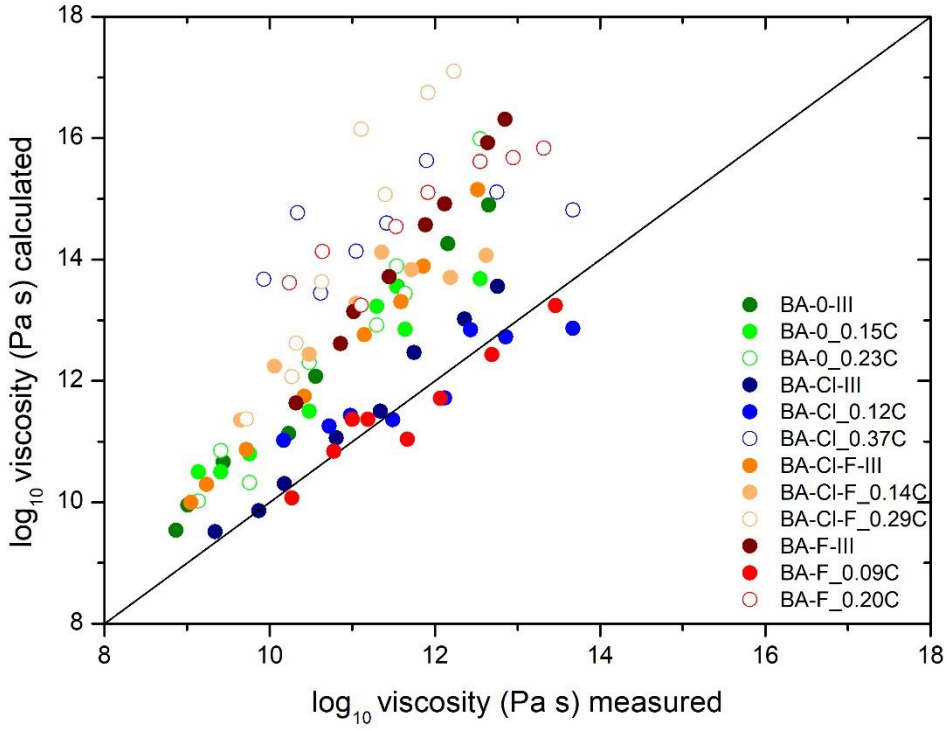

Figure 146: Comparison of the measured viscosity with the calculated data from model of Duan (2014). The error bars are smaller than the symbols.

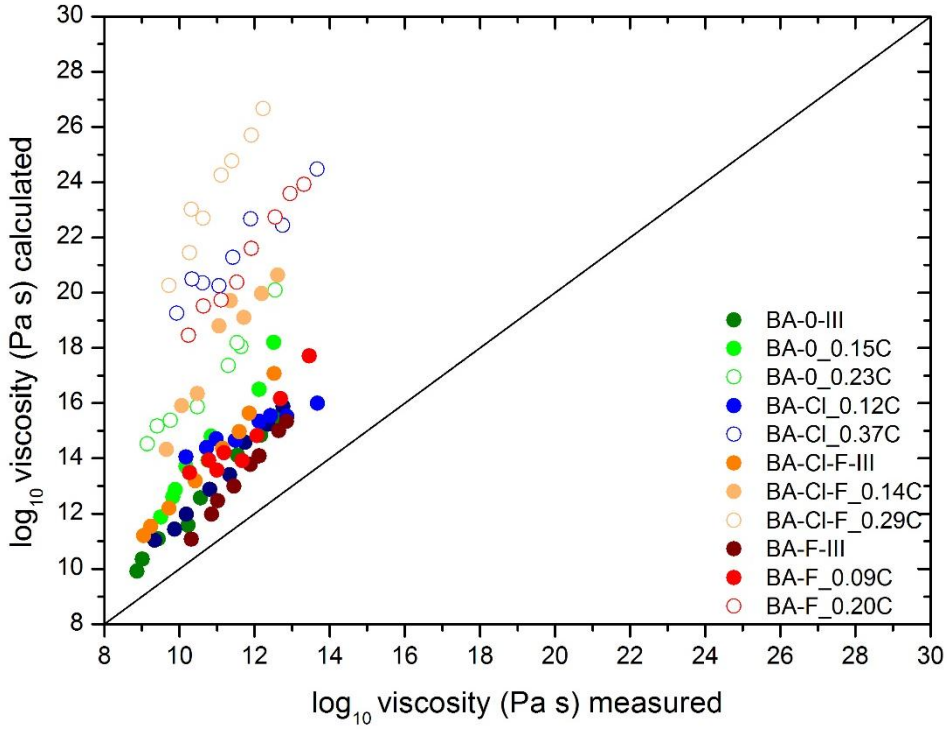

Figure 147: Comparison of the measured viscosity with the calculated data from model of Sehlke and Whittington (2016). The error bars are smaller than the symbols.

6.3.3. Models for the calculation of heat capacity

6.3.3.1. Models for the calculation of heat capacity for H_2O-bearing melts

The measured liquid (C_{pl}) and glass (C_{pg}) heat capacity compared to literature models are illustrated in figure 148 (Stebbins et al. 1984; Richet and Bottinga 1984; Richet 1987; Lange and Navrotsky 1992). The model from Stebbins et al. (1984) and Lange and Navrotsky (1992) does not work and C_{pl} are overestimated for the hydrous halogen-free and -bearing basaltic melts. In contrast to that, the model by Richet and Bottinga (1984) is reproduced by the experimental data but the melts with a high water content (> 3.47 wt% H_2O) are overestimated by the model.The calculated glass heat capacity (C_{pg}) describes the model by Richet (1987) and correlates well for all hydrous basaltic glasses. This shows the best model of C_{pg}, which considers the H_2O content in the melts.

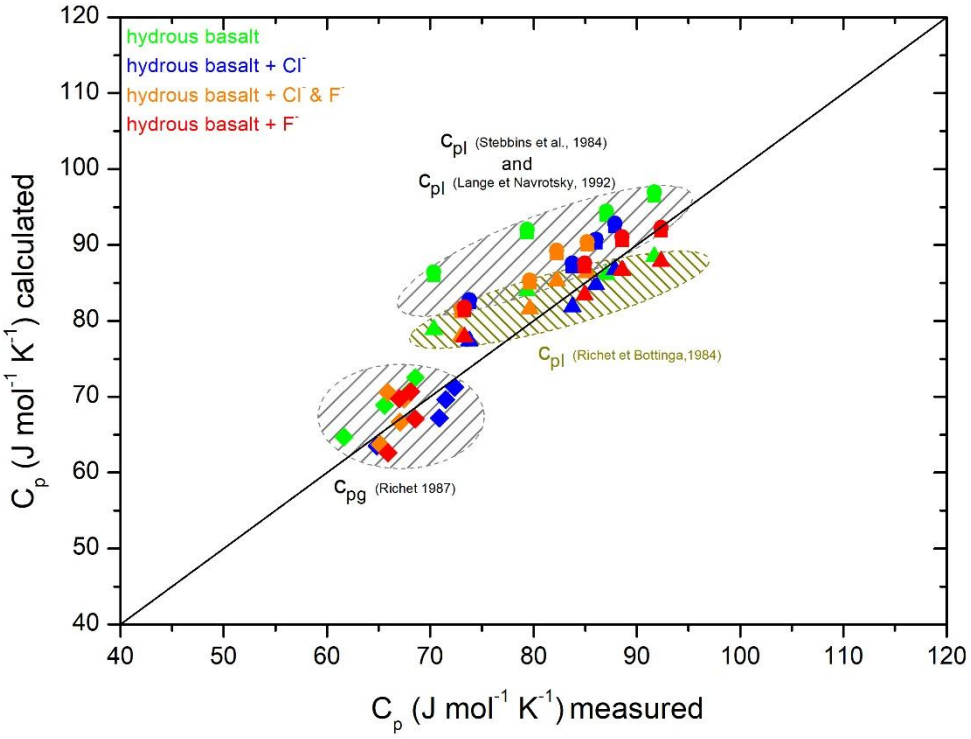

Figure 148: Comparison of calculated and measured heat capacity data of hydrous halogen-free and halogen-bearing basaltic glasses. The symbols represents a comparison between the measured and the calculated data from Stebbins et al. (1984) model (rectangle), Lange and Navrotsky (1992) model (circle), Richet and Bottinga (1984) model (triangle) and Richet (1987) model (rhombus). The error bars are smaller than the symbols.

6.3.3.1. Models for the calculation of heat capacity for CO_2-bearing melts

In figure 149, the literature models (Stebbins et al. 1984; Richet and Bottinga 1984; Richet 1987; Lange and Navrotsky 1992) are compared with the measured liquid (C_{pl}) and glass (C_{pg}) heat capacity. The model does not include CO_2 content into the calculation, nevertheless all c_{pl} models show a good correlation for the CO_2-bearing basaltic melts (green rectangles, circles and triangles). The low CO_2 content in basaltic melts does not change the total melt composition significantly, whereby the models can work. In contrast to that, the addition of a low halogen and CO_2 content to basaltic melts show a good correlation of the measured C_{pl} by (Stebbins et al. 1984; Richet and Bottinga 1984; Richet 1987; Lange and Navrotsky 1992) and Lange and Navrotsky (1992). Therefore, the largest deviation shows the (Cl^- + F^-)-bearing basaltic melts with a total halogen content by 6.1 mol% (orange symbols). The literature model by Richet (1987) describes the heat capacity of glass (C_{pg}) and this model correlates well with all CO_2-bearing basaltic melts.

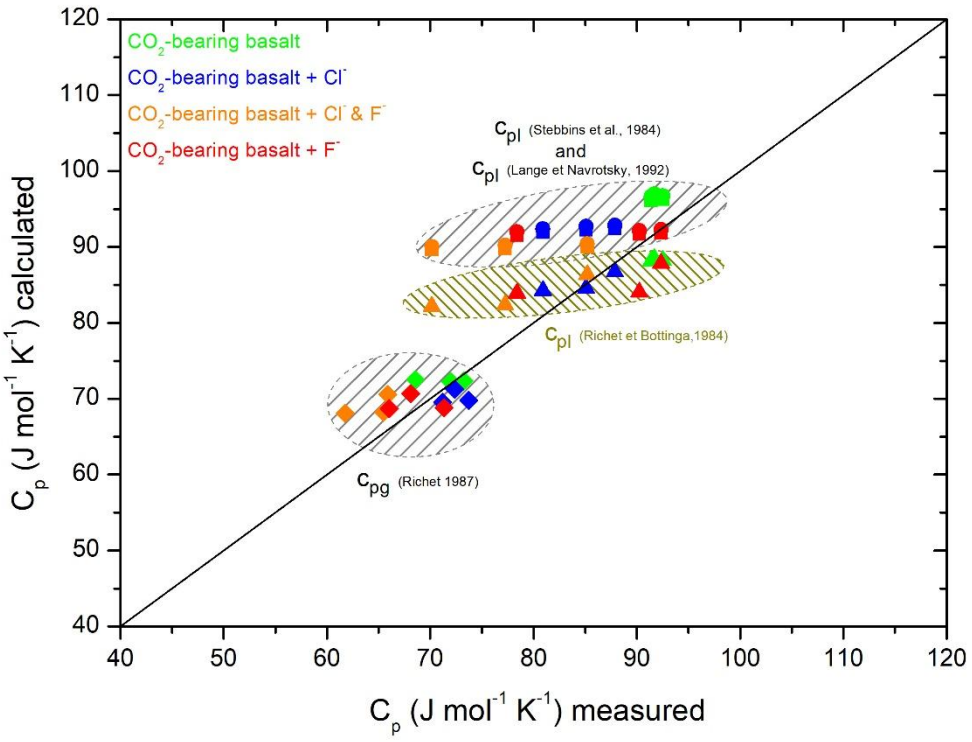

Figure 149: Comparison of calculated and measured heat capacity data of CO_2-bearing halogen-free and halogen-bearing basaltic glasses. The symbols represents a comparison between the measured and the calculated data from Stebbins et al. (1984) model (rectangle), Lange and Navrotsky (1992) model (circle), Richet and Bottinga (1984) model (triangle) and Richet (1987) model (rhombus). The error bars are smaller than the symbols.

7. Conclusion

In conclusion, the increasing H_2O content in halogen-bearing basaltic melts results in a relative decrease in OH groups and an increase in molecular H_2O and the same is true for the halogen-free basaltic melts (Scholze 1960; Stolper 1982a). The presence of OH groups in halogen-free and –bearing basaltic glasses shows a decrease in Fe^{2+}/Fe_{total}. This decreasing Fe^{2+}/Fe_{total} results in a polymerisation of the melt structure, but this effect is contrasted by the depolymerisation effect due to the increasing H_2O content. Both processes result in a decrease in NBO/T compared to the redox equilibrated glasses. Thus, the Raman spectra are sensitive to redox changes that allow an easy differentiation between halogen-free and -bearing basaltic glasses by Fe^{2+}/Fe_{total} and total water content. Regarding of OH groups (water species) allows the understanding of the effect of H_2O on iron speciation due to the reaction with bridging oxygen, whereas the molecular water does not affect the network structure.

The addition of 3.41 wt% H_2O to basaltic glasses results in a strong decrease in viscosity by 5.2 log units (see figure A). The presence of H_2O in halogen-bearing basaltic glasses shows a similar decreasing effect in viscosity. The effect of water on the viscosity should be more effective in iron-free melts, which is represented by Baasner et al. (2013b). The authors observed that the addition of ~ 13 mol% H_2O to peralkaline melts (NACS) decreases T_g^{12} by 400 K compared to the decrease in T_g^{12} by 150 K for the present basaltic glasses. Therefore, the effect of H_2O on the viscosity of iron-free basaltic melts will describe the intensity of the polymerisation effect of redox on the present basaltic melts.

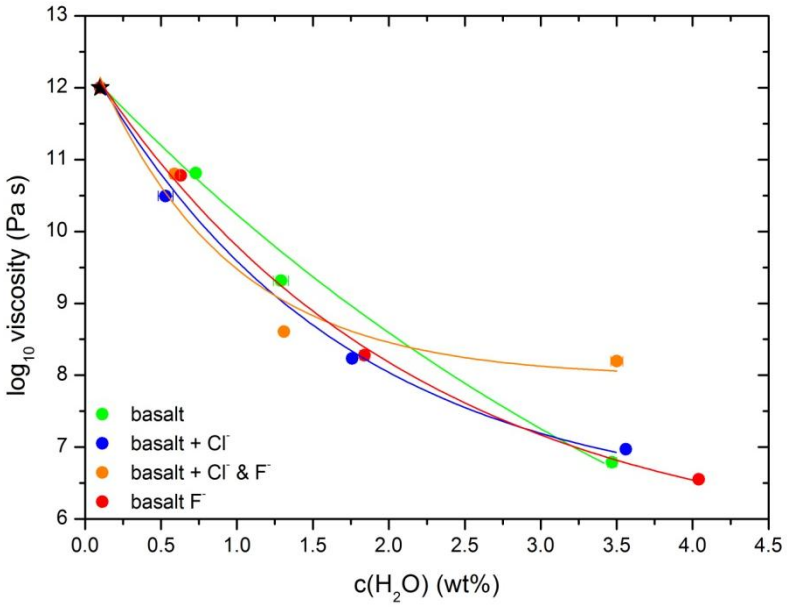

A: The change in viscosity due to the addition of H_2O at the same temperature as the original melts at 10^{12} Pa s for halogen-free and –bearing basaltic melts (original figure 130). The error bars are smaller than the symbols.

Besides the presence of H_2O, the CO_2 in basaltic melts is dissolved in form of carbonate, which can be observed by the splitting of carbonate peak (asymmetric vibration) in infrared spectroscopy (Ni and Keppler 2013). There is no dependence of increasing CO_2 content on Fe^{2+}/Fe_{total}. The Raman spectra do not show a consistent structural change due to increasing CO_2 content. The addition of 2199 ppm CO_2 to basaltic melts results in a decrease in viscosity by 0.7 log units (see figure B). The addition of 3658 ppm CO_2 to chlorine-bearing basaltic melts shows a similar decrease in viscosity despite the higher CO_2 content, whereas the presence of 1853 ppm in fluorine-bearing basaltic melts results in the highest decrease in viscosity up to 2.0 log units. Consequently, the effect of CO_2 on the viscosity has to be included in further models. Furthermore, the effect of CO_2 on the viscosity of peralkaline melts has to be checked by the synthesis of CO_2-bearing iron-free basaltic melts to avoid the influence of the redox effect.

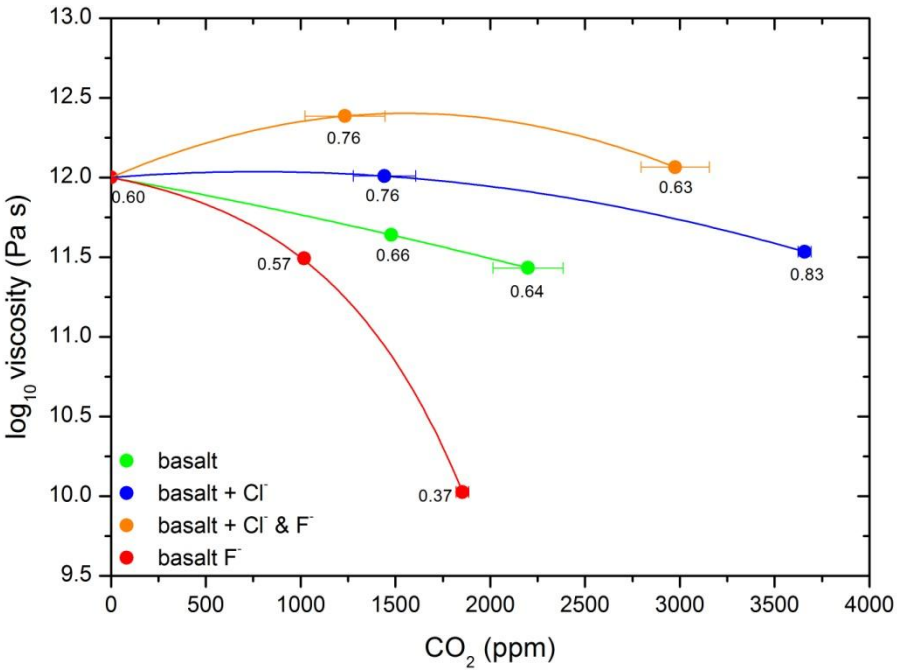

B: The change in viscosity due to the addition of CO_2 at the same temperature as the original melts at 10^{12} Pa s for halogen-free and –bearing basaltic glasses (original figure 139). The numbers represent the Fe^{2+}/Fe_{total}. The error bars of log_{10} viscosity are smaller than the symbols.

Part D – Falling-sphere technique

1. Abstract

The viscosity of CO_2- and H_2O-bearing basaltic melts in the low viscosity range between 10^0 and 10^5 Pa s was investigated using the falling sphere method. The CO_2-bearing glasses were synthesised at 1550 ± 10 K and 200 MPa for 24 h in the internally heated pressure vessel (IHPV) at a log fO_2 of -3.56 to -2.56. After the synthesis, Pt sphere was added to the glass cylinder and embedded inside the glass by a short melting procedure (1550 ± 10 K for 15 min). The actual viscosity measurements on chlorine-bearing basalt with 1550 ppm CO_2 were performed at 1223 ± 10 K and 200 MPa for 5 h in a cold sealed pressure vessel (CSPV) at NNO+0.6. During these measurements it was observed that the tendency of these basaltic melts to crystallise at the temperatures of interest is enhanced by the presence of CO_2. Thus, the falling sphere experiments were not successful for the present basaltic composition. As a result, no further falling sphere experiments were performed on this melt composition, but this study suggests that the use of X-ray tomography is an optimal method for defining the position of a Pt sphere in glass cylinders by 2D and 3D images.

2. Introduction

The viscosity of CO_2- and H_2O-bearing basaltic melts in the low viscosity range from 10^0 to 10^5 Pa s can be determined using the falling sphere method. Literature data on low viscosity of andesitic melts (Vetere et al. 2006; Vetere et al. 2008), shoshonitic and latitic melts (Misiti et al. 2011) and flux-rich pegmatitic melts (Bartels et al. 2011) have illustrated the feasibility of the falling sphere experiments. However, no data on low viscosity of basaltic melts doped with CO_2 and H_2O exists. Furthermore, the experimental low viscosity data can be used to check the accuracy of the Arrhenius and VFT fit.

3. Experimental and analytical methods

3.1. Starting materials and synthesis of CO_2- and H_2O-bearing samples

Four different starting glasses were prepared from a mixture of oxides, carbonates and halogens. This mixture was melted at 1473 K in Pt crucible in a 1 atm $MoSi_2$ furnace for 4 to 9 h. A detailed description can be found in chapter A (3.1. Starting materials) and the melt composition is shown in table 22. The starting glasses were added with specific amounts of silver oxalate ($Ag_2C_2O_4$) or distilled water to dope the basaltic glasses with CO_2 and H_2O. The sample synthesis took place in 20 mm long $Au_{75}Pd_{25}$ capsules (4 mm diameter and 0.2 mm wall thickness). The detailed capsule preparation is explained in chapter C (3.2. Synthesis of H_2O-CO_2-bearing glasses).

The experiments were performed in an Internally-heated pressure vessel (IHPV). The measurements were conducted at the same melting temperatures (1550 ± 10 K for 24 h) as used in series III, but at lower pressure conditions of 200 ± 5 MPa due to the maximum pressure of 200 MPa in the subsequent falling sphere experiments with cold sealed pressure vessel (CSPV).

3.2. Falling sphere method

The falling sphere method enables the viscosity measurement in the low viscosity range from 10^0 to 10^5 Pa s. The measurement is performed by the exact determination of the vertical position of an introduced sphere in the melt. It is important that the sphere position is measured before and after the falling sphere experiments (Vetere et al. 2006). The viscosity η is calculated with Stokes law:

$$\eta = \frac{2*t*g*\Delta\rho*r^2*C_F}{9*d} \qquad \textit{Equation 17}$$

where t represents the run time, g is the acceleration due to gravity (9.81 m s^{-2}), r describes the radius of the sphere, C_F represents the Faxen correction, d is the difference between the density of the platinum sphere and the melt and d is the falling distance (Vetere et al. 2006). If the glass cylinder was intact after the sample synthesis in the IHPV, 2 mm glass discs were cut off at each end. Afterwards, one of the glass discs was added to the bottom of a new 20 mm $Au_{75}Pd_{25}$ capsule that was sealed on the bottom with a PUK welding device. Afterwards, a thin reference layer of palladium powder (1.2 to 2.5 µm grain size) was added in front of the glass cylinder. After the positioning of the cylinder in the capsule, a thin layer of the original basaltic glass powder was added to the glass cylinder with an embedded 150 to 300 µm diameter Pt sphere (ρ – 12 g cm^{-3}). The Pt spheres were produced by melting of a platinum wire (0.125 mm diameter) with a short current impulse. The spheres were checked to be consistent in shape and the diameter was measured using a Keyence-microscope. The powder is intended to support the stabilisation of the Pt sphere. The final step in the assembly is to add the other glass disc on top and the capsule was closed by welding.

The positioning of the Pt sphere in the melt was performed by a short run in IHPV at 1550 ± 10 K and 200 ± 5 MPa for 15 min. Then, the glass cylinder were removed from the capsule and the intact cylinder was measured with XRCT 4.0 X-ray machine (see 3.3. Computer tomography). An optical determination of the Pt spheres was not possible due to the high iron content and the resulting light transmission. Afterwards, the glass cylinder was repacked in an $Au_{75}Pd_{25}$ capsule and synthesised in a rapid quench cold seal pressure vessel (RQ-CSPV) at 1223 K and 200 MPa for 5 h. Then the capsule was reopened and the intact glass cylinder was measured with X-ray tomography. The low viscosity can be calculated by the distance of fallen sphere at a given runtime after equation 17.

3.3. Computer tomography

The determination of the Pt sphere position in the glass cylinder was performed using an XRCT 4.0 X-ray machine. The X-ray tomography is based on a large number of X-ray images of the target object from diverse directions, whereby a 2D or 3D image is generated. A detailed description of the principle function and modification of the resolution of computer tomography can be found in Maire and Withers (2013). Each glass cylinder was acquired with an acceleration voltage of 35 kV and an exposure time of 0.5 s. The analysis enables an observation of the cylinders from all direction, whereby the exact positioning of the Pt sphere can be determine and optically evaluated.

4. Results and Discussion

4.1. Micropenetration viscosity technique

Before the falling sphere experiment could be started, the measurement condition was calculated on the basis of the micropenetration viscosity data and the interpolation/extrapolation in the range of 10^0 to 10^5 Pa s. Figure 150 illustrates this extrapolation of the Arrhenian fit (dashed line) compared to the interpolation VFT fit assuming a value of -4.55 at infinite temperature (line) of the viscosity data of CO_2-free and 1479 ppm CO_2-bearing halogen-free basalt. Both fits were extrapolated to a viscosity of 10^0 Pa s, whereby the temperature of specific viscosity can be read off.

Table 40 lists the theoretical temperature (K) in the viscosity range of 10^0 to 10^5 Pa s for CO_2-free and 1479 ppm CO_2-bearing basalt. The theoretical temperature was determined by the Arrhenius fit and VFT fit. It is clearly shown that the VFT fit results in a higher temperature for the lower viscosity range than the temperature calculated by Arrhenius fit. At a viscosity of 10^0 Pa s, the CO_2-free basalt shows a theoretical temperature of 1401 K for Arrhenius fit, whereas the VFT fit results in a higher theoretical temperature of 1600 K. The addition of 1479 ppm CO_2 to the halogen-free basalt shows a lower theoretical temperature of 1372 K for Arrhenius fit and the VFT fit reflects a temperature of 1513 K (at 10^0 Pa s). Generally, the VFT fit describes the viscosity data as a curve in the low viscosity region. Based on literature data (Fulcher 1925; Tammann and Hesse 1926) the viscosity in the range of 10^0 to 10^{13} Pa s can be described more accurately by the VFT fit than the Arrhenius fit. However, the theoretical temperature of the Arrhenius fit was used for the following falling sphere experiment, due to the maximum temperature of 1273 K of the used CSPV.

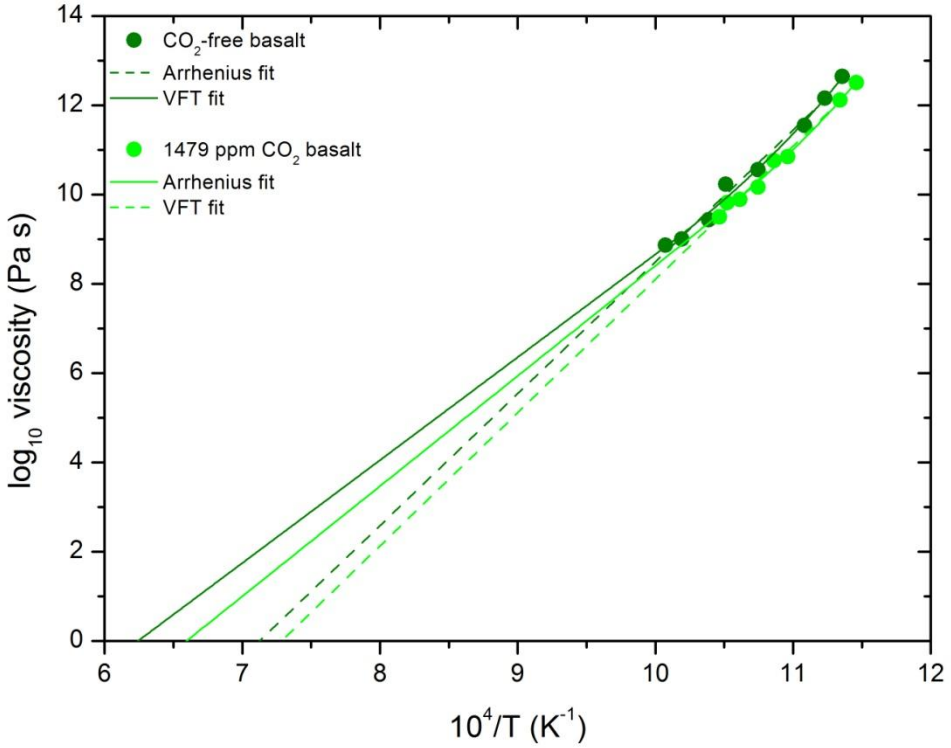

Figure 150: Comparison of Arrhenian fit (dashed line) and VFT fit (solid line) of the viscosity data of CO_2-free halogen-free basalt (dark green) and 1479 ppm CO_2 halogen-free (light green) basalt. The error bars are smaller than the symbols.

Table 40: Extrapolated viscosity data of CO_2-free basalt and 1479 ppm CO_2-bearing basalt with associated theoretical temperatures.

CO_2-free basalt				1479 ppm CO_2 basalt			
Arrhenius fit		VFT fit		Arrhenius fit		VFT fit	
T (K)	$\log_{10}\eta$ (Pa s)	T (K)	$\log_{10}\eta$ (Pa s)	T (K)	$\log_{10}\eta$ (Pa s)	T (K)	$\log_{10}\eta$ (Pa s)
1133.8	5	1189.2	5	1116.2	5	1161.4	5
1179.2	4	1267.4	4	1158.9	4	1213.6	4
1227.0	3	1324.5	3	1204.8	3	1280.4	3
1285.3	2	1404.5	2	1259.4	2	1348.3	2
1341.2	1	1497.9	1	1311.8	1	1430.6	1
1401.3	0	1600.0	0	1372.0	0	1512.9	0

4.2. Optical determination of the Pt sphere position

Before the falling sphere experiment can be started, the proportions of the glass cylinder and the positioning of the Pt sphere have to be measured. On the basis of 200 projections, the position of the Pt sphere was checked, whereby the sphere cannot be located close to the sides of the capsule. For high accuracy, a stainless steel cylinder was prepared on a fixed length of 20.01 mm and measured by XRCT 4.0 X-ray machine (figure 151). Thus, a length correction can be performed for all following falling sphere experiments.

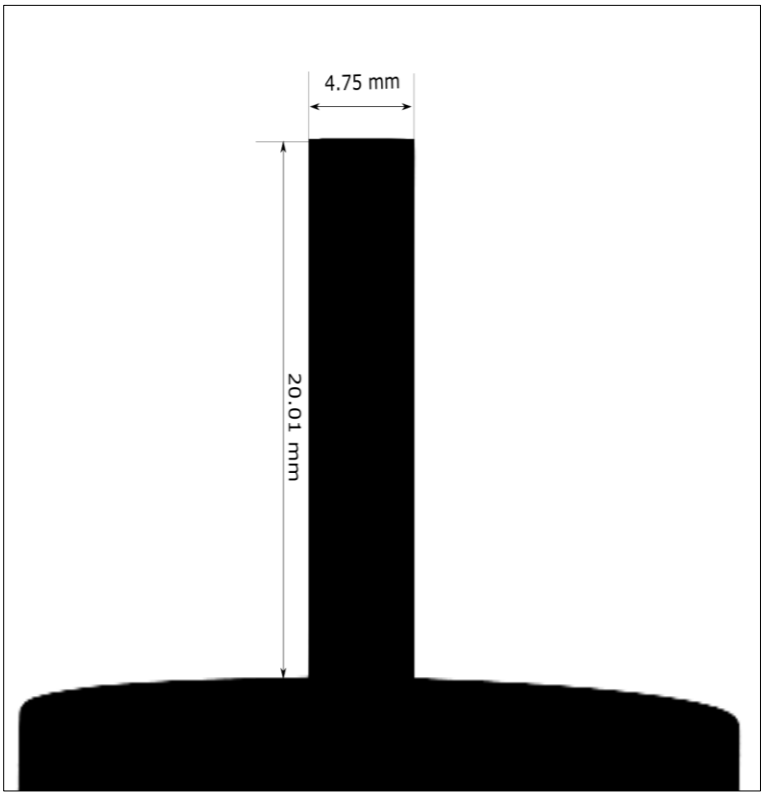

Figure 151: Computer tomography image of stainless steel cylinder with a length of 20.01 mm.

The image of basalt with 1450 ppm CO_2 with a Pt sphere as well as the dimensions is shown in figure 152. It is notable, that the Pt sphere is located close to the constriction in the glass cylinder, but all 200 images reflect that the sphere is not too close to the rim. The added palladium powder cannot be observed with the computer tomography, because the layer was too thin. Besides the CO_2 halogen-free basalt, the 1550 ppm CO_2 chlorine-bearing basalt was synthesised with an added platinum sphere (figure 153). After a verification of the positioning of the Pt sphere, both glass cylinders were prepared in new capsules and the falling sphere experiments were performed.

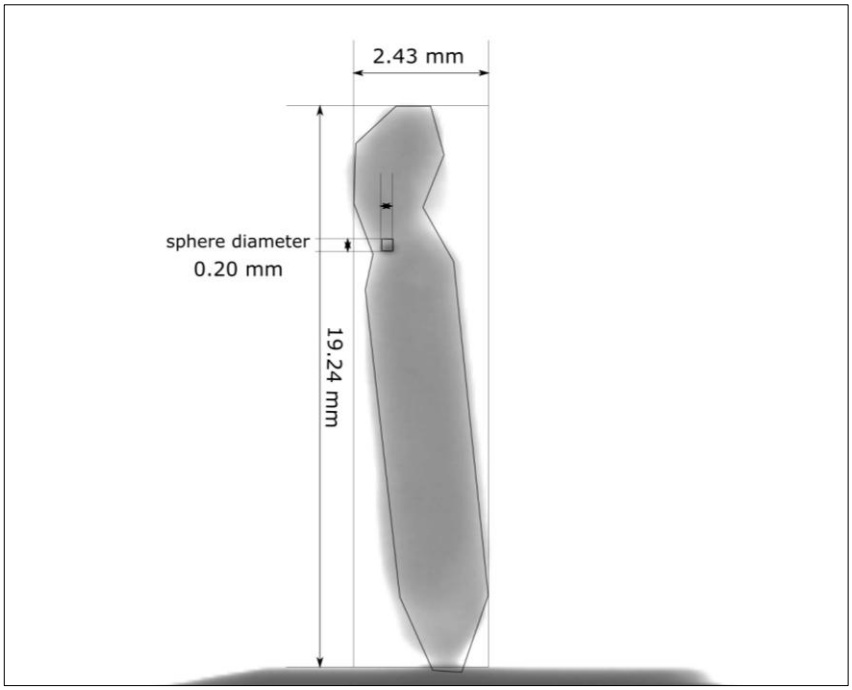

Figure 152: Computer tomography image of 1479 ppm CO_2 -bearing basalt with a Pt sphere (before the falling sphere experiment).

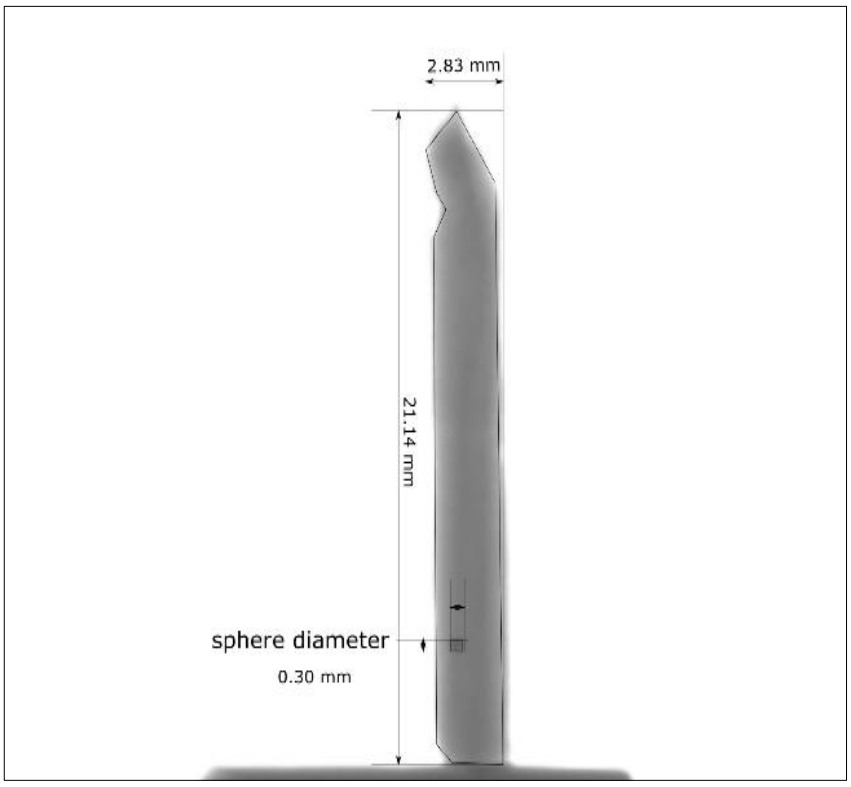

Figure 153: Computer tomography image of 1550 ppm CO_2 chlorine-bearing basalt with a Pt sphere (before the falling sphere experiment).

After the first falling sphere experiment, the chlorine-bearing basalt with 1550 ppm CO_2 has changed optically and showed a crystallised surface. Figure 154 shows the optical change of the glass cylinders during the 5 h falling sphere experiments. A cross section indicates a total crystallisation in the glass. The sample was is analysed by electron microprobe to identify the crystals (figure 155). The BSE image confirms the assumption that the glass crystallised and the crystals can be identified as plagioclase.

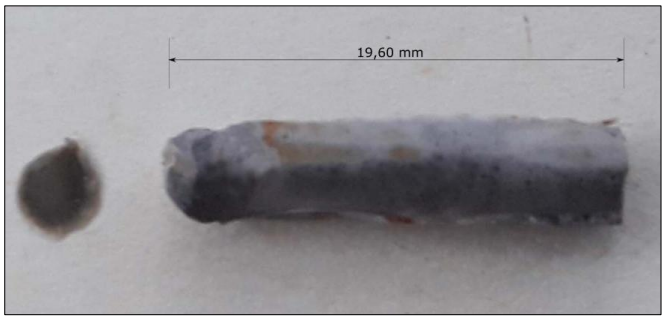

Figure 154: After the 5 h falling sphere experiment, an image of 1550 ppm CO_2 chlorine-bearing basalt with a crystallised surface.

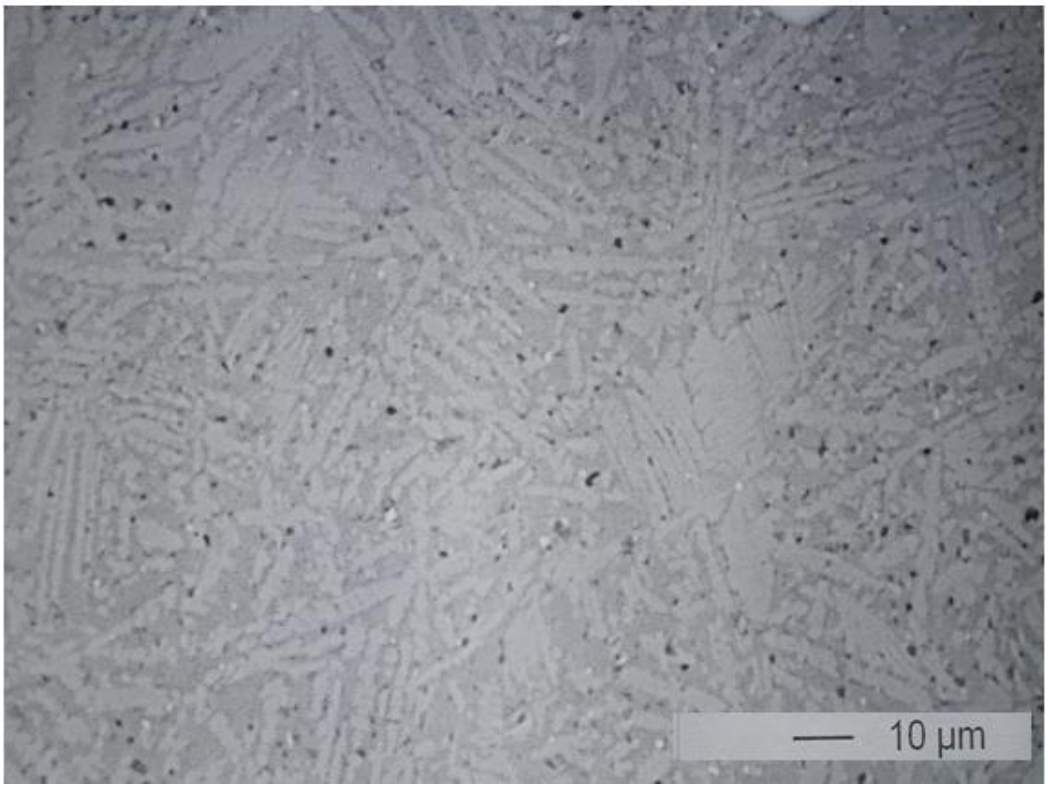

Figure 155: Microprobe analysis - BSE image of 1550 ppm CO_2 chlorine-bearing basalt (after the 5 h falling sphere experiment) showing plagioclase crystals.

Despite the crystallisation effect, the Pt sphere fell down during the falling sphere experiment in CSPV. Therefore, the glass cylinder was analysed with XRCT 4.0 X-ray machine (see figure 156). The image processing of selected projections does not provide insights into the crystallised glass cylinder. Thus, the Pt sphere cannot be located inside the cylinder or is covered by the plagioclase crystallisation.

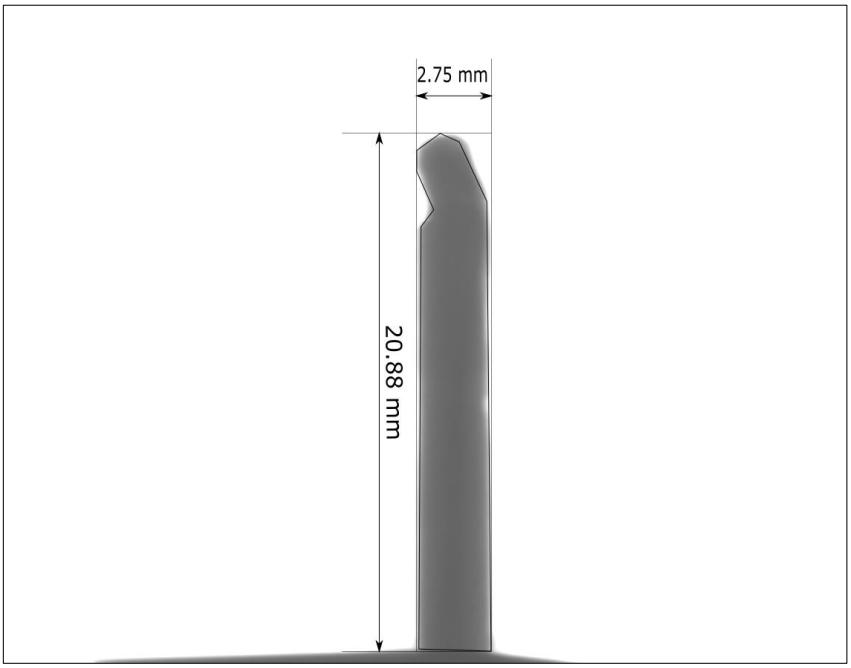

Figure 156: After the falling sphere experiment, Computer tomography image of 1550 ppm CO_2 chlorine-bearing basalt with a Pt sphere.

In order to explain the crystallisation effect of the first falling sphere experiment, the CO_2-free, 0.15 wt% CO_2-bearing halogen-free and chlorine-bearing basaltic glasses were heated up to diverse temperatures with a heating rate of 20 K min^{-1} and held for 1 h at a constant temperature (table 41). The presence of CO_2 in halogen-free basaltic glasses does not change the temperature at which the crystallisation starts, whereas the addition of CO_2 to chlorine-bearing basaltic glass shows a decrease in the beginning of crystallisation from 980 to 965 K. Consequently, a falling sphere experiment above these temperature (begin of crystallisation) is not possible with this basaltic composition.

Table 41: Heating experiments of 1479 ppm CO_2 -bearing halogen-free basalt and 1550 ppm CO_2 chlorine-bearing basalt delimiting the range of crystallisation.

Temperature (K)	CO_2-free BA-0_III	BA-0_0.15C	BA-Cl_0.15C
850	no crystals	no crystals	no crystals
950	no crystals	no crystals	no crystals
965	no crystals	no crystals	**begin of crystallisation**
980	**begin of crystallisation**	**begin of crystallisation**	crystals
1050	crystals	crystals	crystals
1150	crystals	crystals	crystals
…	crystals	crystals	crystals
1523	crystals	crystals	crystals
1548	melting temperature	melting temperature	melting temperature

5. Conclusion

This study demonstrates the problems that occur in the temperature range required for low viscosity conditions (range of 10^0 to 10^5 Pa s) for CO_2-free and –bearing basaltic melts. An alternative method to the estimation of the low viscosity data based on Arrhenius and VFT fits of the micro penetration data is the performance of falling sphere experiments near the melting temperature of 1548 K. However, most of the investigated basaltic melts tend to crystallise above 965 to 980 K which is enhanced by the presence of CO_2. The problem is not that the melt crystallises during the fall of the sphere, but that it crystallises upon cooling and the sphere cannot be found using X-rays. These investigations yield to the finding that XRCT 4.0 X-ray computer tomography is the optimal analysis for defining the position of Pt spheres in discoloured and crystal-free glasses. The range of the liquidus temperature and low viscosity has to be tested in further experiments, where crystallisation effects occur within the present basaltic composition.

Final conclusion

This work provides new information about the effect of volatiles (Cl^-, F^-, H_2O and CO_2) on the viscosity and Fe^{2+}/Fe_{total} of basaltic melts. The viscosity is measured by the micropenetration method in a range between $10^{8.5}$ and $10^{13.5}$ Pa s and the Fe^{2+}/Fe_{total} by colorimetric micro-determination of ferrous iron.

The effect of Cl^- and F^- on the viscosity of basaltic melts shows different trends (see figure C). The addition of F^- to basaltic melts results in a decrease in viscosity due to the formation of Si-F bonds and a decrease in Fe^{2+}/Fe_{total}. The increasing F^- content results in an increasing number of network formers (Fe^{3+}), whereby a polymerisation of the network structure occurs. This effect is weaker than the resulting depolymerisation of the melt due to the addition of F^- to the structure and viscosity decreases with the addition of F^-. The presence of Cl^- up to 2.53 mol% results in an increase in viscosity, whereas the further addition of chlorine results in a decrease in viscosity. The increasing viscosity results from the formation of Na-Cl and Ca-Cl_2 complexes (Baasner et al. 2013a) and the decreasing viscosity occurs by Si-Cl bonds (Giordano et al. 2004). The observed correlation between Cl^- and Fe^{2+}/Fe_{total} by Webb et al. (2014) cannot be confirmed by the present chlorine-bearing melts.

Besides the halogens, the decreasing oxygen fugacity results in a decrease in viscosity by 0.3 log units due to increasing Fe^{2+}/Fe_{total} from 0.16 to 0.82. The increasing number of network modifiers (Fe^{2+}) reflects a depolymerisation of the melt structure. The Raman spectroscopy shows a decreasing intensity in the low frequency region due to decreasing oxygen fugacity. The dependence of LF/HF intensity ratio and Fe^{2+}/Fe_{total} enables a differentiation between silicate melts with different NBO/T, FeO_{total} content and Fe/Al. The oxygen fugacity of natural melts can be calculated by Kress and Carmichael (1991), but the melting temperature has to be known. Generally, the high viscosity of natural melts can be measured, but evidence of a viscosity trend requires a 1 atm and volatile-free natural melt. A rough estimation of viscosity can be done by Fe^{2+}/Fe_{total} using the information that the viscosity decreases by 0.1 log units (in the 10^8 – 10^{13} Pa s range) due to increasing Fe^{2+}/Fe_{total} of 0.2.

The presence of 3.47 wt% H_2O in halogen-free basaltic melts results in a decrease in viscosity by 5.2 log units (see figure C) and a decrease in Fe^{2+}/Fe_{total} from 0.6 to 0.2. The presence of OH groups in halogen-free and –bearing basaltic glasses shows a nearly linear decrease in Fe^{2+}/Fe_{total}, whereas the total water content shows an exponential trend. The OH groups describe the water species, which is incorporated in the melt structure due to bonding to an oxygen. The increasing number of network formers (Fe^{3+}) results in a polymerisation of

the structure, whereas the depolymerisation effect is enhanced due to increasing water content. Baasner et al. (2013b) suggested that the presence of 12.58 mol% H_2O to NACS decreases T_g^{12} by 400 K, whereas the addition of 12.56 mol% H_2O to the present basaltic melt decreases in T_g^{12} by 150 K. Consequently, the effect of H_2O is more effective in iron-free melts. One also needs to take into account how much OH is present and not the total water content. The addition of 0.34 mol% CO_2 to basaltic melts shows a decrease in viscosity by 0.7 log units (see figure C), whereas no clear dependence between CO_2 content and Fe^{2+}/Fe_{total} was found. Furthermore, the study suggests that a sample synthesised in IHPV decreases the viscosity by 2 log units due to an increase in oxygen fugacity (log fO_2: 0.68 to -3.56 to -2.56).

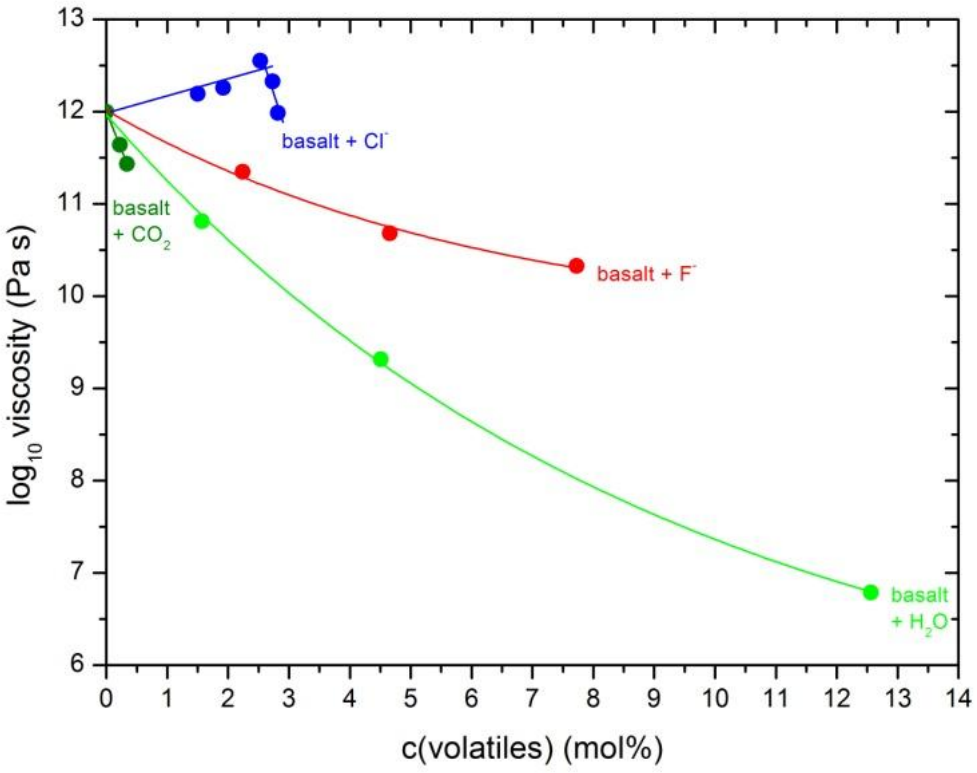

C: The change in viscosity due to the addition of volatiles (Cl^-, F^-, H_2O, CO_2) at the same temperature as the original melts at 10^{12} Pa s. The error bars are smaller than the symbols.

Outlook

This study describes the effect of volatiles and redox state on the viscosity and Fe^{2+}/Fe_{total} of halogen-free and –bearing basaltic melts. The new findings result in new questions and limitations for previous models.

It is not proven that the addition of < 2.53 mol% Cl^- to basaltic melts replaces the Si-O-Si bonds by Si-Cl bonds. The environment of chlorine should be analysed with NMR spectroscopy and can give the answer of the two different viscosity trends of chlorine bearing melts observed here. The presence of Cl^- in peralkaline melts effects the viscosity in different ways and the increase in Fe^{2+}/Fe_{total} of 0.2 results in a decrease in viscosity by 0.1 log units. These results should be considered in further viscosity models, whereby a high accuracy of calculated viscosity can be obtained. The best results for the present basalt are given by the model of Sehlke and Whittington (2016), which can be modified with the halogen contents.

Furthermore, the model of Fe^{2+}/Fe_{total} after Kress and Carmichael (1991) is too imprecise for natural compositions, because the model does not consider all components especially the halogens and H_2O content. This H_2O and CO_2-bearing basaltic composition should be synthesised without iron, whereas the decreasing effect of viscosity is enhanced due to the contrary effect by decreasing Fe^{2+}/Fe_{total}. The effect of CO_2 on basaltic melts results in a decrease in viscosity by 0.7 log units and these new results should be include in further viscosity models.

This study demonstrates the problem that basaltic melts tend to crystallise above 965 to 980 K, which is enhanced by the presence of CO_2. The range of viscosity above the liquidus temperature needs to be investigated using alternative techniques in order to avoid the growth of crystals.

Curriculum Vitae

Personal data:

Wiebke Pischel

Born in Hildesheim (Germany) 11/04/1989

EDUCATION & STUDIES:

Since 10/2015	PhD student at the Department for Applied and Experimental Mineralogy at Georg-August University Göttingen (Germany) Topic: "Influence of oxygen fugacity on the viscosity of CO_2, H_2O-, and halogen-bearing basaltic melts"
04/2013 – 04/2015	Master studies in geoscience at Leibniz University Hannover (Germany) Master thesis: "The influence of water on the structure and properties of boro-phosphate glasses"
10/2009 – 03/2013	Bachelor studies in geoscience at Leibniz University Hannover (Germany) Bachelor thesis: "Structural analysis of lithium borate glass"
06/2009	General university entrance qualification at CJD Christophorusschule Elze

References

Adam, Gerold; Gibbs, Julian H. (1965): On the Temperature Dependence of Cooperative Relaxation Properties in Glass-Forming Liquids. In *The Journal of Chemical Physics* 43 (1), pp. 139–146. DOI: 10.1063/1.1696442.

Baasner, A.; Schmidt, B. C.; Dupree, R.; Webb, S. L. (2014): Fluorine speciation as a function of composition in peralkaline and peraluminous Na_2O–CaO–Al_2O_3–SiO_2 glasses. A multinuclear NMR study. In *Geochimica et Cosmochimica Acta* 132, pp. 151–169. DOI: 10.1016/j.gca.2014.01.041.

Baasner, A.; Schmidt, B. C.; Webb, S. L. (2013a): Compositional dependence of the rheology of halogen (F, Cl) bearing aluminosilicate melts. In *Chemical Geology* 346, pp. 172–183. DOI: 10.1016/j.chemgeo.2012.09.020.

Baasner, A.; Schmidt, B. C.; Webb, S. L. (2013b): The effect of chlorine, fluorine and water on the viscosity of aluminosilicate melts. In *Chemical Geology* 357, pp. 134–149. DOI: 10.1016/j.chemgeo.2013.08.020.

Bartels, Alexander; Behrens, Harald; Holtz, Francois; Schmidt, Burkhard C.; Fechtelkord, Michael; Knipping, Jaayke et al. (2013): The effect of fluorine, boron and phosphorus on the viscosity of pegmatite forming melts. In *Chemical Geology* 346, pp. 184–198. DOI: 10.1016/j.chemgeo.2012.09.024.

Bartels, Alexander; Vetere, Francesco; Holtz, Francois; Behrens, Harald; Linnen, Robert L. (2011): Viscosity of flux-rich pegmatitic melts. In *Contrib Mineral Petrol* 162 (1), pp. 51–60. DOI: 10.1007/s00410-010-0582-3.

Behrens, Harald; Romano, Claudia: Nowak, Marcus; Holtz, Francois: Dingwell, Donald B. (1996): Near-infrared spectroscopic determination of water species glasses of the system MAlSi,O, (M = Li, Na, K) : inter laboratory study. In *Chemical Geology* 128, pp. 41–63.

Berndt, Jasper; Liebske, Christian; Holtz, Francois; Freise, Marcus; Nowak, Marcus; Ziegenbein, Dieter et al. (2002): A combined rapid-quench and H_2 membrane setup for internally heated pressure vessels; Description and application for water solubility in basaltic melts. American Mineralogist, 87, pp. 1717-1726.

Black, Benjamin A.; Elkins-Tanton, Linda T.; Rowe, Michael C.; Peate, Ingrid Ukstins (2012): Magnitude and consequences of volatile release from the Siberian Traps. In *Earth and Planetary Science Letters* 317-318, pp. 363–373. DOI: 10.1016/j.epsl.2011.12.001.

Bockris, J. O'M; Tomplinson, J. W.; White, J. L. (1956): The structure of the liquid silicates: partial molar volumes and expansivities. In *Trans. Faraday Soc.* 52, pp. 299–310.

Bourgue, Emmanuelle; Richet, Pascal (2001): The effects of dissolved CO_2 on the density and viscosity of silicate melts: a preliminary study. In *Earth and Planetary Science Letters* 193, pp. 57-68.

Brearley, Mark; Montana, Art (1989): The effect of CO_2 on the viscosity of silicate liquids at high pressure. In Geochimica et Cosmochimica Acta, 53, pp. 2609-2616.

Brey, G. (1976): CO_2 solubility and solubility mechanisms in silicate melts at high pressures. In *Contr. Mineral. and Petrol.* 57 (2), pp. 215–221. DOI: 10.1007/BF00405226.

Byers, Charles D.; Garcia, Michael O.; Muenow, David W. (1986): Volatiles in basaltic glasses from the East Pacific Rise at 21°N: implications for MORB sources and submarine lava flow morphology. In *Earth and Planetary Science Letters* 79, pp. 9–20.

Cartigny, Pierre; Pineau, Françoise; Aubaud, Cyril; Javoy, Marc (2008): Towards a consistent mantle carbon flux estimate. Insights from volatile systematics (H_2O/Ce, δD, CO_2/Nb) in the North Atlantic mantle (14° N and 34° N). In *Earth and Planetary Science Letters* 265 (3-4), pp. 672–685. DOI: 10.1016/j.epsl.2007.11.011.

Christie, David M.; Carmichael, Ian S.E.; Langmuir, Charles H. (1986): Oxidation states of mid-ocean ridge basalt glasses. In *Earth and Planetary Science Letters* 79 (3-4), pp. 397–411. DOI: 10.1016/0012-821X(86)90195-0.

Danyushevsky, Leonid V. (2001): The effect of small amounts of H_2O on crystallisation of mid-ocean ridge and backarc basin magmas. In *Journal of Volcanology and Geothermal Research* 110 (3-4), pp. 265–280. DOI: 10.1016/S0377-0273(01)00213-X.

Deines, Peter; Nafziger Ralph H.; Ulmer, Gene C.; Woermann, Eduard (1974): Temperature - oxygen fugacity tables for selected gas mixtures in the system C-H-O at one atmosphere total pressure. Earth and Mineral Sciences, experimental station, 88, pp 1-134.

Di Genova, D.; Romano, C.; Alletti, M.; Misiti, V.; Scarlato, P. (2014): The effect of CO_2 and H_2O on Etna and Fondo Riccio (Phlegrean Fields) liquid viscosity, glass transition temperature and heat capacity. In *Chemical Geology* 377, pp. 72–86. DOI: 10.1016/j.chemgeo.2014.04.001.

Di Genova, Danilo; Hess, Kai-Uwe; Chevrel, Magdalena Oryaëlle; Dingwell, Donald B. (2016): Models for the estimation of Fe 3+ /Fe tot ratio in terrestrial and extraterrestrial alkali- and iron-rich silicate glasses using Raman spectroscopy. In *American Mineralogist* 101 (4), pp. 943–952. DOI: 10.2138/am-2016-5534CCBYNCND.

Di Muro, Andrea; Métrich, Nicole; Mercier, Maxime; Giordano, Daniele; Massare, Dominique; Montagnac, Gilles (2009): Micro-Raman determination of iron redox state in dry natural glasses. Application to peralkaline rhyolites and basalts. In *Chemical Geology* 259 (1-2), pp. 78–88. DOI: 10.1016/j.chemgeo.2008.08.013.

Dingwell, D. B.; Hess, K. U. (1998): Melt viscosities in the system Na-Fe-Si-O-F-Cl; contrasting effects of F and Cl in alkaline melts. In *American Mineralogist* 83 (9-10), pp. 1016–1021. DOI: 10.2138/am-1998-9-1009.

Dingwell, Donald B. (1991): Redox viscometry of some Fe-bearing silicate melt. In *American Mineralogist,* 76, pp. 1560–1562.

Dingwell, Donald B.; Webb, Sharon L. (1990): Relaxation in silicate melts. In *ejm* 2 (4), pp. 427–451. DOI: 10.1127/ejm/2/4/0427.

Dingwell, Donald. B.; Mysen, Bjorn O. (1985): Effects of water and fluorine on the viscosity of albite melt at high pressure: a preliminary investigation. In Richard Stone (Ed.): Introduction to Internal Combustion Engines. London: Macmillan Education UK, pp. 1–21.

Duan, X. (2014): A model for calculating the viscosity of natural iron-bearing silicate melts over a wide range of temperatures, pressures, oxygen fugacites, and compositions. In *American Mineralogist* 99 (11-12), pp. 2378–2388. DOI: 10.2138/am-2014-4841.

Elementar Analysensysteme GmbH (2016): Flyer rapid CS cube EN 09-2016-A. Available online at https://www.elementar.de/fileadmin/user_upload/Elementar_Website/Downloads/Flyer/Flyer-rapid-CS-cube-EN.pdf, updated on 12/15/2016, checked on 9/10/2018.

Evans, K. A.; Mavrogenes, J. A.; O'Neill, H. S.; Keller, N. S.; Jang, L.-Y. (2008): A preliminary investigation of chlorine XANES in silicate glasses. In *Geochem. Geophys. Geosyst.* 9 (10), n/a-n/a. DOI: 10.1029/2008GC002157.

FAIRBAIRN, H. W., et al. (1950-51): A Cooperative Investigation of Precision and Accuracy in Chemical, Spectrochemical, and Modal Analysis of Silicate Rocks. In *UNITED STATES GOVERNMENT PRINTING OFFICE* 980.

Ferraro, John R.; Nakamoto, Kazuo (Eds.) (1994): Introductory Raman Spectroscopy. Academic Press Inc. Harcourt Brace & Company, Publishers.

Fine, Gerald; Stolper, Edward (1985): The speciation of carbon dioxide in sodium aluminosilicate glasses. In *Contr. Mineral. and Petrol.* 91 (2), pp. 105–121. DOI: 10.1007/BF00377759.

Flude, Stephanie; Haschke, Michael; Storey, Michael (2017): Application of benchtop micro-XRF to geological materials. In *Mineral. mag.* 81 (04), pp. 923–948. DOI: 10.1180/minmag.2016.080.150.

Fulcher, G. S. (1925): Analysis of recent measurements of the viscosity of glasses-II1. In *J American Ceramic Society* 8 (12), pp. 789–794. DOI: 10.1111/j.1151-2916.1925.tb18582.x.

Furukawa, Toshiharu; Fox, Karen E.; White, William B. (1981): Raman spectroscopic investigation of the structure of silicate glasses. III. Raman intensities and structural units in sodium silicate glasses. In *The Journal of Chemical Physics* 75 (7), pp. 3226–3237. DOI: 10.1063/1.442472.

Gill, Robin (2010): Igneous rocks and processes. A practical guide. 1st ed. Wiley-Blackwell.

Giordano, D.; Romano, C.; Dingwell, D. B.; Poe, B.; Behrens, H. (2004): The combined effects of water and fluorine on the viscosity of silicic magmas. In *Geochimica et Cosmochimica Acta* 68 (24), pp. 5159–5168. DOI: 10.1016/j.gca.2004.08.012.

Giordano, Daniele; Russell, James K.; Dingwell, Donald B. (2008): Viscosity of magmatic liquids. A model. In *Earth and Planetary Science Letters* 271 (1-4), pp. 123–134. DOI: 10.1016/j.epsl.2008.03.038.

Gütlich, Philipp; Bill, Eckhard; Trautwein, Alfred X. (2010): Mössbauer Spectroscopy and Transition Metal Chemistry. Fundamentals and Applications. Springer Science & Business Media.

Häggström, L.; Wäppling, R.; Annersten, H. (1969): Mössbauer Study of Oxidized Iron Silicate Minerals 33, p. 741.

Harris, Daniel C. (2014): Lehrbuch der Quantitativen Analysen. In *Springer Verlag* 8. DOI: 10.1007/978-3-642-37788-4_18.

Jayasuriya, Kasthuri D.; O'Neill, Hugh ST.C.; Berry, Andrew J., Campbell, Stewart J. (2004): A Mössbauer study of the oxidation state of Fe in silicate melts. In *Applied Thermal Engineering* (89), pp. 1597–1609.

Knipping, Jaayke L.; Behrens, Harald; Wilke, Max; Göttlicher, Jörg; Stabile, Paola (2015): Effect of oxygen fugacity on the coordination and oxidation state of iron in alkali bearing silicate melts. In *Chemical Geology* 411, pp. 143–154. DOI: 10.1016/j.chemgeo.2015.07.004.

Kohn, S. C. (2000): The dissolution mechanisms of water in silicate melts; a synthesis of recent data. In *Mineralogical Magazine* 64 (3), pp. 389–408. DOI: 10.1180/002646100549463.

Kohn, Simon C.; Dupree, Ray; Smith, M. E. (1989): Proton environments and hydrogen-bonding in hydrous silicate glasses from proton NMR. In *Nature* 337, pp. 539–541.

Koleszar, A. M.; Saal, A. E.; Hauri, E. H.; Nagle, A. N.; Liang, Y.; Kurz, M. D. (2009): The volatile contents of the Galapagos plume; evidence for H2O and F open system behaviour in melt inclusions. In *Earth and Planetary Science Letters* 287 (3-4), pp. 442–452. DOI: 10.1016/j.epsl.2009.08.029.

Konschak, Alexander; Keppler, Hans (2014): The speciation of carbon dioxide in silicate melts. In *Contrib Mineral Petrol* 167 (5). DOI: 10.1007/s00410-014-0998-2.

Kress, Victor C.; Carmichael, Ian S. E. (1991): The compressibility of silicate liquids containing Fe2O3 and the effect of composition, temperature, oxygen fugacity and pressure on their redox states. In *Contr. Mineral. and Petrol.* 108 (1-2), pp. 82–92. DOI: 10.1007/BF00307328.

Kress, Victor C.; Carmichael, Ian S. E. (1988): Stoichiometry of the iron oxidation reaction in silicate melts. In American mineralogist, 73, pp. 1267-1267.

Lange, Rebecca A.; Navrotsky, Alexandra (1992): Heat capacities of Fe_2O_3-bearing silicate liquids. In *Contr. Mineral. and Petrol.* 110 (2-3), pp. 311–320. DOI: 10.1007/BF00310746.

Le Roex, A. P.; Frey, Frederick A.; Richardson, Stephen H. (1996): Petrogenesis of lavas from the AMAR Valley and Narrowgate region of the FAMOUS Valley, 36°-37°N on the Mid-Atlantic Ridge. In *Contributions to Mineralogy and Petrology* 124 (2), pp. 167–184. DOI: 10.1007/s004100050183.

Liebske, Christian; Behrens, Harald; Holtz, François; Lange, Rebecca A. (2002): The influence of pressure and composition on the viscosity of andesitic melts. In Geochimica et Cosmochimica Acta, 67 (3), pp. 473-485.

Long, D. A. (1977): Raman spectroscopy. In *McGraw-Hill; New York*.

Maier, Chas. G.; Kelley, K. K. (1932): AN EQUATION FOR THE REPRESENTATION OF HIGH-TEMPERATURE HEAT CONTENT DATA 1. In *J. Am. Chem. Soc.* 54 (8), pp. 3243–3246. DOI: 10.1021/ja01347a029.

Maire, E.; Withers, P. J. (2013): Quantitative X-ray tomography. In *International Materials Reviews* 59 (1), pp. 1–43. DOI: 10.1179/1743280413Y.0000000023.

Mandeville, Charles W.; Webster, James D.; Rutherford, Malcolm J.; Taylor, Bruce; Timbal, Adrian; Faure, Kevin (2002): Determination of molar absorptivity for infrared absorption bands of H2O in andesitic glasses. In *American Mineralogist* 87, pp. 813–821.

Markl, Gregor (2015): Minerale und Gesteine. Mineralogie-Petrologie-Geochemie. 3rd ed.: Springer Verlag.

McMillian, Paul (1984): Structural studies of silicate glasses and melts-applications and limitations of Raman spectroscopy. In *American Mineralogist* 69, pp. 622–644.

Meerlender, G. (1974): Viskositäts-Temperaturverhalten des Standardglases I der DGG. Glas-technischer Bericht 47, pp. 1–3.

Misiti, V.; Vetere, F.; Freda, C.; Scarlato, P.; Behrens, H.; Mangiacapra, A.; Dingwell, D. B. (2011): A general viscosity model of Campi Flegrei (Italy) melts. In *Chemical Geology* 290 (1-2), pp. 50–59. DOI: 10.1016/j.chemgeo.2011.08.010.

Morizet, Y.; Kohn, S. C.; Brooker, R. A. (2001): Annealing experiments on CO_2-bearing jadeite glass. An insight into the true temperature dependence of CO_2 speciation in silicate melts. In *Mineralogical Magazine* 65 (6), pp. 701–707. DOI: 10.1180/0026461016560001.

Morizet, Y.; Vuilleumier, R.; Paris, M. (2015): A NMR and molecular dynamics study of CO2-bearing basaltic melts and glasses. In *Chemical Geology* 418, pp. 89–103. DOI: 10.1016/ j.chemgeo.2015.03.021.

Morizet, Yann; Nichols, Alexander R.L.; Kohn, Simon C.; Brooker, Richard A.; Dingwell, Donald B. (2007): The influence of H_2O and CO_2 on the glass transition temperature. Insights into the effects of volatiles on magma viscosity. In *Eur. J. Mineral.* 19 (5), pp. 657–669. DOI: 10.1127/0935-1221/2007/0019-1751.

Moynihan, Cornelius T.; Easteal, Allan J.; DeBolt, Mary Ann (1976): Dependence of the Fictive Temperature of Glass on Cooling Rate. In *Journal of the American Ceramic Society* (59).

Mysen, B. O. (1991): Relations Between Structure, Redox Equilibria of Iron, and Properties of Magmatic Liquids. In *In: Perchuk L.L., Kushiro I. (eds) Physical Chemistry of Magmas* 9, pp. 41–98. DOI: 10.1007/978-1-4612-3128-8_2.

Mysen, B. O.; Richet, P. (Eds.) (2005): Silicate Glasses and Melts — Properties and Structure. Elsevier, Amsterdam (10).

Mysen, Bjorn O. (1999): Structure and properties of magmatic liquids: From haplobasalt to haploandesite. In *Geochimica et Cosmochimica Acta* 63, pp. 95–112.

Mysen, Bjorn O. (2007): The solution behavior of H_2O in peralkaline aluminosilicate melts at high pressure with implications for properties of hydrous melts. In *Geochimica et Cosmochimica Acta* 71 (7), pp. 1820–1834. DOI: 10.1016/j.gca.2007.01.007.

Mysen, Bjorn O.; Virgo, David (1985a): Interaction between fluorine and silica in quenched melts on the joins SiO2-AlF3 and SiO2-NaF determined by Raman spectroscopy. In *Phys Chem Minerals* 12 (2), pp. 77–85. DOI: 10.1007/BF01046830.

Mysen, Bjorn O.; Virgo, David (1985b): Structure and properties of fluorine-bearing aluminosilicate melts: the system Na_2O-Al_2O_3-SiO_2-F at 1 atm. In *Contr. Mineral. and Petrol.* 91, pp. 205–220.

Ni, H.; Keppler, H. (2013): Carbon in Silicate Melts. In *Reviews in Mineralogy and Geochemistry* 75 (1), pp. 251–287. DOI: 10.2138/rmg.2013.75.9.

Okrusch, Martin; Matthes, Siegfried (2009): Mineralogie: Eine Einführung in die spezielle Mineralogie, Petrologie und Lagerstatten. Springer Spektrum.

Perkampus, Hein-Helmut (Ed.) (1986): UV-VIS-Spektroskopie und ihre Anwendungen. Springer-Verlag.

Pocklington, H. C. (1940): Rough measurement of high viscosities. In *Math. Proc. Camb. Phil. Soc.* 36 (04), p. 507. DOI: 10.1017/S0305004100017564.

Pressnall, Dean C.; Brenner, Norma L. (1974): A method for studying iron silicate liquids under reducing conditions with negligible iron loss*. PII: 0016-7037(74)90161-6. In *Geochimica et Cosmochimica Acta*., 38, pp. 1785-1788.

Richet, Pascal (1984): Viscosity and configurational entropy of silicate melts. In *Geochimica et Cosmochimica Acta,* 48, pp. 471–483.

Richet, Pascal (1987): Heat capacity of silicate glasses. In *Chemical Geology* 62 (1-2), pp. 111–124. DOI: 10.1016/0009-2541(87)90062-3.

Richet, Pascal; Bottinga, Yan (1984): Heat capacity of aluminum-free liquid silicates. In *Geochimica et Cosmochimica Acta*., 49, pp. 471-486.

Richet, Pascal; Robie, Richard A.; Hemingway, Bruce S. (1986): Low-temperature heat capacity of diopside glass (CaMgSi, OJ: A calorimetric test of the configurational-entropy theory applied to the viscosity of liquid silicates. In *Geochimica et Cosmochimica Acta* 50, pp. 1521–1533.

Robert, Geneviève; Knipping, Jaayke L.; Scherbarth, Stefanie; Robertson, Timothy E.; Stechern, André; Behrens, Harald; Whittington, Alan G. (2015): Heat capacity and viscosity of basaltic melts with H_2O±F±CO_2. In *Chemical Geology* 418, pp. 51–65. DOI: 10.1016/j.chemgeo.2014.07.015.

Robie, R. A.; Hemingway, B. S.; Fische, J. R. (1978): Thermodynamic Properties of Minerals and Related Substances at 298.15 K and 1 bar (105 pascals) Pressure and at Higher Temperatures. US Geological Survey Bulletin 2131.

Rossano, Stephane; Mysen, Bjorn (2012): Raman Spectroscopy of Silicate Glasses and Melts in Geological Systems. In Giovanni Ferraris, J. Dubessy, M.-C Caumon, F. Rull (Eds.): Raman spectroscopy applied to Earth sciences and cultural heritage: European Mineralogical Union, pp. 321–366.

Sack, R. O.; Carmichael, I. S. E.; Rivers, M.; Ghiorso, M. S. (1980): Ferric-ferrous equilibria in natural silicate liquids at 1 bar. In *Contr. Mineral. and Petrol.* 75, pp. 369–376.

Sandland, Travis O.; Du, Lin-Shu; Stebbins, Jonathan F.; Webster, James D. (2004): Structure of Cl-containing silicate and aluminosilicate glasses. A ^{35}Cl MAS-NMR study. In *Geochimica et Cosmochimica Acta* 68 (24), pp. 5059–5069. DOI: 10.1016/j.gca.2004.07.017.

Schaeffer, Helmut A.; Langefeld, Roland; Benz-Zaumer, Margareta (2012): Glastechnik; Werkstoff Glas, Glass: The Material.

Schmidt, Burkhard C.; Behrens, Harald (2008): Water solubility in phonolite melts. Influence of melt composition and temperature. In *Chemical Geology* 256 (3-4), pp. 259–268. DOI: 10.1016/ j.chemgeo.2008.06.043.

Scholze, Horst (1960): Zur Frage der Unterscheidung zwischen H_2O-Molekeln und OH-Gruppen in Gläsern und Mineralen 47 (226-227).

Scholze, Horst (2012): Glass: Nature, Structure and Properties: Springer Science & Business Media.

Schuessler, Jan A.; Botcharnikov, Roman E.; Behrens, Harald; Misiti, Valeria; Freda, Carmela (2007): Oxidation state of iron in hydrous phono-tephritic melts. In *American Mineralogist* 93, pp. 1493–1504. DOI: 10.2138/am.2008.2795.

Sehlke, Alexander; Whittington, Alan G. (2016): The viscosity of planetary tholeiitic melts. A configurational entropy model. In *Geochimica et Cosmochimica Acta* 191, pp. 277–299. DOI: 10.1016/j.gca.2016.07.027.

Shishkina, T. A.; Botcharnikov, R. E.; Holtz, F.; Almeev, R. R.; Portnyagin, M. V. (2010): Solubility of H_2O- and CO_2-bearing fluids in tholeiitic basalts at pressures up to 500MPa. In *Chemical Geology* 277 (1-2), pp. 115–125. DOI: 10.1016/j.chemgeo.2010.07.014.

Stabile, Paola; Webb, Sharon; Knipping, Jaayke L.; Behrens, Harald; Paris, Eleonora; Giuli, Gabriele (2016): Viscosity of pantelleritic and alkali-silicate melts. Effect of Fe redox state and Na/(Na+K) ratio. In *Chemical Geology* 442, pp. 73–82. DOI: 10.1016/j.chemgeo.2016.09.003.

Stebbins, J. F.; Carmichael, I. S. E.; Moret, L. K. (1984): Heat capacities and entropies of silicate liquids and glasses. In *Contr. Mineral. and Petrol.* 86 (2), pp. 131–148. DOI: 10.1007/BF00381840.

Stebbins, Jonathan F. (2016): Glass structure, melt structure, and dynamics. Some concepts for petrology. In *American Mineralogist* 101 (4), pp. 753–768. DOI: 10.2138/am-2016-5386.

Stebbins, Jonathan F.; Zeng, Qiang (2000): Cation ordering at fluoride sites in silicate glasses: a high-resolution 19F NMR study. In *Journal of Non-Crystalline Solids* 262, pp. 1–5.

Sternheimer, R. M. (1967): Density Effect for the Ionization Loss of Charged Particles. II. In *Phys. Rev.* 164 (2), pp. 349–351. DOI: 10.1103/PhysRev.164.349.

Stolper, Edward (1982a): The speciation of water in silicate melts. In *Geochimica et Cosmochimica Acta* 46 (12), pp. 2609–2620. DOI: 10.1016/0016-7037(82)90381-7.

Stolper, Edward (1982b): Water in silicate glasses: An infrared spectroscopic study. In *Contributions to Mineralogy and Petrology* 81, pp. 1–17.

Tammann, G.; Hesse, W. (1926): Die Abhängigkeit der Viskosität von der Temperatur bei unterkühlten Flüssigkeiten. In *Zeitschrift für anorganische und allgemeine Chemie* 156, pp. 245–257.

Toplis, Michael J. (1998): Energy barriers to viscous flow and the prediction of glass transition temperatures of molten silicates. In *American Mineralogist* 83 (5-6), pp. 480–490. DOI: 10.2138/am-1998-5-608.

Vetere, F.; Behrens, H.; Holtz, F.; NEUVILLE, D. (2006): Viscosity of andesitic melts—new experimental data and a revised calculation model. In *Chemical Geology* 228 (4), pp. 233–245. DOI: 10.1016/j.chemgeo.2005.10.009.

Vetere, Francesco; Behrens, Harald; Schuessler, Jan A.; Holtz, Francois; Misiti, Valeria; Borchers, L. (2008): Viscosity of andesite melts and its implication for magma mixing prior to Unzen 1991–1995 eruption. In *Journal of Volcanology and Geothermal Research* 175 (1-2), pp. 208–217. DOI: 10.1016/j.jvolgeores.2008.03.028.

Virgo, David; Mysen, Bjorn O. (1985): The structural state of iron in oxidized vs. reduced glasses at 1 atm: A ^{57}Fe Mössbauer study. In *Physics and Chemistry of Minerals* 12, pp. 65–76.

Wallace, Paul J. (2005): Volatiles in subduction zone magmas. Concentrations and fluxes based on melt inclusion and volcanic gas data. In *Journal of Volcanology and Geothermal Research* 140 (1-3), pp. 217–240. DOI: 10.1016/j.jvolgeores.2004.07.023.

Wang, Zifu; Cooney, Thomas F.; Sharma, Shiv K. (1993): High temperature structural investigation of $Na_2O_{0.5}$ Fe_2O_3 $3SiO_2$ and Na_2O FeO SiO_2 melts and glasses. In *Contr. Mineral. and Petrol.* 115 (1), pp. 112–122. DOI: 10.1007/BF00712983.

Wanless, V. D.; Perfit, M. R.; Ridley, W. I.; Wallace, P. J.; Grimes, C. B.; Klein, E. M. (2011): Volatile abundances and oxygen isotopes in basaltic to dacitic lavas on mid-ocean ridges. The role of assimilation at spreading centers. In *Chemical Geology* 287 (1-2), pp. 54–65. DOI: 10.1016/j.chemgeo.2011.05.017.

Weast, Robert C. (1989): CRC handbook of chemistry and physics. In *CRC Press, Inc., Boca Raton, Florida* 69.

Webb, Sharon (2005): Structure and rheology of iron-bearing Na_2O-Al_2O_3-SiO_2. In *Eur.J.Mineral.* 17 (2), pp. 223–232. DOI: 10.1127/0935-1221/2005/0017-0223.

Webb, Sharon L. (2008): Configurational heat capacity of Na_2O–CaO–Al_2O_3–SiO_2 melts. In *Chemical Geology* 256 (3-4), pp. 92–101. DOI: 10.1016/j.chemgeo.2008.04.003.

Webb, Sharon L.; Murton, Bramley J.; Wheeler, Andrew J. (2014): Rheology and the Fe^{3+}–chlorine reaction in basaltic melts. In *Chemical Geology* 366, pp. 24–31. DOI: 10.1016/j.chemgeo.2013.12.006.

White, Bradford S.; Art, Montana: The effect of H_2O and CO_2 on the viscosity of sanidine liquid at high pressures. Journal of Geophysical research, 95, pp. 15683-15693.

Wilson, A. D. (1960): The Micro-determination of Ferrous Iron in Silicate Minerals by a Volumetric and a Colorimetric Method. In *Analyst* 85 (1016), pp. 823–827. DOI: 10.1039/AN9608500823.

Yamashita, Shigeru; Behrens, Harald; Schmidt, Burkhard C.; Dupree, Ray (2008): Water speciation in sodium silicate glasses based on NIR and NMR spectroscopy. In *Chemical Geology* 256 (3-4), pp. 231–241. DOI: 10.1016/j.chemgeo.2008.06.029.

Yang, Yang; Teng, Lidong; Seetharaman, Seshadri (2012): Kinetic Studies on Evaporation of Liquid Vanadium Oxide, VO x (Where x = 4 or 5). In *Metall and Materi Trans B* 43 (6), pp. 1684–1691. DOI: 10.1007/s11663-012-9742-3.

Zachariasen, W. H. (1932): THE ATOMIC ARRANGEMENT IN GLASS. In *J. Am. Chem. Soc.* 54 (10), pp. 3841–3851. DOI: 10.1021/ja01349a006.

Zeng, Qiang; Stebbins, Jonathan F. (2000): Fluoride sites in aluminosilicate glasses: High-resolution 19 F NMR results. In *American Mineralogist* 85, pp. 863–867.

Table 42: Summary of the data Part A – Fe^{2+}/Fe_{total}, halogen content, density and molar volume of the glasses, T_g^{12}, T_f^{20}, C_p^{conf} and S_{conf}.

Melt	Fe^{2+}/Fe_{total}	Cl^- (mol%)	F^- (mol%%)	ρ (g cm^{-3})	V_m (cm^3 mol^{-1})	T_g^{12} (K)	T_f^{20} (K)	C_p^{conf} (J mol^{-1} K^{-1})	S^{conf} (J mol^{-1} K^{-1})
BA-0	0.18	0.02	n.a.	2.693	23.45	949.16	949	18.86	11.55
BA-Cl	0.18	2.82	0.12	2.673	23.29	948.46	948	19.18	12.65
BA-Cl-2	0.17	2.53	0.13	2.675	23.28	960.48	960	17.58	9.94
BA-Cl-3	0.21	2.73	n.a.	2.674	23.38	955.60	954	19.01	11.19
BA-Cl-4	0.18	1.92	n.a.	2.672	23.44	953.40	953	18.29	9.36
BA-Cl-F	0.18	2.15	1.13	2.678	23.15	922.57	923	17.27	13.25
BA-Cl-F-2	0.16	1.96	5.25	2.677	22.53	915.27	916	20.13	15.09
BA-Cl-F-3	0.29	3.28	2.35	2.679	22.78	941.92	942	17.58	12.49
BA-F	0.13	n.a.	2.24	2.693	23.14	932.32	932	18.91	12.16
BA-F-2	0.08	7.73	0.08	2.701	22.61	906.21	905	21.99	15.50

Table 43: Summary of the data Part B – Fe^{2+}/Fe_{total}, halogen content, density and molar volume of the glasses, T_g^{12}, T_f^{20}, C_p^{conf} and S_{conf}.

Melt	Fe^{2+}/Fe_{total}	Cl^- (mol%)	F^- (mol%)	ρ (g cm^{-3})	V_m (cm^3 mol^{-1})	T_g^{12} (K)	T_f^{20} (K)	C_p^{conf} (J mol^{-1} K^{-1})	S^{conf} (J mol^{-1} K^{-1})
BA-0_II	0.16	0.01	n.a.	2.704	23.41	944.76	945	18.86	11.55
BA-0_N3	0.50	0.01	n.a.	2.730	22.91	943.51	944	20.22	12.27
BA-0_N1	0.65	0.01	n.a.	2.635	23.53	939.57	940	17.39	10.25
BA-0_N-1	0.82	0.01	n.a.	2.596	23.82	933.53	934	16.20	9.94
BA-Cl_II	0.19	1.50	n.a.	2.679	23.36	952.66	953	18.28	9.36
BA-Cl_N3	0.54	0.92	n.a.	2.699	22.98	953.33	953	25.22	18.11
BA-Cl_N1	0.70	0.74	n.a.	2.677	23.05	946.39	946	22.60	13.85
BA-Cl_N-1	0.81	1.29	n.a.	2.669	23.00	940.49	941	17.28	11.29
BA-Cl-F_II	0.29	1.42	0.76	2.680	22.93	948.71	950	17.27	13.25
BA-Cl-F_N3	0.44	1.13	0.20	2.821	21.29	946.38	946	21.78	15.30
BA-Cl-F_N1	0.61	1.32	0.51	2.702	22.92	939.29	939	17.26	10.96
BA-Cl-F_N-1	0.85	1.28	0.48	2.591	23.66	925.55	926	16.88	11.82
BA-F_II	0.11	0.01	2.33	2.701	22.71	942.11	944	16.23	12.16
BA-F_N3	0.41	0.02	1.35	2.790	22.32	937.21	937	17.71	15.61
BA-F_N1	0.66	0.02	1.25	2.715	22.74	933.59	934	16.65	15.68
BA-F_N-1	0.72	0.01	1.87	2.603	23.52	909.98	910	12.10	9.09

Table 44: Summary of the data Part C – Fe^{2+}/Fe_{total}, H_2O, OH and CO_2 content, density and molar volume of the glasses, T_g^{12}, T_f^{20}, C_p^{conf} and S_{conf}.

Melt	Fe^{2+}/Fe_{total}	H_2O (wt%)	OH (wt%)	CO_2 (ppm)	ρ (g cm^{-3})	V_m (cm^3 mol^{-1})	T_g^{12} (K)	T_f^{20} (K)	C_p^{conf} (J mol^{-1} K^{-1})	S^{conf} (J mol^{-1} K^{-1})
BA-0_III	0.60	n.a.	~ 0.10	n.a.	2.719	23.22	893.97	894	23.13	20.17
BA-0_0.73H	0.52	0.21	0.52	n.a.	2.708	23.32	862.14	862	19.06	16.81
BA-0_1.29H	0.29	0.50	0.79	n.a.	2.678	23.58	821.59	822	13.80	11.64
BA-0_3.47	0.19	1.82	1.65	n.a.	2.669	23.66	748.10	748	8.71	8.86
BA-0_0.15C	0.66	n.a.	~ 0.10	1479	2.695	23.43	884.43	884	19.28	16.76
BA-0_0.23C	0.64	n.a.	~ 0.10	2199	2.646	23.86	878.98	879	19.39	16.34
BA-Cl_III	0.60	n.a.	~ 0.10	n.a.	2.692	22.97	900.67	901	15.49	12.98
BA-Cl_0.53H	0.40	0.08	0.45	n.a.	2.661	23.23	863.67	864	14.54	11.04
BA-Cl_1.76H	0.32	0.72	1.04	n.a.	2.644	23.38	801.74	802	12.87	11.25
BA-Cl_3.56H	0.26	1.78	1.77	n.a.	2.635	23.46	747.47	747	8.96	10.90
BA-Cl_0.12C	0.76	n.a.	~ 0.10	1442	2.686	23.02	900.89	901	11.36	9.09
BA-Cl_0.37C	0.83	n.a.	~ 0.10	3658	2.567	24.08	889.33	889	9.71	7.68
BA-Cl-F_III	0.61	n.a.	~ 0.10	n.a.	2.712	22.41	876.52	877	19.32	17.09
BA-Cl-F_0.59H	0.50	0.05	0.54	n.a.	2.681	22.67	849.32	849	14.78	9.95
BA-Cl-F_1.31H	0.27	0.31	1.00	n.a.	2.649	22.94	788.72	789	12.54	11.51
BA-Cl-F_3.50H	0.21	0.99	2.51	n.a.	2.622	23.18	759.28	759	7.82	10.02
BA-Cl-F_0.14C	0.76	n.a.	~ 0.10	1234	2.708	22.44	886.49	886	11.75	10.27
BA-Cl-F_0.29C	0.63	n.a.	~ 0.10	2975	2.676	22.71	878.19	878	8.41	7.20
BA-F_III	0.58	n.a.	~ 0.10	n.a.	2.720	22.43	905.75	906	24.22	22.22
BA-F_0.63H	0.39	n.a.	0.12	0.50	2.692	22.66	867.16	867	21.56	15.37

Melt	Fe^{2+}/Fe_{total}	H_2O (wt%)	OH (wt%)	CO_2 (ppm)	ρ (g cm^{-3})	V_m (cm^3 mol^{-1})	T_g[12] (K)	T_f[20] (K)	C_p^{conf} (J mol^{-1} K^{-1})	S^{conf} (J mol^{-1} K^{-1})
BA-F_1.84H	0.27	0.58	1.26	n.a.	2.686	22.71	815.55	816	16.37	15.11
BA-F_4.04H	0.22	1.83	2.22	n.a.	2.674	22.81	763.22	763	7.41	9.54
BA-F_0.09C	0.57	n.a.	~ 0.10	1018	2.737	22.29	890.73	891	18.89	16.00
BA-F_0.20C	0.37	n.a.	~ 0.10	1853	2.687	22.62	860.29	860	12.36	8.84

Table 45: Composition of the silicate glasses from Baasner et al. (2013a), Webb et al. (2014) and Robert et al. (2015) determined by electron microprobe.

Oxides/ ions mol%	X24[a]	X24 Cl-1[a]	X24 Cl-2[a]	X24 F[a]	HX24[a]	HX24 Cl-1[a]	HX24 Cl-2[a]	sb[b] synthetic basalt	fu06[b] Fuego basalt
SiO_2	54.79	55.01	54.75	53.73	54.80	54.94	55.25	51.93	52.70
Na_2O	2.75	2.29	1.95	2.64	2.72	2.58	1.48	3.21	3.21
K_2O	0.21	0.17	0.14	0.21	0.24	0.20	0.18	0.46	0.41
TiO_2	1.10	1.09	1.08	1.03	1.10	1.08	1.09	0.88	0.77
FeO (* FeO_{total})	1.10	2.00	3.06	1.41	n.a.	n.a.	n.a.	n.a.	9.42*
Fe_2O_3	3.82	5.00	2.01	3.54	n.a.	n.a.	n.a.	n.a	n.a.
Al_2O_3	9.77	9.74	9.71	9.49	13.60	13.62	13.66	11.07	11.05
MgO	13.81	13.64	13.54	13.39	14.88	14.87	14.86	22.37	11.86
CaO	12.46	12.31	12.19	12.06	12.48	12.33	12.57	10.09	10.25
MnO	0.16	0.15	0.14	0.17	0.17	0.15	0.13	n.a.	n.a.
Cl^-	n.a.	1.14	2.82	n.a.	n.a.	0.42	1.56	n.a.	n.a.
F^-	n.a.	n.a.	n.a.	4.68	n.a.	n.a.	n.a.	n.a.	n.a.
P_2O_5	n.a.	n.a.	n.a.	n.a.	n.a.	n.a.	n.a.	n.a.	0.33

Literature data: [a] Webb et al. (2014) and [b] Robert et al. (2015)

Oxides/ ions mol%	NCS[c]	NCS 1.9Cl[c]	NACS[c]	NACS 1.1Cl[c]
SiO_2	74.59	74.00	66.62	65.96
Na_2O	18.98	17.71	16.87	15.57
K_2O	n.a.	n.a.	n.a.	n.a.
TiO_2	n.a.	n.a.	n.a.	n.a.
FeO (* FeO_{total})	n.a.	n.a.	n.a.	n.a.
Fe_2O_3	n.a.	n.a.	n.a.	n.a.
Al_2O_3	n.a.	n.a.	11.28	11.73
MgO	n.a.	n.a.	n.a.	n.a.
CaO	6.42	6.36	5.23	5.61
MnO	n.a.	n.a.	n.a.	n.a.
Cl^-	n.a.	1.93	n.a.	1.13
F^-	n.a.	n.a.	n.a.	n.a.
P_2O_5	n.a.	n.a.	n.a.	n.a.

Literature data: [c] Baasner et al. (2013a)